University of Trento, Italy

UNIVERSITÀ DI TRENTO

Department of Industrial Engineering

Doctoral School in Materials, Mechatronics and System Engineering

Layered double hydroxide based smart protective coating systems

Muhammad Ahsan Iqbal

33rd Cycle

Muhammad Ahsan Iqbal

Layered double hydroxide based smart protective coating systems

Doctoral Thesis

Supervised by

Professor Michele Fedel

Department of Industrial Engineering

33rd cycle

Materials, Mechatronics and System Engineering

UNIVERSITY OF TRENTO

Preface

The thesis is submitted to fulfill the requirement of the Ph.D. degree in Material Mechatronics and System engineering at the University of Trento, Italy during the period 1 January 2018 to December 2020 under the supervision of Professor Michele Fedel. The Ph.D. funding was awarded by the University of Trento and most of the experimental work was completed at the University of Trento, while partially in the University of Connecticut, USA during the 6 months visiting research period from December 2018 to June 2019.

Acknowledgments

I would like to express my deepest gratitude to my Ph.D. supervisor, Professor Michele Fedel (University of Trento) for his guidance, knowledge, advice, caring, and patience for the entire period of my thesis work. I am grateful to him for providing me a healthy, friendly, informative research environment. I would also like to acknowledge Prof. Luyi Sun (University of Connecticut) for his guidance and help. My sincere thanks also go to the Department staff, especially Luca Bendedetti (University of Trento) for his valuable assistance in experiments and eagerness to teach me how to use the different instrumentation located at the department facilities. Special thanks to Dr. Maria Secchi for performing and interpreting Raman Spectroscopic analysis, and Professor Caterina Zanella (Jonkoping University) for providing her help in conducting FIB-SEM analysis and her useful advice. My gratitude goes to my colleagues in the lab for all the memorable moments and positive energy work environment. I would also like to thank the University of Trento for my financial support.

Objective of the Thesis

Corrosion protection of aluminum and its alloys is a challenging subject to widen the service life of material and its industrial usage. Numerous protective measures have been employed for the corrosion protection of aluminum alloys. Chromate based coatings system was in use for a long time to protect the light metals alloys, but after the ban on Chromates based coating (2017) in European Union due to strict health and safety rules and regulations, there is a need to develop environmentally friendly, greener coating systems to functionalize aluminum surface and to provide sufficient chemical and electrochemical stability against the aggressive environment and can possess multifunctional properties.

The present study investigates the designing of the "Layered double hydroxide (LDHs)" based system for the protection of AA6082 alloy, which until now has given not much attention. LDHs demonstrate unique characteristic which helps to obtain special microstructure to attain multi-functional properties along with improved corrosion resistance properties. The methodology proposed the utilization of various LDH based systems and their modifications to achieve active and passive protection. Interests are focused to develop long-term stable, anti-corrosion systems possessing influential corrosion resistance properties and stable compact structures. Besides understandings the utilization of LDHs for corrosion resistance properties, efforts are made to introduce a double-doped LDHs system where self-healing characteristics contribute to the development of advanced coating systems.

Construction of Thesis

The novel environmentally friendly “Layered double hydroxides” (LDHs) thin films were synthesized, through chemical conversion approach, directly on the

aluminum AA6082 substrates, and precisely characterized by various physical and electrochemical approaches. The defining of proper synthetic conditions for the synthesis of LDH is problematic due to the influence of certain parameters which made an impact not only on the structural properties of the LDHs but also on the anticorrosion behavior of LDH. This study focused on the thorough investigation of the optimization of synthetic conditions for LDHs and their effect on LDH assembly, surface morphology, thickness, interaction with corrosion inhibitors to control the corrosion resistance properties.

The first step of the work is to control the synthetic parameters to obtain unique LDHs structural geometries for the development of anti-corrosion thin films. The addition of a complexation agent i.e. urea, ammonium hydroxide was also introduced to obtain distinct surface morphologies. Various LDHs classes were developed on the aluminum substrate in that scenario, for example, MgAl-LDH, ZnAl-LDH, NiAl-LDH, CaAl-LDH, and a detailed comparative study is reported about the dependency of structural- electrochemical relationships. The aim was to find the ideal films' properties, which leads to widening the potential window of corrosion resistance films in the defined electrolytes. To analyses high-temperature applications, calcination of developed MgAl-LDHs is investigated to understand the effect of thermal treatments on the LDHs structure, basal spacing, intercalated anions, and its effects on corrosion resistance properties.

The second part of the thesis is focused on the modification of the LDHs. Initially, graphene is introduced inside the LDHs network due to graphene chemical inertness and electrochemical characteristics. A thorough investigation is reported about the interaction of graphene with LDHs, and the ability of graphene to tune the properties of LDH for the designing of improved protective LDHs films. Specifically, the research focused on the use of graphene to seal the micropores

of LDHs films to promote barrier properties and explore the graphene interaction with the LDHs. Overall, the impedance modulus of the films was compared with the results of virgin LDHs and the efficacy of the graphene-based LDH system is described.

In the third part of the thesis, cerium modified LDHs are developed on the anodic AA6082 substrate to understand the self-healing characteristic of the modified LDHs based system and their long-term protective ability. Rare earth elements found to have a significant inhibiting effect and are the object of considerable scientific interest, exhibiting nontoxic nature. Conceptually, the cerium modified LDH grown on the anodized surface can seal the micropores of the anodized surface (improved barrier properties), while LDHs themselves provide active protection via entrapment of aggressive species and through self-healing properties. The final part of the thesis comprises the introduction of a double-doped effect, where cerium was introduced inside LDHs galleries and further doped with superhydrophobic species to obtain compact LDH multifunctional films with enhanced LDHs corrosion resistance properties. In the case of the double doped cerium-based LDHs films, the improvement in the corrosion resistance properties were observed during the long-term EIS measurements, while superhydrophobic, self-cleaning characteristics, and UV radiation impact on coating was thoroughly reported. Double doped LDHs lead to an influential increment in corrosion resistance properties, durability, and long-term stability.

Furthermore, the role of LDHs as adsorbents for the heavy metals present in drinking water is also reported. Different adsorption models are studied, and adsorption kinetics is reported to understand the adsorption behavior of LDHs against arsenic impurities. The results depicted the successful removal of arsenic

from drinking water with high efficiency than traditionally used materials. Figure 1 demonstrated the general workflow conducted in the Ph.D. academic duration.

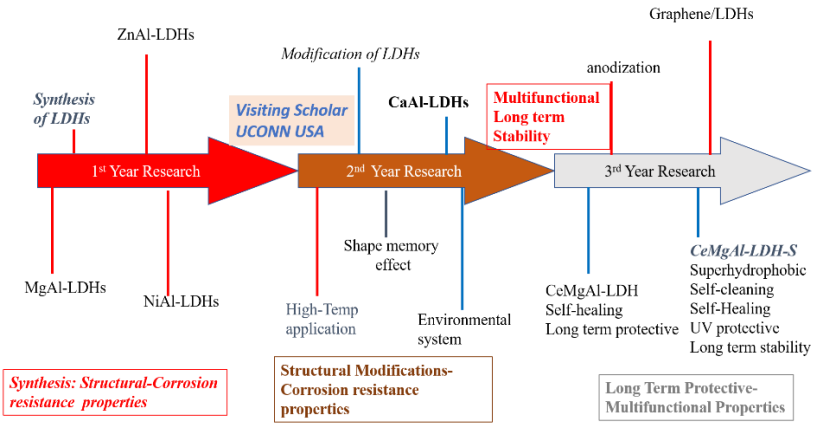

Figure 1. The general timeline of the workflow conducted in the tenure of the Ph.D. research.

Publications during candidature

1. **Iqbal, Muhammad Ahsan**, and Michele Fedel. "The effect of the surface morphologies on the corrosion resistance of in situ growth MgAl-LDH based conversion film on AA6082." *Surface and Coatings Technology* 352 (2018): 166-174.
2. **Iqbal, Muhammad Ahsan**, and Michele Fedel. "Effect of synthesis conditions on the controlled growth of MgAl–LDH corrosion resistance film: structure and corrosion resistance properties." *Coatings* 9.1 (2019): 30.
3. **Iqbal, Muhammad Ahsan**, and Michele Fedel. "Effect of operating parameters on the structural growth of ZnAl layered double hydroxide on AA6082 and corresponding corrosion resistance properties." *Journal of Coatings Technology and Research* 16.5 (2019): 1423-1433.
4. **Iqbal, Muhammad Ahsan**, Humaira Asghar, Muhammad Adeel Iqbal, and Michele Fedel. "Sorption of As (V) from aqueous solution using in situ growth MgAl–NO 3 layered double hydroxide thin film developed on AA6082." *SN Applied Sciences* 1, no. 7 (2019): 666.
5. **Iqbal, Muhammad Ahsan**, Luyi Sun, and Michele Fedel. "Synthesis of novel cone-shaped CaAl-LDH directly on aluminum alloy by a facile urea hydrolysis method." *SN Applied Sciences* 1.11 (2019): 1415.
6. **Iqbal, Muhammad Ahsan**, and Michele Fedel. "Ordering and disordering of in situ grown MgAl-layered double hydroxide and its effect on the structural and corrosion resistance properties." *International Journal of Minerals, Metallurgy and Materials* 26.12 (2019): 1570-1577.

7. **Iqbal, Muhammad Ahsan**, Luyi Sun, Anna Marie LaChance, Hao Ding, and Michele Fedel. "In situ growth of a CaAl-NO 3−-layered double hydroxide film directly on an aluminum alloy for corrosion resistance." *Dalton Transactions* 49, no. 13 (2020): 3956-3964.
8. **Iqbal, Muhammad Ahsan**, Luyi Sun, Humaira Asghar, and Michele Fedel. "Chlorides Entrapment Capability of Various In-Situ Grown NiAl-LDHs: Structural and Corrosion Resistance Properties." *Coatings* 10, no. 4 (2020): 384.
9. **Iqbal, Muhammad Ahsan**, Luyi Sun, Allyson T. Barrett, and Michele Fedel. "Layered Double Hydroxide Protective Films Developed on Aluminum and Aluminum Alloys: Synthetic Methods and Anti-Corrosion Mechanisms." *Coatings* 10, no. 4 (2020): 428.
10. **Iqbal, Muhammad Ahsan**, and Michele Fedel. "Protective Cerium-Based Layered Double Hydroxides Thin Films Developed on Anodized AA6082." *Advances in Materials Science and Engineering* 2020 (2020).
11. **Iqbal, Muhammad Ahsan**, Humaira Asghar, and Michele Fedel. "Double doped cerium-based superhydrophobic layered double hydroxide protective films grown on anodic aluminium surface." *Journal of Alloys and Compounds* 844 (2020): 156112.
12. **Iqbal, Muhammad Ahsan**, Maria Secchi, Muhammad Adeel Iqbal, Maurizio Montagna, Caterina Zanella, and Michele Fedel. "MgAl-LDH/graphene protective film: Insight into LDH-graphene interaction." *Surface and Coatings Technology* 401 (2020): 126253.
13. Iqbal, Muhammad Ahsan, Humaira Asghar, and Michele Fedel. "Ce-Doped-MgAl Superhydrophobic Layered Double Hydroxide for

Enhanced Corrosion Resistance Properties." *Solids* 2, no. 1 (2021): 76-86.

Collaborative Research works

1. Sheremetyev, Vadim, Sergey Dubinskiy, **Iqbal, Muhammad Ahsan**, Konstantin Lukashevich, Sergey Prokoshkin, and Vladimir Brailovski. "Effect of Dynamic Chemical Etching on the Pore Structure, Permeability, and Mechanical Properties of Ti-Nb-Zr Scaffolds for Medical Applications." *Journal of Manufacturing Science and Engineering* 143, no. 5 (2020).
2. **Iqbal, Muhammad Ahsan**, Muhammad Asim Iqbal, and Michele Fedel. "Fire retardancy of aluminum hydroxide reinforced flame retardant modified epoxy resin composite." *Russian Journal of Applied Chemistry* 91.4 (2018): 680-686.
3. Iqbal, Muhammad Asim, **Iqbal, Muhammad Ahsan**, and Atif Javaid. "Synergistic effect of aluminum hydroxide and antimony trioxide on the flammability of phosphorous modified epoxy resin." *Pakistan Journal of Engineering and Applied Sciences* 24 (2019).
4. Asghar, Humaira, Muhammad Adeel Iqbal, and **Iqbal, Muhammad Ahsan**. "Silicon-based carbonaceous electrocatalysts for oxygen reduction and evolution properties in alkaline conditions." *SN Applied Sciences* 1.11 (2019): 1396.

List of Tables

List of Figures

Contents

Chapter 1

1. Introduction

1. Corrosion and corrosion aspects of aluminum alloys

Aluminum is the most utilized industrial material after iron, and possess numerous attractive properties for numerous applications i.e. high conductivity for electricity and heat, readily fabricate into different designs for customer goods, demonstrate one-third of the density compare to the steel, stiffness, strength to weight ratio, and also highly recyclable. Therefore, aluminum alloys are the pillars of industrial materials. Figure 2 shows the total primary production of aluminum alloys for 2017. The corrosion resistance of aluminum alloys is one of the biggest challenges to its cost and economic growth [1]. The weight loss studies reported the 0.03 to 4 μm/year which varies in different atmospheric conditions [2]. To overcome the corrosion reactions various approaches have been employed i.e. surface treatments, anticorrosion coatings, metallography techniques which have been found influential to deal with corrosion [3]. Coatings can support to manage of materials operations, material saving, reduction of environmental pollutants, and can introduce new functional properties for a variety of applications. Strict health and safety regulations demand to design of a new greener, environmentally friendly coating system to substitute the traditional coatings like chromate, phosphate-based, and also there is a need to advance the coating systems to open the new windows of industrial applications. Chromium-based coating systems are used for a long time to protect light metallic materials, but due to health and safety rules and regulation, the usage of carcinogenic chromate coating systems have declined and been banned in European union, while the zinc-based coating systems are discouraged due to zinc price fluctuations. Hybrid materials, composites, unfunctionalized graphene, polymeric coatings, metallic coatings are widely investigated approaches to substitute the traditional coating systems [4].

Corrosion is termed as the metals surface degradation and depends upon several factors i.e. material constituents, electrochemical reactions, material metallography, environmental conditions, and so on. Other definitions of corrosion are;- "Physicochemical interaction between a metal and its environment which results in changes of the material properties which may often lead to impairment of the function of the metal, the environment, or the technical system of which these form a part (ISO 8044-1986)", “Corrosion is an irreversible interfacial reaction of a material with its environment which results in the consumption of the material or dissolution (International Union of Pure and Applied Chemistry (IUPAC))”. Corrosion caused severe expense to the industrial costs due to the massive waste of resources and by the damage of the developed materials [5][6]. Every material has its properties in a specific set of media, which defined the material corrosion reactions [7]. The term reaction is also being used in classifying corrosion based on its mechanism; which can be physical, chemical, or electrochemical [8]. The most significant is the electromechanical reaction, involving the transfer of electrons which initiate corrosion reaction. The word environment is described as the factors/species that caused the corroding of metal at the time of reaction. Such an environment is called corrosive and the material is called corrodible. The defining factors of the environment are thermodynamics, kinetics, metallurgical factors, and nature.

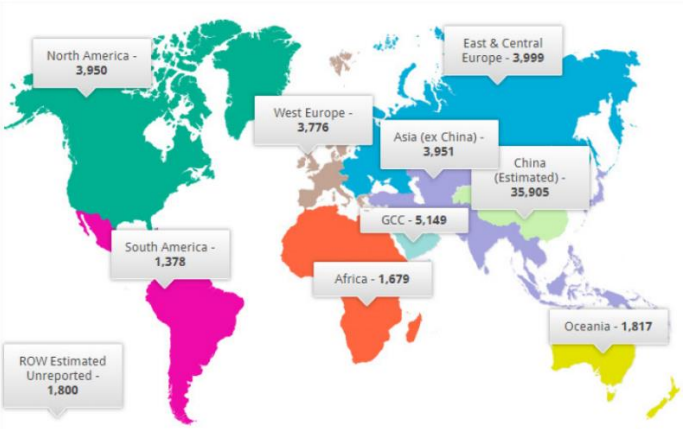

Figure 2. Aluminum production (2017) [9].

1.1. Mechanism of corrosion

Electrochemistry and thermodynamics are considered the main controlling phenomena to control corrosion. Based on the mechanism of corrosion reaction, corrosion is classified generally into three categories (a) Physical, (b) Chemical, and (c) electrochemical. Physical corrosion is a type where solid metal in contact with liquid materials caused dissolutions/penetration into grain boundaries [10]. Chemical corrosion is referred to laws of kinetics accompanied by the electric current, where corrosion of metallic surface in dry gas/nonelectrolytes caused the etching and degradation of parent material [11]. The electrochemical reaction causes the most industrial corrosion followed by anodic and cathodic reactions, where anodic reaction caused the dissolution of the material at the cathodic site, which results in material degradation at specific areas. The electrode is considered as the boundary between the liquid phase (environment) and the solid phase (metallic material), where the reaction process has taken place at the phase boundary. The basic corrosion cell includes the following components; - cathode,

anode, connection, and electrolyte. In general, the removal of any component from the system can obstruct corrosion reaction and that can provide a way to stop the corrosion process. On the other hand, the corrosion in aqueous solution is charge/or electron transfer took place by the electron activity, potential differences, and are affected by the nature of the metal surface. Thermodynamics involves the energy changes due to electrochemical reactions that control the corrosion chemical reaction. The understanding of thermodynamics helps to control the conditions which are the basics of corrosion reactions, but it is difficult to estimate the corrosion rate once it is initiated. The more active half-cell/negative cell has the potential to oxidize, while the noblest metal tends to reduce, and such alloy combinations will initiate corrosion. Industrially the major concern is the control of corrosion rate, and the prediction of conditions on which corrosion reaction depends, which determines the mechanism of the overall process.

1.2. Forms of corrosion

The corroded metals are generally grouped in the following forms of corrosion (ASM 2000), localized corrosion, Uniform corrosion, filiform corrosion, galvanic corrosion, deposition corrosion, intergranular corrosion, erosion-corrosion, stress cracking corrosion, filiform corrosion, cavitation corrosion, Microbiological induced corrosion [12].

1.2.1. Localized Corrosion

A micro galvanic cell is formed when the intermetallic element of different electrochemical activity contributes to an alloy formation and the alloy comes to contact with the electrolyte. The phase with lower electro potential acts as an anode, while the other with higher electro-potential serves as the cathode. The

aluminum oxide protective film formed on the surface did not provide protection uniformly all over the surface due to the presence of intermetallic and caused defects which promote localized corrosion. Figure 3 demonstrates the overall view of localized corrosion on the surface of the aluminum. (a) The more noble electrochemical phases caused the cathodic process and initiate oxygen reduction reactions by the formation of hydroxyl ions, (b) The aluminum dissolution in the aluminum matrix results in the anodic process, (c) Electron transfer between cathode and anode in the bulk alloy taken place, (d) Acidification produced inside the pits due to hydrolysis and cause acidification of the solution at the anodic sites.

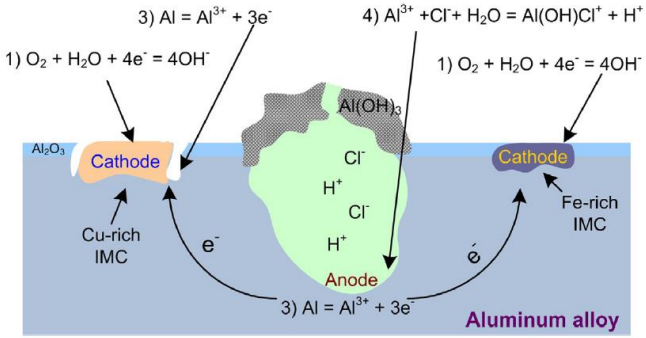

Figure 3. Localized corrosion attack on aluminum alloy [13].

1.2.2. Uniform Corrosion

Uniform corrosion also termed General corrosion occurs in solutions such as concentrated solutions, rich in chlorides with varying pH from mild to acute. Aluminum alloys are most susceptible to uniform corrosion in acidic or alkaline media, thus are the cause of uniform corrosion. Crevice corrosion is a form of Localized corrosion that results from the gap or overlap of two metallic parts i.e. between the structure and the bolt. When water/electrolytes enter the gap and caused deaeration, results in an oxygen reduction reaction (more acidic) thus

increases the corrosion rate. Figure 4 demonstrated the crevice corrosion mechanism for corrosion reactions.

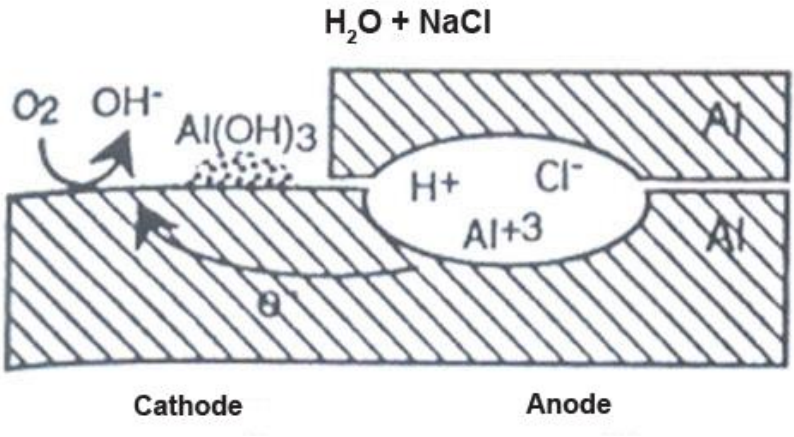

Figure 4. A schematic representation of crevice corrosion of an aluminum alloy [14].

The pitting potential is another extreme form of localized corrosion, manifested in the random formation of pits/cavities. Pitting of aluminum alloys occurs at defects (phase particles/ grain boundaries) in the low level of anions concentration. Figure 5 represents the general representation of the pitting corrosion mechanism.

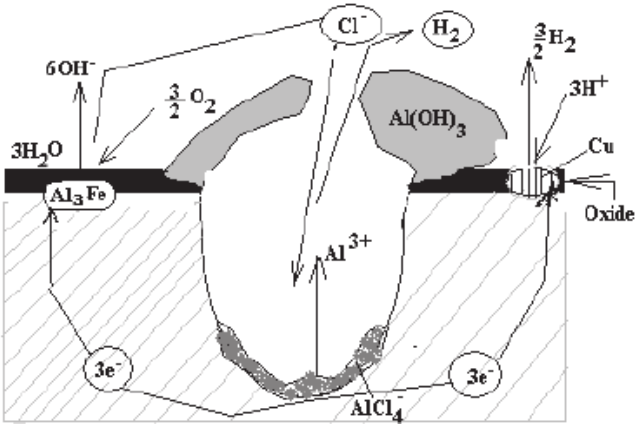

Figure 5. General representation of pitting corrosion [15].

1.2.3. Galvanic Corrosion

Galvanic corrosion in the case of aluminum occurs when aluminum relates to more noble metals and both come into contact with electrolytes. The galvanic couple formed due to potential differences and cause degradation.

1.2.4. Deposition Corrosion

Several metals that are more cathodic than aluminum alloys can reduce the metallic form of corrosion during the designing of aluminum alloys. Reduction of these heavy metals (copper, lead, mercury, nickel, and tin), even in small number, lead to severe localized corrosion during to galling cell formation on aluminum palates.

1.2.5. Intergranular Corrosion

Intergranular corrosion occurred at the grain boundaries/ closely adjacent regions, caused due to the different thermodynamic treatments and the presence of different materials in alloy formation. This caused the different anodic paths on the grain boundaries locations and caused the depletion of elements i.e. copper in AA2xxx alloys etc. Among the developed aluminum alloys, the AA6xxx series have shown reasonable resistance for this sort of corrosion, However, intergranular attacks can be initiated in aggressive media.

Exfoliation corrosion can be considered the class of intergranular corrosion, which is caused due to the grains flattened during the rolling of the material and subject to deformation. Such corrosion processes are more commonly observed in AA2xxx, AA7xxx series of alloys, where grain boundary regions are more vulnerable to depletion and can be handled by the remedies just like intergranular corrosion reactions.

1.2.6. Erosion-Corrosion

Erosion corrosion of aluminum alloys occurred in high-velocity fluids and accelerated in high pH especially in carbonated and high silica contents in water. Generally, aluminum is considered stable in water and becomes corroded in acidic/alkaline media. To reduce the erosion-corrosion, pH level, solution concentration and velocity of fluid managing is a crucial factor.

1.2.7. Stress Corrosion Cracking (SCC)

Stress corrosion cracking (SCC) happened in suspectable aluminum alloys in a humid environment when tensile stress caused the propagation of cracks and thus can form intergranular stress corrosion cracking and transgranular stress corrosion

cracking, followed by the crack in grain boundaries and cracks cut through grains respectively.

1.2.8. Corrosion Fatigue

Corrosion fatigue is the repeatedly stressed condition on the aluminum structure in a corrosive environment that can initiate crack and it can propagate under crack opening stress. Corrosion fatigue is more dominant in the low-stress air environment, compared to seawater or other conditions. The trans-granular fracture appears in corrosion fatigue and required a water presence for corrosion propagation.

1.2.9. Filiform Corrosion

Filiform corrosion is the general problem of painted aluminum alloys, where paint defects/pinholes act as initiation sites for corrosion initiation. Filiform corrosion propagates under the presence of chlorides and high humidity.

1.2.10. Microbiological Induced Corrosion

Microbiological induced corrosion (MIC) is caused by the accumulation of biological organisms, where the growth of fungus/microorganisms at the metallic surface developed oxygen/fuel interface and excrete an acid that caused pits/cracks and further the corrosion. To overcome the MIC, it is recommended either to manage the fuel quality and control the water into the fuel supplies in the fuel tanks, or fungicides are sometimes introduced in the system.

A general comparison of different forms of corrosion is discussed in Figure 6, and the systematic classification of different forms of corrosion is demonstrated in Table 1.

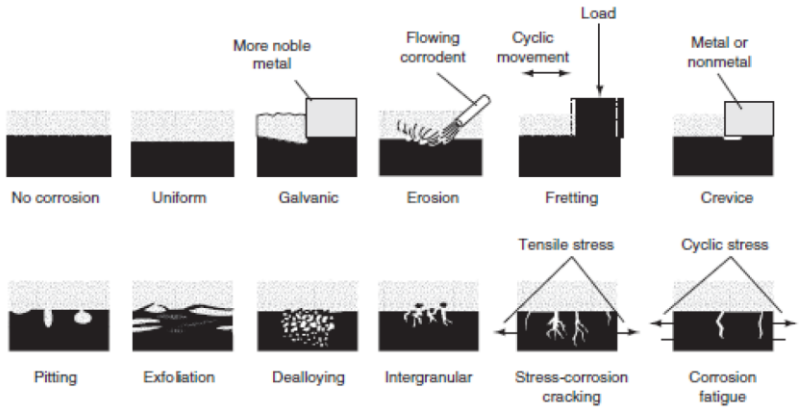

Figure 6. Schematic summary of the various forms of corrosion (ASM, 2000).

Table 1. ASM classifications of corrosion types.

Generally, corrosion	Localized corrosion	Metallurgical influenced corrosion	Mechanically assisted degradation	Cracking/environmental
Corrosion attack by uniform thinning	Metal penetration at a specific site	Heat treatment and metallurgy	Mechanical component corrosion	Environmental Stress-induced corrosion
Galvanic corrosion	Filiform corrosion	Dealloying corrosion	Fretting corrosion	Hydrogen damage
Stray current corrosion	Pitting corrosion		cavitation	Liquid metal embrittlement
Atmospheric corrosion	Crevice corrosion	Intergranular corrosion	Erosion corrosion	Stress cracking erosion
Biological corrosion	Localized biological corrosion		Corrosion fatigue	Solid metal induced embrittlement
High-temperature corrosion				
Molten salt corrosion				

1.3. The role of chemistry on corrosion

The addition of alloying elements in aluminum brings specific chemical and mechanical characteristics with a heterogeneous microstructure that make a compromise on the materials corrosion resistance properties. Every alloy element demonstrated a different effect on aluminum corrosion and that makes a prominent factor to design aluminum alloys. The general E-pH diagram may provide the prediction of corrosion processes but in the presence of several parameters on the industrial scale, it becomes difficult to consider the exact

corrosion rate. The possible factors in that sense are; - temperature, the various concentration of electrolytes, alloying elements, mode of corrosion, corrosion kinetics, etc. For general representation, the E-pH diagram of the aluminum is shown in Figure 7, where it provided a conclusive thermodynamic process that allows us the understanding to design an alloy because of corrosion resistance properties. The diagram provides a general estimation of the conditions for the aluminum corrosion attacks, stability, passivity, and immunity for the corrosion. However, the E-pH diagram did not indicate the passivity under strong acidic solutions. The effect of different alloying elements is discussed in the below section.

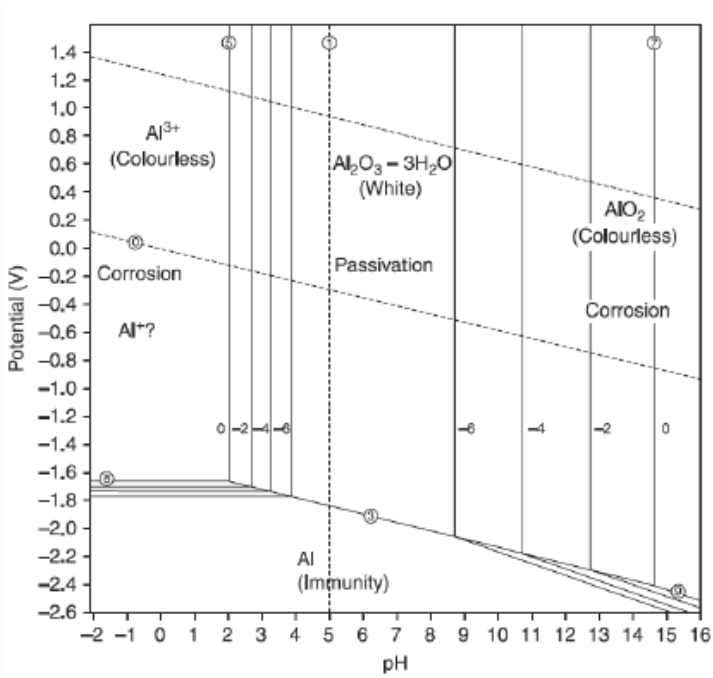

Figure 7. E-pH diagram of Aluminum [15].

1.3.1. Influence of magnesium

Magnesium is found one of the major elements in the 6xxx series and is found to improve the mechanical properties of the alloy and stabilize the GP zone and decrease the alloy density. Furthermore, Mg decreases the rate of cathodic reactions and increases corrosion resistance. However, excess Mg in the alloy will cause the precipitation at grain boundaries [16,17] [18] [19][20] and are known to be anodic concerning aluminum matrix and can become susceptible to localized corrosion [21–23]. This is also reported that magnesium in the 6xxx series can precipitate with other alloying elements and can strengthen the alloy [24–27].

1.3.2. Influence of silicon

The addition of silicon in 6xxx series with magnesium alloy in conjunction precipitate Mg_2Si which enhances the mechanical properties [28,29] [30,31]. The composition provides the strength but also causes pitting corrosion, where Mg_2Si acts as more anodic than the aluminum matrix and dissolute in the matrics with intergranular corrosion and stress cracking corrosion. Excess silicon however enhances cathodic reaction rate [31].

1.3.3. Influence of copper

Copper in the aluminum matrix formed cathodic particles Al_2Cu and has a determining role in corrosion protection. Copper is low quantity in 6xxx provides strength with improve hardness. Al_2CuMg (S- phase) present in Al-Cu-Mg alloys caused a potential difference between more noble and Mg contents phases, which caused the dissolution of magnesium in the matrix and copper redistributed at/near the sites of Al_2CuMg [32,33], [34].

1.3.4. Influence of zinc

In the 6xxx series, zinc in a low amount is added for hardening and stimulate precipitation where the intermetallic like $MgZn_2$ is evenly distributed throughout the aluminum matrix [31,35].

1.3.5. Influence of manganese

Maganese in the 6xxx series is found effective to reduce the pitting corrosion and modify the ferrous-containing intermetallic particles by reducing the iron concentration and make it nobler with the formation of Al_6MnFe [36]. However, it is also reported that excess manganese can lead to the cathodic reaction when are beyond the soluble limit.

1.3.6. Influence of other elements, including Zr, Cr, Sc, Ti, W, and Sr

These elements are added in very small amounts to refine the grains, reduce recrystallization, and avoid undesired intermetallic compounds [21]. Their effect besides metallurgical characteristics is the corrosion resistance properties by minimizing the intermetallic to avoid localized and stress-induced corrosion. Microstructure tunes the corrosion resistance properties and such elements addition provide improved corrosion resistance properties [37]. The corrosion potential of different intermetallic alloys is represented in Table 2.

Table 2. Intermetallic corrosion potential in 0.1M NaCl solution [15].

Phase	Corrosion Potential mV (SCE)
Al_3Fe	-539
Al_2Cu	-665
Al_6Mn	-779
Al_3Ti	-603
Mg_2Al_3	-1013
$MgZn_2$	-1029
Mg_2Si	-1538
Al_7Cu_2Fe	-551
Al_2CuMg	-883
$Al_{20}Cu_2Mn_3$	-565

1.4. The role of microstructure on corrosion

The role of the microstructure is a vital parameter to understand the corrosion resistance properties of aluminum alloys. Alloying elements contribute to the alloy microstructure and have a significant impact on determinable corrosion behavior. For homogenous alloys, corrosion attack is low due to the lack of microstructural defects and attack sites. However, heterogeneous alloys are of specific interest that mentioned superior mechanical properties but also is susceptible to localized corrosion attacks. The most common reason for the corrosion attack is the intermetallic particles and are categorized into the following classes, (a) Constituent particles, including the insoluble elements, impurities in the size of few microns to tens of microns, (b) Precipitates formed from nucleation and growth in the range of nm [38]. Each microstructural variation brings different electrochemical characteristics that provide potential differences and attacking sites for corrosion reactions. Numerous authors have reported comprehensive work on the simulation of microstructural features and corrosion reactions and demonstrate the corrosion mechanisms in detail [39][25]. However, there are still uncertainties in multi intermetallic particle roles and their

contribution to corrosion measurements under different stimuli. In multi ternary and above alloying elements incongruent dissolution of alloying elements decide the anodic and cathodic sites an [32] intermetallic contains Cu and Mg, whereby the corrosion attack is also dependent upon pH, temperature, and humidity conditions which decided the pitting corrosion phenomenon and localized intermetallic attack. but this does not necessarily mean the pit will propagate deeper [40]. Alloying elements control the microstructure of the aluminum alloys and further contribute to the corrosion resistance properties. Corrosion potential of different aluminium alloys is described in Table 3.

Table 3. Corrosion potential of aluminum alloys in 1M NaCl solution containing H_2O_2 [15].

Material	Corrosion potential (V_{SCE})
Pure aluminum	-0.75
Pure Cu	0.00
Mg	-1.64
Fe	-0.55
Zn	-0.99
2024-T3	-0.60
3003-	-0.74
5052-	-0.76
6063-	-0.74
7075—T6	-0.74
8090-T7	-0.75

1.5. Corrosion prevention and control

One way to suppress the corrosion rate is the modification of the properties of the material, change in environmental conditions, applications of coatings, and play with electrochemical reactions of the materials and electrolytes. Further, it is also an estimation point, either corrosion is needed to be avoided or merely controlled. The decision of control of corrosion, where it must be suppressed, avoided, or just

merely controlled solely depends upon the economics of the materials involved and the process of the reactions. Corrosion prevention of materials depends upon the modification of environmental introduction of corrosion-resistant materials, and electrochemical approaches, In that scenario, the introduction of coatings and their importance is the key parameters and prevention techniques i.e. barrier effects, cathodic protection, inhibitions, materials selection are the factors generally employed to control the corrosion. Generally, the mechanism of anticorrosion coating is differentiated into the following categories (a) Inhibition of the corrosion reactions, (b) creating barrier between the environment and the materials of contact, (3) introduction of corrosion resistance coating acting as sacrificial materials. Recently, the new concepts of collective active and passive corrosion protection is employed, where barrier layers formed provide passive protection, while the corrosion inhibitors in the coating system provide the active protection against corrosion where the active and passive layers, impede the corrosion half-reaction resulting in the depletion of electrons [41]. Electrochemical protection involves the controlling of surface potential, which is either more positive (anodic polarization) or more negative (cathodic polarization), where electrons are either removed from the surface which results in positive protentional or electron are supplied to the metallic surface which slows the reaction rate and develops negative potential. These factors are considered crucial parameters in the development of preventing coating systems.

1.6. Developments in Corrosion Protection

Thermodynamically, corrosion is possible for most environments and that makes primary attention to know how to protect and control the corrosion. Chemical kinetics predict the corrosion rate and corrosion reactions, and fundamental laws

of electrochemical reaction assist to protect the alloys from corrosion reactions and to develop more corrosion-resistant material [42]. Electrochemical reactions involve the release or acceptance of electrons and thus that flow measures the corrosion current. A general overview of the corrosion protective approaches is demonstrated in Figure 8, where the following ways are reported to manage corrosion control:- (a) Design improvement of material, (b) Alter the material properties, (c) influence the environmental conditions, (d) potential changes of metals, (e) Coatings. Coatings illustrate the facile approach to protect the underneath material by benefiting the system cost, service life, stability, and where additional properties of the material are needed. The formulation of corrosion inhibitors and their incorporation in the coating system is illustrated in Figure 9. The step-by-step approach conducting on the corrosion inhibitors enables the formulation of a protective coating system for metallic alloys.

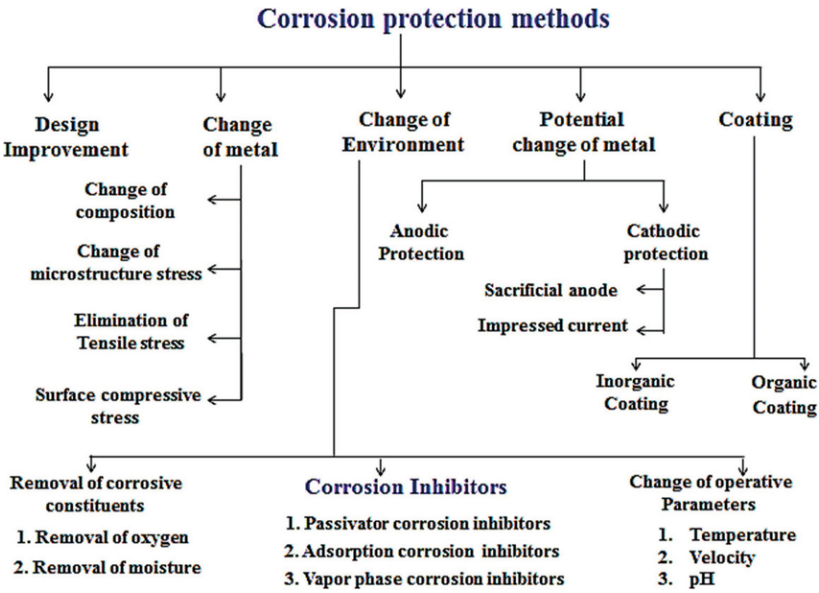

Figure 8. Corrosion protection methods [43].

1.7. Coatings

Coatings are a mostly considered multi-layered system, where the function of each layer is interactive and specific. Coatings that can be organic, inorganic, or metallic are found to provide barrier properties, thus mostly act as sacrificial coatings. Metallic coatings are mostly applied by spraying, chemical conversion, diffusion, electrodeposition, and generally exhibit formability with sufficient barrier characteristics. Organic coatings provided a thin barrier between the environment and the substrate, but coatings porosity/defects can cause accelerated localized attacks because of galvanizing defects. The other commonly applied protective coating systems are:- chemical vapor deposition, physical vapor deposition, electro galvanizing, and thermal spraying, ion beam, immersion, welding, etc. Environmental and health regulations have made the restriction on

the usage of phosphate and chromate based coating system, therefore continuous efforts are devoted to finding the replacement by taking into consideration rare earth metals, silicate-based, titanium oxide, and zirconium oxide-based systems, and so on [44] [45] [46–50].

Generally, barrier effect is considered the main mechanism for materials coating protection, and further addition of corrosion inhibitors is taken as an active approach to enhance corrosion resistance properties. Surface passivation can also be formed due to the firmly bonded upper coating layer. For example, aluminum formed an aluminum oxide layer, which acts as a barrier layer and can protect the aluminum from corrosion except in the silane environment [51,52]. Corrosion is caused by the formation of electrochemical cells, where anodic sites are depleted and benefit the cathode. Electrochemical cells are formed whenever surface uniformity is disturbed and results in the cathodic and anodic area whereby moisture, oxygen act as an electrolyte. In sacrificial coating, the preferential dissolution of the coating takes place to protect the substrate and is termed as sacrificial protection. The introduction of various corrosion inhibitors inside the coating system is regarded as active protection, where inhibitors act as additional corrosion protection beyond the general coating barrier layers and offered enhance corrosion protection. However, the choice of corrosion inhibitors is related to system complexity, technical and economic difficulties. To solve that problem, the self-healing concept is deployed, where inhibitors are added in the conventional coating system to heal the damaging effect of corrosion. Numerous works are conducted on the deployment of ceramic coatings, but over time ceramic materials have proven to be brittle and fail to protect the constructive materials. *Zhang and Tang et al* [53] published a thorough review of the patents

for polymeric corrosion resistance materials and concluded the pro and cons of various polymeric materials as anti-corrosion materials.

Organic coatings are the most employed coating films to protect metallic alloys with vase applications in different sectors of metallic materials. It consists of alloy pre-treatment, primer, and top coating as shown in Figure 9. Numerous variables affect the choice of suitable organic coatings such as the nature of electrolytes, environmental conditions, and are characterized by various functional groups. Organic polymeric materials are characterized by different functional groups and materials corrosion resistance properties influentially depend upon the coating functional groups, thickness, friction resistance, shape, and so on [53]. Composite materials demonstrated the properties of good adhesion, self-healing, strain recovery, conductivity. To replace traditional coating systems, many environmentally friendly composite coatings such as vanadate based, fluorometallate based systems are actively investigated [54].

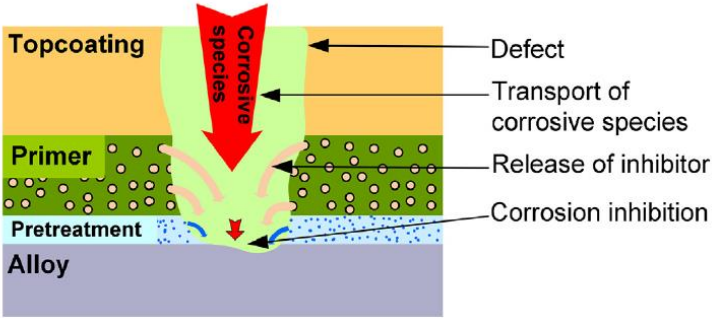

Figure 9. Schematic representation of the active corrosion protection system for aluminum alloys [61].

1.8. Anti-corrosion coating: New and emerging materials

In recent years, efforts are made to develop a new generation of emerging and novel coating materials that are much of the coating industry's interest. The emergence of specific design, active materials may support the reduction of expenses expand on the corrosion of materials. The researchers also focused on the development of stimuli-responsive smart coating, which can be engineered for large-scale industrial applications. The smart coating is developed based on their electric current, humidity, temperature, pressure, pH-controlled stimuli, and applications in those fields. Smart coatings are generally described by three categories; (a) microcapsule healing, (b) Self-healing characteristics, (c) Anticorrosion coatings. The self-healing concept was modeled based on the coating healing process, which can be linked to the coating underlying performance. The introduction of corrosion inhibitors into the coatings for healing can be achieved by various synthetic approaches [55]. Nanocoating composites are the recent trends to control corrosion and develop anti-corrosion thin films due to their unique physical and electrochemical properties due to the encapsulation/incorporation of the nanoparticles inside the coatings for specific features [56]. To replace chromate treatments, various chemical conversion approaches of phosphorous, titanate, zirconate, rare earth and electrochemical process like organic polymeric coatings, anodic coatings, silane films, etc are introduced. The following approaches are used to incorporate the corrosion inhibitors inside the coatings; -

(a) Inorganic anion-exchange containers
(b) Core-shell containers
(c) Functional layers for storage
(d) Direct incorporation of inhibitors in the matrix

(e) Layer-by-layer assembled nanocontainers

Layer-by-layer assembly of thin-film coatings is used as an efficient treatment in corrosion protection of aluminum alloys, where nanocontainers can be stored inside the active coating system and provide active and passive protection. The coatings that held nanocontainers showed better inhibitive properties and self-healing abilities. The general approach of self-healing includes the incorporation of inorganic/organic pigments inside the layered structure of the films due to charge difference and on contact with a basic solution, the coatings release the corrosion inhibitors. Layered double hydroxide (LDH) are a unique class of ion-exchange materials where the controlled release of corrosion inhibitors, incorporation of inorganic/organic pigments inside the LDH framework made them suitable coating system for further investigation. The main difference between an ion-exchange container with other nanocontainer materials is loading efficiency, facile synthesis growth, sample preparation, and interaction with the substrate and the environment. This thesis emphasizes the fundamental understanding of the LDH synthesis and the parameters that affect the structural growth, geometry, interlayer thickness, adhesion, uniformity, and the relation of structure to the corrosion resistance properties. This knowledge is effectively used to optimize the synthetic conditions following the anticorrosion behavior and potential towards an ion-exchange mechanism for different classes of LDHs. Afterward, the modification of the LDH structure to enhance the corrosion resistance properties is explored by introducing the graphene flakes and by the calcinations. Finally, a detailed investigation is made on the effect of the introduction of rare earth elements inside the LDH, and understanding of self-healing characteristics are monitored and finally, the double doped effect is introduced where two different corrosion inhibitors are introduced for the sake of

long service life and to achieve special characteristics i.e. superhydrophobicity, self-cleaning, UV resistance, etc. Such systems can become the choice to replace chromium-based coating systems due to compatibility with inorganic/organic pigments, inhibitors storage, self-healing characteristics. The best systems must have combined properties of long service life, stability performance, efficiency, and facile synthesis approach.

Chapter 2

2. Literature Review

2.1. Layered double hydroxide

Layered double hydroxides are expressed by the general expression $[M^{2+}_{1-x}M^{3+}_{x}.\ x(OH)_2]A^{n-}_{x/n}\cdot mH_2O]$, where M^{2+} are divalent cations, while M^{3+} is trivalent metal cations and "A" represents the n-valent anions. The LDH structure is organized when M^{2+} is substituted by M^{3+} and A^{n-} anions are used to balance the net positive charge [57–60], and the molar ratio of $M^{3+}/(M^{2+} + M^{3+})$ range from 0.20 to 0.33 [61, 62]. Due to the anion exchange capability of LDHs, various anions can be successfully incorporated inside the LDH interlayer to modify the chemistry of LDH for specific applications: for instance, supercapacitors, environmental sciences, catalysts, adsorption, and so on Figure 10 [63–69]. The possibility of the development of layered three-dimensional structures incorporated with inorganic components opens new windows for novel properties.

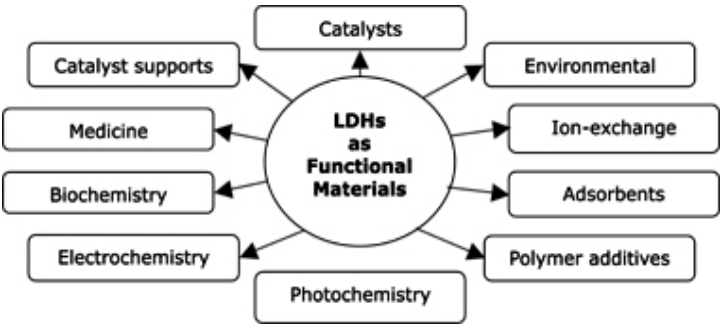

Figure 10. Applications of Layered double hydroxide [70].

Recently, in the subject of anti-corrosion materials, layered double hydroxide (LDH) based coating systems have gain attention due to LDH's peculiar morphology, a wide range of cationic/anions combinations, environmental friendliness, barrier properties, high surface to volume ratio, and multifunctional design along with the capability to intercalate various species, such as metal ions

of mixed valences, complex inorganic, organic molecules in the in LDH interlayers, and thus can be utilized as multifunctional coating systems. The LDHs film thickness, number of layers, composition, surface geometry, and morphology are found to influence the ability of LDH to encapsulate various functional groups and can be controlled with the adjustment of synthetic conditions, fabrication methodology, and initial salt concentrations [71–73]. Furthermore, the interlayer anions and ratio of metal cations can largely impact orientation, crystal structure, and surface geometry [74]. The LDH protective mechanism includes the following key features; (a) the anion-exchange ability, (b) the self-healing mechanism, and (c) barrier effect, which are found to improve the anti-corrosion properties. Considering the ion exchange equilibrium constant, the nitrate ions demonstrate the lower value in the following order: $NO_3^- < Br^- < Cl^- < F^- < OH^- < MoO_4^{2-} < SO_4^{2-} < CrO_4^{2-} < HAsO_4^{2-} < HPO_4^{2-} <$ Naphthol Yellow^{2-} $< CO_3^{2-}$ [75]. That's the reason a lot of research has been conducted on LDH-NO_3, where nitrate groups act as active precursors to modify the LDH chemistry with different anticorrosion inhibitors through ion-exchange and can design multifunctional coating systems for corrosion protection. To develop a compact LDH coating system, two main strategies have been pursued: (a) loading of corrosion inhibitors/anticorrosion pigments inside the LDHs; (b) LDHs dispersed/coated with polymeric coating matrix to protect the metallic surface.

The following advantages made LDHs a promising choice to consider for the investigation of anticorrosion films.

1. Easy synthesis routes.
2. Low-cost precursors
3. High surface to volume ratio
4. Positively charges layers neutralize by interlayered anions

5. High loading efficiency
6. Adsorbents
7. Chemical and structural stability
8. Easy availability of precursors
9. Interaction with inorganic/organic pigments

2.2. Synthesis of LDH on aluminum and aluminum alloys

Given LDH based protective coatings, coprecipitation and in situ growth methods are the widely investigated approaches with various customized reaction/host modifications to develop LDH based systems. Here, we discussed in detail these two approaches and their modifications in terms of coating resistance properties.

2.2.1. Coprecipitated synthesis

The coprecipitation approach is an illustration of the ex-situ method where the LDHs precursors are initially synthesized in powder form and applied on the aluminum surface by using certain techniques. The coprecipitated LDH precursors are synthesized by the combination of divalent and trivalent cationic salt solutions and exhibit the advantages of high purity, crystallinity, controlled chemical composition, and significant interaction with organic/inorganic inhibitors. On the other side, the adhesion to the surface is inconsistent. In recent years, several reviews sum up the work on the synthesis of layered double hydroxide and the parameters/conditions affecting their formation [76–81]. *Frederick et al.* did a comprehensive review of the synthesis of LDH by the coprecipitation method [81]. Recently, *Bukhtiyarova et al* [74] reported a concise review on LDHs synthesis and discussed in detail the various parameters that affect the growth of

LDH i.e. synthetic solution pH, salts concentration, nature of alkaline solution (NaOH, urea, ammonia, ammonium carbonate, etc), aging time, reaction temperature, and molar cationic ratios. The synthetic conditions - including the initial concentration of salts, crystallization time, solution pH, precipitating agents, and the ratio of divalent to trivalent cations have been found to have an influential impact on LDH structure, functional properties, and crystal structure parameters [82]. To enhance the corrosion resistance properties, the LDHs coating system can also be modified either with the various corrosion inhibitors/ anticorrosion pigments by taking the advantage of LDHs anion exchange, or by the utilization of dispersed LDH in the polymeric/organic systems. The self-healing capability of LDHs also makes them a viable material to enhance the corrosion resistance properties. *Buchheit et al.* initially developed ZnAl-LDH based coating system by using the coprecipitation method and further introduced it on the aluminum 2024 alloy [83] and reported the intercalation of decavanadate corrosion inhibitor inside LDH galleries [84]. *William et al.* [85] synthesized ZnAl-LDH intercalated with nitrate, carbonate, and chromate and processed it on organic coated AA2024 alloy. They also investigated the various anti-corrosion pigments (oxalate, benzotriazolate, ethyl xanthate) to protect the AA2024 [86]. *Zheludkevich et al.* [87] synthesized MgAl and ZnAl-LDH loaded with divandate anions in the LDH interlayers and investigated the controlled release behavior and corrosion resistance properties of resultants to protect the aluminum AA2024.

2.2.2. In situ growth method

In situ growth approach is considered a promising choice to develop LDH directly on the substrate with the advantage of a more facile approach, controlled film thickness/size, distinct surface morphologies, strong adhesion between LDH and the substrate, and feasible to coat complex geometries. The successful intercalation with various inorganic/organic anions can be achieved by controlling the differential growth of LDH islands on the surface-active intermetallic/active zones. The aluminum alloys act as a source of Al^{3+}, where the aluminum surface starts dissolution in a basic solution to form aluminum oxides. $Al(OH)_3$ reacts with water to form a mixture of precipitated divalent cations and OH^- on the surface of $Al(OH)_3$. The substitution of divalent cations with Al^{3+} ions results in the coexistence of $Al(OH)_3$ and $M^{2+}(OH)_2$ to form the LDH structure. On the other hand, the hydroxyl ions present inside the galleries were exchanged by the solution anions (depending on ionic radii's). LDHs formed a compact layer at LDH/interface, followed by a comparatively porous LDH network.

In recent years, the introduction of various corrosion inhibitors has been reported in in-situ growth LDHs to develop hybrid LDH/polymeric structures to achieve better stability. Polymeric primer layer can provide enough binding support and inhibit the diffusion reactions. However, the basic issue of self-healing is still not thoroughly investigated in different situations, and defects/scratches may remain open for continuous interference of aggressive species with the coating systems.

Synthetic conditions have many crucial parameters to control the in situ growth of LDHs; reaction temperature and aging time strongly affected the crystallinity and geometry of LDH. The pH of the synthetic solution is another factor that can influence the composition of developed LDH. For example, in the

case of Zn-based LDH, it is reported that a solution pH higher than 12.6 causes an increase in the wt% ratio of ZnO/LDH. while ZnO is found highly soluble in NaCl solution, thus a reduction in corrosion resistance properties is reported. Elevated pH can also cause cracks and defects and can favor the formation of secondary phases.

Urea hydrolysis is another approach to obtain the fine distribution of crystallites and a high degree of crystallinity, but urea hydrolysis promotes the formation of carbonate ions in the system which restricts the anion exchange capabilities of LDHs [88]. The complete overview of synthetic approaches and relevant parameters is mentioned in Table 4.

Table 4. Synthetic conditions for the development of LDHs.

LDH	Anion-exchanger	Precursors	Alkaline media	Method	Al alloy	Synthetic condition			Ref.
						°C	pH	Aging time (h)	
ZnAl	V	$ZnCl_2$, $AlCl_3$	NaOH	coprecipitation	2024	55	6.3-6.5	12	[83]
ZnAl	V	$ZnCl_2$, $AlCl_3$	NaOH	coprecipitation	2024	55	6.3-6.5	12	[84]
MgAl	(MBT)/ (QA)	$Mg(NO_3)_2$, $Al(NO)_3$	$NaNO_3$	coprecipitation	2024	65	10	24	[89]
ZnAl		$Zn(NO_3)_2$, $Al(NO)_3$			2024	65	10	24	
$ZnAlVO_3$		$Zn(NO_3)_2$, $Al(NO_3)_3$, $NaVO_3$	NaOH	coprecipitated	2024	65	9.5	24	[87]
$MgAlVO_3$		$Mg(NO_3)_2$, $Al(NO_3)_3$, $NaVO_3$	NaOH	coprecipitated		65	9.5	24	
ZnAl	V	$Zn(NO_3)_2$, $Al(NO_3)_3$,	$NaNO_3$	coprecipitation		65	10	24	

MgAl	V	$Zn(NO_3)_2$, $Al(NO_3)_3$,	$NaNO_3$	coprecipitation		65	10	24	
ZnAl	4-ABSA, 3-ABSA 3,4-HHBA	$ZnCl_2$, $AlCl_3$	NaOH	coprecipitation	2024	30	9	12	[90]
ZnAl		$ZnCl_2$, $AlCl_3$	NaOH	coprecipitation	2024	30	10	12	[91]
ZnAl	NaCO3	$ZnCl_2$, $AlCl_3$	NaOH	coprecipitation	2024	30	9	12	
ZnAl	K_2CrO4	$ZnCl_2$, $AlCl_3$	NaOH	coprecipitation	2024	30	10.5	12	
ZnAl	$Na_2C_{10}H_{14}N_2O$	$ZnCl_2$, $AlCl_3$	NaOH	coprecipitation	2024	30	10	12	
ZnAlCe		$Zn(NO_3)_2$, $Al(NO_3)$,$Ce(NO_3)_3$	$NaNO_3$	coprecipitation	2024	65	10	18	[92]
ZnAl	V	$Zn(NO_3)_2$,	--	Insitu	2024	<100	7	-----	[93]
ZnAl*	laurate	$Zn(NO_3)_2$,	NH_4NO_3	Insitu	Al	45	6.5	36	[94]
MgAl	8HQ	$Mg(NO_3)_2$	NH_4NO_3	Insitu	Al	100	9	48	[95]
MgAl	C_6H_5COON	$Mg(NO_3)_2$, urea	NH_4NO_3	Insitu	6061	45	10	24	[96]
ZnAl*	V	$Zn(NO_3)_2$,	NH_4NO_3	Insitu	2198	45	7	------	[97]

ZnAl*	V	$Zn(NO_3)_2$		NH_4NO_3	Insitu	2024	95	6.5	0.5	[98]
ZnAl*	V	$Zn(NO_3)_2$		NH_4NO_3	Insitu	2024	95	6.85	0.5	[99]
NiAl		$Ni(NO_3)_2$, NH_4NO_3		NH_4OH	Insitu	Al	85		40	[100]
MgAl		$Mg(NO_3)_2$, NH_4NO_3			Insitu	5005	125	8-10.5	1-8	[101]
MgAl	Laurate, Stearate, oleate	$Mg(NO_3)_2$, urea			Insitu	Al	70		24	[102]
ZnAl		$Zn(NO_3)_2$, NH_4NO_3		NH_4OH	Insitu	Al	120	6.5	---	[103]
MgAl	Stearic acid	$Mg(NO_3)_2$, NH_4NO_3		NH_4OH	Insitu	5005	125	10	4	[104]
ZnAl	Mo, graphene	$Zn(NO_3)_2$, NH_4NO_3,			insitu	2024	45	8.8	6	[105]
MgAl	Sol gel	$Mg(NO_3)_2$, $Al(NO_3)_3$		NaOH	coprecipitation	2024	70		18	[106]
ZnAl	Stearic acid	$Zn(CH_3COO)_2$		NH_4OH	insitu	Al	60		4	[107]
ZnAl	V	$Zn(NO_3)_2$	NH_4NO_3,	NH_4OH	insitu	2024	95	6.5	0.5	[108]
MgAl	PFDTMS	$Mg(NO_3)_2$		NH_4OH	insitu	2198	45	7	80	[109]

CoAl		$Co(NO_3)_2$								
NiAl		$Ni(NO_3)_2$								
ZnAl		$Zn(NO_3)_2$								
ZnAl	MBT/8HQ/V/PA/Mo	$Zn(NO_3)_2$			coprecipitation	2024	60		20	[110]
LiAl	Vanillin, aspartic acid	$Li(NO_3)_2$			In situ	A6N01	60		0.33	[111]

2.3. The corrosion resistance of LDH films

Among the possible solutions, LDHs incorporated with corrosion inhibitors seem to be a feasible choice that is found to protect the metallic surface, while, the compatibility with organic matrices makes it a powerful option to provide long-term stability and to effectively reduce the corrosion rate.

2.3.1. Corrosion resistance of in-situ growth LDHs

LDH based coatings have been pursued to achieve high corrosion resistance. The mechanisms through which these materials can provide the underlying substrate with improved corrosion resistance are manifold. Alongside being a physical barrier against water and ions migration, LDH based coatings are recognized for their capability to encapsulate functional species in between the charged lamellae. As a result of this specific property, coatings based on these materials have a self-healing potential if proper corrosion inhibitors are embedded and released *in situ* upon a specific trigger. LDH coatings commonly show a two-layered structure (schematically depicted in Figure 11): an inner relatively compact layer and an outer porous layer formed by the interconnection of the different platelets. Figure 11 (c) demonstrated the cross-sectional image of layered double hydroxide on AA5005. It can be seen that LDHs have shown two distinct layers i.e. upper porous layer and bottom dense layer and this is in agreement with the above explanation. *Liang et al* [112] described the formation of LDHs on AA2099-T83 Al-Cu-Li alloy, and further explain the role of intermetallic particles on the formation of LDHs and corrosion resistance properties. Iron-containing intermetallic particles act as a preferential site for the formation of nucleation and growth of LDHs and compact, uniform LDHs developed on the aluminum surface. Overall, intermetallic particles like iron contribute to the formation of LDHs, and

other non-reactive elements with LDHs i.e. silicon covered by LDHs nest-like morphology [113].

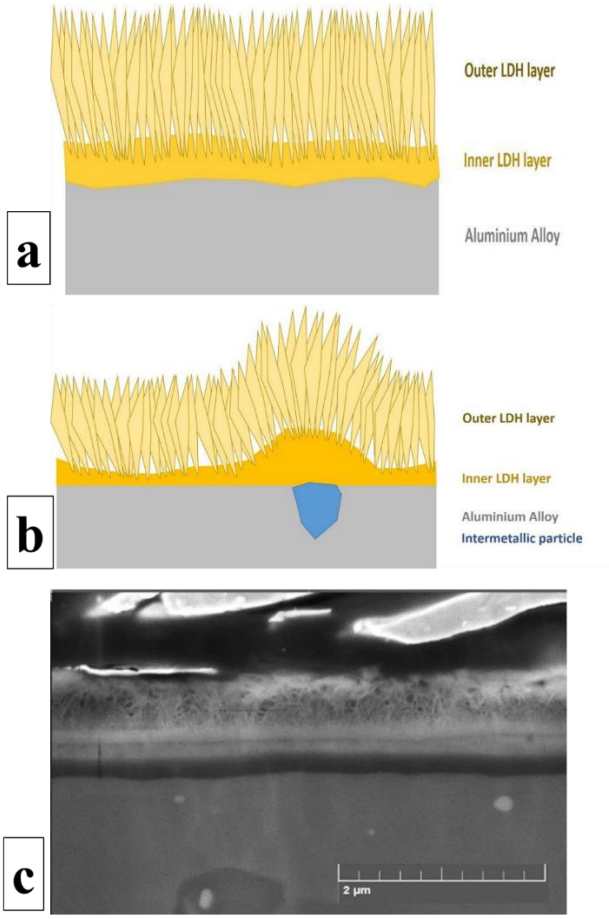

Figure 11. Structure of LDH based coatings: (a) schematic representation of the structure of the film; (b) schematic representation of the structure of the film in presence of intermetallic particles; (c) cross-sectional FIB-SEM image of LDH developed on AA5005.

Notice that in correspondence with the active intermetallic particles (Figure 11 b), a differentiated growth of island-like LDHs occurs [60]. The inner compact layer is responsible for the physical barrier effect of the coating while the platelets, which form the outer layer, mainly provide the ion exchange reactions. Regardless of the synthesis technique employed for the development of LDH films either by the in-situ method or the two-step method, LDHs suffer from corrosion induced by halogen ions such as chlorides. The durability of LDH coatings can also be increased with embedding corrosion inhibitors in between the platelets. LDHs anion exchange reactions are generally assumed to take place too tactically, even if precipitation mechanisms have been also proposed [114,115]. Nitrate-based LDHs might be a possible option to enhance the corrosion resistance by trapping the chloride ions through anion exchange process and release corrosion inhibitors [116]. *Tedim et al.* [116,117] described the synthesis of ZnAl-LDH (NO_3) and ZnAl-V LDH developed on AA2024 and chlorides entrapment capability of LDH-NO_3 and possible diffusion process which affects the stability of the coating against corrosion and leads to the damaging of the LDH/substrate interface.

LDHs with intercalating corrosion inhibitors are a better choice, as they are expected to deliver the inhibitors upon damaging of the matrix and can provide self-healing property. Vanadate exchanged LDHs were utilized by various research groups, either directly on the aluminum substrate (in-situ) or co-precipitated on the substrate, but, in both cases, the vanadate's were found to enhance the corrosion resistance of LDH [83,118], [78,84,93][97].

2.3.2. Corrosion resistance co-precipitated LDHs in organic and hybrid matrices

LDH dispersions in polymeric matrices have been studied to enhance the coating stability against corrosion and provide better mechanical properties along with stress dissipation ability. To achieve an enhancement in terms of corrosion properties, LDH particles are embedded inside an organic or organic/inorganic hybrid matrix to: (1) act as a physical barrier against moisture and oxygen permeation and (2) provide a controlled release of corrosion inhibitors (Figure 12). Layered double hydroxides dispersed inside a polymeric matrix improves the barrier properties of organic coatings by increasing the length of the pathway water and other species take to reach the metal interface, similar to other lamellar pigments [119].

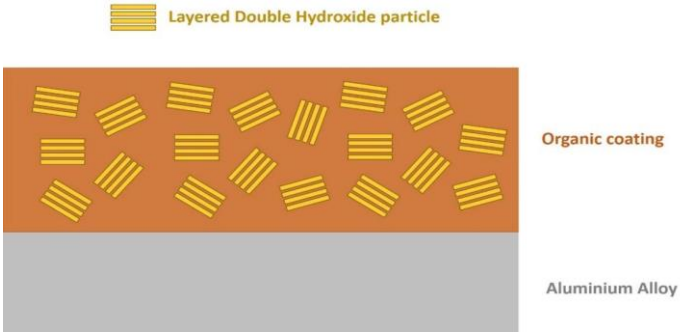

Figure 12. Schematic representation of the co-precipitated LDH dispersed into an organic coating.

The inhabitation effect of MgAl-LDH mixed at various proportions with hybrid sol-gel compose of (tetra-n-ropoxyzirconium (TPOZ) and 3-glycydoxy propyl trimethoxysilane (GPTMS)) were synthesized, and enhancement in corrosion resistance was monitored [106]. *Subasri et al* [110] reported a comparative study of the utilization of various corrosion inhibitors in different proportions, for instance, vanadate group, 2-mercapto benzothiazole, 8-

hydroxyquinoline, phytic acid intercalate4d LDH - and studied the effect of resultant dispersion in the sol-gel matrix to investigate the compactness and corrosion resistance properties of LDH to protect the AA2024 substrate.

2.4. Testing and evaluation of LDH coatings or co-precipitated particles

Electrochemical Impedance Spectroscopy (EIS) is considered a basic approach to evaluate the coating properties and barrier properties. Impedance measurements are recognized to supply valuable information about protective coatings applied on metals and about their degradation mechanism, as well [120–122]. Impedance modulus and impedance phase graphs (quite often referred to as "Bode plots") and Nyquist plots are used to show the impedance spectra collected over coated metals immersed in different electrolytes. From these graphs it is possible to gain a preliminary knowledge of the protective properties of the coatings: scientists refer to the modulus of the impedance in the low-frequency range (commonly in the 0.015-0.010 range) as a rough estimation of the quality of the protection system, following the claims of *Bacon* [123] and *Murray and Hack et al* [124], as highlighted by *Amirudin* and *Thierry et al* in their review [52]. To get some insight into the mechanisms through which coatings can protect the substrate, very often the experimental EIS data are studied through the nonlinear least-squares fit technique [122,125], which has been recognized to be a valuable tool for analyzing complex frequency dispersion data [126]. For this purpose, passive circuit elements (called "e.e.c., electrical equivalent circuits") are commonly employed to fit impedance data arising from different experimental systems. Despite the implicit ambiguity claimed by *McDonald et al* [127] of the different possible geometrical arrangements of the circuit elements, the exploitation of the e.e.c. for the fit of an experimental set of EIS spectra is widespread. In this context, LDH developed in situ on aluminum alloys has been

often investigated by EIS and diverse e.e.c. have been suggested by different groups to fit the EIS experimental data and to assess the corrosion protection properties of the coatings. Various equivalent circuits were used due to the dynamic nature of LDH coating systems, where capacitance is replaced generally by a constant phase element (CPE), which describes the non-homogenous nature of the LDH system and how it deviates from the ideal capacitive behavior. CPE approach is used extensively in equivalent circuits for fitting the experimental data and is attributed to the surface activity, inhomogeneity, factual geometry, roughness, electrode porosity, etc. It is believed to describe the current and potential distribution associated with the electrode geometry [128].

Wang et al [129] introduced the circuit depicted in Figure 13(a) to fit the experimental EIS data of MgAl LDH developed on 99.9% Al. In the model employed by the authors, Rs refers to the solution resistance, $R_{pore,}$ and CPE_{pore} to the conductive path in the films and double layer capacitance in the pores of the films, respectively; R_{ct} and CPE_{dl} to the polarization resistance and double-layer capacitance, respectively; R_{film} to the inner film resistance and CPE_{film} the constant phase element of the film.

A similar circuit (depicted in Figure 13b) has been proposed by *Zhou et al* [130] for the interpretation and fit of the EIS data set collected over ZnLaAl LDHs developed on AA6061. Also, in this case, the presence of a three-time constant has been suggested. A time constant has been attributed to the Faradic process and modeled by a charge transfer resistance, R_{ct}, in parallel with the double layer capacitance (CPE_{dl}); a second time constant has been related to the oxide film between the aluminum substrate and LDHs: R_{OX} represents the resistance of film in parallel with the capacitance (CPE_{OX}); a third time constant has been introduced to account for the contribution of the LDH layer itself: the LDHs film resistance (R_{LDHs}) in parallel with the layer capacitance (CPE_{LDHs}). Similarly, *Tedim et al.*

[93] identified three-time relaxation processes in the EIS spectra collected over ZnAl LDHs on AA2024. The time constant in the high-frequency range has been associated with the LDH layer response, a second-time constant attributed to the aluminum oxide present on the alloy surface, and a third-time constant attributed to the corrosion process.

Wang et al [131] introduced two relaxation processes e.e.c. (Figure 13c) where R_s represents the solution resistance; R_{ct} and R_f are the charge transfer resistance and the film of the MgAl LDHs resistance, $CPE_{f,}$ and CPE_{dl}, are the capacitance of the LDH film and the electrical double layer, respectively.

A two-time constant model (Figure 13c) has been employed also by *Liang et al* [112] investigating the properties ZnAl LDHs on AA2099. According to the attribution given by the authors, in addition to the resistance of the electrolyte (R_S), R_f and CPE_f represent resistance and component of the constant phase elements of the LDH/natural alumina film, respectively; R_{ct} and CPE_{dl} (charge-transfer resistance and component of the double layer constant phase, respectively) account for the faradic process. AC techniques and EIS provide a general description of the LDH system but these techniques refer to the average surface response, and localized defects cannot be truly estimated by those approaches.

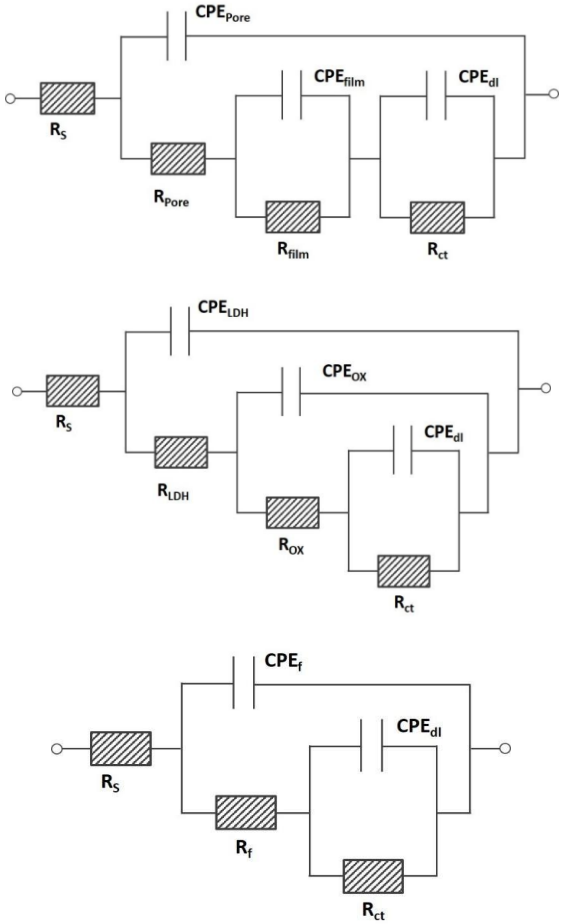

Figure 13. Schematic of the circuits employed to fit the experimental data set of LDH coatings developed on aluminum alloys: (a,b) three-time constants and (c) two-time constants.

As far as LDH dispersions in polymeric matrices are concerned, EIS spectra are fitted employing the well-established e.e.c. developed for organic coatings [124,132,133]. In particular, ionically conducting low resistive paths in

the coatings, due to discontinuities or defects, are modeled with a resistance (namely "porosity resistance", "pore resistance", R_{po}) [134]. The dielectric behavior of the coating is modeled employing a pure capacitance (namely "coating capacitance", C_c). The corrosion process occurring under the paint is modeled employing a charge transfer resistance (R_{ct}) in parallel with a double layer capacitance (C_{dl}). It has to be underlined that in some cases the response of an aluminum/coating/electrolyte system is also modeled employing a CPE which accounts for an oxide layer existing on the aluminum alloy electrode instead of the time constant attributed to the faradic process (R_{ct}, C_{dl}) [135].

Figure 14 suggests the possibility to significantly increase the corrosion protection properties of LDH layers by exchanging the anions in the lamellar structure with corrosion-inhibiting species.

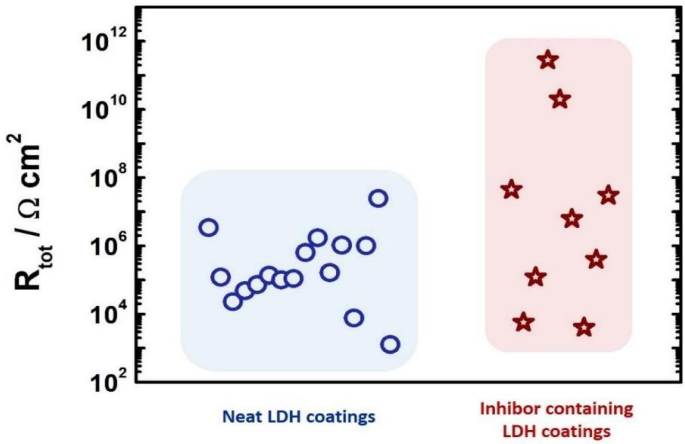

Figure 14. Comparison of the total resistance obtained from EIS spectra fitting for neat and inhibitor exchanged LDH coatings; data taken from ref [102-117].

Chapter 3

3. Experimentation, Characterization and Testing Methods

3.1. Materials Synthesis

3.1.1. Materials

The AA6082 extruded bar was pursed (Metal center, Italy) and were cut into the specimen dimension (3.14 × 3.14 cm^2) with the following chemical composition (Table 5);

Table 5. Chemical composition of AA6082.

Magnesium	Silicon	Copper	Manganese	Iron	Aluminum
0.6-1.2	0.7-1.3	0.4-1.0	0.5	0.5	Balance

The following chemicals are used in the thesis work;- $Zn(NO_3)_2 \cdot 6H_2O$, $Mg(NO_3)_2 \cdot 6H_2O$, $Ni(NO_3)_2 \cdot 6H_2O$, $Ca(NO_3)_2 \cdot 6H_2O$, $Ce(NO_3)_2 \cdot 6H_2O$, (purity 98%), Urea, NaOH (purity ≥98%), and NH_4NO_3 (purity 95%) were purchased from Sigma-Aldrich Corporation (Saint Louis, MO, USA). The graphene powder was provided by COMETOX s.r.l. (Milan, Italy). The sheets have an average thickness of 6 nm with an average particle diameter of 25 μm.

3.1.2. Pretreatment

The AA6082 specimens were initially ground with silicon-carbon paper, starting from 500 grit paper to 1000, 2400, and 4000-grit respectively. The samples were cleaned with deionized water and further ultrasonically in pure ethanol for 15 min. Lastly, the specimens were immersed in a 0.1 M aqueous NaOH solution for one minute to etch the oxide layer on the surface of the alloy.

3.1.3. Fabrication of LDHs

LDHs in this thesis are developed by the insitu growth approach, where the film is directly developed on the aluminum 6082 substrate, where the aluminum alloy is dipped in the divalent cation source ($MgNO_3$, $ZnNO_3$, etc). Aluminum alloy act as the source of trivalent cations and the support for the formation of LDHs. The direct synthesis on the aluminum alloys provides better adhesion of LDH film on the surface, controlled synthesis, facile fabrication approach, easy synthesis route, low cost, control synthesis on the complex shapes.

Due to element segregation and the presence of secondary phases in aluminum alloys, a possible potential difference can form which causes the formation of corrosion microcell on the aluminum surface (equation 1-3). While hydrogen bubbles can also be formed during LDH preparation (equation 3). Porous outer and inner compact Al_2O_3 layers formed and transformed into $Al(OH)_3$, which act as a precursor to form LDHs on the aluminum surface on reaction with divalent cations. The anion exchange step further allows to incorporation of various anti-corrosion inhibitors inside the LDHs interlayers and also can precipitate on the metal/LDH interface (Equation 1-6) [130]. It can be said that the thickness of the LDH correlates with the number of cations, pH, reaction temperature, aging time, alkali solution, and so on [74]. However, on consistent values of all the describe factors, that the morphological quality of LDH nanostructures increases with the increase of nitrate concentration in the solution. In an aqueous solution containing metallic aluminum and nitrate anions several electrochemical processes involving anodic dissolution of aluminum and cathodic reduction of nitrates and oxygen can occur. The cathodic processes generate hydroxyl ions and create a pH gradient. Although the reduction of nitrates to nitrite has been proven, there are other possible reactions involving nitrate and nitrate anions, producing nitrogen gas or ammonia, which may contribute to the overall reduction process [136] and thus can affect the film thickness as well surface morphology. Figure 15 demonstrates

the schematic representation of LDH synthesis directly on the aluminum alloy and further modification concept with various organic/inorganic pigments.

$$Al \rightarrow Al^{3+} + 3e^{-} \quad (1)$$

$$O_2 + 2H_2O \rightarrow 4OH^{-} \quad (2)$$

$$H_2O + 2e^{-} \rightarrow H_2 \uparrow + 2OH^{-} \quad (3)$$

$$Al_2O_3 + 3H_2O \rightarrow 2Al(OH)_3 \quad (4)$$

$$M^{2+} + OH^{-} \rightarrow M(OH)^{+} \quad (5)$$

$$M(OH)^{+} + Al(OH)_3 + A_n^{-} + H_2O \rightarrow MAl - LDH \quad (6)$$

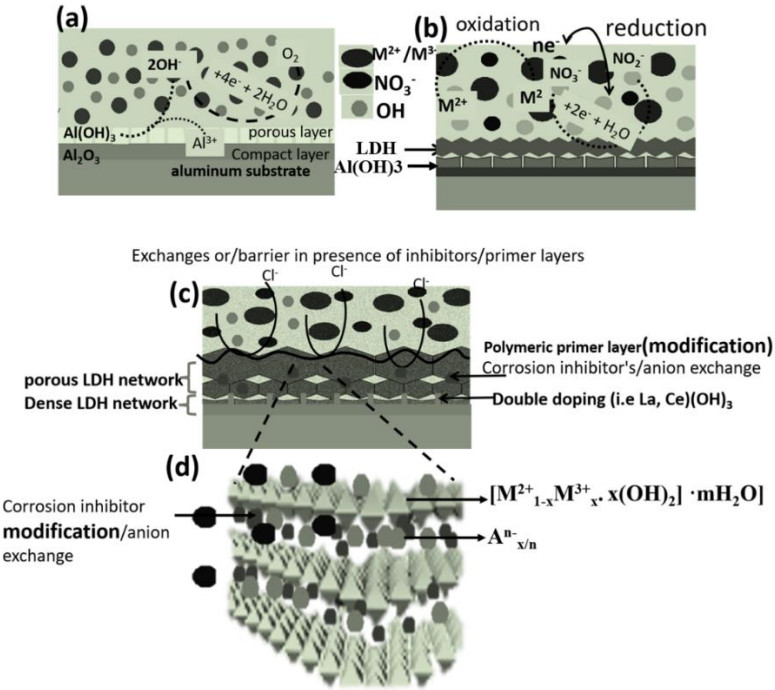

Figure 15. (a-c) Synthesis procedures of in situ growth LDH and possible modification approaches, (d) general representation of an LDH structure.

3.2. Characterization & Testing Techniques:

To understand and characterize intermediates and final products, it is recommended to thoroughly identify the step-by-step process of the synthetic route. There are numerous characterizing techniques but in current research, approaches like SEM, XRD, and TGA/DTA are mainly employed to investigate and characterized structural composition, the phase, microstructures, and effect of material structure on its thermal analysis of the powdered samples and free-standing layers. The following are some of the characterization and testing methods employed to study the samples prepared in this research work.

3.2.1 Ultra-Sonicator

The technique named sonication utilizes sound waves for the agitation of particles in the solution. The process utilizes an ultrasonic frequency of greater than 20 kHz that leads to the practice named ultra-sonication or ultrasonication. Samples are placed in the water bath and the sonicator generates sound waves, or it might be the probes that are inserted right into the solutions whose sonication is required as shown in Figure 16. Though both the systems apply ultrasound to the sample, still, there are noteworthy differences in efficiency, process capabilities, and effectiveness.

Figure 16. Bath and Probe Ultrasonicator.

3.2.2. X-ray Diffraction:

X-ray diffraction (XRD) shown in Figure 17 is an analytical and more distinctly non-destructive technique employed for calculating unit cell dimensions and identification of phases of crystalline material. Apart from that it also reveals information on crystal structure type, average crystallite size, crystal defects, and preferred orientation of crystals along with other strain parameters. For the identification of phase, structure, etc., of the materials, intensities, and positions of the peaks are used.

Suppose two monochromatic parallel X-ray beams having the λ as wavelength that is falling on the successive planes at θ angle which undergoes constructive interference to reveal the XRD pattern. The incident x-rays interact with the sample and when Bragg's law is satisfied, they undergo constructive interference. The mathematical representation of Bragg's law is given below:

$$n\,\lambda = 2dsin\theta$$

Where “λ”, is taken as the wavelength of x-ray, “n” is an integer, “d” is the crystal plane separation and “θ” is the angle among the reflected and incident beam.

Through an appropriate analysis of x-ray line broadening, we can calculate the crystallite size of particles. The peaks are obtained from the diffraction of x-rays at specific angles. Crystallite size “D” of any material in nanometers (nm) can be found from the equation given below using XRD significant peaks:

$$D = \frac{0.9\lambda}{\beta cos\theta}$$

Here the parameter “β” is considered as the full width half maximum, while “θ” is termed diffraction angle.

XRD patterns of the investigated were recorded by X-ray diffraction (X’Pert High Score diffractometer, Rigaku, Tokyo, Japan) at ambient conditions by using cobalt Kα (λ = 1.789 Å) and copper Kα (λ = 1.54 Å) emission source at 10 mA and 30 kV conditions. The lattice parameters of MgAl layer double hydroxide were calculated by that Equation [34], where *d* is the lattice spacing calculated by Braggs law.

$$\frac{1}{d^2} = \frac{4}{3}\left(h^2 + hk + \frac{k^2}{a^2}\right) + \frac{l^2}{c^2}$$

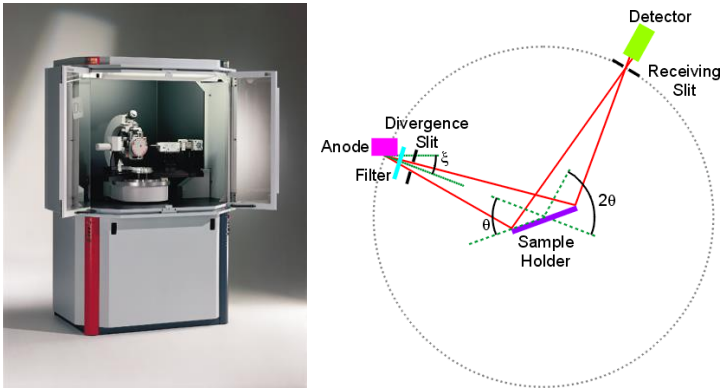

Figure 17. X-Ray Diffractometer and its Principle

3.2.4. Scanning Electron Microscopy:

Morphological information, cracks, delamination, and battery degradation mechanisms studies often benefit from SEM characterization technology. The contrast of the SEM image depends on the detector being used, which collects the backscattering or the secondary electrons. The interaction of materials chemistry with the electron beam generates signals to provide the specimen's morphology and a constituent of materials. In principle, the electron emitted by the electron gun beamed onto the samples with the support of a series of lenses (Figure 18). Scanning electron microscopy (SEM) provides essential information on the microstructure and surface morphologies of the developed layered double hydroxide.

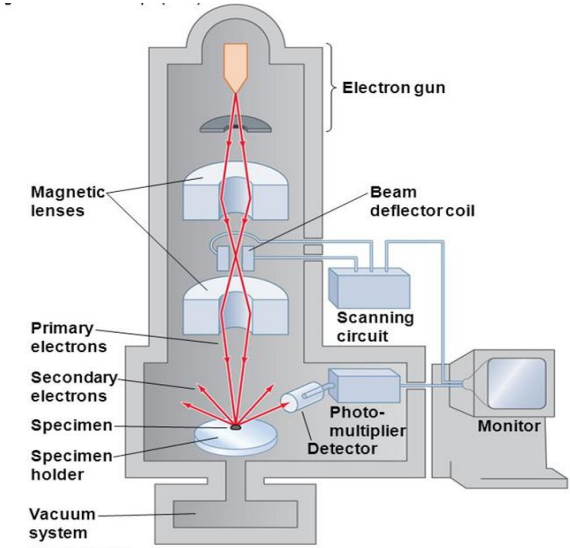

Figure 18. Schematic of SEM.

3.2.5. Energy Dispersive Spectroscopy

Energy dispersive x-ray spectroscopy (EDX/EDS) is another non-destructive X-ray analysis technique used to study the elemental and chemical composition of elements having an atomic number of more than 3. Principally, EDS comprises of spotting the characteristic x-rays created by every element after bombarding a sample with high-energy electrons in an electron microscope. Using a process known as x-ray mapping, information about the elemental composition of a sample can then be overlaid on top of the magnified image of the sample.

EDS/EDX is used to analyze the elemental composition of selected areas using SEM or TEM imaging as well as for defect identification/mapping. Every element has its characteristic x-ray. When the sample is bombarded with the source of high-energy electrons or protons, the atoms on the surface of the sample eject

electrons resulting in the generation of vacancies in the structure. These vacancies are subsequently filled with electrons from higher energy states releasing x-ray due to balancing the energy difference between the two electronic states. EDS detector records the plenty of x-rays released from the sample against their energy, consequently, results in an EDX spectrum.

Limitations:

There are some limitations like:

- The size of the sample must be well-suited with TEM /SEM.
- Mostly, semi-quantitative analysis is possible.
- Coatings can limit subsequent surface analysis.
- There should be a vacuum compatible with the samples and mostly not best for wet organic materials.
- Overlap of various elemental peaks is possible, therefore, a careful review of the spectra is needed.

3.2.6. Fourier Transform Spectroscopy

Fourier transform infrared spectroscopy (FT-IR) is the material characterization approach, where infrared radiation is absorbed by the material results in molecular transmission and absorption (Figure 19) and can be taken as a unique Fingerprint for that material. FT-IR demonstrated the unique absorption peaks, which are associated with the vibrations between the bonds, and thus provide qualitative analysis of various kinds of materials. Further, the peak size, intensity can provide information about the amount of material present by using various software's thus can take information about the quantitative analysis of the materials.

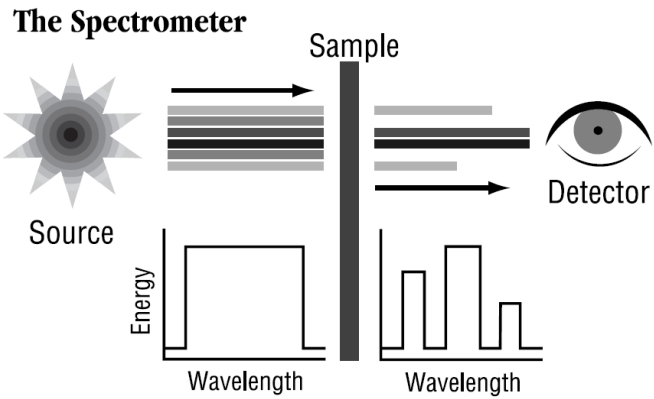

Figure 19. The basic instrumentation of FT-IR analysis [137].

3.2.7. Focused ion beam (FIB)

The localized ion beam technique (FIB) allows both imaging information and ablation of the sample at the nanometre or micrometer scale. At first glance, the FIB shows many similarities with SEM microscopy, from which however it differs in that the beam is now ionic and no longer electronic. From the interaction between the ion beam with the surface of the sample, secondary electrons are generated from which high-spatial-resolution images can be obtained at the nanometer scale. Usually, the ion used in the FIB is the gallium type, whose sputtering action allows a very precise ablation of the sample. The newly manufactured FIB instrumentation also combines a column for an electron beam with the column of the ion beam, then the SEM technique is approached to the FIB one obtaining double beam instrumentation. To obtain a focused ion beam the source must be characterized by very small dimensions the more satisfied this requirement is, the more current can be focused on a single point. The high-resolution ion beams are generated by a source field ionization characterized by an ion emitter with very small dimensions, having a final tip radius of 10 mm,

which allows the beam to be focused very much at 4-6 nm. Currently, the most used FIBs are based on the liquid gallium ion source (LMIS) positioned in the upper part of the column allowing the production of Ga+ ions. In an LMIS source, contact is made between the heated metallic gallium and a tungsten needle which is moistened by the first.

Thanks to a very large electric field, greater than 1010 V/m present on the tip of the needle, Ga atoms are emitted and ionized. As with electrons in the SEM, ions flow through lenses before ending up on the surface of the sample, which will be scanned. Unlike the electron beam seen in the SEM that was directed to the surface through electromagnetic components to scan the surface, the ion beam needs electrostatic components to be addressed. This variation derives from the fact that the focusing force of the electromagnetic lenses is correlated to the charge/mass ratio of the particle, therefore for the ions it is practically impossible to realize electromagnetic lenses adequate since they would have a hypothetical weight measurable in tons. An ion, when it hits a solid, loses part of its kinetic energy transferring it to the atoms with which it impacts. This phenomenon generates a series of different processes:

- ion reflection and backscattering
- electron emission
- electromagnetic radiation
- atomic sputtering and ion emission sample damage
- sample heating

The impacted ion usually remains inside the lattice, it is called ion implantation. The collision between the Ga ions and the sample atoms, then the kinetic energy and the momentum transferred to the solid can occur both in an elastic and inelastic way. The first way allows the material to be removed, while in a second

way the emission of secondary electrons and ionized atoms from the sample occurs. Thanks to the inelastic collision, imaging can be achieved.

3.2.8. Raman Spectroscopy

Raman spectroscopy is used to observe rotational, vibrational, and low frequent modes. The materials scattered small amounts of the beam in all directions on exposure to the radiations, Raman scattering associated with the quantities of vibrations changes with IR spectra and can provide information about molecular structure. Raman is based on inelastic scattered, stokes and anti-stokes proportion, and is helpful to analyze vibrational energies of metals. Raman studies are considered potential experimentation to understand the graphene interaction with the materials, structure, coordination compounds. Figure 20 represents the general instrumentation of Raman spectroscopy.

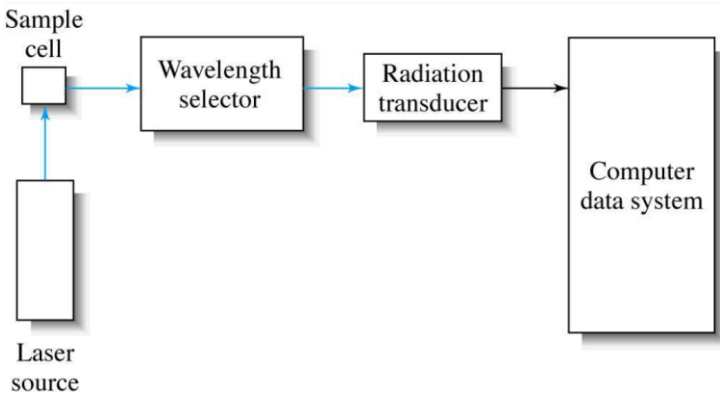

Figure 20. Raman spectroscopy instrumentation.

3.2.9. Thermal Analysis of Samples

In the thermal analysis, the substance can experience chemical decompositions or phase transitions throughout the heat practice. Phase transitions involve heat

effects like endothermic or exothermic. Different gaseous by-products can be formed during a chemical or electrochemical reaction during the process which causes material degradation, deterioration, and effect the material structure phases and sometimes mass loss or addition due to corrosive behavior of materials. Thermal analysis techniques have a wide range of approaches used to characterize, here three different main techniques are taken into consideration.

- Thermo-gravimetric analysis (TGA)
- Differential thermal analysis (DTA)
- Differential scanning calorimetry (DSC)

These analyses can provide worthy information regarding phase transformations of the sample, melting, crystallization, decomposition and sublimation temperatures, enthalpy changes, desorption, absorption, redox reactions, and nature of reactions involved that is endothermic or exothermic. Figure 21 shows a typical TG/DTA scheme and the main components of the devices.

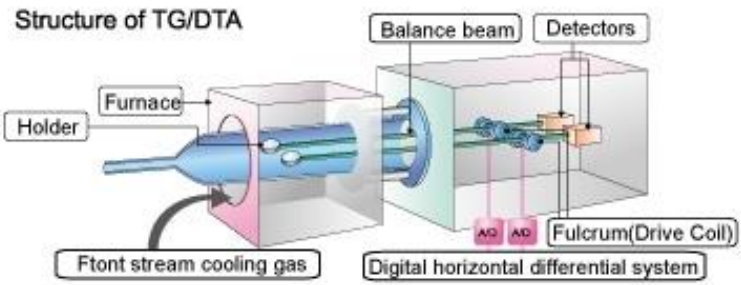

Figure 21. Schematic View of Thermogravimetric Analyzer

The thermo-gravimetric analysis is another main a widely used thermal analysis approach whereby, weight gain or weight loss of a sample can be measured up to

a wide range of temperatures and over a fixed period. Samples may be isothermally kept at a fixed temperature. Thermo-balances with µg sensitivity are offered in the current generations of thermo-gravimetric systems.

Differential thermal analysis (DTA) method usually combined with a TGA unit used to determine the heat flow through the sample over a wide temperature range and fixed time duration. In DTA, one measures and records the difference (T_s-T_r) where T_s is the sample temperature while T_r is the reference temperature and that conveys information about the nature of the reaction occurring in the sample. For an exothermic reaction, it shows an upward deflection but in the case of an endothermic reaction, a downward deflection appears in the DTA plot.

3.2.10. Potentiodynamic polarization measurements

Potentiodynamic polarization is considered a destructive measurement technique. From potentiodynamic measurements, it is possible to know which is the trend of the current density (i) as a function of the potential (E). Current density means the current intensity (I) compared to the area of the electrochemical cell used in the analysis. This technique, like all electrochemical techniques, is based on the presence of a measurement solution, a working electrode consisting of the material to be analyzed (W_E), the reference electrode (R_E) concerning which the ΔE is evaluated and the electrode (CE) to close the circuit. Ag/AgCl electrode is used as a reference electrode, which has a potential equal to +207mV compared to the standard hydrogen electrode (SHE). A general illustration of potentiodynamic curves is shown in Figure 22.

The redox reaction to which the current exchanged in the electrochemical process is connected occurs at the interface between the metal and the electrolytic measurement solution. The equilibrium of the system is reached when the anodic

current density is equal to the cathodic current density. Sweeping potentials progressively far from the equilibrium in absolute terms, the system polarizes in an anodic sense. This occurs if the imposed potential increases concerning E_{corr}. Vice versa, imposing cathodic overpotential, the system it polarizes in a cathodic sense. In other words, by polarizing towards positive values of the potential it will tend to force the anodic half-reaction (oxidation of the metal) while polarizing towards negative values the tendency is to force the cathodic half-reaction (oxygen reduction). Polarizing, thus evolving the system to take it out of the equilibrium condition, there will be an exchange of current with the external environment. The ratio between the current and the area of the sample exposed to the electrolytic solution, gives the total current density measured. Usually, in the measurement of potentiodynamic curves, the attention is placed on the anodic branch since it provides characteristic information of the electrochemical behavior of the material. If the material is passivated or has a protective oxide layer at the interface between the metal and the solution.

For a material with passive behavior, at potential $E < E_{eq}$ there is the zone of immunity where the material does not corrode. For potentials between E_{eq}, and the primary passivation potential, E_{pp}, corresponding to the maximum anodic current density value, there is the activity zone, or even said active branch of the anodic characteristic. In the initial part, an increase in anodic current density is observed and the material is not covered by protective layers but passes into solution. The maximum current density exchanged by the metal before entering the next zone is called critical passivity current density, i_{cp}. For potential values between the primary passivation potential, E_{pp}, and the potential from which the anodic current density stops to decrease, called the passivity potential, E_p, there is the transition zone. This area is the one that leads to the formation of surface films, hence where the complete oxide layer is created. The part of the anodic branch with a negative

slope is not, however, representative of stable operating conditions. The current density, however, as one might think, does not go down to the zero value but only up to the passivity current density value, i_p, since an equilibrium condition is reached. The passivity zone is placed at E values between E_p and the trans passivity potential, E_{tr}, (or pitting potential, E_{pit}, if present). This area is characterized by a very low dissolution rate of the metallic material due to the presence of the protective surface film, measured by the passivity current density, i_p. This rate does not vary (or varies very little) with the potential, and is up to 10-6 times lower than the i_{cp}. Out of the passivity zone, polarizing to potentials higher than E_{tr}, anodic processes enter in competition with the dissolution processes, and therefore the passivating oxide is no longer stable, and it can break so that the anodic current density increases also very quickly. This area is called the trans-passivity zone.

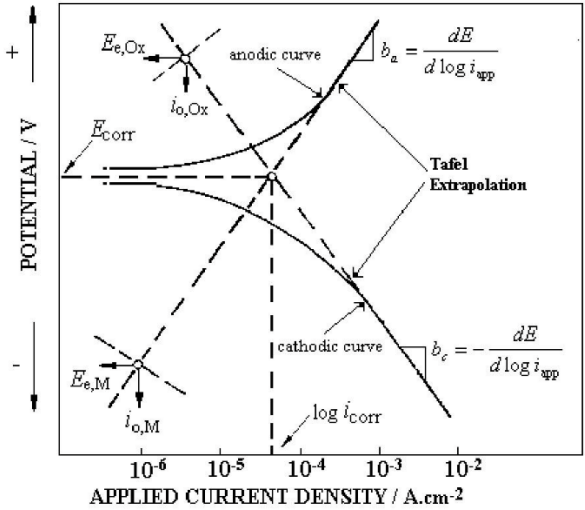

Figure 22. Evaluation of potentiodynamic curves.

3.2.11. Electrochemical impedance spectroscopy (EIS)

EIS is a non-destructive electrochemical measurement that is commonly used to characterize corrosion behavior and provides sufficient information about the kinetics of the reaction. The systematic arrangement to measure EIS is much simple, three different electrodes in an electrolyte are used, namely reference electrode, working electrode, and electrode whose impedance must measure. EIS helps to find out impedance and provides analysis during alternating current resistivity, conductivity, and inductivity. The theory behind electrochemical impedance spectroscopy (EIS) is based on the imposition of a signal of potential or alternating current and the evaluation of the associated response (Ohm law), where the resistance is the ratio between voltage and current. This well-known relationship with one circuit element is limited and used for the ideal resistor.

$$R = \frac{E}{I}$$

Impedance, a function of angular frequency, is defined as the relationship between the applied potential *E(t)* and the consequent pulse of the current variable in time that the surface of an electrode emits, *I(t)*. However, there is much complex behavior and use impedance which is a measure of the ability of a circuit to resist the flow of electrical current.

$$E(t) = E(o)\sin(\omega\, t)$$

Where E_0 is the amplitude of the signal, and E_t is the potential at time t, and ω is the radial frequency, expressed in hertz:-

$$\omega = 2\pi f$$

Further, the response signal, I_t, is shifted in phase (Φ) and has a different amplitude than I_0. On the electrode, there are electrochemical processes that absorb energy

at different frequencies between them. This aspect is what generates the delay described by the phase angle between the impulse imposed from the outside and the response of the system.

$$I(t) = I(o)\sin(\omega t + \varphi)$$

So we can use the mathematics expression:-

$$Z = \frac{E(t)}{I(t)} = \frac{E_o \sin(\omega t)}{I_o \sin(\omega\omega t + \varphi)}$$

The impedance as a complex function can be described as:

$$E(t) = E_o \exp(j\omega t)$$

and the current response as:

$$I(t) = I_o \exp(j\omega t - \theta)$$

The impedance is then represented as a complex number,

$$Z(\omega) = \frac{E}{I} = Z_o \exp(j\varphi) = Z_o(cos\varphi \ + jsin\varphi)$$

Where the maximum variation of current density, while I_o is the value around which the sinusoidal oscillation occurs, a value that generally corresponds to i_{corr}. This sinusoidal modulation *I(t)* is however out of phase by the phase angle, compared to the potential, *E(t)*.

The data resulting from the EIS measurements can be represented in two ways (Figure 23):

- Through the Bode diagrams.
- Through the Nyquist diagrams.

EIS measurement is performed with a low potential excitation amplitude to maintain linearity, typically 10 mV. The frequency range usually ranges from 100

kHz up to 1 mHz. Equivalent circuits are associate with characteristics of the system with elements of an electrical circuit (capacitors, resistors, inductances, etc.) are discussed in Chapter 2.

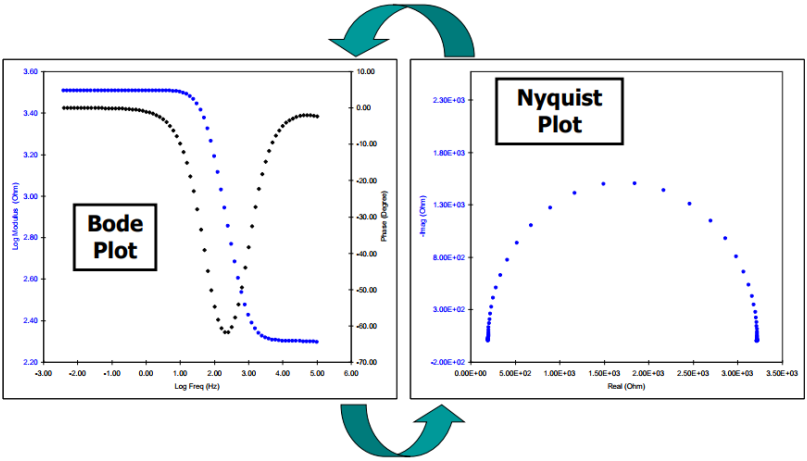

Figure 23. Nyquist and Bode's plots obtained through EIS

Bode Plot:

- Using the Bode plot option, the individual charge transfer process can be measured.
- The frequency of the system is the explicit function here
- Easy to measure small impedances too here.

Nyquist Plot:

- Individual charge transfer processes are also measured able in Nyquist Plot.
- Frequency, in that case, is not obvious.
- Small impedances are swapped to larger impedance.

The instrumentation used for this test is the Metrohm Autolab potentiostat/galvanostat, which consists of inside the apparatus must then be included the potentiostat, a frequency response analyzer, a generator of alternating voltage pulses, and finally the computer that allows having an interface between user and analysis system. Where the AC signal is scanned over a wide range of frequencies to generate an impedance spectrum for the electrochemical cell under test. EIS differs from direct current (DC) techniques in that it allows the study of capacitive, inductive, and diffusion processes taking place in the electrochemical cell. The electrochemical measurements were conducted (PAR Parstat 2273) in 0.1M NaCl solution to understand the anti-corrosion properties performed at ambient conditions under the faraday cage to minimize the external noise on the system. A relatively diluted electrolyte (0.1M) has been employed to better highlight the differences among the investigated samples. The traditional three-electrode setup was used, where the platinum mesh was used as a counter electrode while MgAl-LDH and Ag/AgCl/KCl (+210 mV vs SHE) were used as working and reference electrode respectively. The MgAl-LDH was exposed to the electrochemical solution for 30 minutes in 0.1M NaCl solution before the measurement, for the system stabilization. The polarization curves were obtained with a sweep rate of 2 mV/s. The impedance measurements (EIS) were performed at the open circuit potential (OCP) over the frequencies ranging from 100 kHz down to 10 mHz at a 5 mV (rms) amplitude.

Chapter 4

Synthesis of X-Al-LDHs (X=Mg, Zn, Ca, Ni): -Structural and corrosion resistance properties

Introduction

The structural and corrosion resistance properties of layered double hydroxide (LDH) actively depend upon the synthetic conditions, which can control the crystal growth rate, geometry, and surface morphologies. In this chapter, various classes of layered double hydroxide, including- MgAl-LDH, ZnAl-LDH, NiAl-LDHs, and CaAl-LDH were synthesized on the aluminum AA6082 substrate by a single step hydrothermal process, and the relation of LDH structural variations to the corresponding corrosion resistance properties are briefly discussed. The comparison of the synthesized LDHs on their ion-exchange capabilities, barrier effect, and their combined effect on corrosion resistance properties is reported. CaAl-LDHs thin films were further grown on an aluminum surface, for the very first time, by using a facile in situ growth method to investigate the anticorrosion behavior of CaAl-LDH. Further, the urea hydrolysis method is used to synthesis novel cone-shaped unique LDH structure which will be helpful to design environmentally friendly CaAl-LDH thin films for numerous potential applications. This chapter includes a detailed investigation to synthesize the various LDHs, their structural-electrochemical relationships, and the factors which affect the LDHs corrosion resistance properties.

4. Material and pretreatment

Aluminum AA6082 ingot (containing 0.80-1.20 wt.% Mg, 0.15-0.40wt.% Cu, 0.40-0.80wt.% Si, 0.25wt.% Zn, 0.15wt.% Mn, 0.04-0.35wt.% Cr, 0.15wt.% Ti, 0.70wt.% Fe and balance Al) purchased from Metal Center Italy were cut into the cylindrical dimension 3.14 cm^2 surface area. The samples were mechanical ground with SiC papers of grit 600#, 1200#, 2400#, 4000# and were washed with deionized water. The specimen was ultrasonically cleaned with ethanol followed by 10 min etching with 0.1M NaOH solution.

4.1. MgAl-LDHs structural geometry and corrosion resistance properties

4.1.1. Synthesis route of MgAl Layered Double Hydroxide Film

A 0.05 M ($Mg(NO_3)_2 \cdot 6H_2O$) solution was prepared in 1000 mL deionized water and the pH of the solution was adjusted to 10.0 by the dropwise addition of ammonium hydroxide solution. The solution was poured into a four-bottleneck heating flask (Sigma-Aldrich Glassware) and pretreated aluminum samples (3.14 cm^2) were immersed vertically in the solution. The experiments were performed at 40, 60, 80, and 100 °C reaction temperature, for 12, 18, and 24 h, under nitrogen bubbling. The samples were washed with deionized water after the completion of the experiments and were dried at room temperature. Figure 24 represents the general schematic diagram of the layered double hydroxide.

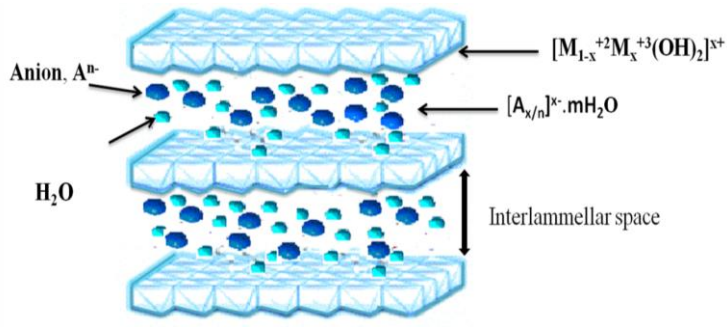

Figure 24. Schematic illustration of layered double hydroxides.

4.1.2. Results and Discussion

Figure 25 shows the XRD pattern of MgAl–LDH thin film developed on the AA6082 at various temperatures and crystallization periods. The XRD pattern of the MgAl layer double hydroxide at 40 °C-24 h and at 60, 80, 100 °C for 12, 18, and 24 h crystallization time, demonstrated the characteristic peaks of layered

double hydroxide structure, described in the literature [113], further the sharpness of the peaks suggested an ordered structure of LDH layers. Synthesis temperature and crystallization time have an influential effect on characteristic peaks. The (003), (006), (009), (110), and (113) characteristics peaks of crystal planes are related to the MgAl LDH film. The intensity and broadness of the reflection peaks vary with the increase of temperature and also depend upon crystallization aging time. When the samples were synthesized at 60 °C and lower aging time (12 and 18 h), the pattern exhibited low intensity and a broader peak which describes their low crystallinity. At a higher temperature range, for instance, 80 and 100 °C, the reflection peaks exhibited sharp and high intense narrow peaks which describe well the crystalline and ordered structure. The intense reflection peaks of (003) at low 2θ value exhibited an interlayer distance of ≈0.80 nm and the reflection peak could further be used to calculate the cell parameter "*c*" by the correlation "$c = 3d_{003}$", while the d_{110} interlayer thickness was used to calculate the cell parameter "*a*" by the correlation "$a = 2d_{110}$". The basal spacing of MgAl LDH slightly shifted to a lower angle with the effect of enhanced temperature and crystallization aging time, indicating the strong intercalation of NO_3^- ions. However, due to the formation of carbonate anions, small absorption peaks of d_{003} at 40 °C–24h, 60 °C–18 h were also observed. Fourier transform-infrared spectroscopy (FT-IR) spectra further confirmed the presence of CO_3^{2-} ions. The interlayer thickness, lattice constants of "*a*" and "*c*", and crystallite size for MgAl LDHs thin film on AA6082 are listed in Table 6.

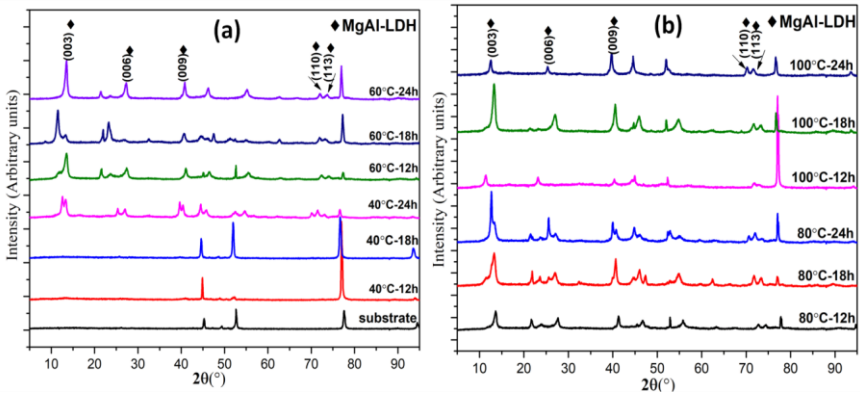

Figure 25. The XRD spectra of Mg-Al layered double hydroxide (LDH) film samples developed on aluminum alloy AA6082 obtained at various reaction temperatures and crystallization times.

Table 6. Cell parameters and sizes of the coherent domains determined for the Mg−Al layered double hydroxide (LDH) precursor powders from X-ray diffraction.

Sample	Cell Parameter, *a* (nm)	Cell Parameter, *c* (nm)	Interlayer Distance, d_{003} (nm)	Interlayer Distance, d_{110} (nm)	Crystallite Size, *D* (nm)
40 °C–24 h	0.308	2.329	0.776	0.154	11.214
60 °C–12 h	0.306	2.296	0.765	0.153	12.908
60 °C–18 h	0.305	2.668	0.889	0.152	7.608
60 °C–24 h	0.305	2.294	0.765	0.152	11.657
80 °C–12 h	0.303	2.275	0.759	0.151	6.685
80 °C–18 h	0.306	2.461	0.820	0.153	6.987
80 °C–24 h	0.311	2.412	0.804	0.155	8.465
100 °C–12 h	0.311	2.691	0.897	0.155	5.929
100 °C–18 h	0.311	2.391	0.797	0.156	6.165
100 °C–24 h	0.311	2.463	0.821	0.157	6.411

The selective samples, synthesized at various temperatures and crystallization times, were further investigated by FTIR analysis. FTIR spectra in attenuated total reflection mode were recorded, as shown in Figure 26. All the samples showed almost similar types of features. The broadbands displayed in the

range of 3370–3427 cm^{-1} were assigned to OH group stretching and the absorption band around, 1627–1633 cm^{-1} was caused due to the flexural oscillation peaks of interlayer water molecules [138]. Moreover, the absorption peaks around 1360 cm^{-1} were assigned to the asymmetric stretching bond of intercalated NO_3^- [139][140][141]. The small peak around 1520 cm^{-1} corresponded to the CO_3^{2-} ions, which shows the presence of a small number of carbonate ions in the LDH phase. The bond at 655, 751, and 1202 cm^{-1} may be associated with Al–OH stretching [137]. The absorption peaks around 550–770 cm^{-1} correspond to the lattice vibration of metal-oxygen bonds (M–O) [142].

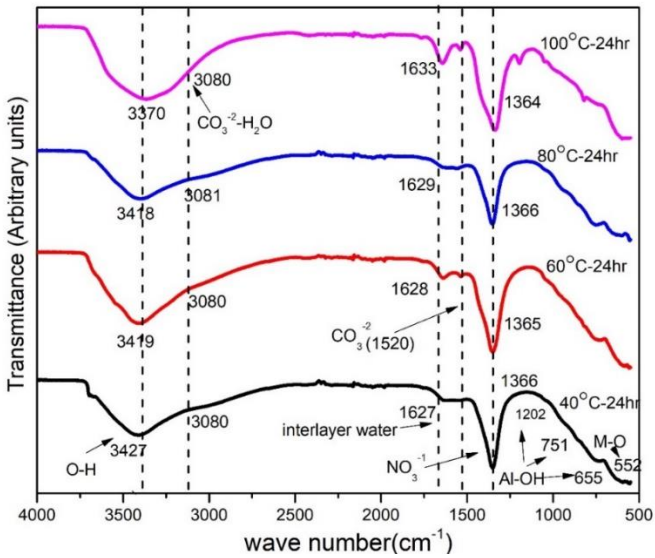

Figure 26. ATR-FTIR spectra of MgAl LDH powder scraped from as-prepared MgAl–LDH coated samples fabricated at different reaction temperatures.

As revealed from the SEM observations, shown in Figure 27, a compact and uniform interviewed LDH structure was obtained by the increase of reaction temperature and of aging time, moreover distinct surface morphological variations

were also observed. Initially, the LDH granules started to originate and developed into distinct platelet structures with an increase of reaction temperature and crystallization time, while on a further increase of the temperature and aging time, the nano-sheets of the LDH structure fused to form a compact blade-like LDH structure. For example, at 80 ˚C temperature and 24 h aging time, a fully groomed curved shaped platelet morphology was obtained which fused on further increase in temperature and appeared as a compact needle-shaped structure. The atomic composition of LDH, calculated by energy disperse spectroscopy (EDS) plane scanning, is listed in Table 7. The EDS findings showed that the coated structure is mainly composed of Mg, Al, N, and oxygen. A small amount of carbon is also evident in the EDS study, caused by contamination from air, which results in the formation of carbonate anions. The atomic ratio of Mg/Al varies with the effect of temperature and crystallization time. Table 7 showed that with higher reaction temperature and crystallization time, a higher ratio of Mg/Al is obtained. The oxygen content also varied with the influence of temperature and time. The atomic ratio of Mg: Al lies in the range of 2.5:1–3.87:1, which provides a rough approximation of the MgAl LDH assembly. Note that the Mg: Al ratio increases with the duration of the treatment regardless of the temperature. The duration of the treatment seems therefore to affect the chemical composition of the LDHs which enrich with Mg during the long immersion time. The possible formation of MgAl LDH on the AA6082 surface may start with the dissolution of aluminum in the basic solution to release Al^{3+} ions (aluminum surface is partially dissolved on contact with the high pH solution and generated aluminum oxides) [143], which react with the water to form $Al(OH)_3$ while the final step is related to the precipitation of Mg^{2+} and OH^- on the surface of the $Al(OH)_3$ surface to form the pre-MgAl LDH hydroxide mixture. The ammonium nitrate continuously hydrolyzed to form NO_3^- in the system, along with the release of ammonium ions

which led to progressively keep the pH in the range of 10. Finally, the divalent Mg^{2+} ions in $Mg(OH)_2$ were substituted by the trivalent Al^{3+} ions, which result in the coexistence of $Al(OH)_3$ and $Mg(OH)_2$ to form a stable hydrotalcite-like LDH structure. On the other hand, the hydroxyl ions present inside the galleries were exchanged by NO_3^- ions present in the solution, and as the average atomic ratio of Mg to Al is approximately around three, as shown in Table 7 (EDS analysis), it can be concluded that the final film of $Mg_3Al(OH)_2{\cdot}xNO_3{\cdot}yH_2O$ was formed on the substrate of AA6082 and formed stacking of LDH layers one above another to form the LBL configuration. The obtained EDS findings agree with the XRD results.

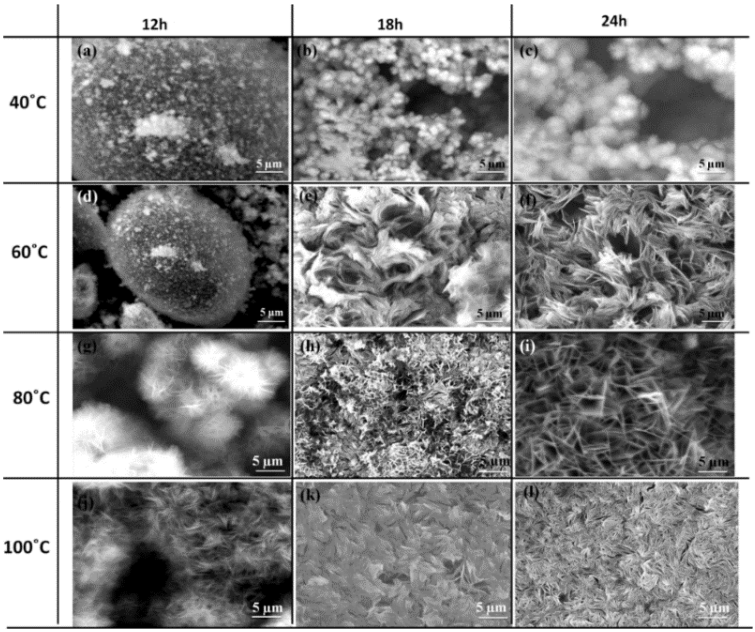

Figure 27. SEM images of LDH films developed at various reaction temperatures and crystallization times.

Table 7. EDS study of atomic percentage at various reaction temperatures and crystallization times.

Sample	Mg (at.%)?	Al (at.%)	N (at.%)	O (at.%)	Mg/Al
40 °C–24 h	17.6	6.8	3.1	64.7	2.6
60 °C–12 h	18.1	7.2	3.0	60.7	2.5
60 °C–18 h	26.2	7.5	3.3	57.4	3.5
60 °C–24 h	27.5	7.5	4.2	57.0	3.7
80 °C–12 h	19.3	7.3	3.1	58.7	2.6
80 °C–18 h	27.2	7.6	4.1	53.8	3.6
80 °C–24 h	24.7	6.6	4.7	56.2	3.8
100°C–12 h	24.5	7.6	4.2	53.9	3.2
100 °C–18 h	28.6	7.5	4.7	53.9	3.8
100 °C–24 h	28.7	7.4	4.3	63.1	3.9

The results from SEM suggest that the synthesis conditions promote the formation of uniform and quite ordered structures. As far as the appearance of the coatings is concerned, it seems that on increasing the treatment temperature from 60 to 100 °C, the LDHs layer becomes more and more compact and homogenous. Also, the duration of the treatment plays a similar role: prolonged immersion in the solution promotes the formation of homogeneous LDHs structures in which the platelets are closely packed.

The effect on the film thickness of the synthesis parameters is reported in Figure 28, which shows also the cross-sectional image of MgAl LDH at 80 °C and 18 h (reported as an example). The results of the film thickness indicated that with the increase of reaction temperature and treatment time, the film thickness of coating increased. The film thickness increased from about 20.8–73.5 µm with the increase of the processing parameters. The high temperature and aging time in this study were shown to promote the growth rate of LDH formation, confirmed also

by XRD and SEM analysis. It was observed that a rapid increase in film thickness was found for 100 °C temperature and 24 h treatment time. However, with the increase of thickness, the interface of the substrate and coating become blurred and also caused an increase in defect density, which promoted loose interaction with the substrate. Some pores were observed at the interface of coating and substrate with the increase of coating thickness. This fact is expected to negatively influence the corrosion protection ability of LDH.

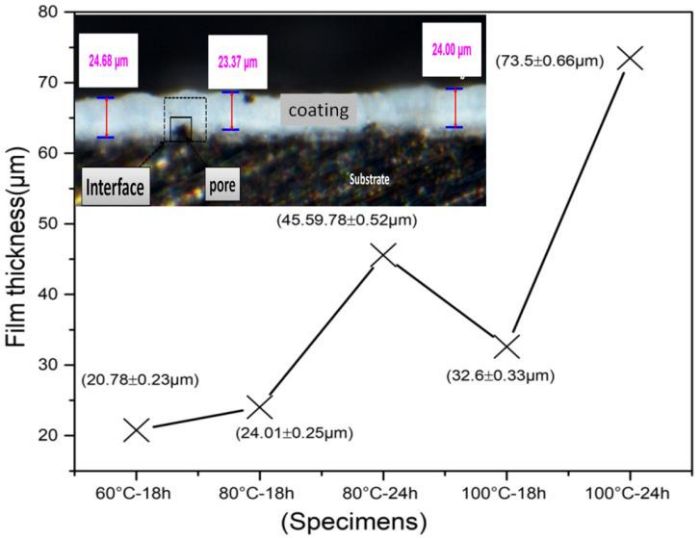

Figure 28. MgAl LDH thickness of the film-coated AA6082 estimated from the cross-sectional optical microscopic images as a function of reaction temperature and treatment time, (for representation, insight is the optical images of LDH at 80 °C and 18 h reaction conditions.

4.1.3. Electrochemical Study

The as-prepared MgAl-LDH anticorrosion behavior was investigated through electrochemical studies. Figure 29 exhibits the potentiodynamic polarization curves of all the tested samples, while the corrosion current density

and corrosion potential are listed in Table 8. With the increase of synthetic reaction temperature and crystallization time, the corrosion current density decreases, and a significant increase in the film resistance is observed. The reduction of both the anodic and cathodic currents suggests an increase in corrosion resistance. The polarization curves of MgAl LDH coating obtained from the specimens developed at 60°C–24h, 80°C–18h, 80°C 24h, 100°C 18h and 100 °C–24 h showed a noticeable decrease in corrosion of both anodic and cathodic current density compared to the bare AA6082. The significant reduction of the current densities suggests that the MgAl LDH thin films can help to decrease the corrosion rate of the substrate. All the developed films on AA6082 showed lower corrosion current density along with a shift of the corrosion potential to higher values compared to bare AA6082. As one can see, for almost all the investigated samples a rise in the corrosion potential was observed as the crystallization time increased. The MgAl LDH is believed to provide corrosion protection due to the following two mechanisms: (1) the barrier effect, as they are dielectric materials that protect the metal surface by avoiding interaction with the metal substrate; (2) by entrapping Cl^- ions and releasing nitrates. In the case of the polarization curves, the main protection mechanism likely observed is the physical barrier effect provided by the LDH layer which promotes a decrease in the flow of current. According to the mixed potential theory, anodic and cathodic reactions can be described by a straight line in the E versus Log(i) plot. For purely activation-controlled anodic and cathodic processes, a linear extrapolation of the Tafel slopes from the experimental curves is possible [144], thus determining the corrosion current density. When one of the reactions (generally the cathodic reaction) is limited by the rate of transport of the reactant to the metallic surface (concentration-controlled processes) the extrapolation of the corrosion current density is still possible, even if it becomes more complex. If a dielectric coating

is present over the metal surface, the ohmic drop due to its insulting nature affects the reliability of the Tafel extrapolation of the corrosion current density. Besides, the extrapolation of corrosion current density values over passive metals such as aluminum in a near-neutral chloride containing media is of doubtful scientific significance. However, there are many literature reports in which the corrosion current density is extrapolated from E versus Log(i) plots in presence of a dielectric film (LDH coating or organic coating) over the surface of aluminum electrodes immersed in neutral chloride containing media. It is our opinion that DC polarization curves collected over coated aluminum samples can provide mainly a qualitative assessment of the quality of the coatings. The flow of direct current in the case of metals coated with insulating materials is mainly possible thanks to the presence of defects and or heterogeneity through which the electrolyte can reach the metallic surface. Therefore, the evolution of the anodic and cathodic current densities can be related to the amount of defect and homogeneity of the coatings.

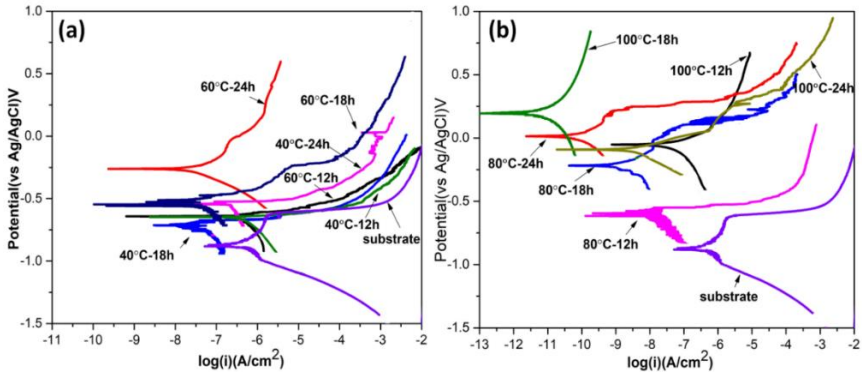

Figure 29. Polarization curves of bare AA6082 and the coated AA6082 in 0.1 M NaCl aqueous solution.

Table 8. The electrochemical parameters estimated from the polarization data in Figure 28.

Specimens	E_{corr} (Ag/AgCl) (V)	I_{corr} (μA/cm^2)
AA6082	–0.879	0.46556
40 °C–12 h	–0.679	0.33138
40 °C–18 h	–0.721	0.07629
40 °C–24 h	–0.564	0.28947
60 °C–12 h	–0.683	0.40345
60 °C–18 h	–0.519	0.07524
60 °C–24 h	–0.254	0.05214
80 °C–12 h	–0.623	0.03121
80 °C–18 h	–0.243	0.00156
80 °C–24 h	+0.016	0.00024
100 °C–12 h	–0.099	0.03903
100 °C–18 h	+0.241	0.00001
100 °C–24 h	–0.122	0.00263

To further understand the corrosion resistance ability of MgAl LDH, EIS analysis was performed. Figures 30 and 31 show the impedance modulus and phase plots, respectively. At low frequency (about 0.01 Hz), higher impedance modulus values ($|Z|_{0.01}$) are a rough estimation of the corrosion resistance properties: It can be seen that the samples 100 °C–24 h and 100 °C–18 h exhibit the highest value of $|Z|_{0.01}$ among the investigated samples. Furthermore, |Z| values follow a general tendency of corrosion resistance, higher temperature, and crystallization time and exhibit a greater propensity of corrosion resistance, according to the higher thickness of the LDH layers. These results are consistent with the results obtained from the potentiodynamic curves. The specimens fabricated at 100 °C–24 h showed comparatively lower corrosion resistance than 100 °C–18 h, which may be due to their greater film thickness which causes more

defects in the coating itself and/or pores at the interface with the substrate. The impedance results suggest that the high temperature and aging time lead to an increase in corrosion resistance, which is probably due to increased crystallization of the layered double hydroxide and a thickening of the layer as well. When the temperature conditions and aging time are moderate, the enhancement in terms of corrosion resistance is less pronounced. Besides, the |*Z*| values of the MgAl LDH film developed at different reaction conditions follow a general tendency: the higher the hydrothermal reaction temperature, the higher is the corresponding |*Z*| value obtained. The thickness of the film also plays a vital role in corrosion protection, and |*Z*| values vary with the increment in film thickness. The sample (100 °C–18 h) showed around 33 µm film thickness and the highest corrosion resistance among all the processed samples.

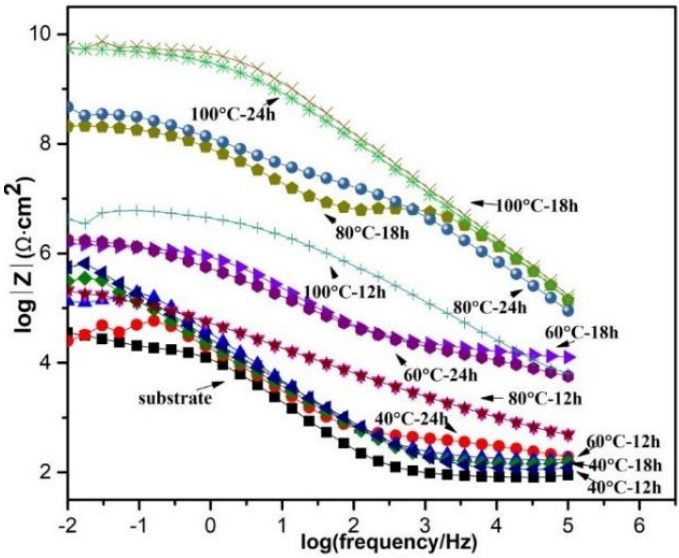

Figure 30. EIS spectra (Bode plots of log(|Z|) vs. log(frequency)) of bare AA6082 alloy and AA6082 alloy coated with LDH film at various reaction temperatures and crystallization times in 0.1 M NaCl solution after 30 minutes.

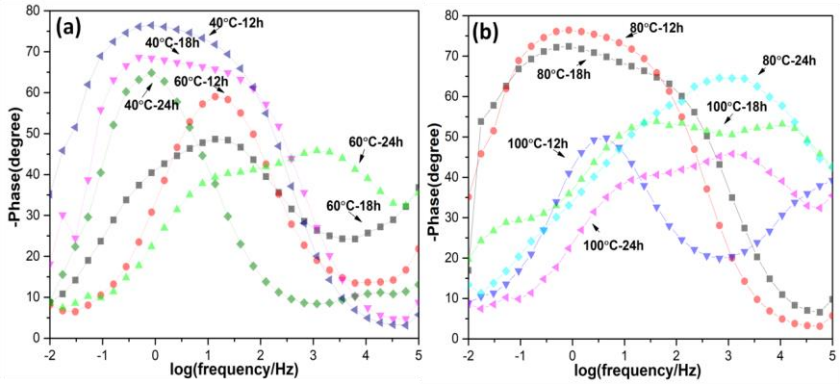

Figure 31. EIS spectra (Phase angle vs. log(frequency)) of bare AA6082 alloy and AA6082 alloy coated with LDH film at various reaction temperatures and crystallization times in 0.1 M NaCl solution after 30 minutes.

Figure 32 shows the evolution with an immersion time of the impedance modulus of the most representative samples among those investigated (data collected after 1, 3, and 7 days of immersion are reported). All the samples show a quite relevant decay of the protection properties during the 7 days of continuous immersion in the electrolyte. Regardless of the synthesis conditions, after one week of immersion, the low-frequency impedance is in the 10^5–10^6 Ω cm^2 range for all the investigated samples. This value is in any case remarkably higher than the $|Z|_{0.01}$ value of the bare substrate at the beginning of the immersion in the electrolyte ($|Z|_{0.01} \approx 10^4$ Ω cm^2). The decrease in impedance observed for the investigated coatings is likely to rely on the presence of porosity and defect in the coating and at the metal/LDH layer interface. According to optical microscope observations of the LDH layer and LDH/metal interface, thicker coatings (i.e., with synthesis conditions that promote higher LDH growth rate) are more defective and porous. This would explain the evolution of the impedance spectra with time: at the beginning, the LDH layers act as a barrier against electrolyte permeation; as time elapses, the solution moves through the defects and pores thus

reaching the metal/coating interface. The latter process promotes a decrease in impedance over all the frequency ranges since coating resistance is reduced and the Faradic process is promoted.

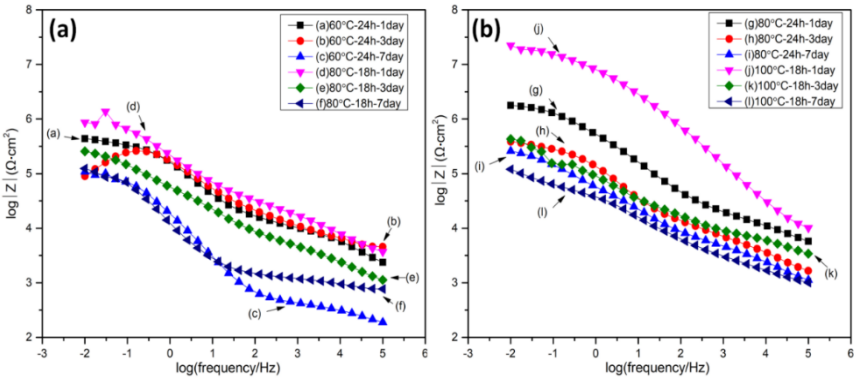

Figure 32. Bode plots of AA6082 samples, coated with MgAl–NO3 LDH thin film after immersion in 0.1 M NaCl: (a) 60 °C–24 h and 80 °C–18 h sample from 1 to 7 days immersion; (b) 80 °C–24 h and 100 °C–18 h 1 to 7 days immersion time.

The EIS spectra reported in Figure (30-31) were fitted to get some insight into the effect of the different parameters on the corrosion protection properties of the investigated coatings. According to Figure 31, all the samples show two relaxation processes, which are located in the middle-high or middle–low-frequency range. Notice that the thickness, as well as the defectiveness, of the coatings, strongly affect the electrochemical response of the diverse samples. For this reason, it is not surprising to observe the dispersion of the relaxation processes in the investigated frequency range. According to the literature [145][146], the EIS response of the LDH covered samples can be analyzed employing a $R_s(CPE_{LDH}(R_{LDH}(CPE_{dl}R_{ct})))$ electrical equivalent circuit. In this circuit, R_s stands for the resistance of the electrolyte. The relaxation process at the higher frequencies is fitted employing a resistance, R_{LDH}, which indicates the pore

resistance of the LDH layer and a constant phase element, CPE_{LDH}, which represents the dielectric properties of the layered double hydroxide coatings. The relaxation process at the lower frequencies is fitted employing a resistance, R_{ct}, which is related to the superimposition of the contribution of the charge-transfer process and of the aluminum oxide and a constant phase element, CPE_{dl}, which represents the double layer capacitance contribution, overlapped to that of the dielectric properties of the aluminum oxide. According to the mathematical representation of a CPE, (i.e. $Z_{CPE} = 1/(Q(\omega j)^{\alpha})$ the parameters Q and α were employed to describe the dielectric response of the electrodes. Table 9 shows the fitting results for the investigated samples. Notice that the parameters α_{LDH} and α_{dl} are almost always far from unity. For this reason, it is not possible to attribute any precise physical meaning to the pre-exponential factors Q_{LDH} and Q_{dl}. As far as the R_{LDH} and R_{ct} parameters are concerned, one can observe a certain scattering during immersion time for the samples 60 °C–24 h and 80 °C–18 h, probably due to the porosity of the coatings and to the consequent localization of the corrosion attack promoted by chlorides. On the other hand, the samples 80 °C–24 h and 100 °C–18 h show a smoother decrease in the corrosion protection properties (described by R_{LDH} and R_{ct}) which indicates that the coatings are more compact (as suggested by the relatively high values of R_{LDH}) and protective (as suggested by the relatively high values of R_{ct}).

Table 9. Evolution with the time of the fitting parameters R_{LDH}, Q_{LDH}, α_{LDH}, R_{ct}, Q_{dl}, and α_{dl}.

Sample	Immersion Time	R_{LDH} (kΩ cm^2)	Q_{LDH} (Ω^{-1} cm^{-2} s$^{\alpha}$)	α_{LDH}	R_{ct} (kΩ cm^2)	Q_{dl} (Ω^{-1} cm^{-2} s$^{\alpha}$)	α_{dl}
60 °C–24 h	1 day	13.0	4.2×10^{-7}	0.51	420.0	1.4×10^{-6}	0.72
	3 days	96.30	1.7×10^{-6}	0.31	828.7	1.1×10^{-6}	0.71
	7 days	98.3	1.1×10^{-5}	0.85	0.5	7.8×10^{-6}	0.46
80 °C–18 h	1 days	5705.0	5.1×10^{-6}	0.91	0.9	7.2×10^{-5}	0.46
	3 days	50.1	7.2×10^{-6}	0.51	270.2	9.9×10^{-6}	0.65
	7 days	118.1	1.7×10^{-5}	0.85	2.2	7.9×10^{-5}	0.19
80 °C–24 h	1 days	41.0	4.6×10^{-7}	0.54	2095.0	8.1×10^{-8}	0.77
	3 days	11.2	2.0×10^{-6}	0.43	372.9	1.8×10^{-6}	0.69
	7 days	7.8	2.5×10^{-5}	0.71	354.8	1.0×10^{-5}	0.93
100 °C–18 h	1 days	6135.0	2.0×10^{-8}	0.69	18420	7.8×10^{-8}	0.68
	3 days	13.0	4.2×10^{-7}	0.51	418.4	1.4×10^{-6}	0.72
	7 days	104.2	8.8×10^{-6}	0.46	97.4	1.2×10^{-4}	1.0

However, one should consider that: (1) in this study the crystallization treatment was prolonged to obtain relatively thick coatings, while in the literature very often only a thin conversion layer of LDHs was investigated; (2) the electrolyte employed in this study is more dilute than 3.5 wt % NaCl (0.1 M ≈ 0.58 wt %): for this reason, higher resistance values are expected. Also, the parameter R_{ct} for the samples investigated in this study is one of the highest compared to other works reported in the literature [146][147][148].

The EIS results seem also to be following the visual observation of the immersed samples as shown in Figure 33: optical microscope photos were taken after the 7 days of immersion in 0.1 M NaCl solution. The bare aluminum sample was badly corroded after the immersion and was covered with a thick layer of

corrosion products. Notice that cracks and blisters are observed on the LDH layers, following the remarkable decrease in R_{LDH} and R_{ct}.

The surface morphologies of the MgAl–LDH after 7 days immersion in 0.1 M NaCl solution are shown in Figure 34. It can be seen that no serious collapse of platelet structure is observed after 7 days of immersion and most of the structure remained almost intact and was shown to be similar to the as-prepared original structure. However, due to the longtime contact, dissolution of some platelets of MgAl–LDH structure was observed at some points Strong Cl^- signals in EDS analysis (inset of Figure 34b) were observed after contact with chloride solution, so we can say that the MgAl–LDH film exhibited anion exchange capability by absorbing Cl^- while the XRD analysis also showed that the interlayer of the MgAl–LDH was able to retain Cl^- inside the structure. The LDH film anion-exchange behavior on the aluminum alloy in the chloride solution can be generally expressed as follows: [149].

$$LDH–NO_3^- + 2Cl^- \rightarrow LDH–2Cl^- + NO_3^- \quad (1)$$

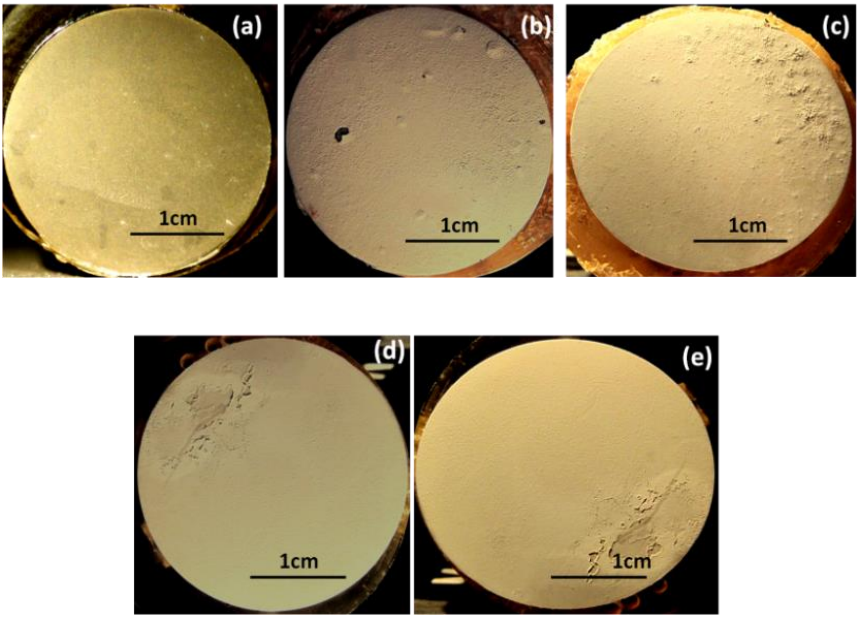

Figure 33. The specimens after 7 days of immersion in a solution of 0.1 M NaCl: (a) bare aluminum surface; (b) coated sample at 60 °C–24 h; (c) 80 °C–18 h; (d) 80 °C–24 h; and (e) 100 °C–18 h.

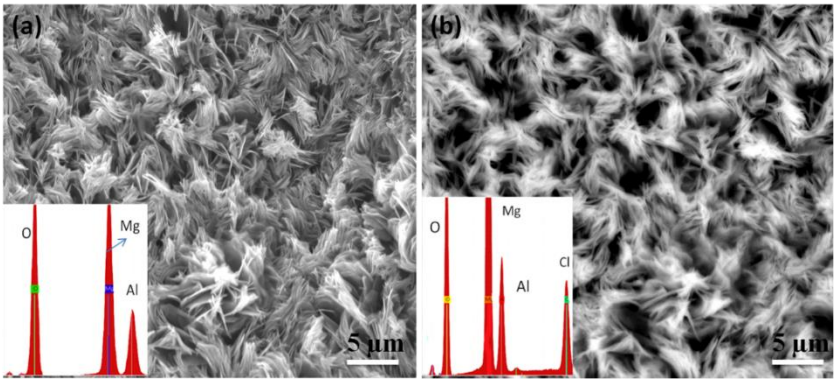

Figure 34. SEM images of (a) original MgAl LDH coating, 60 °C–24 h sample, and (b) an immersed sample soaked in 0.1 M NaCl solution for 7 days (Insets are the corresponding EDS spectra).

4.1.4. Conclusions

The finding demonstrated that the reaction temperature and crystallization times have an influential effect on the growth mechanism of layered double hydroxide which ultimately has a strong impact on its corrosion resistance behavior. Well-grown uniformed structures were obtained at 80 and 100 °C with crystallization times of 18 and 24 h while the thickness of the obtained films lay in the range of 24–74 µm, which also imparted a significant influence on the corrosion resistance properties. The results from polarization curves confirmed that MgAl LDH stands as improved corrosion protection thin film, which demonstrates significantly high impedance and low corrosion current density as compared to the substrate. The thicker coatings (>30 µm, obtained on treating the substrate at 100 °C for 18 and 24 h) showed a remarkable decrease of the corrosion current (3–4 orders of magnitude) and a remarkable increase in low-frequency impedance (|Z|0.01) compared to the bare substrate. However, the long-term durability of the investigated coating is still an issue as after about one week of immersion in the

0.1 M NaCl solution, the impedance in the low-frequency range showed a decrease of a few orders of magnitude. Compared to the bare substrate the investigated coatings were revealed to be in any case quite protective compared to the bare AA6082 substrate.

4.2. MgAl-LDHs surface morphologies and their effect on the corrosion resistance

4.2.1. Synthesis of MgAl- layered double hydroxide film

Considering the reaction temperature and salt concentrations, the Mg-Al layer double hydroxide film is synthesized by the in-situ crystallization method on the aluminum AA6082 alloy. The four different molar solutions of $MgNO_3.6H_2O$ and NH_4NO_3 were prepared to synthesize various morphological structures of MgAl layer double hydroxide. The solutions were separately prepared according to the salt concentrations listed in Table 10 and were dissolved (1:1) in a 1000mL four bottleneck heating flask (Sigma-Aldrich Glassware). The pH of the solutions was adjusted at 10, with a drop-by-drop addition of ammonium hydroxide solution. The pretreated aluminum samples were immersed vertically in the solution at different reaction temperatures i.e. 40˚C, 60˚C, and 80˚C for the 24 hrs crystallization time (conditions adjusted based on our preliminary results) under nitrogen gas bubbling. The samples were washed with deionized water after completion of film growth and were dried at room temperature.

Table 10. The compositions of the salts for the formation of MgAl LDH on AA6082.

Solution composition	$MgNO_3.6H_2O$	NH_4NO_3
(a)	0.008M	0.048M
(b)	0.008M	0.024M

(c)	0.028M	0.168M
(d)	0.028M	0.084M
(e)	0.05M	--------

4.2.2. Results and Discussion

The XRD pattern of the as-prepared MgAl LDH films developed at various salt concentrations and reaction temperature, under the same crystallization time (24hr) and pH (10), are presented in Figure (35-36). XRD patterns of the samples were well consistent with the formation of MgAl LDH and well resolved and distinct reflection peaks of typical LDH phases are observed. As presented in Figure 35 (a-b), at various salt concentrations ratios, almost a strong characteristic reflection of LDH phase is observed for 40˚C, 60˚C, and 80˚C reaction temperature, but the XRD pattern at salt concentrations of 0.008M $MgNO_3.6H_2O$-0.048M NH_4NO_3, and 0.008 M $MgNO_3.6H_2O$-0.024 MNH_4NO_3, almost no characteristic peak is observed for 40˚C reaction temperature. The characteristics peaks of (003), (006), (009), (110), and (113) crystal planes can be attributed to the presence of MgAl-NO_3 LDH [150]. In addition to characteristics peaks of LDH, $Mg(OH)_2$ peak was also observed, especially in the case of fabrication by the amount of 0.008M $MgNO_3.6H_2O$ and 0.048 MNH_4NO_3, as shown in Figure 35(a). That may be due to the excess hydrothermal treatment, where the sample was found to decompose and the excess Mg^{+2} ions phase separate as $Mg(OH)_2$ [151]. A decrease in peak intensity of MgAl-LDH at high temperature and salt concentrations could imply an increase in film thickness. At higher temperatures, 80˚C & 100˚C, the reflection peaks exhibit sharp and high intense narrow peaks which describe well crystalline and ordered structure.

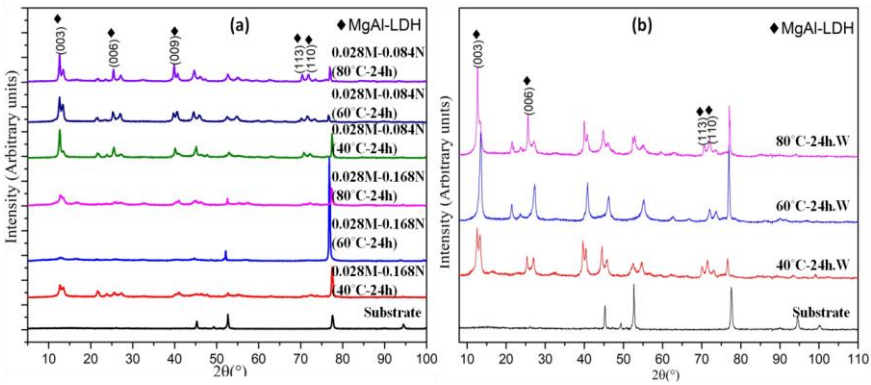

Figure 35. The XRD spectra of MgAl-LDH film samples developed on AA6082 obtained at various reaction temperatures and salt concentrations: -(M=MgNO3.6H2O, N= NH4NO3, W=without NH4NO3).

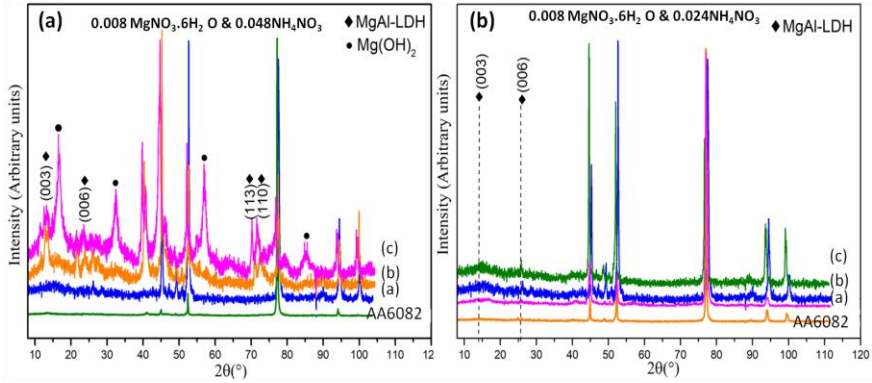

Figure 36. The XRD spectra of Mg-Al LDH film samples developed on AA6082, Fig (2a), a) 40˚C-24hr, b) 60˚C-24hr, c) 80˚C-24hr, Fig (2b) a) 40˚C-24hr b) 60˚C-24hr c) 80˚C-24hr at specified salt concentrations.

Figures (37, 38, 39) exhibits the surface morphologies of specimens synthesized at different conditions of reaction temperature and initial salt concentration at a pH of 10 and for an aging time of 24 hr. With the change of the molar ratio of salt concentrations and reaction time, the nanoarchitecture of LDH varied which could

prove a significant morphology influence on corrosion properties, owing to the ion exchangeability with the chlorine ions and it also acts as a barrier that protects the substrate from aggressive species. The optimized pH of 10 can cause the dissolution of the surface of aluminum alloys and cause the generation of aluminum oxides, which interact with Mg to form MgAl LDH on the aluminum substrate. Considering the process reaction conditions, different morphologies of MgAl-LDhH were obtained. Among them, three distinct morphologies were observed, namely: - flower-shaped lamellar or plate-like structure, stone-shaped, cauliflower structure as shown in Figures (37, 38, 39). The LDH microcrystals almost blanket the entire surface, perpendicular to the substrate. It is clear from the SEM images that the LDH granules start to originate at a lower temperature and crystallization time, which grows further with the increase of reaction temperature and aging time, and finally, at optimum conditions of both parameters, a distinct well-developed layer double hydroxide structure produced. The EDS results showed that the abraded Al surface was mainly composed of Mg, Al, and O, and a small percentage of C, caused by the contamination from the air. The film thickness of the obtained structure is studied through cross-sectional analysis, analyzed by optical microscopy. The increase in the temperature and initial salt concentrations remarkably influenced the thickness of LDH. The film thickness increased from 8 µm to 59 µm with the variation of reaction temperature and salt concentrations, as shown in Figure 40. With the increase of reaction temperature at the same initial salt concentrations, a significant increment in film thickness was also observed. As the film thickness getting thicker, there was also evident some pores at the interface of the substrate and the film, which can cause poor corrosion resistance properties. The film thickness of processed parameters at 60˚C for the molar ratio of 0.028M $MgNO_3.6H_2O$ and 0.168M NH_4NO_3 is shown in Figure 41.

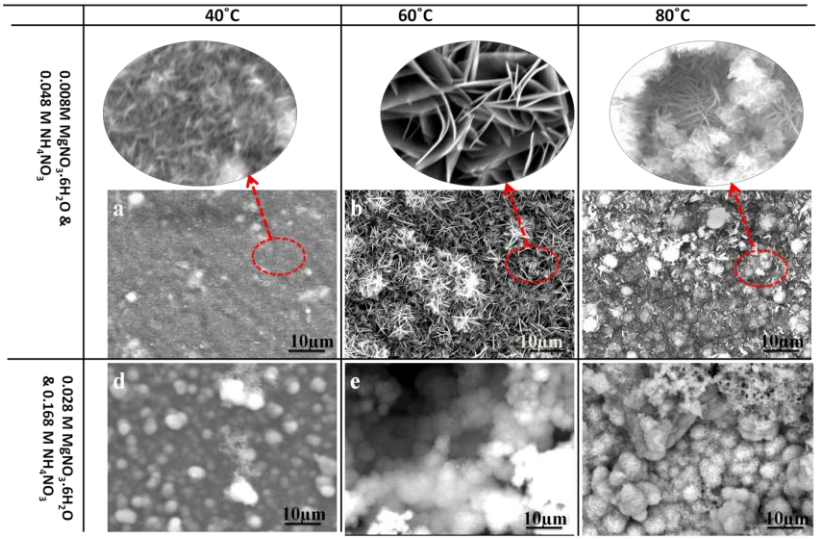

Figure 37. SEM images of LDH films obtained at various salt concentrations and reaction temperatures at 24 hr synthesis conditions.

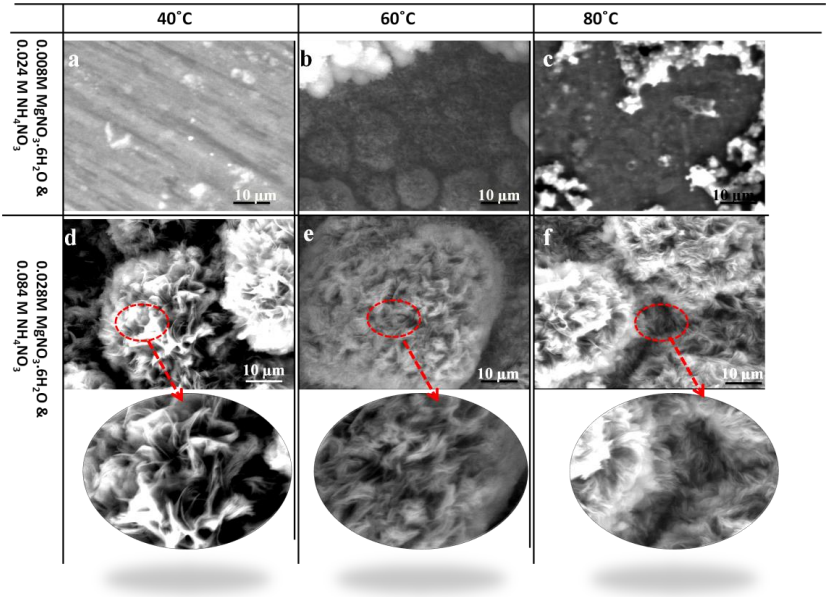

Figure 38. SEM images of LDH films obtained at various salt concentrations and reaction temperatures at 24 hr synthesis temperature.

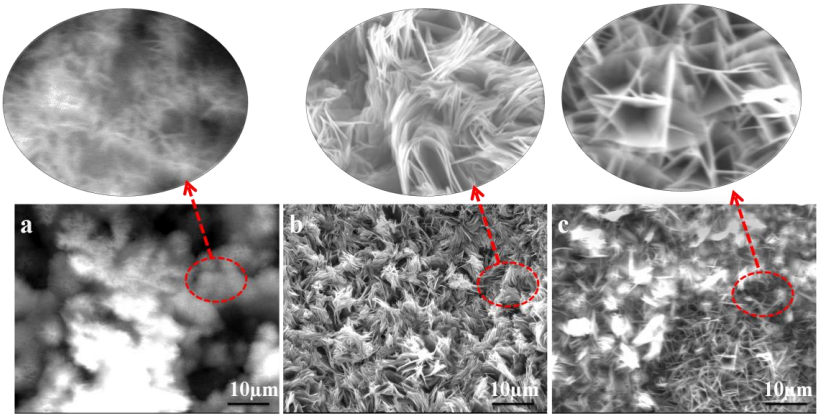

Figure 39. SEM images of LDH films obtained at 0.5M MgNO3.6H2O concentrations and various reaction temperatures for 24 hr at a synthesis temperature of (a) 40°C, (b)60°C, (c) 80°C.

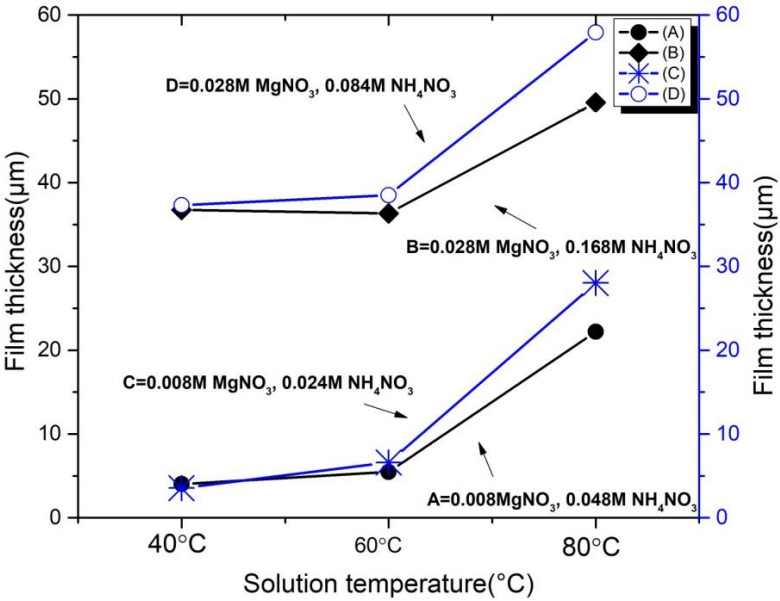

Figure 40. MgAl LDH thickness of the films coated AA6082 estimated from the cross-sectional optical microscopic images as a function of reaction temperature and salt concentrations.

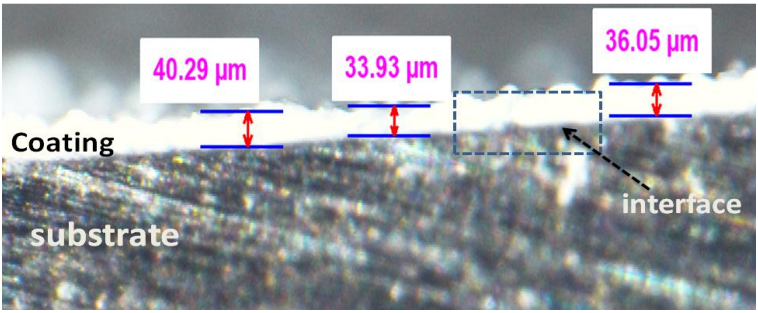

Figure 41. Cross-sectional optical images of the MgAl LDH films coated on AA6082 alloy at 60˚C for the molar ratio of 0.028M MgNO3.6H2O and 0.168M NH4NO3.

The corrosion resistance of obtained MgAl LDH film at various reaction temperatures and crystallization time is investigated by electrochemical studies. The potentiodynamic polarization curves of all the tested samples are shown in Figure 42. The corrosion potential and corrosion current density of each developed sample, extracted from polarization curves, are listed in Table 11. The corrosion current density of the MgAl LDH film prepared at 80˚C with 0.008 M $MgNO_3.6H_2O$ & 0.024 M NH_4NO_3 and 60˚C with 0.008 M $MgNO_3.6H_2O$ & 0.048 M NH_4NO_3 molar concentrations have shown a significant decrease as compared to the substrate while demonstrating the film thickness of around 6 and 38 µm, respectively. A significant increase in corrosion resistance was also observed for 0.028M $MgNO_3.6H_2O$ and 0.168 M NH_4NO_3 at 80˚C temperature. It is also to be noted, that with the increase in salt concentrations and even reaction temperature, the film thickness also varies, which also remarkably affects the electrochemical properties. There are two possible assumptions from the above results, on the one hand, the ion exchangeability of the MgAl-LDH film causes an increase in the corrosion resistance ability of the films, while On the other hand, the increases of the film thickness act as a protective layer, which provide an additional barrier between the contact of corrosive ions and the aluminum substrate. But the higher thickness of LDH may cause loose interaction with the substrate due to high defect density and pores formation at the interface of coating and substrate. A smoother and more regular morphology is expected to guarantee better wear and corrosion resistance. The calculated corrosion rate of treated samples is much lower than the corrosion rate of the untreated sample and up to a decrease of 5 order magnitude in corrosion current density is observed.

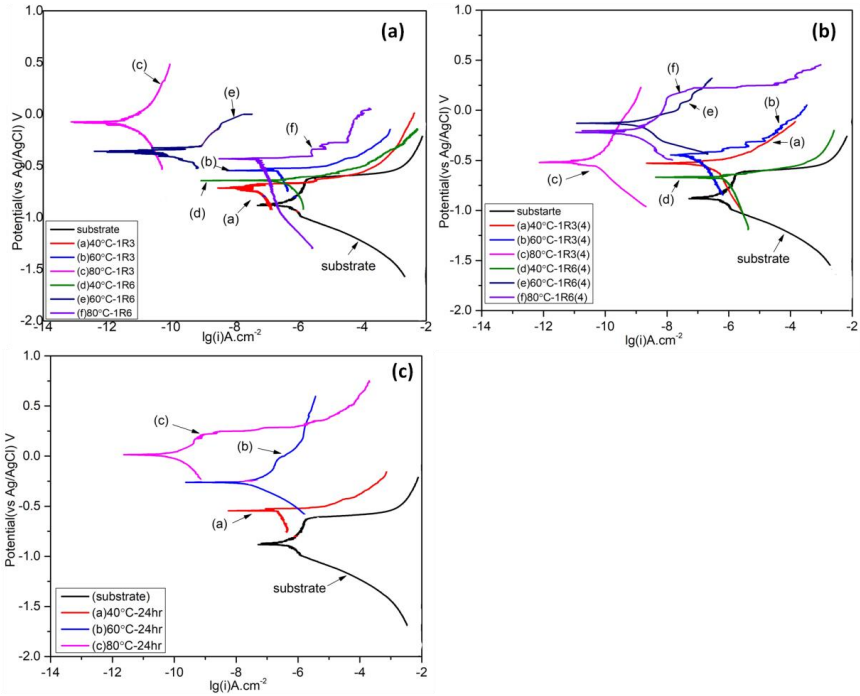

Figure 42. Polarization curves of bare AA6082 and the coated AA6082 in 0.1M NaCl aqueous solution.

Table 11. The electrochemical parameters estimated from polarization data in Figure 42.

Specimens	E(Ag/AgCl)V	I (μA/cm^2)
40˚C -1R3-N	-0.712	6.61E-02
60˚C -1R3-N	-0.594	2.29E-01
80˚C -1R3-N	-0.169	6.95E-06
40˚C -1R6-N	-0.701	6.31E-01
60˚C -1R6-N	-0.381	1.23E-04
80˚C -1R6-N	-0.495	9.12E-02
40˚C -1R3-4	-0.512	3.09E-01
60˚C -1R3-4	0.486	1.05E-01

80˚C -1R3-4	-0.554	1.73E-05
40˚C -1R6-4	-0.920	8.13E-01
60˚C -1R6-4	0.019	1.23E-03
80˚C -1R6-4	-0.249	8.32E-04
40˚C -24hr	-0.563	1.45E-01
60˚C -24hr	-0.263	5.13E-02
80˚C -24hr	0.009	7.42E-05

To further analyze the corrosion resistance properties of LDH films, which developed at different reaction conditions, EIS spectra were acquired in 0.1M NaCl solution after the 30 min delay for the system stabilization Figures (43-44). It can be observed from the Bode plots that the LDH-coated samples exhibit higher impedance in the low-frequency domain (0.1-0.01 Hz) compared with the bare aluminum alloy sample. It is also worthy to note that the impedance modulus of MgAl-LDH at feasible conditions has nearly five orders of magnitude higher than that of the Al substrate at 0.01 Hz. The strong shift of the impedance in the middle-high frequency range is related to the presence of the coating. The presence/absence of the shift in impedance in this range provides information related to the real presence of a dielectric coating on the surface of the metal. As far as Figures 43(a) and 43(c) is concerned, the samples produced at 80°C have shown an almost capacitive behavior in the middle-high frequency range, thus suggesting the presence of a dielectric LDH coating. For the coating derived from 0.008M $MgNO_3.6H_2O$ & 0.048M NH_4NO_3 solution, a similar EIS response is observed even when the temperature was 60°C. The other coatings in Figures 43a and 43c have shown much lower values of the electrochemical impedance in the investigated frequency range. The presence of two partially overlapped peaks in the phase angle spectrum (Figure 43c) and the limited increase in impedance seem to suggest that an LDH layer is present on the surface of the samples (in agreement

with XRD findings) but it is likely to be thin (or defective) and, therefore, only slightly protective. Considering Figures 43 (b-d), the EIS response suggests that only the coatings derived from 0.028M $MgNO_3.6H_2O$ & 0.168M NH_4NO_3 and treated at 80°C are characterized by a capacitive response in the middle-high frequency range. The low-frequency impedance of these coatings is also remarkably high compared to the other samples, indicating that the LDH layer is protective. The samples derived from 0.028M $MgNO_3.6H_2O$ & 0.084M NH_4NO_3 and treated at 60 and 80°C have shown a relevant increase of the low-frequency impedance (from 10^4-10^5 to 10^7-10^8 Ωcm^2) compared to the bare aluminum sample. However, a purely capacitive response was not observed. These coatings seem to be protective, thanks to the relevant increase in impedance but they are likely to be partially porous, permeable, and/or defective as they do not show a clear capacitive behavior. The EIS spectra of the other coatings reported in Figure 43(b-d) seem to indicate that all the LDH layers provide corrosion protection to a certain extent, as suggested by the increase in the low-frequency impedance compared to the bare sample. However, also in this case the conversion layer is likely to be thin or defected, as no remarkable increase of the impedance values in the middle-high frequency range was observed, compared to the low-frequency range values.

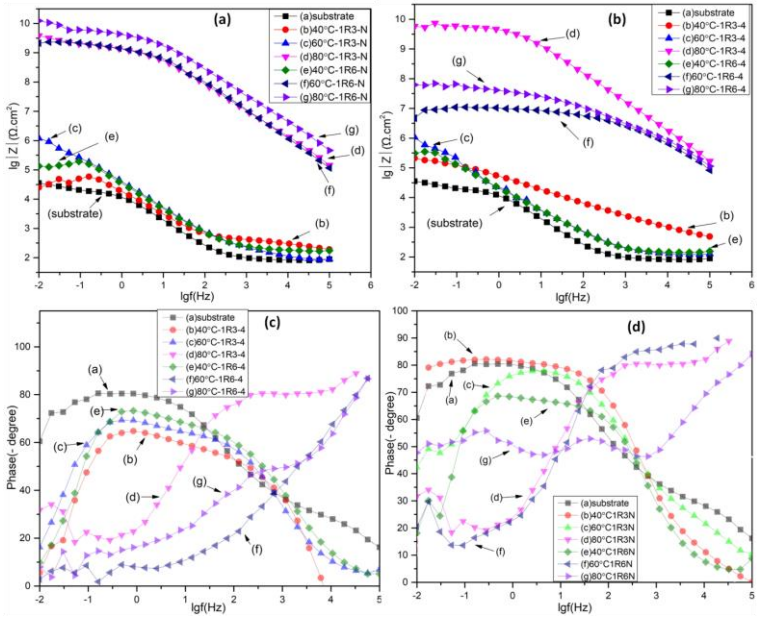

Figure 43. Bode plots of bare AA6082 alloy and AA6082 alloy coated with MgAl LDH film at various reaction temperatures and salt concentrations, in 0.1M NaCl solution. *1R3-N=0.008M MgNO3.6H2O&0.024M NH4NO3, *1R6-N=0.008M MgNO3.6H2O & 0.048M NH4NO3, *1R3-4 =0.028M

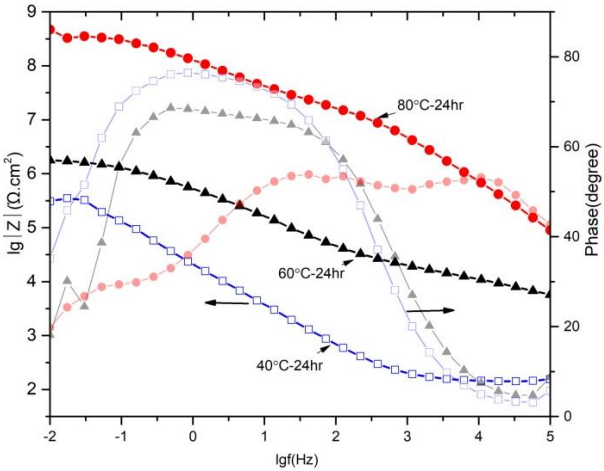

Figure 44. Bode plots of MgAl LDH film developed at 0.05M MgNO3.6H2O for different reaction temperatures.

4.2.3. Conclusion

In this part, we prepared the MgAl-LDH films on AA6082, exhibiting various morphologies, while their corresponding structural and corrosion resistance behavior is discussed. The finding obtained from SEM and XRD confirms the MgAl -LDH formation on the substrate and the results reveal that the reaction temperature and salts concentrations exert a significant effect on the LDH morphologies and growth rate. Among the developed morphologies, the flowers-like morphologies were of interest due to their curved or contoured nano-sheets structure, which is expected to increase the ion exchangeability of LDH with chloride ions. It was also confirmed that at the same salt concentration, uniformity and film thickness also increased with the increase of reaction temperature and concerning high salt concentrations, which influences the anticorrosion property. According to the electrochemical studies, the cauliflower structure and platelet structure had an eminent corrosion resistance performance in comparison to other

morphologies. The corrosion current density of the MgAl-LDH coatings is decreased up to five orders of magnitude compared with that of the AA6082 alloy, thus has proved effective protection against aggressive species.

4.3. ZnAl-Layered double hydroxide and corresponding corrosion resistance properties

4.3.1. Synthesis of Zn-Al layered double hydroxide film

Zinc nitrate hexahydrate with a concentration of 0.035M (Zn $(NO_3)_2.6H_2O$) and 0.210 (NH_4 $(NO_3)_2.6H_2O$) solution was mixed in 1000 mL deionized water to have a 1:6 of salts concentrations. The pH of the solutions was adjusted at three different pH values i.e 6.0, 6.5, and 7.0 by the ammonium hydroxide addition. The solution was poured into four bottleneck heating flask (Sigma-Aldrich Glassware) and a pretreated aluminum sample (3.14cm^2) was immersed vertically in the solution. The experiments were performed at different reaction temperatures i.e. 40˚C, 60˚C, and 80˚C, for the reaction times of 18h and 24h under nitrogen gas bubbling. The samples were washed with deionized water after the completion of the experiments and were dried at room temperature.

4.3.2. Results and Discussion

The XRD patterns of ZnAl-LDH synthesized at various reaction conditions have shown in Figure 45(a-c), which is well consistent with the formation of LDH structure, and well-resolved distinct reflection peaks of typical LDH phases were observed [152]. The characteristics peaks of (003), (006), (012), (110) crystal planes are attributed to the presence of layered double hydroxide. The 003 planes of the ZnAl-LDH correspond to the interlamellar distance of the nitrated intercalation inside the layer double hydroxide. The cell parameters “c” is

measured by three times the interlayer distance d_{003}, and “a” is calculated by the two times of the d_{110}. The calculated cell parameters are listed in Table 12. The findings have shown small variations in the cell parameters “*a”* and “*c”* which indicate effective incorporation of divalent cations (Zn^{2+}) in the brucite LDH structure. The cell parameter “c” of ZnAl-LDH for d_{003} lies around ~ 3.0 nm which relates to nitrated LDH. The small variation of the “*c”* parameter is due to the different arrangement of the nitrate anions, which is strongly entitled to the LDH synthesis parameters. The cell parameter “c” was found to elevate possibly due to different size, strength, and bonding orientation of the hydroxyl group and nitrate anions inside the brucite-like structure, with the effect of the increasing reaction treatment time and temperature, [153]. While other low-intensity reflection peaks were observed that attributed to the presence of a secondary phase, $(Al_2O_3)_4$. H_2O) crystalline secondary phase $(Al_2O_3)_4$. H_2O is a commonly observed phase in the brucite-like structure when the synthesis condition of pH is adjusted lower than 8. As presented in Figure 45, the samples developed at 6.0 and 6.5 pH for 40˚C and 60˚C and 24 hr crystallization time, have shown the strongest reflection peaks with sharp and high intense narrow peaks. and also for 60˚C-18 hr for 7.0 pH reaction conditions, which describe well crystalline, ordered structure, and proper stacking of the ZnAl-LDH layers. The diffraction peaks of the ZnAl-LDHs alloy have almost disappeared at 80˚C temperature for the treatment time of 24 hr for 6 and 7 pH solution, possibly due to high thermal treatment and result in relatively thicker and flatter surface structure, as can see in SEM images the LDH platelet structure found to be fused and no curved platelet structure were observed.

Table 12. Cell parameters of ZnAl-LDH structure at various synthetic conditions.

Sample	Cell Parameter, *a* (nm)	Cell Parameter, *c* (nm)	Interlayer Distance, d_{003} (nm)
40 °C–24 h-6.0pH	0.298	2.801	0.934
40 °C–18 h-6.5pH	0.299	2.887	0.963
40 °C–24 h-6.5pH	0.298	2.798	0.933
40 °C–18 h-7.0pH	0.311	2.691	0.897
40 °C–24 h-7.0pH	0.311	2.673	0.891
60 °C–24 h-6.0pH	0.334	3.139	1.047
60 °C–18 h-6.5pH	0.334	3.169	1.056
60 °C–24 h-6.5pH	0.336	3.089	1.030
60 °C–18 h-7.0pH	0.336	3.205	1.068
60 °C–24 h-7.0pH	0.334	3.192	1.064
80 °C–18 h-6.0pH	0.336	3.179	1.060
80 °C–18 h-6.5pH	0.335	3.222	1.074
80 °C–24 h-6.5pH	0.336	3.169	1.060
80 °C–18 h-7.0pH	0.335	3.381	1.147

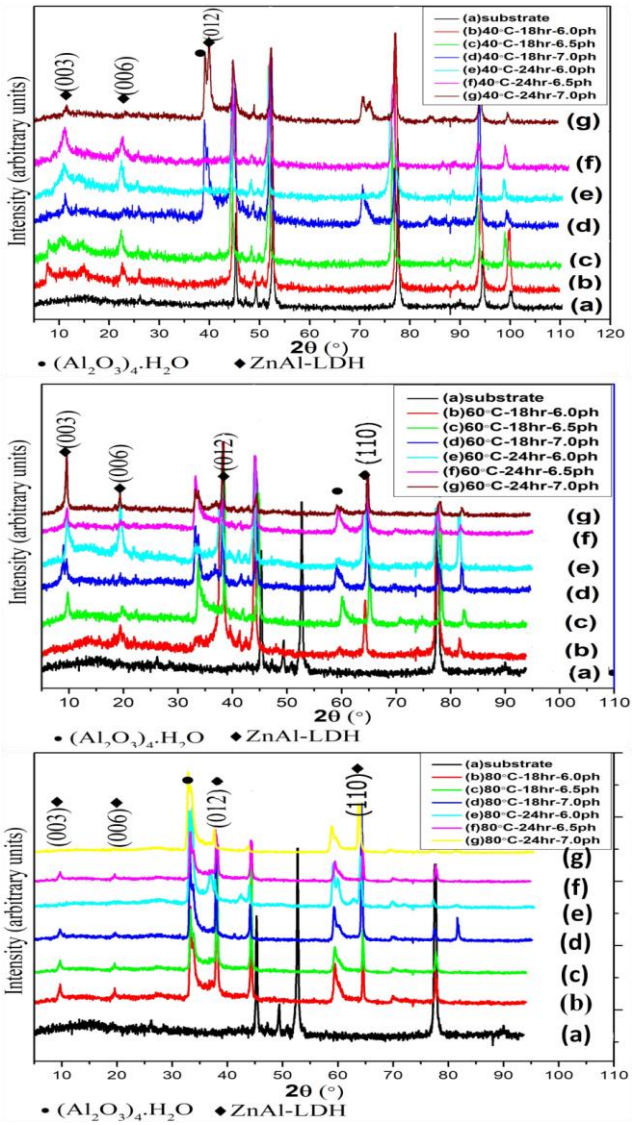

Figure 45. The XRD spectra of ZnAl-LDH film samples developed on AA6082 obtained at the extended reaction temperature, crystallization time, and different pH conditions.

Figure (46-48) exhibits the surface morphologies of the specimens synthesized at different conditions of reaction temperature and reaction time, at pH values of 6.0, 6.5, and 7.5. With the variation of synthesis parameters, the nanoarchitecture of LDH varied, which has a significant effect on the LDH structural growth and corresponding corrosion properties. The pH of 6.5 has shown the well-established architecture of surface morphology at 40˚C-24hr, where Al interacts with Zn to form a distinct ZnAl LDH film on the substrate. It is clear from the SEM images that the LDH granules start to originate at a lower temperature and crystallization time. They grow further with the increase of synthesis conditions, and at optimum conditions of both parameters, a distinct well-developed layer double hydroxide structure is produced. With the further increase of reaction temperature and aging time, the LDH plates fused and a flat layer of LDH is formed on the substrate. The LDH microcrystal's in most cases homogeneously blanket the entire substrate surface, perpendicular to the substrate. With the increase of reaction conditions, a regular increment in film thickness was also observed as shown in Figure 49. On the other hand, at the same values of reaction temperature and aging time, the pH has shown to cause an increase in the film thickness and this trend is more evident at higher reaction temperature conditions. This may be due to the increase of nucleation at higher pH, resulting in higher growth of LDH, as suggested by Abderrazek et al [152]. The LDH film thicknesses of the obtained structures are studied through cross-sectional analysis (optical microscopic) of the LDH coated specimens and shown that the increase in the pH, reaction time, and reaction temperature remarkably influenced the LDH thickness. The film thickness increased from 5 µm to 49 µm with the synthesis parameters, as shown in Figure 49. As the film thickness is thicker, it became evident that some pores at the interface of the substrate and the film, which can cause poor corrosion resistance properties.

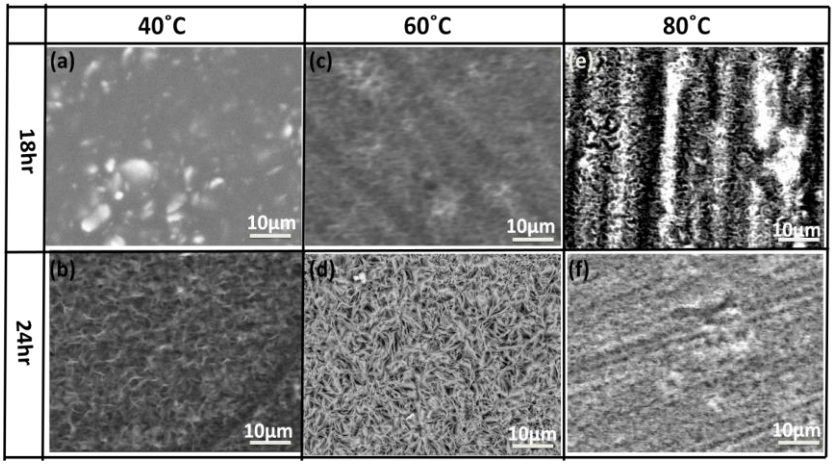

Figure 46. SEM images of ZnAl-LDH films obtained at a pH of 6.0.

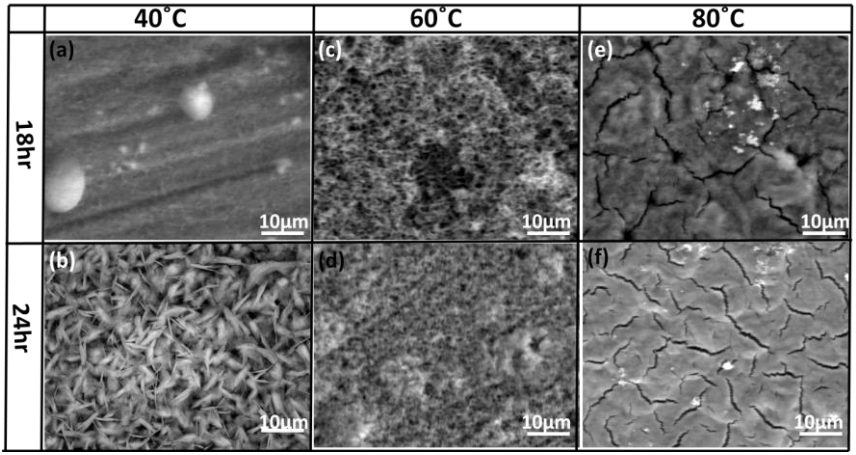

Figure 47.SEM images of ZnAl-LDH films obtained at a pH of 6.5.

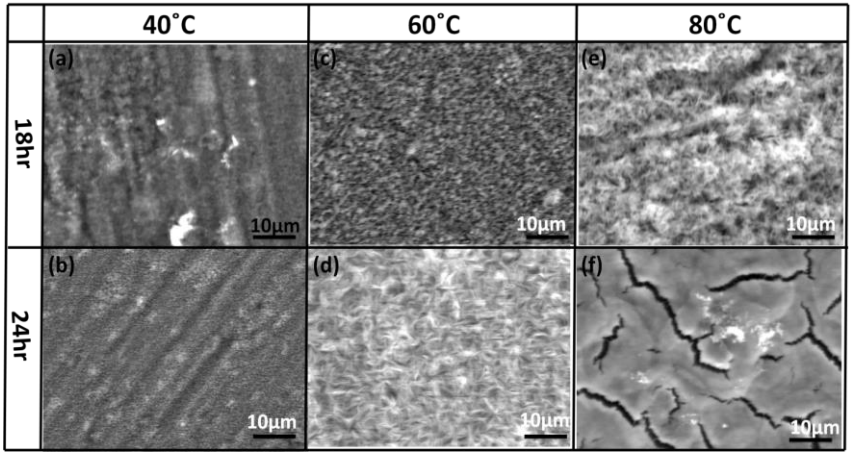

Figure 48. SEM images of ZnAl-LDH films obtained at a pH of 7.0.

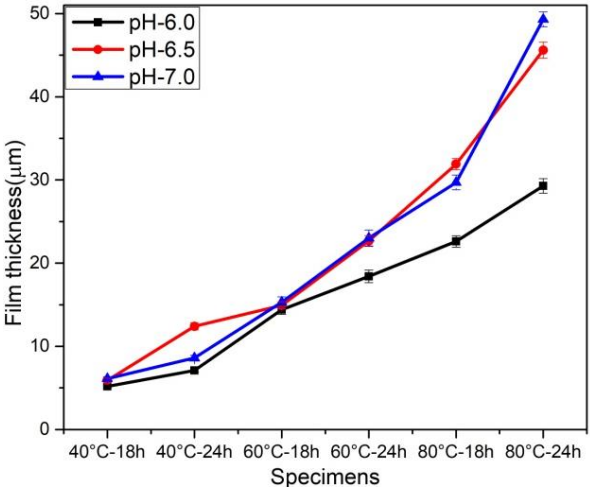

Figure 49. ZnAl LDH thickness of the films coated AA6082 estimated from the cross-sectional optical microscopic images as a function of reaction time, pH, and reaction temperature.

The corrosion resistance of ZnAl LDH fabricated at various conditions is investigated by electrochemical studies. The potentiodynamic polarization curves of all the tested samples are shown in Figure 50. At a constant pH value, generally with the increase of reaction temperature and crystallization time, it is found to have significant decreases of the corrosion current density and thus an increase in the corrosion resistance of LDH is observed. With the increase of reaction conditions, it is also found that the LDH microstructure transforms into compact architecture, which acts as a barrier film against the aggressive media and helps to increase the ZnAl-LDH corrosion resistance. On the other hand, a well-developed platelet structure is formed at moderate conditions, especially at 40˚C-24hr reaction conditions for a pH of 6.5 that also cause a significant increase of ion-exchange area for the intercalation of Cl^- ions and effectively reduce the corrosion current density with high corrosion potential, as shown in the polarization curves (Figure 50). At 80˚C reaction temperature, there was observed the lowest corrosion current density among all sets of specimens developed at different pH. Although cracks appeared on the surface of LDH film at the high temperature, due to high film thickness it can be suggested that cracks did not go deeper inside the film, thus the overall structure acts as a strong barrier against the aggressive environment and up to a 3 order of reduction in corrosion current density was observed. The open-circuit potential is found to be shifted toward nobler values with increasing temperature and immersion time. In particular, 40˚C-24hr-6.5pH derived samples have shown relatively high corrosion potential (-0.091 V vs Ag/AgCl), probably due to the well-developed distinct LDH structure. The overall polarization curves of the ZnAl LDH coating have shown an increase in the corrosion resistance compared to the bare AA6082. The significant reduction of the cathodic and anodic branches of the curves of ZnAl LDH implies that the thin films can help decrease the corrosion rate of the metallic

substrate. A remarkable anodic and cathodic current density reduction is observed for the samples treated at 80°C for 18-24 h at pH 6.5 and 7.0. For these samples, both anodic and cathodic current densities are decreased up to three orders of magnitude compared to the untreated sample. The ZnAl LDH provides corrosion protection due to the following two mechanisms: (1) barrier effect, as they are dielectric materials that protect the metal surface by avoiding the interaction of the aggressive environment with the metal substrate; (2) and also by entrapping Cl^- ions inside the brucite structure [154]. In this case (from polarization curves), it seems that the main protection mechanism is a barrier effect which decreases the flow of current acting as a physical barrier.

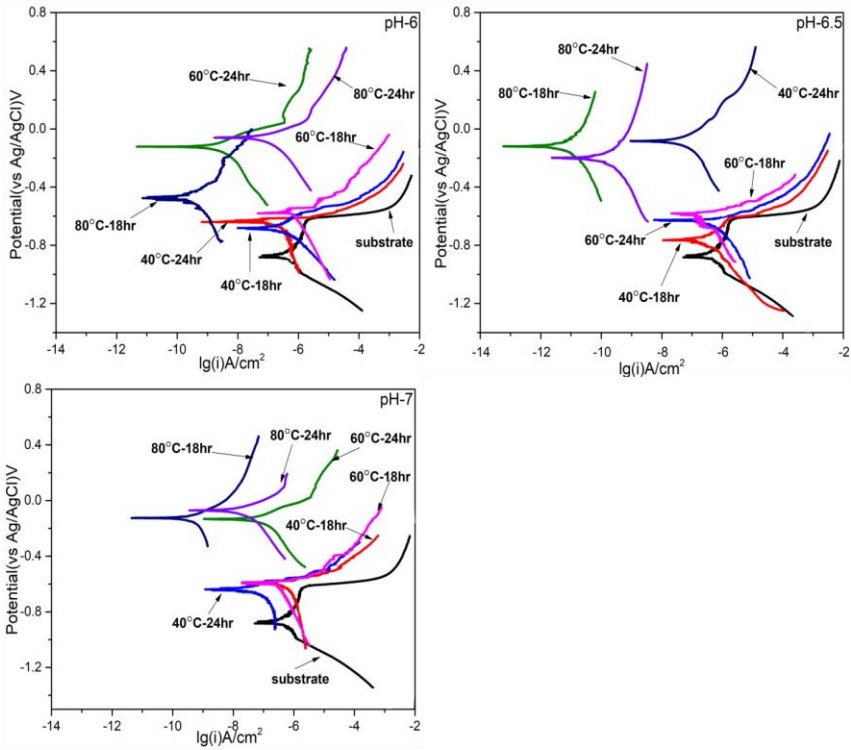

Figure 50. Polarization curves of bare AA6082 and the coated AA6082 in 0.1M NaCl aqueous solution.

To further understand the corrosion resistance ability of ZnAl LDH, EIS analysis was performed, as shown in Figure (51-52). At low frequency, higher |Z| depicts higher corrosion resistance, it can be seen that LDH film developed at the high reaction temperature conditions exhibit a higher value of |Z| compare to low-temperature conditions. Although moderate temperature conditions cause the formation of a well-developed platelet structure which increases the ion-exchange area with the Cl^- ions. However, the film developed at high temperature exhibits a compact formation of the LDH layer with the fusion of LDH structure and thus acts as a strong barrier against aggressive media. Furthermore, it is clear from Figure 51, |Z| values follow a general tendency of corrosion resistance, at each pH value, higher temperature and crystallization time exhibit greater propensity of corrosion resistance and it is consistent with the results obtained from the potentiodynamic curves and also from SEM and XRD results. The LDH films developed at 80˚C reaction temperature for different pH values observed a capacitive behavior in the middle-high range frequencies. This suggested the presence of the dielectric film and almost a similar trend was found for the specimen developed at 60˚C-24hr for 6.5 pH. A dramatic increase in EIS was also observed for the specimen developed at 40˚C-24hr-6.5 pH, which was consistent with the polarization curves. The samples developed at lower reaction temperatures have shown much lower values of the electrochemical impedance in the investigated frequency range and that limited increase in impedance suggested the presence of LDH film on the surface of the samples is not properly homogeneous or porous, therefore only slightly protective. The samples treated at 80°C-18 h and 24 h have shown a significant increase in the low-frequency impedance (from 10^4-10^5 to 10^7-10^8 Ωcm^2) compared to the bare AA6082. However, overall a purely capacitive response of the frequency range was not observed in the developed LDH films, which suggested that LDH films are likely

to be partially porous, permeable, and/or defective. The EIS spectra indicate that all the LDH layers provide corrosion protection to a certain extent, as suggested by the increase in the low-frequency impedance compared to the bare sample. Based on the qualitative comparison of the impedance modulus spectra, the extended reaction conditions seem to make a strong impact on the corrosion resistance properties, in addition to coming sufficiently higher than the traditional platelet structure.

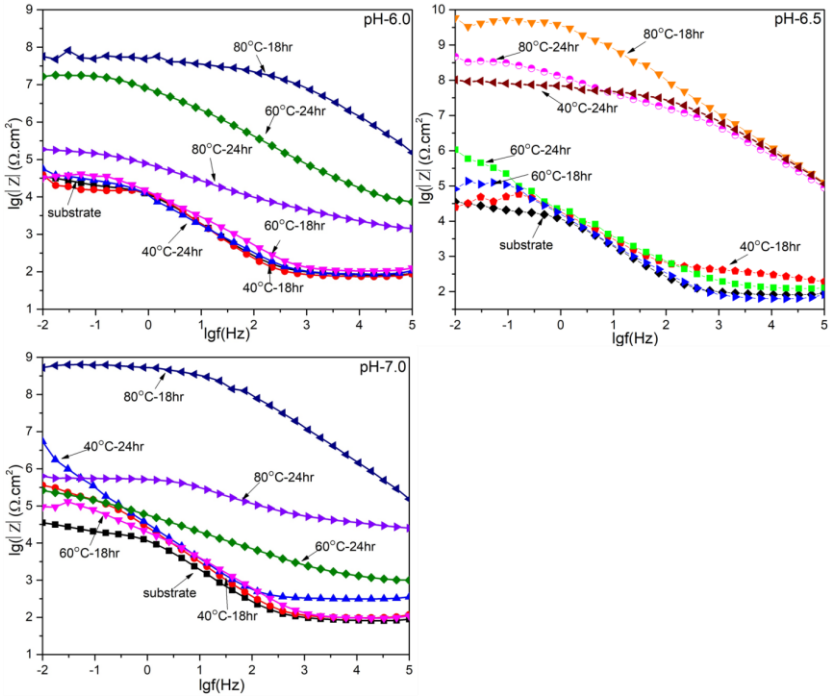

Figure 51. EIS spectra, (Bode plots of log (|Z|) vs.log(frequency)) of bare AA6082 alloy and AA6082 alloy coated with ZnAl-LDH film at various reaction temperatures and crystallization time at 6.0,6.5 and 7.0 pH, in 0.1M NaCl solution.

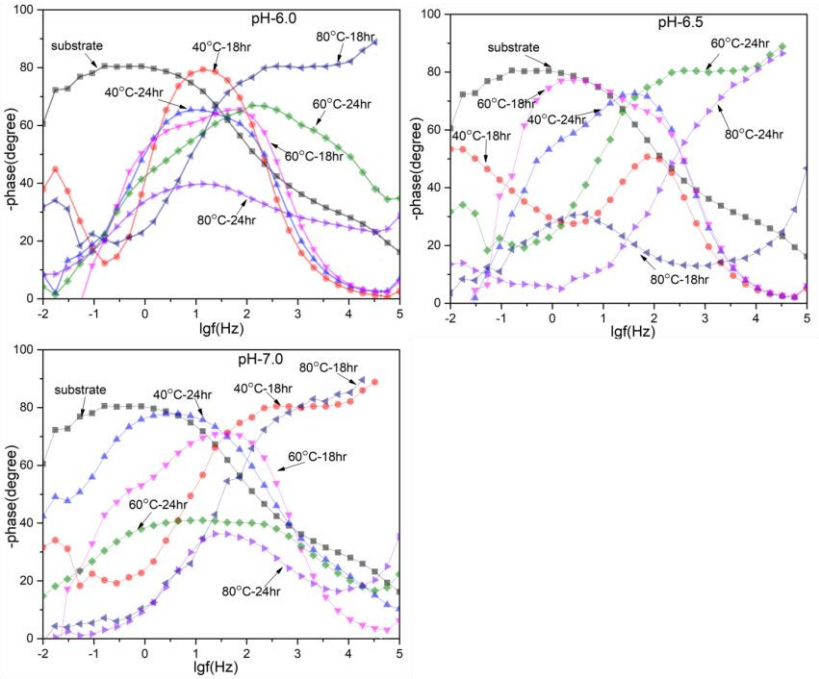

Figure 52. EIS spectra (-phase angle vs frequency) of bare AA6082 alloy and AA6082 alloy coated with ZnAl-LDH film at various reaction temperatures and crystallization time at 6.0,6.5 and 7.0 pH, in 0.1M NaCl solution.

The EIS spectra reported in Figures 51 and 52 have been furtherly investigated utilizing electrical equivalent circuits (e.e.c.) to get a deeper knowledge of the corrosion protection properties of the investigated coatings. The phase angle spectra reported in Figure 52 shows two partially overlapped relaxation processes, which are in the middle-high or middle-low frequency range. According to the relevant increase in thickness obtained by increasing the treatment temperature and/or duration, the electrochemical response of the investigated samples remarkably differs from one sample to another. A dispersion of the relaxation processes in the investigated frequency range is therefore

expected. The presence of inhomogeneities and defects, occurred during the synthesis of the coatings, furtherly exacerbates the differences among the EIS spectra of the samples. Having said this, the impedance modulus experimental curves of Figure 51 suggest that the samples treated at 80°C during 18h provides the substrate with the most relevant improvement in terms of corrosion protection among the investigated LDH based treatments. Notice that this observation is valid regardless of the pH of the solution. For this reason, the impedance spectra corresponding to the LDH layer obtained at 80°C during 18h at the different pH values, have been fitted employing a $R_e(CPE_{LDH}R_{LDH})(CPE_{dl}R_{ct})$ electrical equivalent circuit (in accordance to literature reports [155][156]. In the above-mentioned circuit, R_e stands for the resistance of the electrolyte. The time constant in the middle high-frequency range has been attributed to the LDH layer. For this reason, a resistive element, R_{LDH}, which indicates the pore resistance of the LDH layer, and a constant phase element, CPE_{LDH}, which represents the dielectric properties of the layered double hydroxides coatings, have been employed in the e.e.c. The relaxation process at the lower frequencies has been attributed to the interface processes: a resistance, R_{ct}, which is related to the superimposition of the contribution of the charge-transfer process and the aluminum oxide and a constant phase element, and a constant phase element, CPE_{dl}, which represents the double layer capacitance contribution, overlapped to that of the dielectric properties of the aluminum oxide, have been employed. According to the mathematical representation of a CPE, (i.e. $Z_{CPE} = 1/(Q(\omega j)^{\alpha})$ the parameters Q and α have been employed to describe the dielectric response of the electrodes. Table 13 shows the values of the parameters employed in the e.e.c.. notice that due to the high scattering in the low-frequency range it has not been possible to fit the time constant corresponding to the interface processes for the sample 80˚C-18h-pH 6.

Table 13. Fitting parameters: RLDH, QLDH, αLDH, Rct, Qdl and αdl (n.d.: not determined).

Sample	R_{LDH} MΩ cm^2	Q_{LDH} Ω^{-1} cm^{-2} s$^{\alpha}$	α_{LDH}	R_{ct} MΩ cm^2	Q_{dl} Ω^{-1} cm^{-2} s$^{\alpha}$	α_{dl}
80˚C-18h pH 6.0	36	$1.1\cdot10^{-9}$	79	18	$3.8\cdot10^{-11}$	0.93
80˚C-18h pH 6.5	4200	$2.4\cdot10^{-11}$	94	n.d.	n.d.	n.d.
80˚C-18h pH 7.0	230	$2.7\cdot10^{-11}$	93	380	$2.0\cdot10^{-10}$	0.87

Notice that it is not possible to attribute to the pre-exponential factors Q_{LDH} and Q_{dl} any precise physical meaning since the parameters α_{LDH} and α_{dl} are quite far from unity (range from 0.79 to 0.94). The fitting parameters reported in Table 13 suggest that the selected coatings decrease the corrosion rate of the aluminium substrate thanks to the remarkable values of R_{LDH} and R_{ct}.

4.3.3. Conclusion

In order to investigate the relation of ZnAl-LDH structural growth and corresponding corrosion resistance behavior, a series of LDH thin films on AA6082 were synthesized by the in-situ growth method at various reaction conditions, for instance, the reaction temperature, reaction time, and pH. The findings from SEM and XRD analysis have shown that proper well-crystallized LDH's were obtained at the synthesis conditions of 40˚C and 60˚C at 24 hr crystallization time for each set of pH values, while at 80˚C for 18 and 24 hr aging time at 6.5 and 7.0 pH, the LDH structure fused and a compact structure formed on the substrate, which acts as a strong barrier against the aggressive media and caused an influential increase in the corrosion resistance. The extended reaction conditions were found to make an influential impact on the anticorrosion

properties of LDH. The thickness of the thin films lies in the range of 5 to 50 µm, which also has shown a significant influence on the corrosion resistance properties. The results from polarization curves have confirmed that ZnAl-LDH stands as effective corrosion protection thin film, and up to a five-order magnitude decrease in the corrosion current density of LDH was observed, compared to the substrate.

4.4. Synthesis of NiAl-LDHs: Structural and corrosion resistance properties

4.4.1. Experimental Section

To synthesize NiAl-LDH, the four different solutions of $Ni(NO_3)_2.6H_2O$ and ammonium nitrate salt were prepared, based on the variation of ammonium nitrate solution (Table 14), as the ammonium nitrate salt is found to be an effective reagent to obtain unique LDH morphological characteristics. The pH of the prepared solutions was adjusted at 10 with a drop-by-drop addition of 0.3 mol/L NaOH solution. 70mL of above-prepared solutions were purged with nitrogen gas for 30 minutes to remove adsorbed gases and were separately transferred into a 100mL Teflon-lined autoclave. The pretreated aluminum substrates, which act as a source of Al^{3+}, were placed in the above-prepared solutions and the system was treated in an oven at 130˚C for 24 h. After experiment completion, the coated specimens were washed with deionized water and were dried with nitrogen gas.

Table 14. The molar concentration of salts for the formation of NiAl LDH.

Specimens	$NiNO_3.6H_2O$	NH_4NO_3
NiAl-LDH_a	0.003M	----
NiAl-LDH_b	0.003M	0.003M
NiAl-LDH_c	0.003M	0.009M

NiAl-LDH$_d$	0.003M	0.018M

4.4.2. Results and Discussion

Figure 53 shows the XRD patterns of the NiAl-LDHs, exhibits distinct reflection peaks around at 2(Θ) 11.7˚, 23.0˚ and 34.9˚, correspond to (003), (006), (012) respectively, demonstrating the characteristics peaks of LDH formation [152]. The "003" reflections of all synthesized NiAl-LDHs were observed almost on the same 2(Θ) angle of ~11.7°, indicating a basal spacing around 0.88 nm, which corresponds to the NiAl-NO_3-LDH [150]. With the variation of ammonium nitrate salt concentration, the intensity and broadness of the reflection peaks vary and diffraction peaks (003) of NiAl-LDH begin to be a bit sharper, depicted the enhanced crystallinity, Table 15. The cell unit parameter is defined as c= $3d_{003}$= $6d_{006,}$ and it is found that from NiAl-LDH$_a$ to NiAl-LDH$_d$ a gradual reduction in the unit cell parameter is observed. As the reflection characteristic of NiAl-LDH gradually increases (Figure 53) with the variation of surface morphologies (Figure 54), it can be concluded that NiAl-LDH$_d$ has shown high intense, sharp narrow peaks compare to NiAl-LDH$_a$, thus describe well crystalline and ordered structure.

Figure 54 shows the SEM images of the synthesized NiAl-LDHs, wherein in all cases, LDHs microcrystals uniformly covered the entire aluminum substrate surface in the lamellar form. By comparing the surface morphologies of obtained LDHs from NiAl-LDH$_a$ to NiAl-LDH$_d$, it can be found that NiAl-LDH$_a$ is a less porous structure than that of NiAl-LDH$_{d,}$ where well ordered LDH platelet-structure is observed. This phenomenon is particularly evident in high-resolution SEM micrographs (Figure 54 b, d, f, h), where four distinct morphologies can be observed, from less porous amorphous structure to well-formed platelet flower-like structure. It can be concluded that due to well organize geometry structure, ion exchange property might be the basic attributes of NiAl-LDH$_d$ to increase the

corrosion resistance of Al AA6082, while the comparatively NiAl-LDH$_a$ less profound to exchange NO_3^- with the Cl^- and exposed to be more dominant barrier layer. The same trend is observed in the other developed NiAl-LDHs i.e. NiAl-LDH$_b$, NiAl-LDH$_c$. Table 16 shown the weight % composition of NiAl-LDHs, calculated by energy dispersive spectroscopy in-plane scanning mode. It is clear that NiAl-LDHs mainly consist of Ni, Al, O, and N. The Ni/Al ratio from amorphous porous structure to platelet structure is found to be increased from 3.44 to 4, which reflects the NiAl-LDH assembly. The effect of structural growth on the film thickness is reported in Figure 55(b), with a cross-sectional image of NiAl-LDH$_d$ in Figure 55(a) (reported as an example). It is clear that the film thickness remains in the range of 30 to 35 µm, and regular platelet NiAl-LDH$_d$ structure has shown slightly higher film thickness (34.6µm) than amorphous NiAl-LDH$_a$ structure (30.01µm).

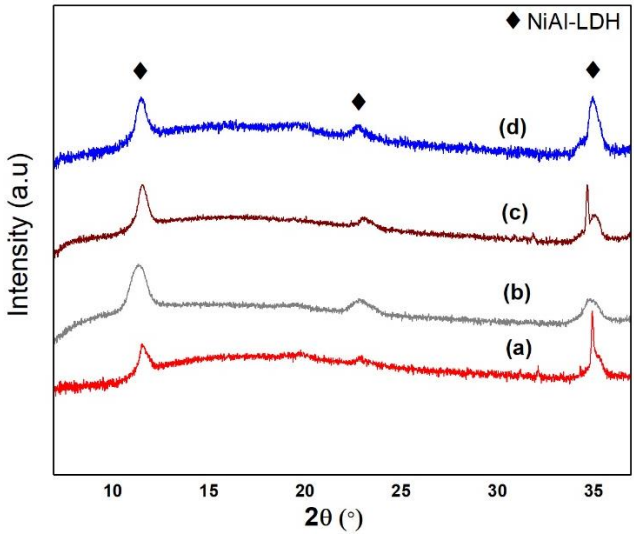

Figure 53. XRD patterns of the developed NiAl-LDH films, (a) NiAl-LDHa, (b) NiAl-LDHb, (c) NiAl-LDHc, (d) NiAl-LDHd

Table 15. Calculated cell parameters of the NiAl-LDHs.

Sample	**Interlayer distance "d_{003}" (nm)**	**Interlayerdistance "d_{006}" (nm)**	**Interlayer distance "d_{012}" (nm)**
NiAl-LDH_a	0.872	0.45	0.298
NiAl-LDH_b	0.878	0.44	0.297
NiAl-LDH_c	0.881	0.34	0.296
NiAl-LDH_d	0.886	0.44	0.296

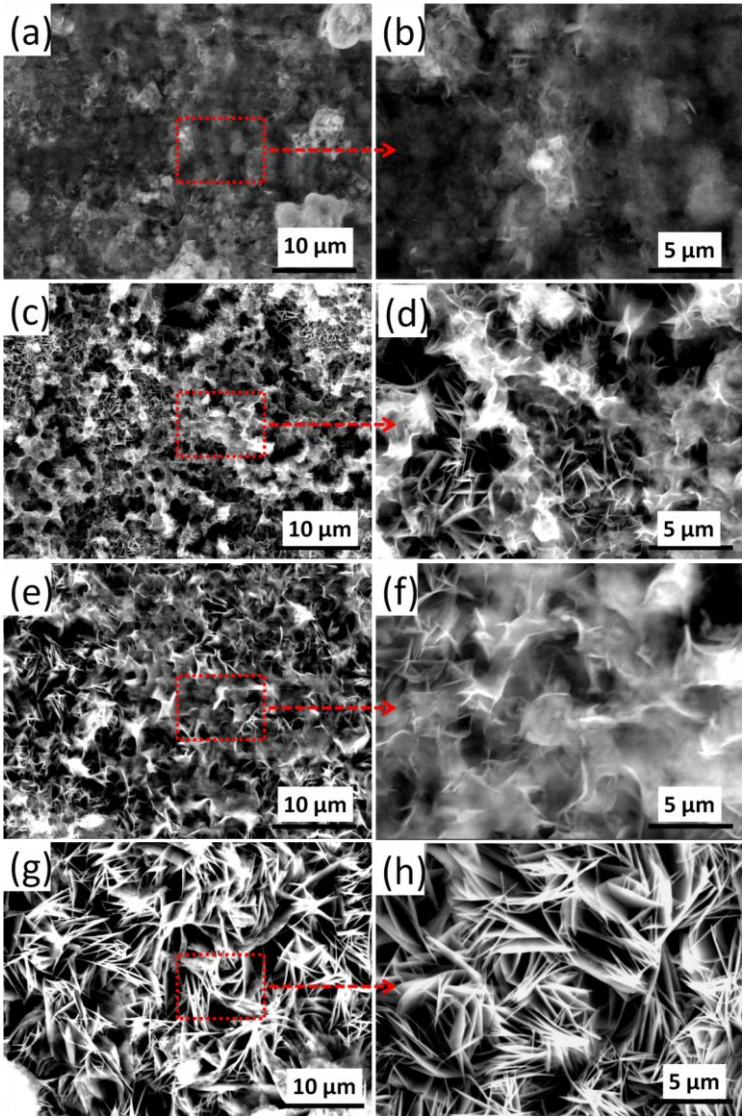

Figure 54. SEM images of the synthesized NiAl-LDH films: (a-b) NiAl-LDHa, (c-d) NiAl-LDHb, (e-f) NiAl-LDHc, and (g-h) NiAl-LDHd.

Table 16. EDS weight percentage of the synthesized NiAl-LDHs

The weight percentage of NiAl-LDHs					
Sample	Ni	Al	N	O	Ni/Al
NiAl-LDH$_a$	26.2	7.60	4.1	56.7	3.44
NiAl-LDH$_b$	26.4	7.51	4.8	57.2	3.51
NiAl-LDH$_c$	31.8	7.48	4.3	52.7	4.25
NiAl-LDH$_d$	34.7	7.42	4.6	53.0	4.67

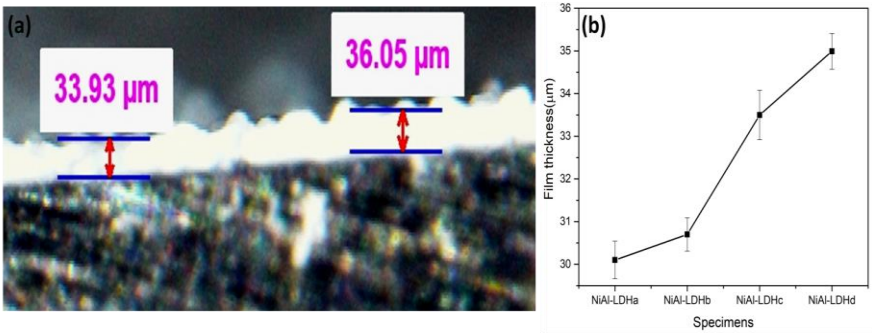

Figure 55. (a) For representation, the optical images of NiAl-LDHd, (b) thickness of the NiAl-LDH films measured from the cross-sectional optical microscope images.

The possible formation mechanism of NiAl-LDH is generally explained in equations (1-6), in simple terms, the aluminum surface dissolved in the basic reaction solution to form Al^{3+} (Eq. 1). The anodic regions (Equation 2, 3) results in the large concentrations of OH^- groups on the surface of the aluminum and favor the formation of $Al(OH)_3$ which act as precursors for the formation of LDH, while the final step is related to the precipitation of Ni, OH and $(NO)_3$ on the surface of $Al(OH)_3$ to form the NiAl-LDH hydroxide mixture. Finally, the divalent Ni^{2+} ions in $Ni(OH)_2$ were substituted by the trivalent Al^{3+} ions, which result in the coexistence of $Al(OH)_3$ and $Ni(OH)_2$ to form a precursor film of hydrotalcite-like LDH structure [157][158].

$$Al \rightarrow Al^{+} + e^{-} \quad (1)$$

$$Al^{3+} + H_2O \rightarrow Al^{3+} + OH^{-} + \frac{1}{2} H_2 \quad (2)$$

$$2H_2O + 2e^{-} \rightarrow H_2 + 2OH^{-} \quad (3)$$

$$Al + 4OH^{-} \rightarrow Al\,(OH)_4{}^{-} + 3e^{-} \quad (4)$$

$$Ni^{2+} + OH^{-} \rightarrow Ni(OH)^{+} \quad (5)$$

$$Al(OH)_4^{-} + Ni(OH)^{+} + yNO_3^{-} + zH_2O \rightarrow Ni_xAl_{1-x}(NO_3)_y(OH)_2.zH_2O \quad (6)$$

The polarization curves of the developed NiAl-LDH on AA6082 are shown in Figure 56. The polarization curves of synthesized NiAl-LDHs coating have shown a decrease in both anodic and cathodic current density compared to the bare AA6082. All the synthesized NiAl-LDHs films on AA6082 have shown lower corrosion current density along with a shift of the corrosion potential to higher values as compared to bare AA6082, however, NiAl-LDH_d has shown the significantly reduced anodic and cathodic current density compared to the substrate and also from other developed NiAl-LDHs. It is also worthy to note that NiAl-LDH_d has shown a relatively higher film thickness of around 35 µm, which may provide a comparatively better barrier film against the aggressive media, and for NiAl-LDH_d up to 3 order reduction in corrosion current density was observed compared to the substrate. Furthermore, the open circuit potential (OCP) is switched toward nobler values with structural variation from NiAl-LDH_a to NiAl-LDH_d, whilst a high corrosion potential of -0.18 V vs Ag/AgCl was observed for NiAl-LDH_d, probably due to the formation of well-ordered platelet structure.

The EIS measurements of as-prepared NiAl-LDHs after one day immersion in 0.1M NaCl solution are shown in Figure 57. The higher value of impedance in the low-frequency domain (impedance modulus at 0.01 Hz, $|Z|_{0.01}$) roughly indicates

higher corrosion resistance properties [27]. From Figure 57(a), NiAl-LDH_d has shown the impedance value around 6.3 Ω.cm^2 at $|Z|_{0.01}$, which is near 2 orders magnitude higher than bare AA6082 alloy. The higher shift of impedance for NiAl-LDH_c and NiAl-LDH_d defined the presence of the strong dielectric protective film which is well consistent with the anti-corrosion behavior obtained from the potentiodynamic curves and also it well explained the ion-exchange effect on the increase in corrosion resistance. The LDHs are related to providing corrosion protection due to: (1) barrier effect, as they are dielectric materials that protect the metal surface by avoiding the interaction with the metal substrate; (2) by ion-exchange capability and entrapping Cl^- ions by releasing nitrates.

Considering the EIS response of the samples, two relaxation processes can be observed in the phase angle spectrum (Figure 57b): The time constant in the high-frequency range (10^3-10^4 Hz) can be attributed to the properties of the LDH layer itself, while the time constants in the middle frequency range 10^0-10^1 Hz are the overlapping of the contributions of the aluminum oxide and the faradic process of substrate and solution interphase. In the case of aluminum AA6082 substrate, two-time constants can also be observed, one related to the formation of the oxide in the middle-frequency range and the other due to corrosion reactions in the low-frequency range. The EIS results (Table 17) were further fitted using "ZSimpWin" software to get more detail of corrosion resistance properties to understand in detail the effect of surface morphologies on the corrosion resistance parameters. As the synthesized coating has shown two relaxation processes from middle-high to low-middle frequency range due to coating systems, while the variation in LDH film thickness can also be responsible for the change in behavior of electrochemical response and so as defects/porosity. The electrical equivalent circuit $R_s(CPE_{LDH}(R_{LDH}(CPE_{dl}R_{ct})))$ is used to analyze the EIS response of NiAl-LDHs, where R_s is the resistance of the electrolyte, while R_{LDH} describes the NiAl-

LDH film resistance with a constant phase element which accounts for the Dielectric properties of the LDH film (CPE_{LDH}) and R_{ct} represents the charge transfer resistance in parallel with constant phase element (CPE_{dl}). According to the mathematical representation of a CPE, (i.e. $Z_{CPE} = 1/(Q(\omega j)^{\alpha})$ the parameters Q and α have been employed to describe the response of the electrodes. The total resistance (R_t) can be used to analyze the protective ability of deposited NiAl-LDHs. Since the R_t values give relative information related to the corrosion rate i.e. higher is the total resistance, lower will be the corrosion rate. It can be seen that total resistance ($R_t = R_{ct} + R_{LDH}$) gradually increases with the change of surface morphologies (porous domains to platelet structure), moreover, a well-formed platelet structure showed a higher value of total resistance. The relatively high values of R_{LDH} values indicate that the LDH coatings are more compact while also protective as suggested by the relatively high values of R_{ct}. This is well consistent with the polarization curves and bode plots analysis, but here it is also important to mention that CPE_{LDH} and CPE_{dl} have a value of α far from 1, and thus the film did not act as a pure capacitance and it is difficult to interpret the real physical meanings of EIS fitting parameters. From electrochemical and physical characterization, we can conclude that the better is the ion-exchange capability to hold firmly the chlorides inside the interlayers, the better is the corrosion resistance properties. The equivalent circuit used to model the impedance results is shown in Figure 58, along with an example of fitting the experimental results of NiAl-LDH_d. The well-organized geometry of NiAl-LDH is found to facilitate better ion exchange with the Cl^- and strongly hold them between the LDH interlayer's thus acts as a strong protective film on aluminum alloy against corrosion. Due to the well-formed Platelet LDH structure, nitrate ions properly intercalate between the interlayers and cause an increase in the chloride uptake and holding capacity, thus leading to the stabilization of the layered structure

which prevents chloride ions migration to the underlying metal. That made LDH structures a compact system for entrapping the chloride ions and prevents the aggressive media from interacting with the aluminum surface.

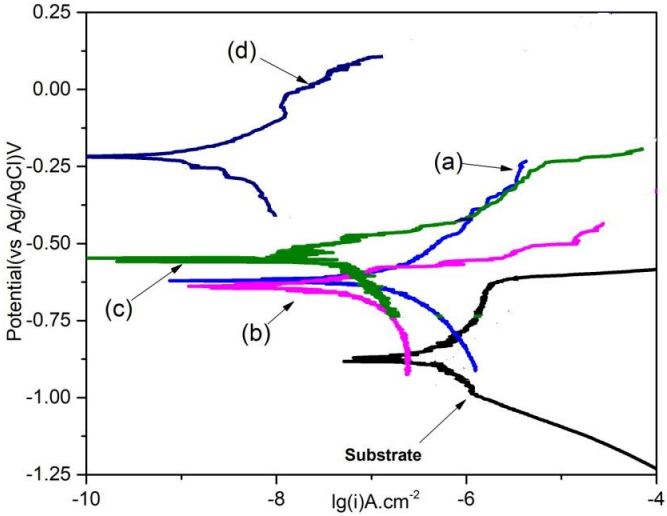

Figure 56. Polarization curves in 0.1 M NaCl aqueous solution: (a) NiAl-LDHa, (b) NiAl-LDHb, (c) NiAl-LDHc, and (d) NiAl-LDHd.

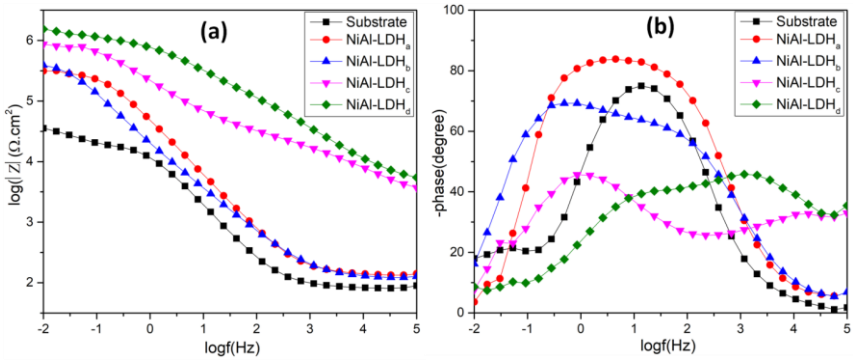

Figure 57. Impedance and phase plots of NiAl-LDH coated specimens at various synthetic conditions in 0.1 M NaCl solution after 1-day immersion.

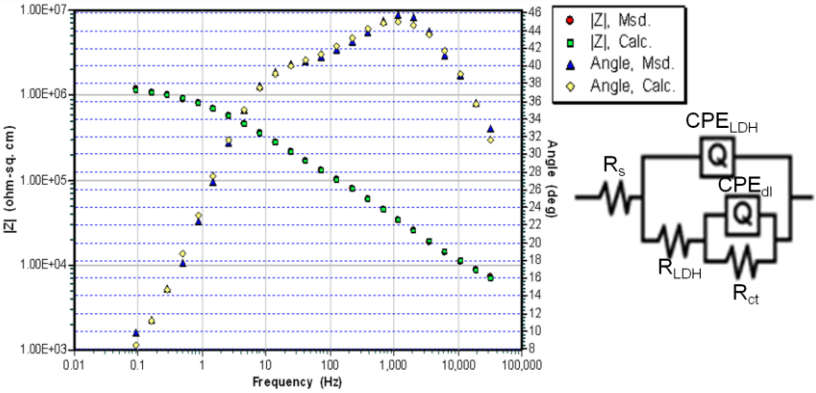

Figure 58. An example of EIS fitting of NiAl-LDHd experimental data, and the equivalent circuit used to model the experimental results.

Table 17. Evolution with a time of the fitting parameters RLDH, QLDH, αLDH, Rct, Qdl, and αdl

Sample	Immersion time	R_{LDH} kΩ cm^2	Q_{LDH} Ω^{-1} cm^{-2} s$^{\alpha_{LDH}}$		R_{ct} kΩ cm^2	Q_{dl} Ω^{-1} cm^{-2} s$^{\alpha}$	α_{dl}
NiAl-LDH$_a$	1 day	11.77	$1.69\cdot10^{-6}$	0.91	308.0	$1.41\cdot10^{-6}$	0.90
NiAl-LDH$_b$	1 day	21.87	$7.62\cdot10^{-6}$	0.83	467	$2.04\cdot10^{-6}$	0.90
NiAl-LDH$_c$	1 day	333.61	$4.92\cdot10^{-7}$	0.51	1391.0	$8.60\cdot10^{-7}$	0.70
NiAl-LDH$_d$	1 day	1208.8	$5.78\cdot10^{-7}$	0.67	1819.9	$4.19\cdot10^{-6}$	0.79

To understand the Chloride entrapment capabilities of NiAl-LDHs, a direct Mohar chloride measurement method is used to measure the chlorine adsorption behavior of LDHs before and after the contact with 0.1M chlorine solution for 1 day. Here, silver nitrate is used as a reagent and potassium chromate as an indicator, the silver nitrate solution was added slowly in the tested chloride solution, and result in the formation of a precipitate of silver chloride, while the endpoint of the titration occurs when all the chloride ions are precipitated and the addition of silver nitrate reacts with the chromate ions (indicator) to form a red-brown precipitate of silver chromate (Figure 59). The calculated concentration of chloride after contact with NiAl-LDH and for comparison the chlorine concentration in 0.1M NaCl solution is listed in Table 18. It can be seen that the chloride uptake value for NiAl-LDH$_d$ is much greater than the other prepared NiAl-LDHs. The mechanisms behind the

chloride removal from the solution are likely to rely on the ion exchange capability of the LDHs. The reduced amount of Cl^- measured upon exposure to the NiAl-LDH is in agreement with an anion's uptake in the film. Among the investigated samples, NiAl-LDH_d has been found to combine the best corrosion protection properties (as suggested by polarization curves and EIS) as well as the highest chloride uptake capability. A hypothesis to explain these findings is to assume that chloride ions are entrapped inside the LDH structure (thanks to anions exchange mechanism), thus reducing the aggressiveness of the salt solution towards the metal substrate. Together with higher thickness, this would help to increase the corrosion protection properties of the LDH coating. Figure 60 shows the optical images of NiAl-LDHs after corrosion analysis and can be seen that the LDH film remains visually intact and uniform, which is in agreement with the observed system stability of the LDHs.

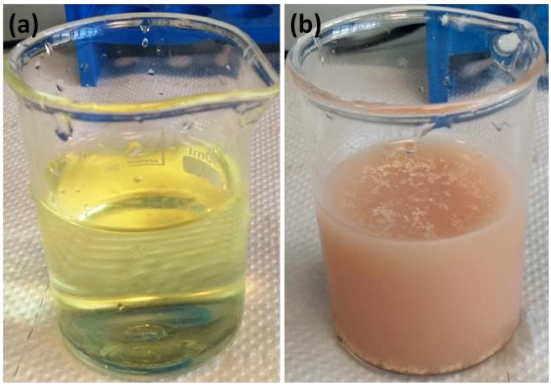

Figure 59. (a) The chromate indicator gives a faint lemon-yellow color of fresh 0.1M NaCl solution, (b). At the endpoint, all the Cl− ions have precipitated and with silver nitrate, precipitates with the chromate indicator giving a slight red-brown coloration.

Table 18. The concentration of chloride in 0.1M NaCl solution before and after contact with NiAl-LDHs after one-day immersion.

	0.1M NaCl (Fresh) $mg.L^{-1}$	NiAl-LDH_a $mg.L^{-1}$	NiAl-LDH_b $mg.L^{-1}$	NiAl-LDH_c $mg.L^{-1}$	NiAl-LDH_d $mg.L^{-1}$
Chloride Conc.	3462	3426	3388	3340	3337

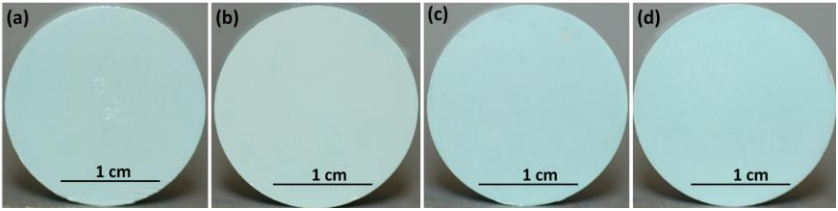

Figure 60. Specimen surfaces after corrosion test: a) NiAl-LDHa, b) NiAl-LDHb, c) NiAl-LDHc, d) NiAl-LDHd

4.4.4. Conclusion

In this study, an insitu growth approach was used to prepare anticorrosive NiAl-LDHs of various morphologies on aluminum AA6082 substrate and the effect of different LDH surface morphologies on their ion exchange capability with Cl^- and corresponding corrosion resistance properties are reported. It is revealed that platelet NiAl-LDH_d structure has shown better ion-uptake behavior compared to other analyzed morphologies. About 122 mg/L chloride uptake was observed from 0.1M NaCl in the electrolyte. Besides, it was found to remarkably reduce both the anodic and cathodic current compared to the bare substrate. The findings from EIS analysis furtherly confirmed the ability of NiAl-LDH_d to protect the underlying metal against corrosion.

Together with a physical barrier effect, the capability of the developed LDH structure to entrapped chloride ions, thus reducing the aggressiveness of the

salt solution towards the metal substrate, are believed to be responsible for the observed increase in the corrosion protection properties of the LDH coating. As a general conclusion, the selection of an appropriate choice of metal cations ratio and microstructure optimization seems to play a key role in the development of LDH coatings with enhanced corrosion protection properties.

4.5. Synthesis of CaAl-LDH: Structural and corrosion resistance properties.

4.5.1. Synthesis of CaAl-NO_3-layered double hydroxide

In our approach, the CaAl-LDH thin films were grown on AA6082 alloy by a facile one-step method at a temperature of 140˚C for different crystallization times, i.e. 12 h, 18h, 24h, and 72 h. 70 mL of 0.02M $CaNO_3.4H_2O$ solution was prepared and purged with nitrogen gas to remove absorbed gases and transferred into a 100mL Teflon-lined autoclave. The pH of the solution was adjusted to 10 with the dropwise addition of NaOH. The pretreated aluminum substrates (3.14 cm^2) which act as a source of Al^{3+} were placed in the above solution and were treated in an oven at 140˚C temperature for 12, 18, 24, and 72h crystallization time for in-situ growth CaAl-LDH on the aluminum alloy. After experiment completion, the coated specimens were washed with deionized water and were dried with nitrogen gas.

4.5.2. Results and Discussion

Figure 61(a-d) shows the SEM images of CaAl-LDH microstructure. It can be seen that with the increase of crystallization time from 12 to 24 h, the CaAl-LDH structure becomes more regular and the crystallite size grows bigger until 140˚C-24h, while for 140˚C-72h the cones were found to have transformed into compact

nest-like microstructures and the intermixed uniform curvy structure can be visualized. The difference in morphology of CaAl-LDH can be related to the extended crystallization time which can be attributed to the variation in Ca/Al weight ratio (examined by EDS analysis) and also due to the variation in absorption of NO_3^{1-} anions inside LDH interlayers (confirmed by XRD analysis). The surface of the LDH matrix was covered with horizontally- and vertically aligned nano-flake arrays, mainly composed of Ca, Al, N, and O. The Ca/Al weight % ratio was found to vary from 1:7 at (140˚C-12h) to 1:5 at (140˚C-72h) and around 1:4 for 72 h specimens. The high Ca/Al ratio and higher NO_3^{1-} ion intercalation caused both an increased growth rate of CaAl-LDH and also an increase of nucleation density of NO_3^{1-} anions, which remarkably influenced the structural geometry of CaAl-LDH.

The layered structure of CaAl-LDH, synthesized at 140 ˚C-24h, could be observed under TEM, as shown in Figure 62. During sample dispersion, the ultrasonication power might destroy the cone-like structure of most crystals, yet some triangular features remained as shown by the arrow in Figure 62a. The corresponding TEM diffraction pattern (Figure 62b) gave rings with bright spots, suggesting that the sample is polycrystalline and has some preferred orientations. The two rings with the smallest radii indicate an interplanar spacing of 3.1 and 2.8 Å, respectively, which accord with the two strongest peaks in the XRD pattern (Figure 63). The layered structures of CaAl-LDH can be seen at higher magnification in Figure 62c.

The crystal structure and phase identification of CaAl-LDH were confirmed with XRD analysis as shown in Figure 63. The XRD pattern of the CaAl-LDH is similar to those previously reported by Szabados, Márton, et al for co-precipitated CaAl-LDHs [159]. The intercalation of NO_3^{1-} anions inside LDH interlayers is confirmed by the (001) reflection peaks at the low 2θ value of 12.4º [159], which

sharpened concerning extended crystallization time indicating the relatively high crystallinity. The peak broadening is generally attributed to crystallite size effects and non-uniform broadening of anisotropic crystallites. The interlayer region mainly contains the hydroxyl groups and nitrate ions to balance the positive charge layers, while the peak at (001) planes of CaAl-LDH was used to measure the basal spacing's of developed films by using Bragg's equation. The interlayer distance of CaAl-LDH at "001" lies around 0.8nm, which on prolonged crystallization time contract slightly, due to different NO_3^{1-} anions and hydroxyl group orientation inside the interlayers. The obtained value of basal spacing corresponds to the sum of nitrate anions and hydroxyl groups, which is in agreement with the literature data [160]. The cell parameter "c" was found to elevate possibly due to the different size, strength, and bonding orientation of the hydroxyl group and nitrate anions inside the brucite-like structure, with the effect of the increasing reaction treatment time. Besides the CaAl-LDH characteristics peaks, few other peaks were also found, which correspond to the formation of $Ca(OH)_2$ and $Al(OH)_3$. It was previously reported that due to exothermic dissolution, $Ca(OH)_2$ and $Al(OH)_3$ are also formed, which did not convert into an LDH structure. However, their concentration was found to decrease with extended crystallization time, and some $Ca(OH)_2$ is also transformed into TCA (Tricalcium-aluminate) [159]. The XRD patterns showed that the overall LDH characteristic structure remained well-preserved during thermal treatment from the 12 to 72 h crystallization time period; however, this extended time period caused the contraction of basal spacing, which is well consistent with the results of the literature study [73,161,162]. The interlayer thickness at d_{001}, full width half maximum, and corresponding crystallite sizes (calculate by Scherrer formula) are listed in Table 19.

Table 19. Cell parameters of the CaAl-LDH structure were synthesized at 140 ˚C for different reaction times.

	12 h	18 h	24 h	72 h
d_{001} (nm)	0.832	0.821	0.818	0.820
FWHM	0.413	0.317	0.231	0.238
Crystallite size (nm)	22.3	29.0	39.3	38.4

The FTIR spectra of all the obtained CaAl-LDHs are shown in Figure 64. The main bands at wavenumber 1365-1389 cm^{-1} and 3450 cm^{-1} are assigned to the presence of the NO_3^{1-} group, and O–H vibration mode of the hydroxyl group and water molecules respectively [139]. A small bending around 1627cm^{-1} corresponds to the bending vibration of water molecules while in the low-frequency range and the band spectra at 532, 785 cm^{-1} corresponds to M-O vibration bonds [163][142]. Due to carbon dioxide contamination from the air during the synthesis of LDH, the broadness of the nitrate band can be attributed to the overlapping of nitrate and carbonate ions from 1360 to 1370 cm^{-1}, especially in the case of the 140˚C-72h specimen; this peak is bit-shifted, probably due to the presence of carbonate groups.

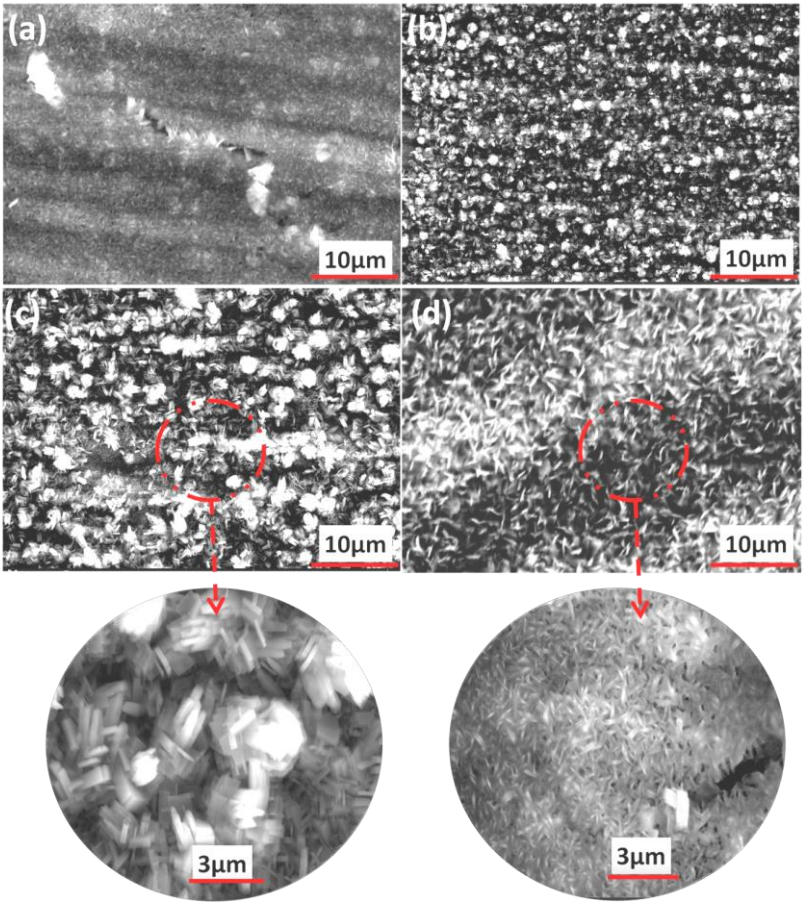

Figure 61. SEM images of the CaAl-LDH films synthesized at various conditions: (a) 140 ˚C-12 h, (b)140 ˚C-18 h, (c) 140 ˚C-24 h, and (d)140 ˚C-72 h.

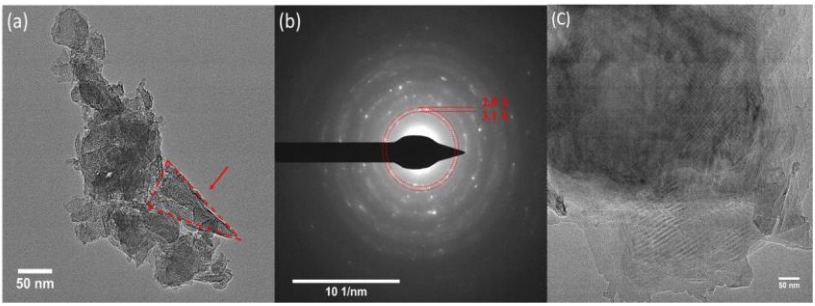

Figure 62. (a) TEM image of the CaAl-LDH film synthesized at 140 ˚C-24h, (b) corresponding diffraction pattern, (c) interplanar spacing lines of a layered structure in the high-resolution image.

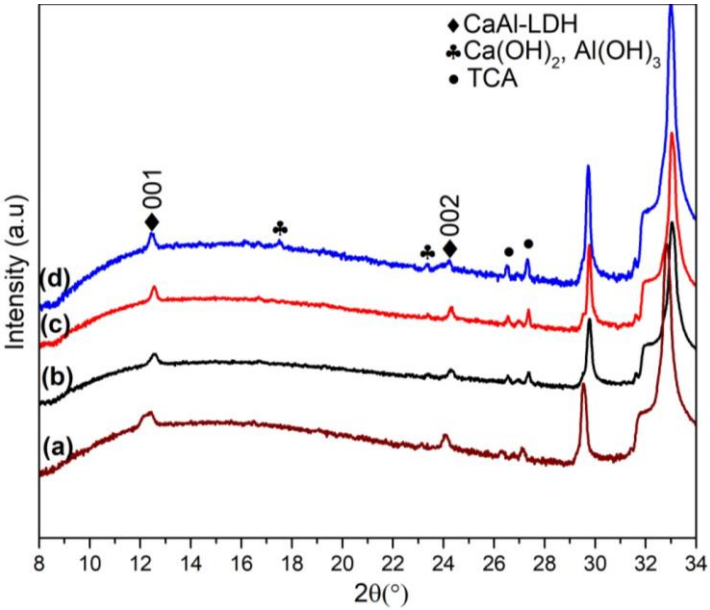

Figure 63. XRD patterns of CaAl-LDH film samples synthesized on AA6082: (a) 140 ˚C-12 h, (b) 140 ˚C-18 h, (c) 140 ˚C-24 h, and (d) 140 ˚C-72 h.

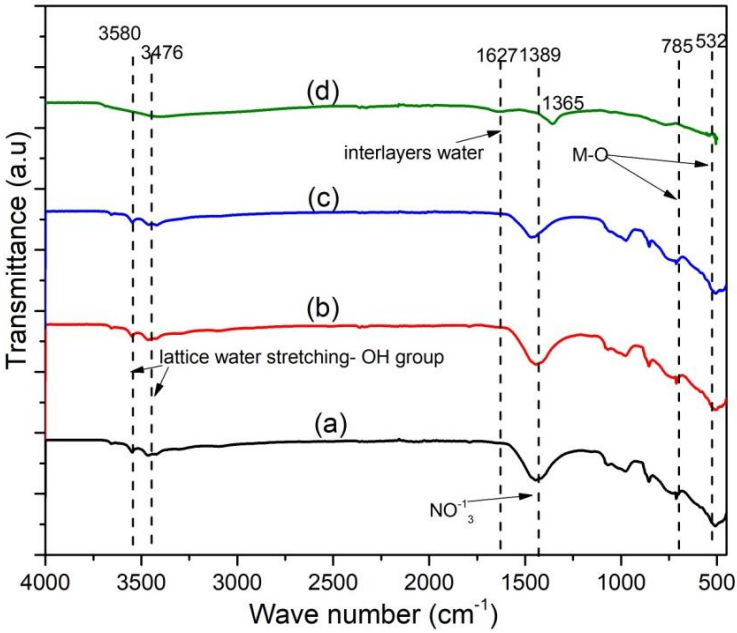

Figure 64. FTIR spectra of CaAl-LDH synthesized at 140 ˚C for different crystallization time: (a) 12 h, (b) 18 h, (c) 24 h, and (d) 72 h.

To understand the corrosion resistance properties of CaAl-LDH, the Tafel polarization curves were employed (Figure 66), which can be an effective way to understand the corrosion current density and corrosion current potential. Notice that the bare AA6082 showed an almost passive current at about 10^{-6} A cm^{-2} for anodic overpotential in the range of 250-300 mV. CaAl-LDH coated substrates did not show any more of a clear passive transient. However, an increase in corrosion potential is observed for all the investigated samples, regardless of the crystallization conditions. The LDH coatings derived from deposition times of 12 and 18 h seem not to provide any significant improvement in terms of cathodic or anodic current density reduction. On the other hand, the CaAl-LDH coated

samples showed a noticeable reduction of both anodic and cathodic corrosion current compared to the bare substrate. In particular, the coating derived from deposition time of 24 h demonstrated a decrease in anodic current density of about 3-4 orders of magnitude. Notice that the reduction in current density is not proportional to the increase in film thickness, as one can observe from Figure 67(b). This finding will be discussed throughout the paper. The film thickness (barrier effect), up to an extent, can also be a responsible factor in reduced anodic and cathodic current densities and therefore is expected to impart an influential impact on the corrosion resistance properties. Figure 65(a) depicts the cross-sectional optical analysis of CaAl-LDH of the 140˚C-24h specimen. The significant reduction of I_{corr} and the more positive corrosion potential of CaAl-LDH specimens is attributed to the reduction of anodic and cathodic sites on the CaAl-LDH surface. As reported in our earlier works, the extended crystallization time can result in the more compact layered-double architecture and such behavior can also reorient the LDH as a strong barrier against the corrosive solutions [113,164], which is well consistent with the current study, where extended crystallization times facilitate to improve the overall CaAl-LDH corrosion resistance properties up to an extent. The increase in corrosion resistance properties of the aluminum can be due to the following factors: (1) the anion exchangeability of the CaAl-LDH film with the Cl^{1-} ions, (2) the strong barrier properties of CaAl-LDH attributed to strong LDH adhesion with the substrate and its compact nest-like structure. The calculated corrosion current density and corrosion potential of developed specimens are listed in Table 20. Figure 65(b) shows the impact of extended crystallization time on the film thickness, which increased from 9.5 to almost 12μm with the increase of crystallization time from 12 h to 72 h.

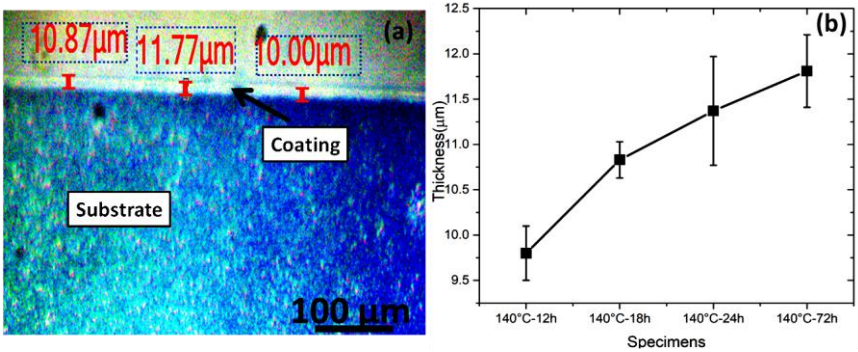

Figure 65. (a) Cross-sectional optical image of the CaAl LDH film coated on AA6082 alloy at 140 ˚C-24 h and (b) measured thickness from a cross-sectional analysis of the as-prepared coatings.

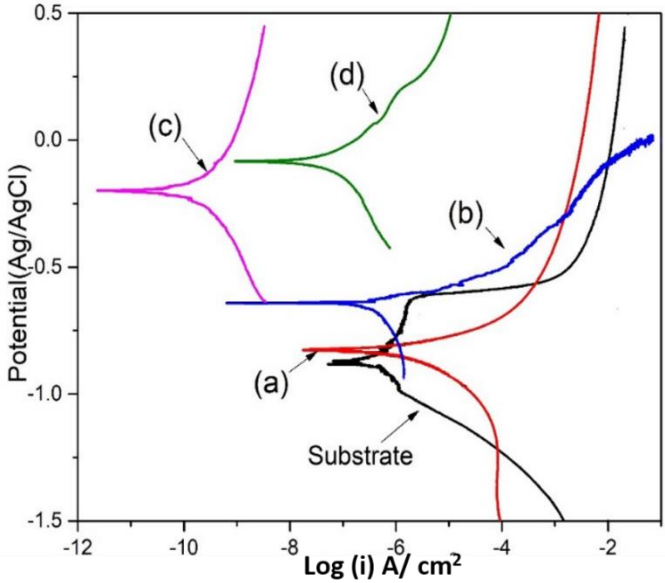

Figure 66. Polarization curves of the bare AA6082 and the CaAl-LDH coated AA6082 specimens in 0.1 M NaCl aqueous solution: (a) 140 ˚C-12 h, (b) 140 ˚C-18 h, (c) 140 ˚C-24 h, and (d) 140 ˚C-72 h.

Table 20. Electrochemical parameters are estimated from the polarization data in Figure 66.

	Corrosion current density ($\mu A/cm^2$)	Potential (Ag/AgCl) V
AA6082	0.7581	-0.879
140 ˚C-12 h	0.6752	-0.831
140 ˚C-18 h	0.3312	-0.649
140 ˚C-24 h	0.0007	-0.473
140 ˚C-72 h	0.0623	-0.087

To further evaluate the electrochemical behavior of CaAl-LDH thins films, EIS characterization was carried out in 0.1M NaCl electrolyte as shown in Figure 67(a-

b). The reason for using a relatively mild electrolyte (0.1M NaCl) relies on the intention to better highlight the small differences among the studied samples, considering the small variation of crystallization time and growth behavior on the corrosion-resistance properties. EIS results of bare AA6082 substrate showed two zones, one capacitive zone in the middle frequency range (10^3-10^0 Hz) and one resistance zone in the low-frequency region (below 10^0 Hz). The low-frequency impedance ($|Z|_{00.1}$) for the bare sample is about 4.5×10^4 Ω cm^2. The impedance modulus at a low frequency, such as $|Z|_{00.1}$ can be used to compare the corrosion-resistant capability of coatings [165]. It can be observed from the Bode plots that the LDH-coated samples exhibit higher impedance in the low-frequency domain (0.1-0.01 Hz) compared with the bare aluminum alloy sample. It is also worthy to note that the impedance modulus of CaAl-LDH at the optimum synthetic conditions (140˚C-24h) has more than two orders of magnitude higher than that of the Al substrate at 0.01 Hz. The strong shift of the impedance in the middle-high frequency range is attributed to the presence of the coating. The presence/absence of the shift in impedance in this range provides information related to the real presence of a dielectric coating on the surface of the metal. The samples developed at 140˚C-24 and 72h have demonstrated an almost capacitive behavior in the middle-high frequency range (Figure 67(a)), thus suggesting the presence of a dielectric LDH coating, and their deviation reflects the LDH surface roughness and degree of homogeneity [166,167]. The other developed coatings at the lower crystallization times have shown much lower values of electrochemical impedance in the investigated frequency range (Figure 67(a)). The specimens at 140˚C-12 h and 18h have shown two partially overlapped peaks in the phase angle spectrum with a slight increase in impedance which likely indicates a nonuniform and defective surface and, therefore, only slight protection. According to the relevant increase in thickness obtained by increasing the treatment time, the

electrochemical response of the investigated samples remarkably differs from one sample to another. The presence of inhomogeneities and defects, which occurred during the synthesis of the coatings, furtherly exacerbates the differences among the EIS spectra of the samples. Considering Figure 67(b), the EIS response suggests that only the coatings at high crystallization time have shown the capacitive response in the middle-high frequency range, with high impedance values which describe well-protective CaAl-LDH thin films. The samples at 140˚C-24 h have shown a relevant increase of the low-frequency impedance (from 10^4 to 10^7 Ωcm^2) compared to the bare aluminum sample. These coatings seem to be protective, thanks to the relevant increase in impedance, but they are likely to be partially porous, permeable and/or defective as they do not show a clear capacitive behavior.

Figure 68(a) shows the XRD spectra of CaAl-LDH thin film developed at 140˚C-24h before and after immersion in 0.1M NaCl solution for 4 and 7 days. It can be seen that the (001) characteristic peak of CaAl-LDH is shifted towards a higher degree after immersion in chloride solution, which indicates the strong intercalation of chloride anions in the LDH galleries, indicative of anion-exchange of NO_3^{1-} with the Cl^{1-}. It is well-consistent with several other reports that describe the chloride exchange behavior with the nitrate ions, due to the higher binding energy of chloride ions compared to the nitrate ions [79]. When compared to a 7-day immersion, the shift towards a higher degree is more evident in a 4-day-immersion (due to a large amount of chloride uptake from the solution after 4 days) and the concentration of chlorides on the solution decreases (which further slows down the diffusion rate); after 7 days, a negligible shift was observed in the diffraction peak of CaAl-LDH. Figure 68(b) depicts the stability of the impedance modulus and its evolution with the immersion time. The specimen (140˚C-24h) were immersed in 0.1M NaCl solution for 4 and 7 days and after that impedance

plots were collected to understand the evolution of impedance on contact with the corrosive solution. The value of decrease is comparatively higher in the low-frequency range ($|Z|_{00.1}$), and after 7 days of immersion, an almost one order magnitude decrease in the low-frequency range was observed. This evolution of decrease in impedance spectra can be explained due to following with time, the electrolyte filled the porous structure of LDH, and as time elapsed, the chloride solution moved through the pores and defects which decrease the film resistance. Figure 69 shows the cross-sectional image of CaAl-LDH (140˚C-24h) after a 7-day immersion in 0.1M NaCl solution. As it can be seen, on contact with the NaCl solution, the CaAl-LDH film remained intact with a strong contact to the substrate, and a bit compactness of the structure can also be observed with almost the same original film thickness. Insets are the surface camera images of the thin film before and after immersion in 0.1M NaCl solution.

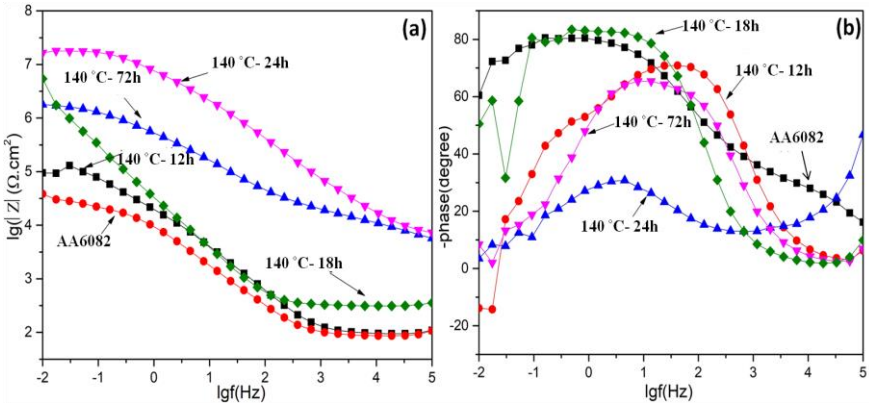

Figure 67(a-b). Impedance and phase plots of CaAl-LDH coated specimens at various synthetic conditions in 0.1 M NaCl solution.

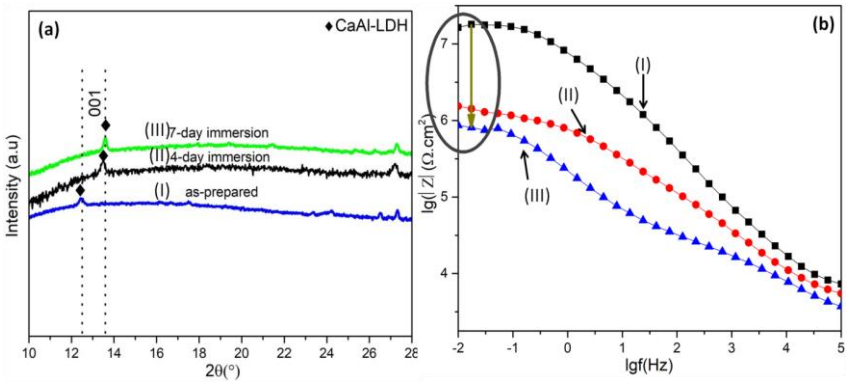

Figure 68. (a) XRD patterns and (b) the corresponding impedance plots of CaAl-LDH synthesized at 140 ˚C-24 h: (I) as-prepared, (II) after 4 days, (III) after 7 days immersion in 0.1 M NaCl solution.

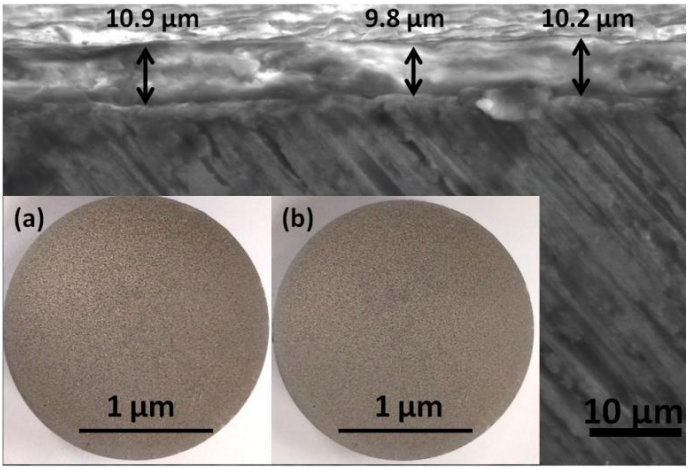

Figure 69. Cross-sectional image of CaAl-LDH after 7 days of immersion in 0.1 M NaCl solution. The insets are digital pictures of the specimen surface: (a) before immersion, (b) after 7 days immersion.

4.5.3. Conclusion

In this contribution, we successfully developed anticorrosive CaAl-LDH thin films on AA6082 substrates by a single step in-situ hydrothermal method. In particular, CaAl-NO_3 LDH uniform vertically aligned structures were formed at 140˚C-24h, which demonstrated excellent corrosion resistance properties with reduction of corrosion current density up to 4 orders of magnitude and impedance of near 3 orders larger at 0.01 Hz compared to bare AA6082 substrate. The orientation of LDH nano-sheets and morphology (as confirmed by XRD, SEM) are responsible for anion exchange and the barrier properties at different crystallization times which controlled the corrosion resistance of the CaAl-LDH. The extended reaction times caused more uniform and compact morphologies with small variations in film thickness, which significantly impacted the corrosion current density of CaAl-LDH. It is believed that NO_3^{1-} anions inside the interlayers can further be replaced with various anions (thanks to the anion-exchange behavior of CaAl-LDH) to further improve the anticorrosion behavior of CaAl-LDH thin films.

4.6. Synthesis of Cone Shaped CaAl-LDH through Facile Urea Hydrolysis Method

4.6.1. Synthesis of Nano Cones CaAl-LDH

The cone-shaped CaAl-LDH thin film was grown through the urea hydrolysis approach. The pretreated aluminum substrate acts as the source of Al^{+3} which provides a building block for the synthesis of LDH on it. 0.03M $CaNO_3.4H_2O$ and 0.18 M urea (1:1) were prepared and were transferred into 100mL Teflon-Lined autoclave, while the pretreated aluminum substrates (3.14cm^2) were placed in the prepared solution and were treated in an oven at 120˚C for 18 hr. The initial pH

of the prepared solution was 5.36, which on completion of the experiment approached 9.7.

4.6.2. Results and Discussion

Figure 70(a-c) depicted the CaAl-LDH SEM images. It can be seen that LDH microcrystals uniformly covered the entire aluminum substrate surface, and a well-developed nano-cone-shaped like structure is formed on the Al 6082 substrate. This phenomenon is particularly evident in the high-resolution SEM micrographs (Figure 70 (b-c)), where nano-cone-shaped morphology can be observed. Figure 70(d) showed a cross-sectional analysis of LDH film, depicting the average thickness of 10.30 µm. The particle size distribution lies in the range of 1.6 to 3.2 µm. Further, the TEM images were recorded to evaluate the morphological characteristics of LDH, as shown by Figure 70(e, f). The TEM analysis was performed for the CaAl-LDH scraped from the substrate, and during sample preparation, the scraped LDH was dispersed in ethanol. The ultrasonication may destroy the cone-like structure of most crystals; however characteristic features of LDH can be seen and the layered structure of LDH is dominant in Figure 70(f). The hydrolysis of urea increases at high temperature i.e 120˚C and caused an increase in pH of the synthetic solution which is found to favor the formation of LDH on the aluminum substrate. Usually, carbonate ions have also been reported inside the LDH layers when synthesized by the Urea hydrolysis method, however, here FTIR analysis did not show the characteristics peaks of carbonate ions. The previous studies have shown that high-temperature synthesis may favor the intercalation of nitrate ions (present in the solution) in the LDH interlayer's [168]. The XRD pattern of CaAl-LDH is shown in Figure 71 (a), where distinct reflection peaks at 2(Ɵ) 12.29˚, 24.1˚, corresponds to (001) and (002) respectively can be seen which confirmed the CaAl-LDH structure [169].

In addition to the CaAl-LDH peaks, there can also be seen TCA (tri-calcium aluminates), because it is arduous to synthesize thermodynamically pure CaAl-LDH phase due to the favor of different secondary phases during the CaAl-LDH synthesis. It is well revealed that Ca^{2+} in CaAl-LDH is coordinated tetrahedrally with the Al, due to the relatively large size of Ca^{2+} [170].

The "001" reflection peak at 2(Θ) of 12.29° indicated a basal spacing of 0.72 nm. The resultant basal spacing is specific for the family of LDHs, where positively charged layers interlayer anions hold the OH^- [171]. Here, the basal spacing did not correlate with the traditional NO_3^{1-} spacing, possibly due to the following reasons; (1) the anions intercalation varies in terms of orientations, for instance, nitrate anions can intercalate in three specific orientations from "flatter" to "stacked" orientation. Among them, flatter orientation can show a reduction in basal spacing [172], (2) the water molecules are trapped inside the interlayers along with anions in various fashions, which affect the d-spacing. (3) Nitrate anions can be absorbed on the diffuse electrical layers of LDH. Further. the formation of Tricalcium aluminate (TCA) may cause the suppression of nitrates inside the interlayers. However, FTIR analysis has shown the characteristics peak of NO_3^{1-} groups and confirmed the presence of nitrate groups in the LDH system. It seems that TCA formation caused suppression of nitrate intercalation and nitrate groups adsorbed on the diffuse electrical layers.

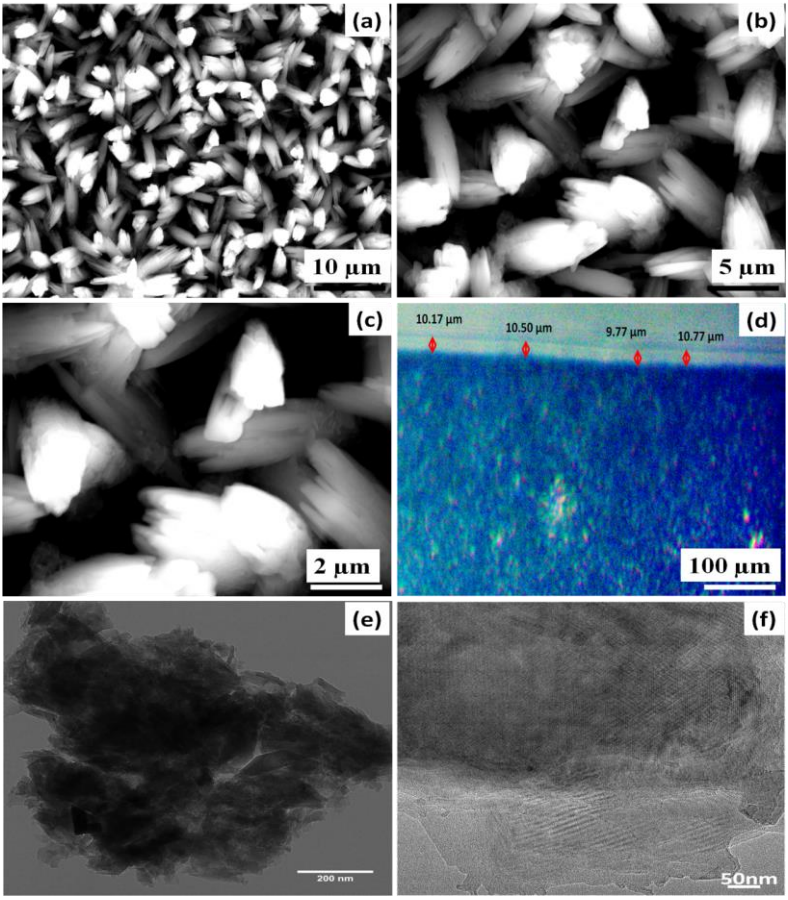

Figure 70 (a-c) SEM images, (d) optical image of the cross-section of CaAl-LDH, (e,f) TEM images of LDH.

FT-IR analysis is shown in Figure 71 (b), the broadband displayed in the range of 3370-3427 cm^{-1} are assigned to OH group stretching, while the absorption band around 1627 to 1633 cm^{-1} is caused due by the flexural oscillation peaks of interlayer water molecules. Moreover, the absorption peaks around 1389 cm^{-1} assigned to the asymmetric stretching bond of intercalated NO_3^{-1} [173]. The bond

at 655, 751, and 1202 cm^{-1} may associate with the Al-OH stretching [137]. The absorption peaks around 550 to 770 corresponding to the lattice vibration of metal-oxygen bonds (M-O) [174]. The obtained findings of FTIR are also well consistent with the TGA-DSC, XRD, and SEM analysis. The TGA-DSC results (Figure 72(a)) describe the LDH structural decomposition, which in general eventuates in two stages: Initially, the dehydration of the interlayer water molecules took place, around 200˚C, while on a later stage, the decomposition of interlayer anions and dehydroxylation occurs (temperature range 200-600˚C). This statement well correlates with the TGA-DSC thermograms in the previous reports related to LDH [51]. The increase in mass loss (40%) is because there are more bounded anionic species, the results correspond to the FT-IR analysis. The EIS measurements of as-prepared CaAl-LDH are shown in Figure 72 (b), the higher value of impedance in the low-frequency domain (impedance modulus at 0.01 Hz, $|Z|_{0.01}$) roughly indicates higher resistance properties. In the insets of Figure 72 (b), the phase angle response is presented, Considering the EIS response of the samples, two relaxation processes can be observed in the phase angle spectrum (Figure 72 b): The time constant in the high-frequency range (10^3-10^4 Hz) can be attributed to the properties of the LDH layer itself, while the time constants in the middle frequency range 10^0-10^1 Hz are the overlapping of the contributions of the aluminum oxide and the faradic process of substrate and solution interphase.

The advantages of novel cone-shaped CaAl-LDH films grown on the metallic substrate will helpful for the design of potentially active LDH for the above-said applications, owing to the unique structure, preferential growth, and geometry due to the activated structure. In a nutshell, this work gives an insight into the insitu grown cone-shaped CaAl-NO_3-LDH structure, and the geometry capable to modify further with inorganic and organic ions due to the low ion exchange equilibrium constant of interlayer NO_3^{1-} anions.

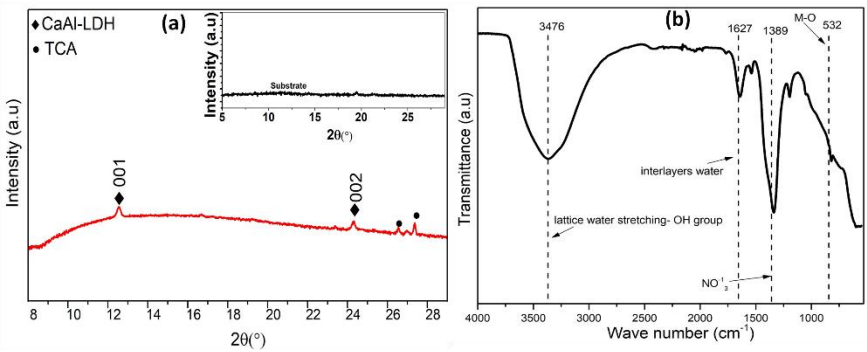

Figure 71. (a) XRD pattern of the CaAl-LDH film samples developed on AA6082, (b) FTIR spectrum of CaAl-LDH (scrapped from the aluminum substrate).

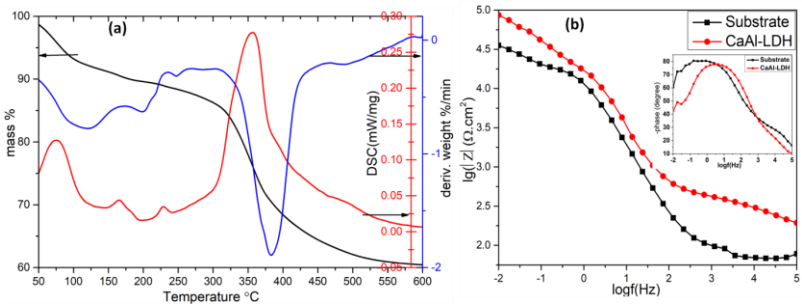

Figure 72. (a)TGA-DSC thermograms of the as-prepared cone-shaped CaAl-NO3-LDH (powder scraped from the specimen), (b) Bode plots in 0.1M NaCl solution.

4.6.3. Conclusion

In summary, we describe the development of cone-shaped CaAl-NO_3-LDH on AA6082 using the urea hydrolysis method. The XRD, FTIR analysis confirmed the formation of CaAl-LDH on the aluminum surface, while microscopic studies have shown a well-ordered cone liked LDH structure. From TGA results, around 40 % of mass losses were observed through the thermal decomposition along with significant impedance response in EIS analysis. In summary, this research provides an insight on the direct synthesis of cone-shaped CaAl-NO_3-LDH on the aluminum surface and provides a view on the structural investigation of well ordered, cone-shaped, uniform homogeneous LDH structure. These features would support our knowledge of the control of environmentally friendly CaAl-LDH thin film, resultant properties, and possible applications.

Chapter 5

Modification of LDHs

5. Introduction

In this chapter, the modification of MgAl-layered double hydroxide is studied by examining the two different approaches. In the first section, MgAl-LDH protective film was developed on AA6082 substrates, and coated substrates were further heat-treated in the air at temperatures from 100 to 250°C to further improve the corrosion resistance of MgAl-LDH by taking advantage of the LDH memory effect, and further, the effect of calcination on MgAl-LDH structural stability and the corresponding corrosion resistance properties were investigated. Thermal treatment of LDH can reorient the anions in the LDH interlayer, which leads to a substantial contraction of the basal spacing, enhanced absorption capacity, high surface area, and variable composition of the LDH structure. Upon heating, LDHs dehydrate and undergo further dehydroxylation and the anions decompose inside the galleries. While in the second section, MgAl-layered double hydroxides thin films, exhibiting two distinct surface morphologies (Platelet and Cauliflower-like), were synthesized directly on the AA6082 substrate and then were further modified with graphene to enhance the corrosion resistance properties of LDHs. The graphene was found to interact with the LDH structure and provide another pathway for the corrosion reactions by restraining the generating electrons to reach cathodic sites. The interaction of graphene with LDHs and their physiochemical properties are briefly discussed.

5.1. Ordering and Disordering of MgAl-LDHs- Structural and corrosion resistance properties

5.1.1. Synthesis of Calcined MgAl-LDH

Cauliflower-shaped MgAl-LDH was synthesized on an AA6082 substrate (0.70wt%–1.30 wt% Si, 0.40 wt%–1.00 wt% Mn, 0.60 wt.%–1.20 wt% Mg, 0.50 wt% Fe, 0.10 wt% Cu, balance Al) supplied by Metal Center (Italy) using the method developed in our previous work [113]. The pretreated AA6082 specimen was immersed vertically in a heating beaker (Sigma-Aldrich Glassware) containing a solution of 0.028 M $MgNO_3 \cdot 6H_2O$ and 0.084 M NH_4NO_3 (purity ≥98%, Sigma-Aldrich Corp.) in a 1000 mL flask under N_2 gas bubbling. The pH of the solution was maintained by the addition of ammonium hydroxide solution and the prepared solution thermally heat-treated at 80°C for 24 h. The specimens were dried after thermal treatment and were further heat-treated at different temperatures, i.e., 100, 150, 200, and 250°C, in an electric furnace for 6 h.

5.1.2. Results and discussion

SEM was used to investigate the microstructure of the uncalcined and calcined MgAl-LDH. Figure 73 (a) clearly shows that, initially, a well-developed and distinct cauliflower-shaped MgAl-LDH structure is formed and remains intact until the heat treatment at 100°C. Upon further thermal treatment (150–250°C), the regular cauliflower-like structure disappeared and a compact, uniform LDH structure was obtained. In the samples treated at 200 or 250°C, the nanosheets of the LDH structure fused to form a regular needle-like flowered structure. The film thickness was (42 ± 1) µm, as measured by cross-sectional analysis of the MgAl-LDH films using an optical microscope.

The EDS spectrum of the LDH treated at 250°C recorded in plane-scanning mode is shown in Figure 73 (e), which depicts that LDH structure is mainly composed of Mg, Al, N, and O. The as-prepared MgAl-LDH showed the following compositions: Mg (23.35at%), Al (4.92at%), O (61.73at%), N (2.93at%), and C (6.04at%). The content of oxygen decreases gradually from 61.7at% to 49.2 at% upon thermal treatment; besides, a relative increase was observed in the Mg/Al atomic ratio but remained in the range from 4 to 5. Conclusively, upon thermal treatment, SEM analysis has shown a regular, uniform, and more compact structure in the range 150 to 250°C. The XRD pattern of the MgAl-layered double hydroxide demonstrated characteristic peaks of the LDH structure (Figure 74): (003), (006), (009), (110), and (113), according to the literature [175]. The interlayer region mainly contains the hydroxyl groups and nitrate ions to balance the positively charged layers, and their concentration gradually decreases upon thermal treatment. The cell parameters calculated from the XRD pattern are shown in Table 21. The unit-cell parameters are defined as $a = 2d_{110}$, $c = 3d_{003} = 6d_{006} = 9d_{009}$. The XRD patterns show that the LDH has characteristic peaks of LDH during thermal treatment from 100 to 250°C but that the thermal treatment causes a contraction of the basal spacing; this behavior is consistent with the results of previous studies [176]. These observations can be attributed to interlayer water loss, partial decomposition of the NO_3^- groups, and a reduction in the interlamellar electron density [177]. The interlayer thicknesses (d_{003}, $d_{006,}$ and d_{009}) gradually decrease with increasing calcination temperature, whereas the d_{009} value remains almost the same. This asymmetric broadening of the (003) and (006) reflection peaks and basal broadening after calcination reflect turbostratic disorder [178]. Because of the high thermal expansion of the AA6082 substrate (24×10^{-6} K^{-1}), the maximum calcination temperature used in this study was 250°C. The XRD and SEM analyses show that the LDH structure compensates for the microstrain

effect of supervenes due to the thermal expansion of the substrate and that the LDH structure remains consistent and well preserved.

The uncalcined and calcined MgAl-LDH specimens were further investigated by FT-IR analysis in ATR mode, as shown in Figure 75. The broadband displayed in the range 3370–3427 cm^{-1} is assigned to OH stretching, and the absorption band at approximately 1627–1633 cm^{-1} is attributed to the flexural oscillation peaks of interlayer water molecules [179]. Moreover, the absorption peak at approximately 1360 cm^{-1} is assigned to the asymmetric stretching band of intercalated NO_3^- [139]. The small peak at approximately 1520 cm^{-1} corresponds to CO_3^{2-} ions, indicating the presence of a small number of carbonate ions in the LDH phase. The bands observed at 655 cm^{-1}, 751 cm^{-1}, and 1202 cm^{-1} are associated with Al–OH stretching[137]. The absorption peaks between 550 and 770 cm^{-1} correspond to the lattice vibration of metal-oxygen (M–O) bonds [174]. With increasing calcination temperature, the intensities of the hydroxyl group peaks decrease, which indicates the loss of the hydroxyl groups in the LDH interlayers. Furthermore, upon thermal treatment, the peak intensities of the NO_3^- groups also decrease, which depicts partial decomposition of the NO_3^- group in the interlayer region, especially within the temperature limit of 250°C. These results suggest that LDH structural decomposition occurs in two stages: initially, dehydration leads to loss of the interlayer water molecules at approximately 200°C; at a later stage, the interlayer anions decompose and dehydroxylation occurs (temperature range 200–800°C). This speculation well correlates with the TGA–DSC thermograms (Figure 76) and with the results of previous work [180]. These FT-IR results are also well consistent with the results of the TGA DSC, XRD, and SEM analysis.

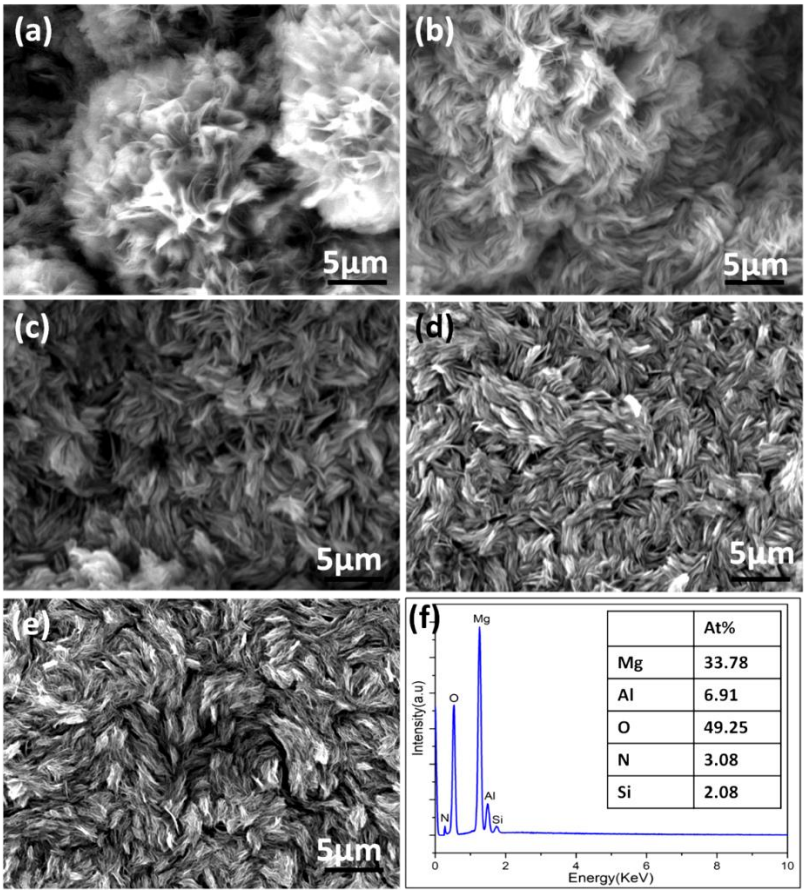

Fig. 73. SEM images of uncalcined and calcined MgAl-LDH films developed on AA6082: (a) as-prepared; (b) MgAl-LDH-100°C; (c) MgAl-LDH-150°C; (d) MgAl-LDH-200°C; (e) MgAl-LDH-250°C. (f) EDS spectrum analysis of MgAl-LDH-250°C.

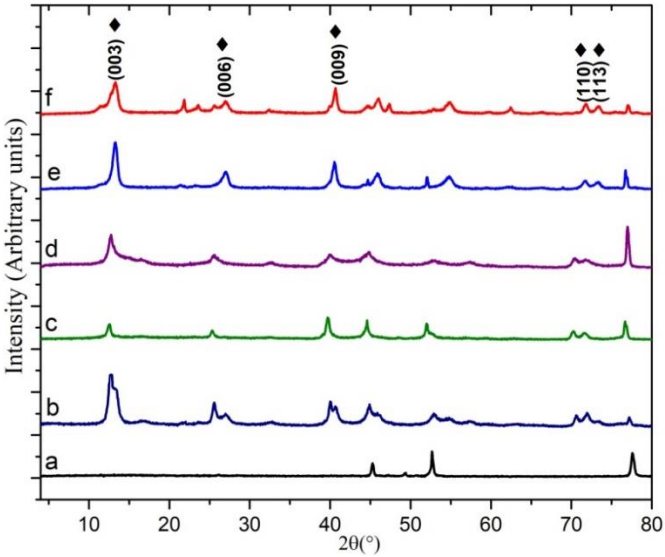

Figure 74. XRD patterns of uncalcined and calcined MgAl-LDH film samples developed on aluminum alloy: (a) AA6082 substrate; (b) as-prepared; (c) MgAl-LDH-100°C; (d) MgAl-LDH-150°C; (e) MgAl-LDH-200°C; (f) MgAl-LDH-250°C.

Table 21. Unit-cell parameters and sizes of the coherent domains determined for the MgAl-LDH precursor powders from their XRD patterns

Specimen	Lattice parameter		Interlayer distance				Crystallite size, D / nm
	a / nm	c / nm	d_{003} / nm	d_{006} / nm	d_{009} / nm	d_{110} / nm	
MgAl-LDH	0.312	2.411	0.811	0.405	0.263	0.156	9.371
MgAl-LDH-100°C	0.311	2.412	0.812	0.406	0.263	0.156	9.277
MgAl-LDH-150°C	0.310	2.398	0.804	0.404	0.262	0.155	8.437
MgAl-LDH-200°C	0.308	2.35	0.779	0.396	0.260	0.154	7.594
MgAl-LDH-250°C	0.308	2.343	0.777	0.395	0.259	0.154	6.984

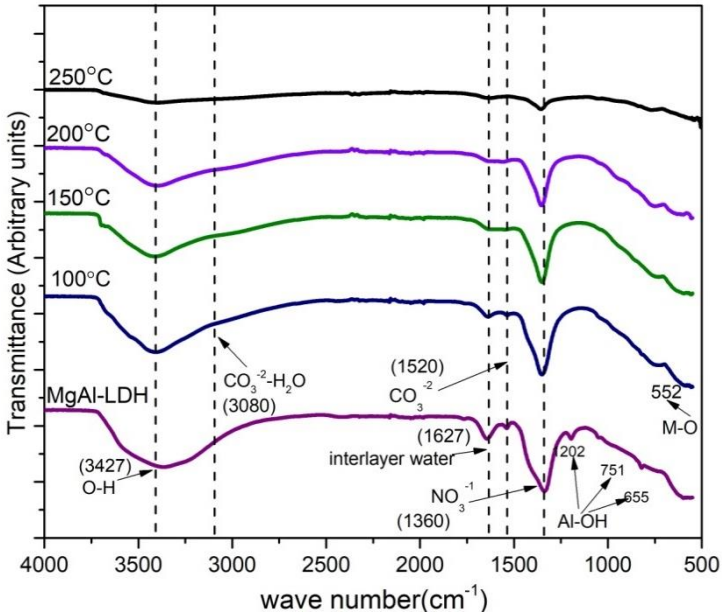

Figure 75. ATR FT-IR spectra of virgin and calcined MgAl-LDH powder scraped from the coated samples.

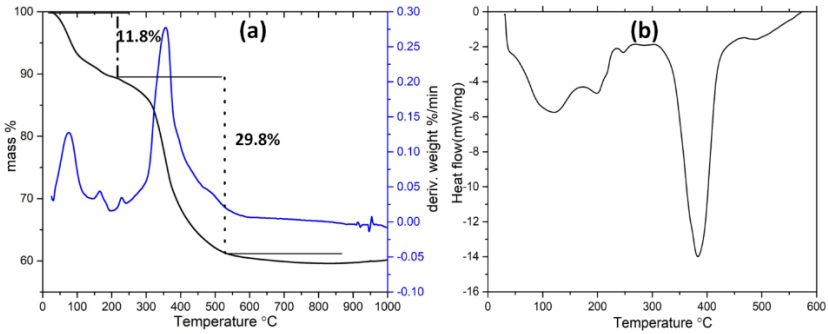

Figure 76. Thermogravimetric analyses of as-prepared MgAl-LDH (powder scraped from the specimen): (a) weight percent and derivative of the weight-percent curves for the TGA of the MgAl-LDH; (b) DSC thermogram of MgAl-LDH.

To understand the effect of thermal treatment on the corrosion resistance properties of the MgAl-LDH, electrochemical studies were performed. The potentiodynamic polarization curves of all specimens are shown in Figure 77. According to previous studies [156][181], an increase in the calcination temperature positively shifts the corrosion potential to higher values, which is likely attributable to the structural evolution of the LDH layer with increasing temperature according to the evolution observed by SEM (see Figure 73). The compact and uniform LDH structure appears to exhibit greater corrosion potential than the regular cauliflower-like structure, likely because of improved barrier properties. Both the cathodic and the anodic current density decreased with increasing calcination temperature, accompanied by a substantial positive shift in the corrosion potential. The remarkable reduction in both anodic and cathodic current density suggests that the MgAl-LDH thin films can decrease the corrosion rate of the substrate. The corrosion current density and related corrosion potential are shown in Table 22. The reduction of both the cathodic and anodic current density and the shift of the corrosion potential to more positive values indicate a reduction of cathodic and anodic active sites on the aluminum surface. Because of the thermal expansion of the AA6082 substrate at 250°C, a few cracks appeared on the LDH surface. However, the cracks did not cause severe distortion of the layered structure even if, in principle, they can provide a pathway for the aggressive media to interact with the aluminum surface. Compared with the diffraction peaks of the as-prepared MgAl-LDH (broader peaks indicating low crystallinity and a basal spacing of 0.81 nm), those of the calcined MgAl-LDH indicate high crystallinity with a basal spacing of 0.77 nm for the samples calcined at 200 or 250°C. This increase in crystallinity increases the LDH absorption capacity and implies strong intercalation of chloride ions into the layer of the MgAl-LDH. We conclude that the strong absorptive effect of LDHs upon thermal

treatment will result in stronger entrapment of chloride ions inside the interlayer compared with the chloride ions entrapped in the as-prepared MgAl-LDH, which did not allow the aggressive solution to interact with the LDH thin film (refer to corrosion current density Figure 77, impedance plots Figure 78). The calcined MgAl-LDH acts as a protective coating, which can be explained by (1) the entrapment of chloride ions in the LDH interlayer [154] and (2) the barrier effect, which protects the metal surface by avoiding interaction with the metal substrate because of the dielectric nature of the MgAl-LDH [73].

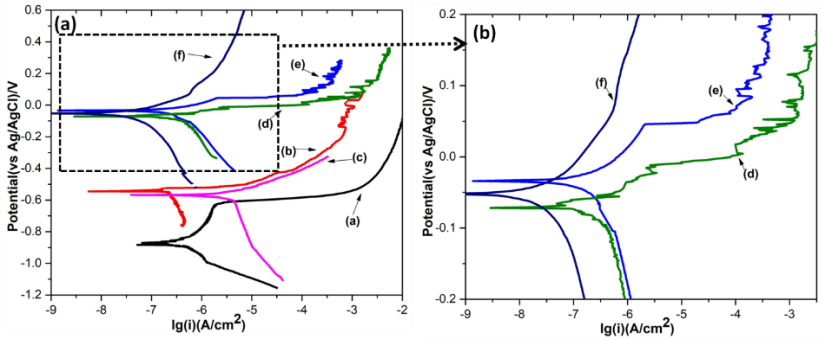

Figure 77. **(a)** Polarization curves of bare AA6082 and the MgAl-LDH thin film in 0.1 M NaCl aqueous solution: (a) AA6082 substrate, (b) as-prepared MgAl-LDH, (c) MgAl-LDH-100°C, (d) MgAl-LDH-150°C, (e) MgAl-LDH-200°C, and (f) LDH-250°C; **(b)** Zoomed polarization curves for clear depiction.

Table 22. Electrochemical parameters estimated from polarization data in Fig. 77.

Specimen	*E*(Ag/AgCl) (V)	*I* / (μA·cm^{-2})
AA6082	−0.879	0.465
MgAl-LDH	−0.513	0.363
MgAl-LDH-100°C	−0.586	1.548
MgAl-LDH-150°C	−0.071	0.256
MgAl-LDH-200°C	−0.031	0.169
MgAl-LDH-250°C	−0.052	0.028

To further understand the corrosion resistance behavior of the calcined MgAl-LDH, EIS analysis was performed (Figures 78(a) and 78(b)). Using the first approximation, the higher value of impedance in the low-frequency domain (impedance modulus at 0.01 Hz, $|Z|_{0.01}$) indicates better corrosion resistance. Figure 78(a) shows that, with increasing calcination temperature, the $|Z|_{0.01}$ value increases approximately six orders of magnitude over that of the bare AA6082 alloy. The large impedance shift in the middle frequency range indicates a strong dielectric protective coating for the specimens treated at 200 or 250°C. This enhanced anticorrosion behavior is also consistent with the potentiodynamic analysis results as well as the SEM and XRD results. In the EIS response of the sample treated at 250°C, two relaxation processes are observed in the phase-angle spectrum (Figure 78(b)): according to the literature [111], the time constant in the high-frequency range (10^3–10^4 Hz) is attributable to the properties of the LDH layer itself, whereas the time constant in the middle frequency range (10^0–10^1 Hz) is attributable to the overlapping contributions of the aluminum oxide and the faradic process at the substrate–solution interphase. Because of thermal degradation of the LDH structure, dehydration and partial decomposition of nitrate ions inside the LDH galleries within the temperature range 150–250°C cause an increase in the LDH absorption capacity. This behavior explains the enhanced corrosion protection properties of the LDH structures cured at higher temperatures. The LDH absorption capacity for chloride ions from the chloride solution is increased, thus leading to a stabilization of the layered structure, which in turn prevents chloride-ion migration to the underlying metal. This effect makes the LDH structure a compact system for entrapping chloride ions inside the LDH galleries and preventing the aggressive media from interacting with the aluminum surface. The specimens calcined at 200 and 250°C have shown a relative increase in impedance from 10^5 to 10^6 $\Omega \cdot cm^2$ in the low-frequency range. The thickness of

the film also plays a vital role in corrosion protection, which inhibits the microcracks during thermal expansion to propagate to the interface. The thermally induced memory effect of dielectric MgAl-LDH is the main factor for anticorrosion behavior; it causes strong intercalation of chloride ions inside the layered structure upon contact with a chloride-containing medium and acts as an effective corrosion resistance film. This observed behavior is consistent with other reports that describe the chloride exchange behavior with nitrate ions, where the chloride ions exhibit higher binding energy compared with nitrate ions [182]. The XRD patterns of the 003 characteristic peak of MgAl-LDH are shifted toward higher angles after calcination, indicative of improved anion-exchange properties of MgAl-LDH with the anionic species [183]. Based on the XRD results, after calcination, the MgAl-LDH exhibits high crystallinity and a reduction in basal spacing, which also supports the conclusion of improved barrier and anion-exchange properties compared with those of uncalcined MgAl-LDH.

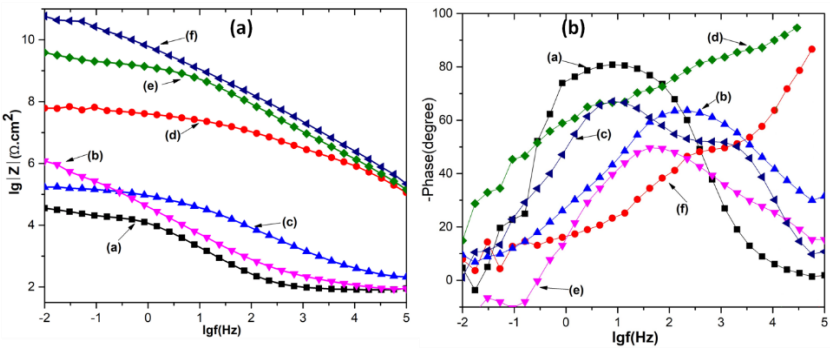

Fig. 78. (a) EIS spectra (Bode plots of log (|*Z*|) vs. log (frequency)) and (b) plot of the phase angle vs. log (frequency) for bare AA6082 alloy and AA6082 alloy coated with an LDH film: (1) AA6082 substrate, (2) as-prepared LDH, (3) LDH-100°C, (4) LDH-150°C, (5) LDH-200°C, and (6) LDH-250°C.

5.1.3. Conclusion

(1) MgAl-LDH protective films were deposited onto AA6082 substrates, and the coated substrates were subjected to a further thermal treatment from 100 to 250°C to investigate the effect of calcination on the LDH structural and corrosion resistance properties. The calcined MgAl-LDH structures in this work are found to be more effective as anti-corrosion materials than uncalcined LDH structures.
(2) The SEM analysis shows that, upon calcination, a more compact and uniform structure is obtained, and the initial cauliflower-like structure disappears. The XRD patterns and FT-IR spectra of the calcined samples show that the initial MgAl-LDH structure remains well preserved upon calcination at 100°C and then caused the loss of water molecules, partial dehydroxylation, and decomposition of nitrate ions inside the galleries at 200–250°C.
(3) The results from polarization curves confirmed that calcined MgAl-LDH shows improved corrosion resistance properties, demonstrating a substantially higher $|Z|_{0.01}$ (by as much as six orders of magnitude) and low corrosion current density (as much as two orders of magnitude lower) compared with those of the bare substrate.

5.2. MgAl-LDH/graphene protective film; Insight into LDH-graphene interaction

5.2.1. Synthesis of MgAl- LDHs/graphene thin film

LDHs platelet and cauliflower-like structures were synthesized on the AA6082 by the in-situ crystallization method, as described in detail in our previous work. In general, the mixture solution of $MgNO_3.6H_2O$ (supplied by Sigma-Aldrich Corporation, purity 98%), and NH_4NO_3 (supplied by Sigma-Aldrich Corporation, purity 95%) was prepared with molar ratios listed in Table 23. The pretreated substrates were vertically immersed in the “heating flask” containing the reaction

solutions to obtain MgAl-LDH film on AA6082 at 60°C for 24h. The pH of the solutions was adjusted at 10 with drop-by-drop addition of ammonium hydroxide solution. On completion, the samples were washed with deionized water and ethanol and were dried at room temperature. For simplicity, the product with a cauliflower-like structure is denoted by “CF” and the platelet-like structure is named as “PL” for future annotations. The LDHs specimens were further modified with graphene by vertical immersion of the LDH specimens in the graphene suspension for 10 minutes. The graphene powder was provided by COMETOX s.r.l. (Milan, Italy). The sheets have an average thickness of 6 nm with an average particle diameter of 25 μm. The graphene suspension was prepared by vigorous ultrasonic treatment (20 kHz) of 0.02g graphene into 50 ml of deionized water for 24 hrs. After that, the specimens were dried at 60˚C for 30 minutes after rinsing with water. The obtained graphene suspension has shown substantial stability which supports obtaining MgAl-LDH/graphene system. The graphene stability in water is limited due to hydrophobicity and large Vander Waal forces [184]. It was found that sonication can help to promote stabilization of graphene suspension for a limited time frame due to strong physical bonds at the graphene interface [185].

Table 23. Synthesis conditions to develop MgAl-LDH on AA6082.

		Solution composition	
Samples	Morphology	$MgNO_3.6H_2O$	NH_4NO_3
PL	Platelet-like	0.008M	0.048M
CF	Cauliflower-like	0.028M	0.084M

5.2.2. Results and Discussion

Figure 79 shows the SEM images (top view) of as-prepared MgAl-LDHs and graphene-modified LDHs deposited on the AA6082 alloy. The LDH microcrystals are found to cover uniformly the entire substrate exhibiting two distinct surface morphologies i.e. Cauliflower-like and Platelet structure, while perpendicular growth of LDHs particles was observed and staggered LDH structure is found due to mutual compression of LDH crystallites during the growth process. Graphene is found to interact with the LDHs structure and adsorbed on the surface of the LDHs (Figure 79 c, e), which may help to seal the micropores/defects of the LDH structure. The interconnected hexagonal LDH microcrystals are curled and perpendicular to the substrate, forming a nest-like structure. To further understand the LDH structure, FIB-SEM cross-sectional analysis of the as-prepared LDHs structures is shown in Figure 80.

The thickness of the as-prepared platelet structure lies around 6.44 µm and around 7.6 µm for cauliflower-like LDH structure. LDH formed a compact lamellar structure, forming two distinct bilayers, (a) a very compact LDH structure formed at the LDH-aluminum interface of around 1.18 and 2.01 µm for platelet and cauliflower-like surface morphologies, (b) a relatively porous LDH geometry on the upper surface. The growth mechanism of the LDH and formation of the inner compact and the outer porous layer is already well explained, where aluminum substrate formed Al_2O_3 layers are formed and transformed into $Al(OH)_3$, which

act as a precursor to form LDHs on the aluminum surface upon reaction with divalent cations [165]. The interaction of graphene with LDHs is investigated and cross-sectional SEM images are shown in Figure 81. Graphene was found to seal the micropores of the LDHs and contribute to interact across the LDH layers (from surface to interface). In the previous study, it was clear that the carbon content was found across the LDH layers, and its depth profile signals decrease from the upper porous layer to the inner compact layer, demonstrating the successful penetration of graphene inside LDHs layers [105]. The interaction of graphene with LDHs can be seen in Figure 81, where a more compact LDH bilayer structure is formed compared to the without graphene LDHs. A relatively thicker dense layer of 1.86 µm can also be observed for PL/g and 2.08 µm for CF/g structure. The relative increase in thickness is possibly attributed to the graphene stabilization close to the interface which results in a more compact inner LDH layer. For better comprehension of LDH structural behavior, EDX mapping is performed to estimate the elemental distribution. For representation, cauliflower-like structure mapping is shown in Figure 82. EDX quantitative analysis (Figure 83) showed the presence of Mg, Al, O, and C as the main elements in the LDH coated specimens. It is also noteworthy that silicon present in aluminum alloys did not obstruct the formation of LDH structure due to the nest-like LDH structure which blankets the entire surface (Figure 82). The Mg/Al atomic ratio for platelet-like and cauliflower-like MgAl-LDH is 0.84 and 1.5 respectively, with a respective weight percentage of 0.75 and 1.25 (Figure 83). However, the content ratio varies from surface to interface, where the interface is shown the lower value of Mg/Al ratio due to higher contents of aluminum [105].

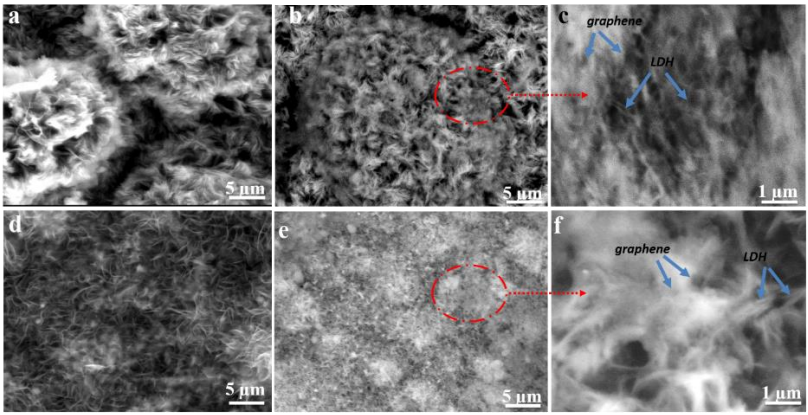

Figure 79. SEM images of MgAl-LDH, (a) CF(b-c) CF/g, (d) PL (e-f) PL/g.

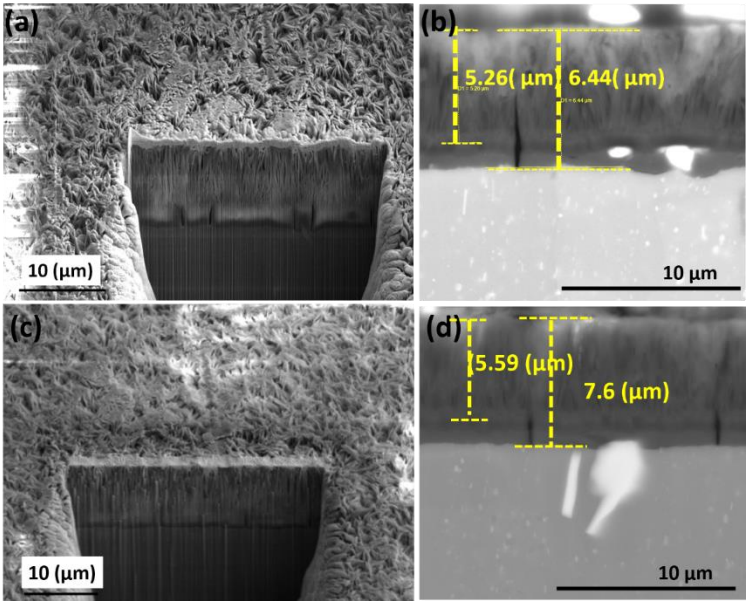

Figure 80. FIB milling of a thick lamella and cutting section, (a) PL structure (c) CF, (b-d) cross-sectional analysis of PL and CF-LDH respectively.

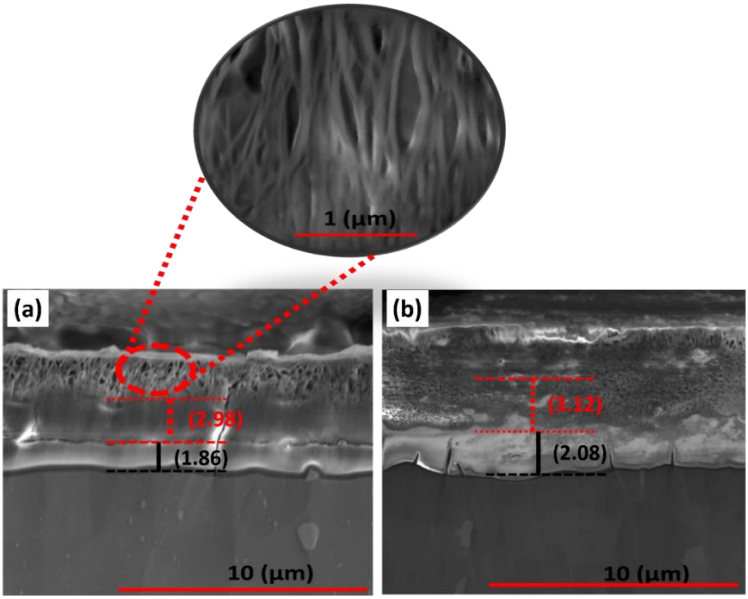

Figure 81 FIB-SEM cross-sectional analysis of MgAl-LDH/graphene, (a) PL/g, (b) CF/g.

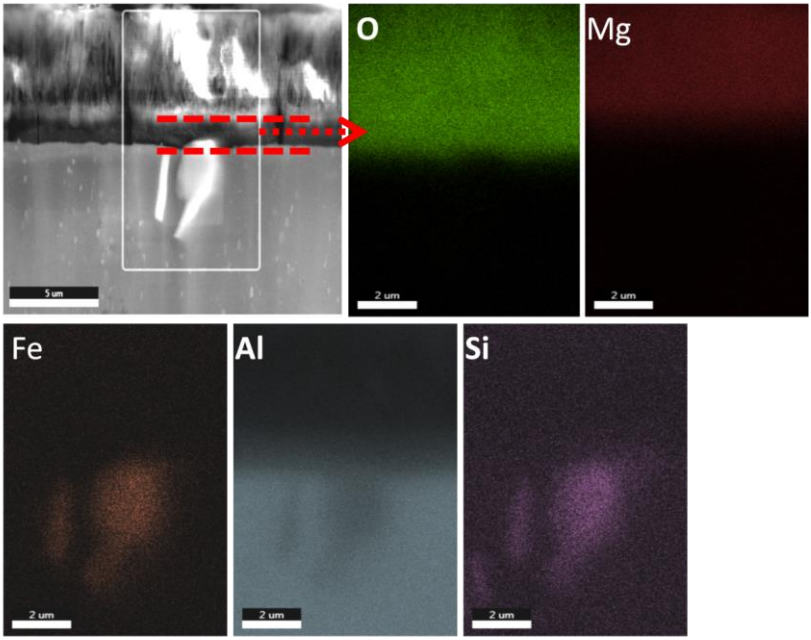

Figure 82. EDS elemental distribution on the surface of the CF-LDH. The elements, such as O, Mg, Fe, Al, Si (green color: O, red color: Mg, light cyan color: Al yellow color: Fe, and magenta color: Si) throughout the surface were identified.

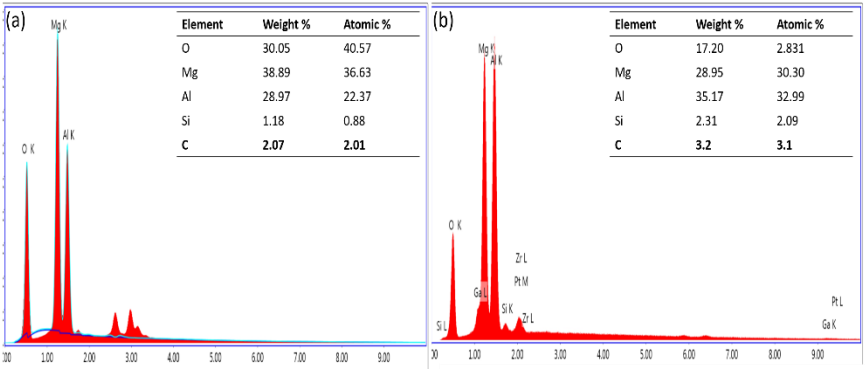

Figure 83. EDS analysis on the surface, (a) CF, (b) PL.

The XRD patterns of investigated specimens are presented in Figure 84, where well-resolved reflection peaks (003), (006), (009), (110), and (113) can be observed, confirming the formation of the LDH structure[186]. In all XRD patterns at d_{003}, the data revealed two distinct values of basal spacings, namely d_1 (0.82 nm) around 12.5˚ and d_2 (0.77 nm) at 13.3˚ of 2Θ. The observed basal spacing of d_1 is related to the nitrate intercalation inside LDH interlayer's, while d_2 suggested the presence of carbonate anions inside the layers [187]. These reflections correspond to the literature work where hexagonal lattice with R-3m rhombohedral symmetry was observed [188]. Furthermore, the nitrate anions found to intercalate from "flatter" to "stacked" orientation, which in turn affect the basal spacing, where flatter orientation showed the minimum nitrate basal spacing among the other orientations [189]. Herein, the basal spacing of nitrates ion in the LDH layers suggested the tilted arrangement of the NO_3 site symmetry in the interlayer's [82]. In XRD patterns, the characteristic peaks of LDHs follow almost the same 2Θ position after graphene modification. However, the decrease in intensity peaks is observed after graphene adsorption, which is attributed to the covered graphene layer. It has been found that graphene forms an impermeable

layer to protect the material without making any alteration in material chemical properties [190].

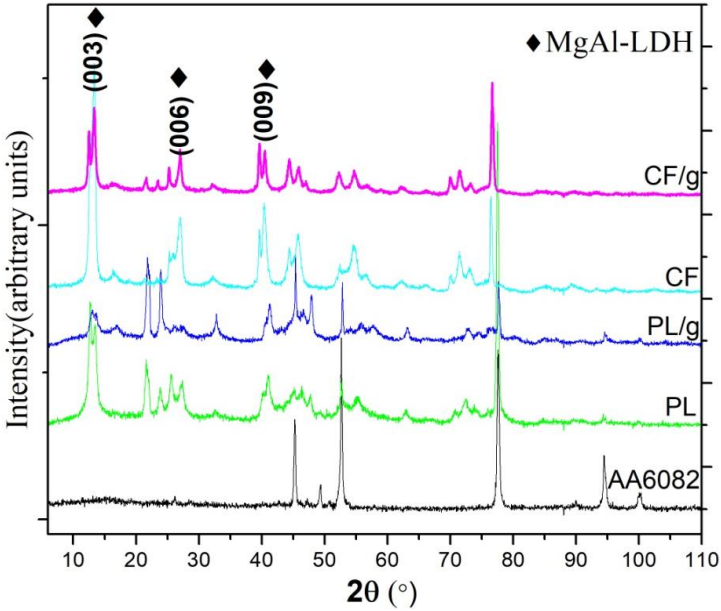

Figure 84. XRD spectra of LDHs and LDHs/graphene films deposited on AA6082.

The LDHs were further investigated by FT-IR (Figure 85) to analyze the chemical structure after graphene adsorption. The as-prepared LDHs were used for comparison to the graphene adsorbed structure. Initially PL and CF-LDH structures shown a similar FT-IR pattern, we include only PL LDH analysis for comparison purposes. The FTIR spectra showed four well-defined regions, demonstrating the characteristics bands of LDH structure. The broadband in the interval 3370-3427 cm^{-1} is related to the stretching vibration of the hydroxyl group while another band around 1630 cm^{-1} is due to the OH bending of the interlayer water molecules [173]. The intercalation of NO_3^- is confirmed by the absorption

peaks at 1370 cm^{-1} due to vibration mode ν_3 [139]. Finally, The bonds at 655 cm^{-1}, 751 cm^{-1}, and 1202 cm^{-1} may be associated with the Al-OH stretching and metal-oxygen lattice vibration [191].

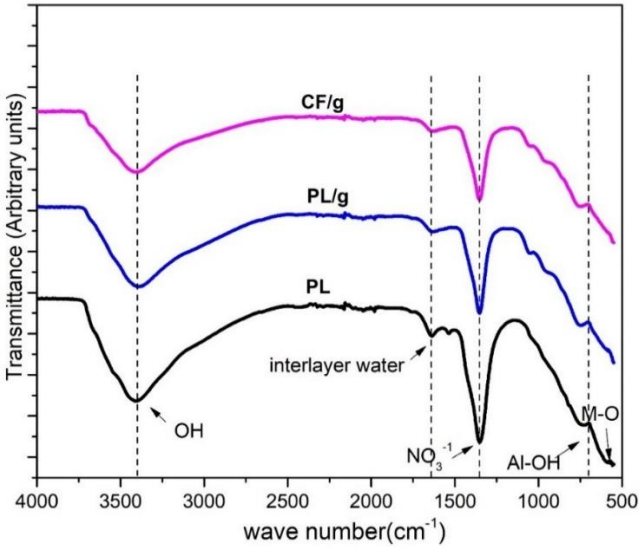

Figure 85. ATR-FTIR spectra of LDH and LDH/graphene powder scraped from the coated samples.

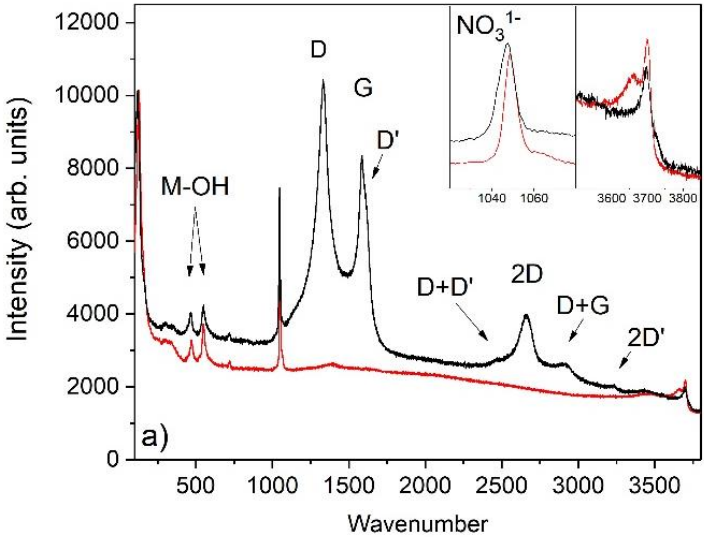

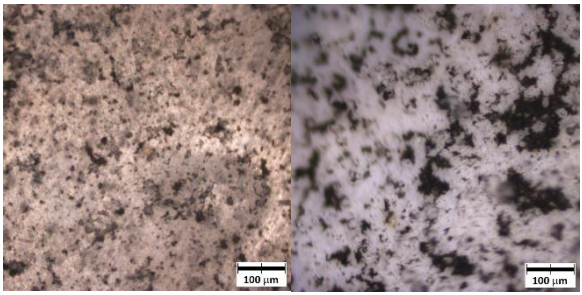

Figure 86. a) Raman spectra of samples PL (red line) and PL/g (black line). The insets show an enlargement of the NO3- peak region at about 1050 cm-1 (left), and the OH stretching region (right). Optical image of sample P (b) and sample C (c).

The Raman analysis is performed to understand the nature of graphene interaction with the LDH geometry. Figure 86 shows the Raman spectra collected on samples PL (red line) and PL/g (black line) in a bright region as visible in Figure 86b. A broad luminescence band is present in both spectra. The Raman band of the MgAl-

LDH are assigned to the Mg-OH and Al-OH hydroxyl group stretching vibrations with two peaks at about 3660 and 3700 cm^{-1} (see right inset Figure 86a), to the Mg-OH and Al-OH translations at about 470 and 550 cm^{-1}, and the NO_3^- stretching at about 1050 cm^{-1} (see left inset Fig. 86 a) [192].

The Raman spectrum of sample PL/g shows the same vibrational modes of sample PL, together with stronger bands due to the deposited graphene (D, G, D', D+D', 2D, D+G, and 2D' bands) [193][194][195]. The two spectra have been normalized at the ~ 1050 cm^{-1} peaks (for having the same area, see left inset to Figure 86 a). This peak appears broader and slightly shifted in the P/g sample. Moreover, the hydroxyl group stretching vibration band shows a different shape in the two samples. In the sample P/g, the lowest frequency peak (3660 cm^{-1}) is no more present, and the 3700 cm^{-1} peak appears broader. These observations prove a structural change in the interlayer regions of MgAl-LDH, where NO_3^- and OH^- are located, resulting in agreement with XRD analysis, which shows a change in the cell parameter. Furthermore, the broadening of all bands, including also the Al-OH and Mg-OH at about 500 cm^{-1}, indicates an increase of the disorder in the crystalline structure. Similar results are obtained for sample Figure 86 (c), with two main differences: a more intense luminescence background and a stronger reduction of the O-H stretching band (not shown for simplicity).

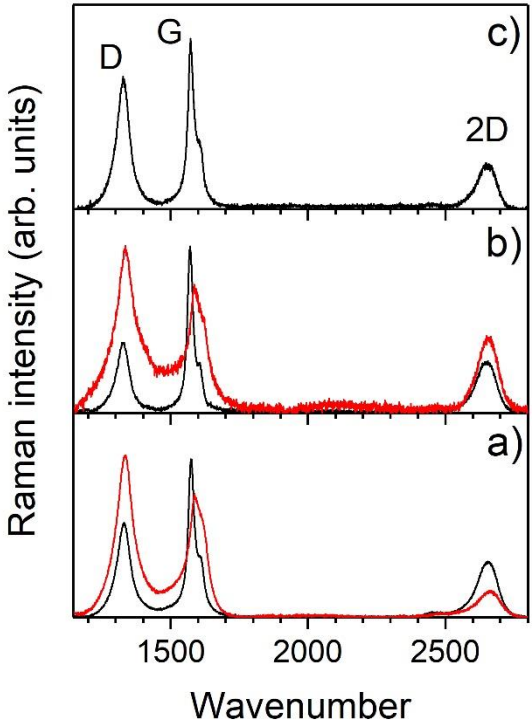

Figure 87. Raman spectra acquired on samples PL/g (a), CF/g (b) graphene powders (c). Black lines correspond to spectra acquired on dark areas, whereas red lines to spectra acquired on bright areas of the sample surfaces.

Figure 87 compares the spectra of samples PL/g and CF/g, taken in bright and in the dark areas (see Figure 86b and c) with the spectrum of the graphene powers used for the sample preparation. Only the region with the main graphene peaks is shown, and the luminescence contribution has been subtracted.

The Raman spectrum of graphene has been studied in detail [193][194][195]: it is possible to deduce the graphene properties (monolayer, bilayer or multilayer, degree of disorder, ion inclusions, etc) from the ratio of the intensity of the

different peaks and their width. The spectrum of graphene powders reported in Figure 87c is typical of a mixture of graphene structures with different numbers of layers. The position of the 2D band (2657 cm^{-1}), which depends on the number of graphene layers, is compatible with the one related to bilayer structures but broader, indicating the superimposition of structures composed by the different number of layers. Moreover, the strong intensity of peak D (~1327 cm^{-1}) and the presence of peak D' (1612 cm^{-1}) indicate a quite large disorder.

The Raman spectra in Figure 87 (a and b) acquired on bright areas of samples PL/g and sample CF/g (red lines) are characterized by a stronger disorder (D band) and a stronger D' band than graphene powder one (Figure 87 c). Different kinds of the disorder can be deduced from the spectrum shape, in particular, the intensity of the 2D peak (~2660 cm^{-1}) is related to stacking order between different planes, whereas the intensity of D' peak (~1612 cm^{-1}) to the presence of point defects inside the graphene layers [30]. Moreover, the possible presence of amorphous carbon is highlighted by a broad band centered at about 1550 cm^{-1} between the D and G bands [194]. Therefore, the graphene on sample CF/g is more disordered if compared to the one on sample PL/g, especially for stacking (2D peak), and shows a more intense amorphous contribution. It seems that the deposition of graphene on a flatter structure, as on platelet-like morphology, produces more ordered layers than in the case of cauliflower-like morphology.

At the micrometric scale, both samples are characterized by the presence of dark agglomerates with a size of about 10-30 µm in sample PL/g and of about 30-100 µm in sample CF/g (Figure 86 b and c). The Raman spectra acquired on these dark areas (black lines in Figure 87 a and b) show structures like one of the graphene powders, but are more ordered than one of the powders itself. They show sharper G peaks and less intense D peaks. We can conclude that the graphene covers all the surface of samples PL/g and CF/g (on a scale of 1 µm, the size of the laser

spot), since also in the bright areas a strong graphene Raman spectrum can be observed, but in a non-homogeneous way, since micrometric agglomerates of graphene-like structures are present. Similar findings are found in literature studies where great promise showing to resolve the pore blocking phenomenon occurred in the graphene-coated polymer foam composites [196,197]. Furthermore, graphene-based coating systems have shown superhydrophobic characteristics and are discussed in detail in previous studies, which can make an impact on electrochemical properties [198], [199].

The corrosion resistance of obtained hybrid LDH films is investigated by the electrochemical studies, before and after the adsorption of graphene. EIS plots of the LDH and LDH/graphene specimens are reported in Figure 88. The graphene-based LDH structure exhibited a higher value of |Z| compare to the only LDH structure. Considering the EIS response of the MgAl-LDHs samples, two relaxation processes can be observed in the phase-angle spectrum (Figure 88b): the time constant in the high-frequency range (10^3-10^4 Hz) can be attributed to the properties of the porous layer of the LDH coating, while the time constant in the middle frequency range 10^0-10^1 Hz to the overlapping of the contributions of the compact LDH layer and the faradic process at substrate and solution interphase. The value of the lower frequency region (namely, $|Z|_{0.01}$) can be assumed as a rough estimation of the corrosion protection properties of the investigated materials [101]. From Figure 88a, CF/g has shown the $|Z|_{0.01}$ value around 6.15 $\Omega.cm^2$, which is nearly two orders of magnitude higher than bare AA6082 alloy. The presence of graphene seems to be beneficial in terms of an increase in the low-frequency impedance: both CF/g and PL/g samples show a rise of one order of magnitude in $|Z|_{0.01}$ compared to as-prepared CF and PL. The graphene in the LDH films likely helps to improve the barrier properties: this hypothesis is supported by the increase in impedance in the middle and high-frequency range

observed in Figure 88. Both structures have shown an increase in impedance after graphene adsorption, but the cauliflower-like structure is found to show comparatively better corrosion resistance (evaluated in terms of $|Z|_{0.01}$). As shown by the above-reported results, the cauliflower MgAl-LDH/graphene structure has shown a slightly more protective structure than the platelet MgAl-LDH/graphene structure. It seems that graphene can partially seal the porous structure, thus enhancing the anti-corrosion properties without disturbing the original LDH structure. The EIS results were further fitted using the "ZSimpWin" software to get more details related to the corrosion resistance properties to better understand the sealing effect of graphene. The electrical equivalent circuit $R_s(CPE_{LDH}(R_{LDH}(CPE_bR_b)))$ is used to analyze the EIS response of LDHs before and after graphene adsorption, respectively [155]. In those circuits, R_s represents the resistance of the electrolyte, R_{LDH} describes the MgAl-LDH film resistance with a constant phase element which accounts for the dielectric properties of the LDH film (CPE_{LDH}), R_b represents the barrier resistance related to the more dense part of the LDH layer with a constant phase element (CPE_b). According to the mathematical representation of a CPE, (i.e. $Z_{CPE} = 1/(Q(\omega j)^{\alpha})$, the parameters Q and α have been employed to describe the response of the electrodes. The total resistance (R_t) can be used to analyze the protective ability of deposited MgAl-LDHs. Since the R_t values give relative information related to the corrosion rate i.e. higher is the total resistance, lower will be the corrosion rate. It can be seen that total resistance ($R_t = R_b + R_{LDH}$) varies with the effect of graphene addition in LDH geometry and a higher value of total resistance further confirm the graphene as an additional layer to enhance corrosion resistance, but here it is also important to mention that CPE has a value of α far from 1, and thus the film did not act as a pure capacitance and it is difficult to interpret the real physical meanings of EIS fitting parameters [165]. The calculated parameters are listed in Table 24. Due to

the well-formed LDH structure, the graphene sealing effect and their entrapment in the LDH network seem to lead to the stabilization of the layered structure which reduces migration of aggressive species to the underlying metal. The permeation of aggressive solution in the porous layer of the layered double hydroxide caused a lower Q_b value compared to the without graphene-modified LDHs structure. The CF-LDH/graphene specimen has shown the highest R_{LDH} and R_b values which describe hindering in corrosion reaction while the lowest Q_b value is shown a relatively dense layer of LDH. A similar result was found in the previous study, where graphene improves near one order of impedance modulus of ZnAl-Mo-LDH due to the graphene sealing effect [105].

R_{LDH} value of CF-LDH/graphene has shown a higher value than PL-LDH/graphene indicating the capability to resist the electrolyte penetration and provide better protection which depicted the influence of graphene on LDH corrosion resistance properties. This can be explained that graphene nanoplatelets, because of their excellent electrical conductivity, provide an alternative path for the electrons generated by the anodic reaction, and thus restraining the electrons from reaching a cathodic site [200].

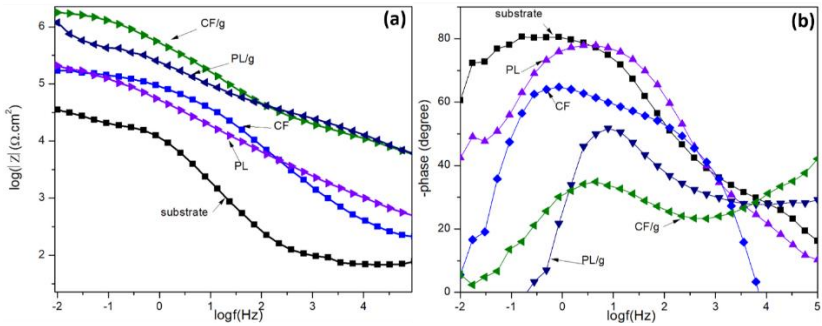

Figure 88. Impedance and phase plots of MgAl-LDH coated specimens before and after graphene adsorption in 0.1 M NaCl solution.

Table 24. Evolution of the fitting parameters RLDH, QLDH, αLDH, and Rb, Qb, αb derived from Figure 88.

Sample	R_{LDH} kΩ cm^2	Q_{LDH} Ω^{-1} cm^{-2} s$^{\alpha}$	α_{LDH}	R_b kΩ cm^2	Q_b Ω^{-1} cm^{-2} s$^{\alpha}$	α_b
PL	41.31	$2.95\cdot10^{-7}$	0.74	233.5	$6.91\cdot10^{-7}$	0.78
CF	52.41	$5.86\cdot10^{-6}$	0.96	462.5	$1.84\cdot10^{-6}$	0.90
PL/g	788.1	$1.98\cdot10^{-6}$	0.76	8109	$1.1\ 10^{-5}$	0.78
CF/g	988.2	$2.79\cdot10^{-6}$	0.72	9789	$3.94\cdot10^{-4}$	0.76

To better understand the graphene/LDHs stability on contact with an electrolyte (0.1M NaCl), the impedance plots of the CF/g were evaluated for 1 h to 240 hrs immersion period, as shown in Figure 89. CF/g sample was particularly selected because of superior corrosion resistance properties among the studied specimens. The specimen shows the decay of the protection properties during the 10 days of continuous immersion in the electrolyte. The impedance modulus value ($|Z|_{0.01}$) of about $10^{6.25}$ Ωcm^2 after 1 hrs of immersion decrease to $10^{5.88}$ Ωcm^2 after 240 hrs immersions, where after 240 hrs of immersion a decrease of $10^{0.3}$ Ωcm^2 was observed. This can be attributed to the protection ability of the graphene inside LDHs layers, which is sealed. The $|Z|_{0.01}$ declining rate during different immersion times for graphene/LDHs is much lower compared to the literature study for only LDHs structures [73]. The $|Z|_{0.01}$ value of CF/g after 10 days of immersion is in any case is higher than the $|Z|_{0.01}$ value of the bare AA6082 at the beginning of the immersion in the electrolyte ($|Z|_{0.01} \approx 10^{4.5}$ Ωcm^2).

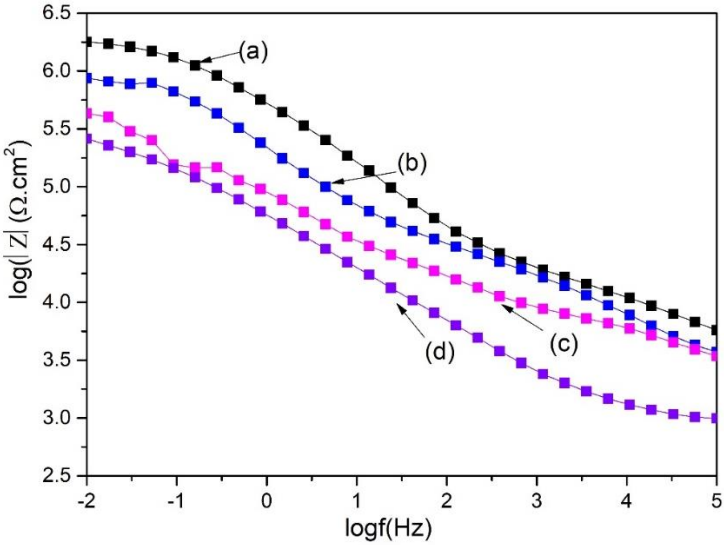

Figure 89. Impedance plots of CF/g after immersion in 0.1M NaCl solution, (a) 1hr, (b) 96 hrs, (c) 168 hrs, (d) 240 hrs.

5.2.3. Conclusion

The adsorption behavior of graphene on two distinct MgAl-LDHs surface morphologies is reported to understand the graphene interaction with LDH on its physicochemical properties. Electrochemical studies demonstrated the resistant nature of graphene against aggressive media penetration and were found to act as an additional pathway for the corrosion reaction. FIB-SEM images confirmed the penetration across the LDHs structure from surface to LDH/substrate interface and promote the compactness of the upper porous and bottom dense layer. Further, the Raman results explained the adsorption behavior of graphene on LDHs, which can enhance the impedance modulus of LDH around one order magnitude in the case of CF-LD H, while one order for PL-LDH structure. The cauliflower adsorbed graphene depicted relatively better corrosion resistance properties

probably due to the relatively higher thickness and more LDH/interface dense area. The graphene is helpful to seal the micropores of LDH up to an extent, while also found to interact with both LDH layers and through sealing of micropores which leads to better barrier properties. This work contributes to supporting our knowledge of the graphene-based LDHs system and resultant properties.

Chapter 6

Double Doped LDHs on anodic AA6082

6. Introduction

Recently, rare earth elements found to have a significant inhibiting effect and are the object of considerable scientific interest exhibiting nontoxic nature. Among rare earth elements, cerium-based coatings attracted significant attention, specifically also in case of incorporation inside the LDH network. In the first section of this chapter, CeMgAl-LDHs protective thin films were developed directly on two different aluminum surfaces i.e. anodized AA6082, and "hot water sealed" anodized AA6082. The effect of both approaches on corrosion performance is compared with unmodified LDHs and the possible mechanism of cerium interaction with LDH is described, where cerium modification has brought long-term stability and better corrosion resistance properties. In the second section, cerium doped MgAl-layered double hydroxide (LDHs) was further modified by PFDTS (1H, 1H, 2H, 2H perfluorododecyl trichlorosilane) through anion exchange reaction to obtain superhydrophobic characteristics for improved corrosion resistance and self-cleaning properties. PFDTS were hydrolyzed in absolute ethanol to obtain $CF_3(CF_2)_9CH_2CH_2Si(O^-)_3$ groups, which were incorporated inside MgAl-LDH and have shown superhydrophobic characteristics by demonstrating the water contact angle of 156.5°, and provide active corrosion resistance, long-term stability, UV radiation protection, and characteristics of self-cleaning against general household items (coffee, tea, cola, basic media, light acidic solution. This new double doped LDHs approach is another effective strategy, where the synergistic effect of introduced inhibitors in the LDH framework is found to provide long-term corrosion resistance properties and multifunctional characteristics.

6.1. Protective Cerium based Layered double hydroxides thin films developed on anodized AA6082

6.1.1. Synthesis of the anodized layer

Aluminum 6082 (wt%;0.50 iron, 0.6-1.2 magnesium, 0.70-1.30 silicon, 0.10 copper, 0.40-1.0 manganese, and balance aluminum) of 3.14 cm^2 surface area were mechanically ground with SiC grit papers i.e. 500, 1000, 2400, 4000 and immersed in 0.1M NaOH solution for 1 minute, followed by 0.1M HNO_3 solution for five minutes, rinsed with distilled water after each step. The anodization process was carried out in 0.1M H_2SO_4 electrolyte at a constant voltage of 14 V for 30 minutes at room temperature. The stainless-steel plate was used as a cathode, while the pretreated AA6082 specimen act as the anode. After anodization, the specimens were divided into two groups: the first group was treated with "Hot boiling water" for 20 minutes to seal the porous anodized structure and further were used to developed LDHs on it, and the other was immersed in the mixture solution of cerium and magnesium nitrates, which act as a building block to fabricate LDH film on the on/into the anodic surface.

6.1.2. Synthesis route of CeMgAl-LDH

(a) To synthesize single-step CeMgAl-LDH, both types of anodized surfaces (hot water sealed and open porous) were vertically immersed in 0.01M $Mg(NO_3)_2.6H_2O$, 0.001 $CeNO_3.6H_2O$, and 0.06 M NH_4NO_3 mixture solution at 80 °C for 18 hr at atmospheric conditions. The precipitation of $Ce(OH)_3$ on the anodized surface at high pH is also a well-explained phenomenon [201]. The pH of the solution was maintained at 10 with a dropwise addition of NH_4OH solution.

(b) For reference, without cerium, MgAl-LDHs were also developed on the above-mentioned anodized surfaces, at the same synthetic conditions (80°C-24hr-10 pH) with similar magnesium salt concentration (0.01 M). The general representation of LDH synthesis on the anodized surface is shown in Figure 90. For simplicity, Table 25 describes the general terms to use further for the developed specimens.

Table 25. Developed LDHs specimens.

	Definition
CeLDH	*CeMgAl-LDH developed on anodized AA6082 surface.*
CeLDH-H	*CeMgAl-LDH developed on "Hot water-sealed" anodized AA6082 surface.*
LDH	*MgAl-LDH developed on anodized AA6082 surface.*
LDH-H	*MgAl-LDH developed on "Hot water-sealed" anodized AA6082 surface.*

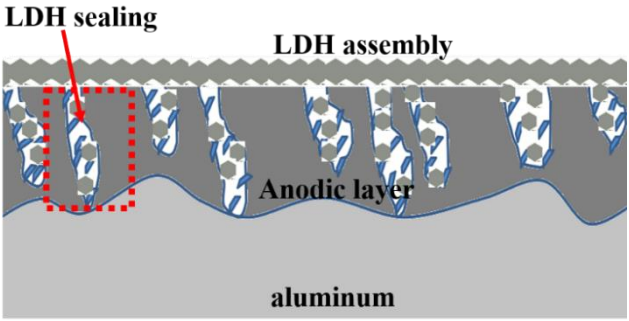

Figure 90. Schematic representation of LDH synthesis on the anodized surface.

6.1.3. Results and Discussion

XRD patterns of the developed LDHs films, with and without cerium addition, are presented in Figure 91. In all the specimens, well-resolved reflections of (003),

(006), and (009) are observed clearly at around 11.8°, 23°, and 34° respectively, that are typical reflection peaks of LDHs. The “003” reflection peak corresponds to 0.75 nm basal spacing, which confirms the presence of carbonates inside LDHs [100]. It is found that the incorporation of cerium ions in LDH structure did not make any dominant difference in LDH characteristics peaks with similar basal spacings, and thus can assume that cerium ions are incorporated in the film in the amorphous form [202]. However, slight variation in peak intensities is observed on cerium addition which indicates a little variation of crystallinity on cerium addition into LDH lamellar layers. No dominant characteristics peaks of CeO_2/ Ce_2O_3 are observed, which describe the successful incorporation of cerium inside LDHs layers in the amorphous form [201].

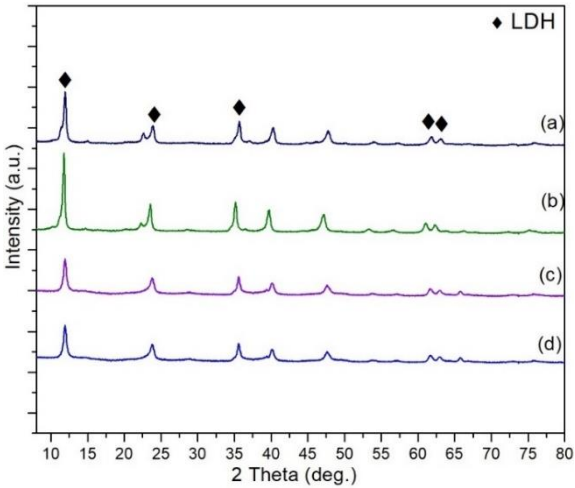

Figure 91. XRD spectra of LDHs films deposited on AA6082, (a) CeLDH, (b) LDH, (c) CeLDH-H, (d) LDH-H.

The top view of SEM images (Figure 92) shown the anodized film before and after the LDH treatments. It is found that LDHs microcrystals grown on the anodized surface covered the entire substrates with a dense network of curvy platelet LDHs

structure (Figure 92(c-f)), compared to a less dense network of LDHs on bare AA6082 surface (Figure 92b). No clear difference was found of LDHs developed on open porous or/ sealed anodized surface, However, the surface morphology of LDHs was affected by the doping of cerium addition where the reduction in the micro-pores size is observed. EDS quantitative results, in planer mode, are shown in Figure 93. The results described the higher amount of cerium in the case of LDH synthesis on the open porous anodized surface (Figure 93d), compared to the sealed anodized surface (Figure 93c). It may be due to the precipitation of more cerium content on open micropores porous aluminum oxide layer than the "Hot water-sealed" one. The elements Mg, Ce, Al, C, and O were found mainly to take part in the film formation. Moreover, the Mg/Ce molar ratio was found to be 7.16, and 3.75 for the hot water sealed (CeLDH-H) and LDH precursors sealed films (CeLDH) respectively. The significant decrease of Mg/Ce contents proposed the incorporation of effective cerium ions inside the CeLDH structure. The addition of cerium leads to a decrease in the number of other elements in LDH surface as shown in EDS quantitatively analysis, which confirmed the presence of cerium ions in the LDHs network, either in amorphous form or/and in the form of intermediate species $Ce(OH)_2$ or $Ce(OH)_3$ that can lead to the formation of CeO_2 [203]. However, XRD analysis supports the incorporation of cerium in the amorphous form in the LDH network and no impure cerium ions phase is observed.

It is found that LDH film grows simultaneously "inward" and "outward" on the substrate, growth inward dense layer formed at LDH/substrate interface, and outward porous network of LDHs formed at LDH/solution interface [204]. The dissolution of the aluminum oxide layer and interaction with the LDH precursors start LDH inward growth, while during that aluminum oxidized to Al^{3+}, cerium ions may reduce to Ce^{3+} and on interaction with OH^- groups; $Al(OH)_3$, $Ce(OH)_3$,

$Mg(OH)_2$ are formed. Besides, cerium ions can diffuse inside LDH layers, resulting in the formation of MgAlCe-LDH. In cross-sectional analysis (Figure 94), a two-layer structure is formed on the substrate, anodic film starts partial dissolving on contact with the LDH precursors and result in the formation of LDH film on the anodic film and formed a compact structure [201]. It is reported that higher pH causes the hydrolysis of Ce^{3+}, and this can promote the precipitation of $Ce(OH)_3$ on the anodized surface. So, cerium participates in the sealing of micropores and the building block of LDHs in the amorphous form [201]. The presence of Ce^{3+} ions may lead to partial oxidation to Ce^{4+} and can form mixed-species containing CeO_2, $Ce(OH)_4$ depending on pH of the surrounding solution [205], and further, the deposition of LDH layer is formed with the increase of synthesis aging time. The measured film thickness of the developed specimens is shown in Figure 94(b), where “Hot water-sealed” LDHs have shown comparatively a little higher film thickness than LDHs grown on microporous anodic film.

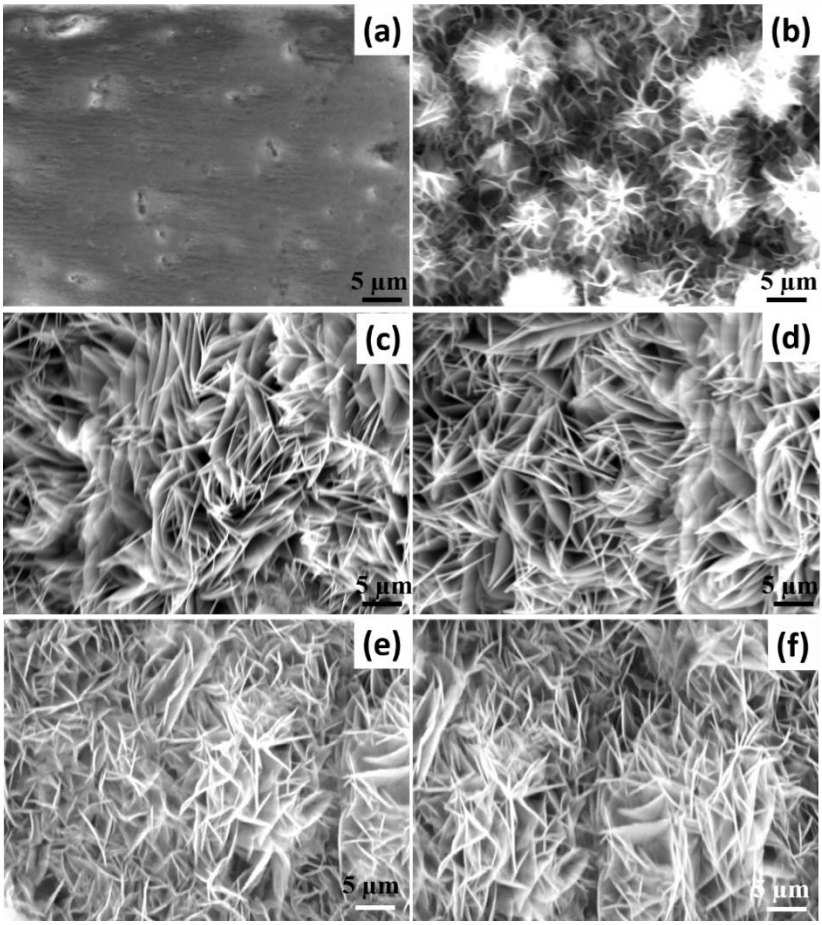

Figure 92. SEM images of LDHs, (a) anodized surface, (b) LDH on bare AA6082 surface, (c) LDH, (d) LDH-H, (e) CeLDH, (f) CeLDH-H.

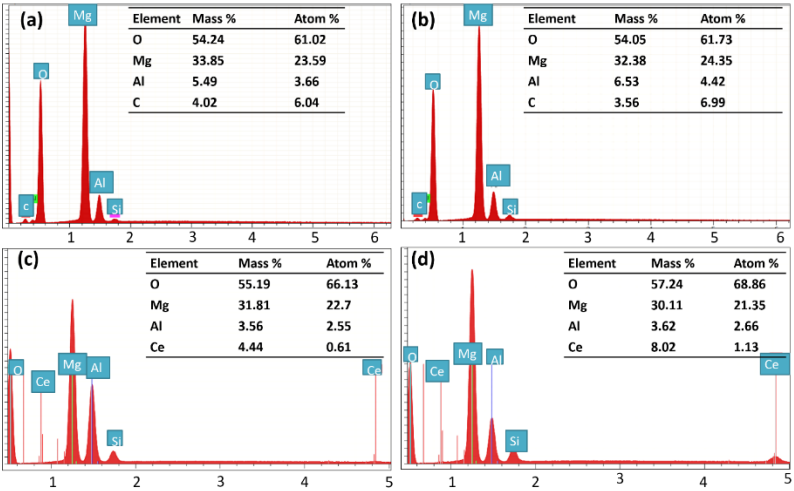

Figure 93. EDS spectra of the developed films and respective quantitive analysis, (a) LDH, (b) LDH-H, (c) CeLDH, (d) CeLDH-H.

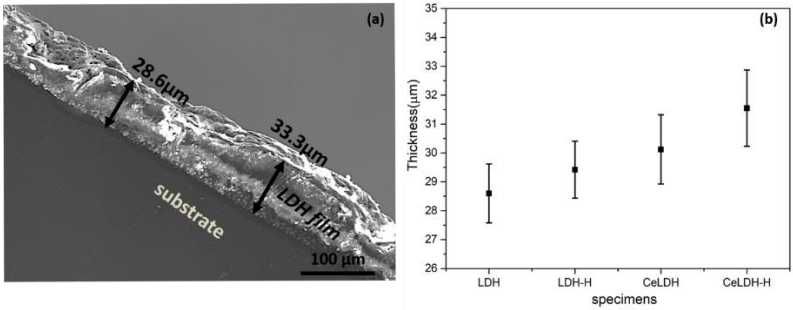

Figure 94. (a) Cross-sectional analysis of CeLDH, (b) film thickness of developed specimens.

To understand the corrosion resistance behavior of modified and unmodified LDHs, Electrochemical Impedance Spectroscopy spectra were collected in 0.1 M NaCl solution. The electrolyte has been selected to promote degradation of the LDH layer which allows us to monitor the inhibitive effect of Ce in the time scale investigated. The EIS spectra acquired after 1 h of immersion are reported in

Figure 95. Impedance modulus and phase plots are shown in order to better highlight the presence of the relaxation processes in the high-frequency range.

For general comparison among different developed LDH films, the impedance modulus in the low-frequency range can be employed for a rough estimation of the stability and corrosion resistance of the investigated samples [206]. Accordingly, as far as the impedance modulus at 0.01Hz is considered ($|Z|_{0.01}$), the introduction of cerium in both forms;- CeLDH, CeLDH-H, have shown initially an improvement compared to the reference samples. In particular, an increase of about 1.5 order magnitude of ($|Z|_{0.01}$) is observed for cerium modified LDHs, compared to the unmodified LDHs (Figure 95a).

The phase plots (Figure 95(b)) of cerium modified and cerium-free LDHs both suggest the presence of two relaxation processes. However, significant differences are observed: in the case of the Ce containing coatings, one time constant is located in the high-frequency range (around 10^4 Hz) and the other in the low-frequency range (around 10^{-1} Hz); while for the LDH and LDH-H, the first time constant is shifted towards lower frequency range (around 10^3 Hz) and the second one towards the middle frequency range (around 10^0-10^1 Hz). To a first approximation, the high-medium frequency relaxation process is attributed to the outer porous surface layer and the other in medium-low frequency relaxation process is associated with the inner barrier layer. The time constant in the low-frequency range is believed to account also for the faradic process occurring at the substrate/film interface. A deeper discussion of the reasons underneath this attribution is provided at a later stage in the manuscript when the electrical equivalent circuits (e.e.c.) employed for the fitting are discussed. Considering the impedance plot in Figure 95a, the CeMgAl-LDH depicted higher impedance values in the middle-high frequency range, suggesting the better resistance of the upper layer as compared to unmodified LDH. As previously anticipated, higher

impedance modulus values also in the low-frequency range have been observed for the Ce-based LDHs, thus suggesting a reduced corrosion rate. The significantly enhanced corrosion resistance of Ce based LDHs can be explained by the following; (i) the passive protection of compact LDH layer, (ii) the presence of cerium in the LDH frame, which was found to protect by its inhibition action by dissolving from the LDHs structure, entering the solution and precipitating at the cathodic sites (the mechanism is explained later in the manuscript). To better investigate the role of Ce in the LDH layers the long-term stability of the developed coatings has been investigated upon exposure to the chloride-containing media.

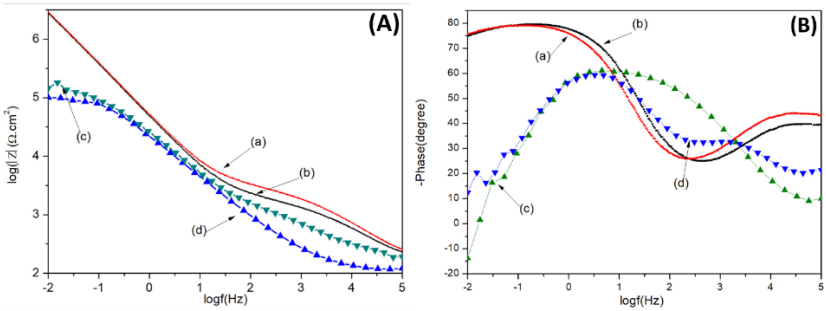

Figure 95. Impedance modulus (A) Phase plots (B) after 1 h immersion in 0.1M NaCl solution ;- (a) CeLDH, (b) CeLDH-H, (c) LDH, (d) LDH-H .

The impedance plots of the unmodified LDH after immersion for 1 h to 168 h are shown in Figure 96 (a-b). Samples LDH and LDH-H display impedance modulus at 0.01 Hz ($|Z|_{0.01}$) of about 10^5 Ωcm^2 after 1 h of immersion in the electrolyte. These layers do not show long-time stability: a decrease of $10^{4.5}\Omega cm^2$ in $|Z|_{0.01}$ was observed after 168h of immersion. The sealing effect is mainly observable, thanks to the |Z| increase in the middle-high frequency range (it is the case) which

can be attributed to an enhancement of the protection ability of the porous layer (which is sealed).

Modified Ce containing LDHs after various time intervals of immersion (from 1h to 1200 h) is shown in Figure 97 (including an enlarged version of the low-frequency impedance modulus in Figure 97b and 97d). Initially, Ce modified LDH, in both cases, has shown almost the same $|Z|_{0.01}$ value ~ $10^{6.5}$ Ωcm^2 after 1 h of immersion. It is observed that the $|Z|_{0.01}$ value reduced more rapidly from 1 to 72 h probably due to the upper porous LDH layer, but at a later stage, a slower reduction rate is observed. On later immersion stages, CeLDH shows a lower decreasing rate of the low-frequency impedance compared to the CeLDH-H sample. The $|Z|_{0.01}$ value of CeLDHs reduced from $10^{6.5}$ to about 10^5 Ωcm^2 after 1200 hrs, while in the case of CeLDH-H, it reduced from $10^{6.5}$ to about $10^{4.5}$ Ωcm^2. This finding suggests higher stability of the CeLDH structure against the corrosive solution compared to the CeLDH-H.

To better compare the investigated samples, the $|Z|_{0.01}$ values of modified and unmodified LDHs as a function of immersion time are shown in Figure 98. The $|Z|_{0.01}$ values of CeLDH are much higher than other developed LDH films throughout the whole immersion period. Moreover, a decrease in the declining rate is observed on exposure with long-term corrosive solutions. At the early stage of the corrosion mechanism, a relatively rapid decrease from $10^{6.5}$ to about $10^{5.5}$ Ωcm^2 was observed for CeLDH, while the decline rate was more severe for CeLDH-H, from $10^{6.5}$ to about $10^{5.2}$ Ωcm^2. On the second stage of the exposure (after about 200 h), a slower degradation process was observed for the CeLDH and CeLDH-H samples. These findings suggest that regardless of the difference between the Ce containing LDH coatings, the presence of Ce in the coatings improves the initial protection properties as well as and the durability upon prolonged immersion in the electrolyte. This effect is believed to be related to the

LDH development inside the anodic film layers and the active role of cerium in providing a sort of healing effect thanks to its recognized effect as a corrosion inhibitor.

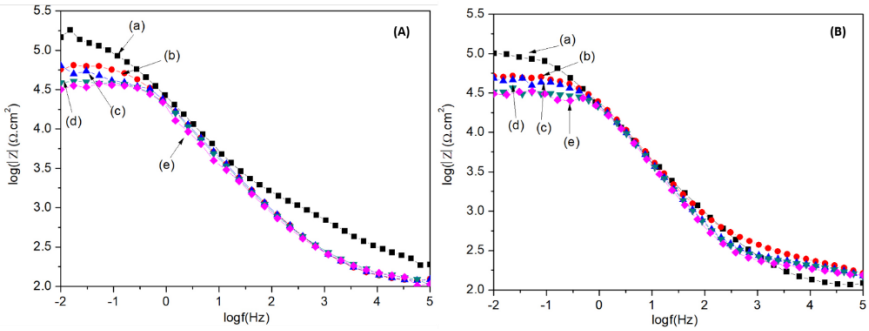

Figure 96. Impedance modulus plots; LDH (A), LDH-H (B) for various immersion times; (a) 1h, (b) 24 h, (c) 72h, (d)120 h, (e) 168h.

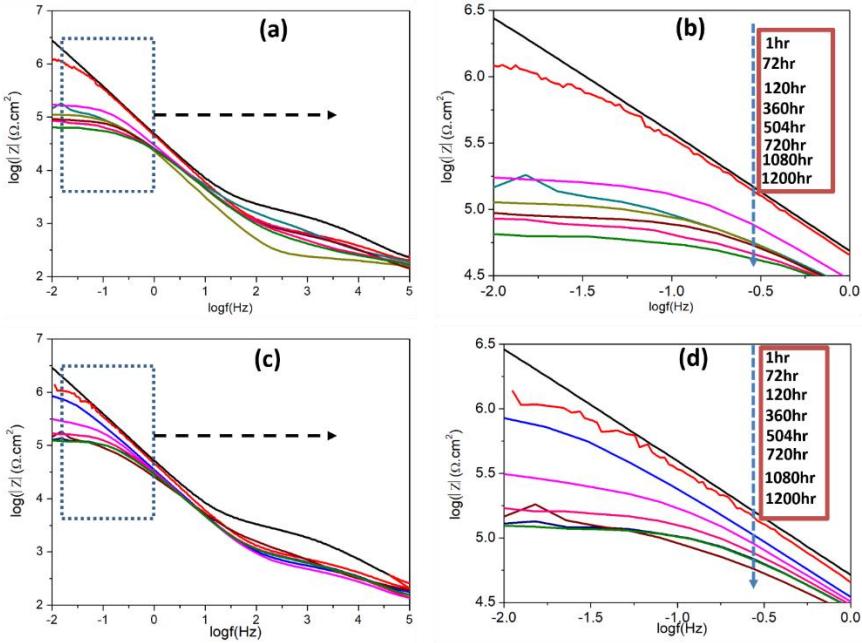

Figure 97. Impedance modulus plots of (a, b) CeLDH, (c, d) CeLDH-H with respective enlarge images for clear depiction at various immersion times, from 1h to 1200 h.

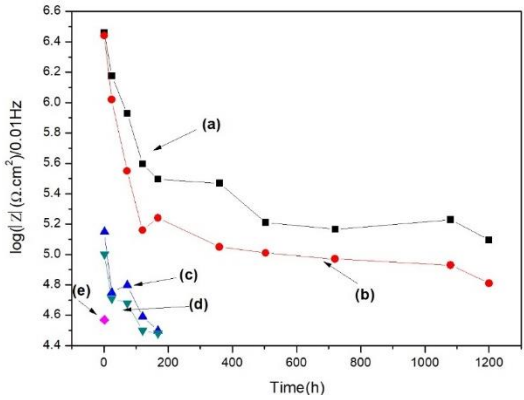

Figure 98. Impedance modulus at 0.01 Hz at various immersion times, (a) CeLDH, (b) CeLDH-H, (c) LDH, (d) LDH-H. (e) anodic AA6082

To further analyze the properties of the developed thin films containing Ce, the EIS data were fitting by using the “ZSimpwin” software [207]. Two different circuits were employed to investigate the EIS experimental data set. At an early stage of immersion (1-120 h), two times constant were observed: one located in the high-frequency range (around 10^4 Hz) and the other in the low-frequency range (around 10^{-1} Hz). According to the literature, it seems quite well established that the former can be associated with the response of the porous anodic oxide / LDH layer covering the metal [208][212][213][214][215][216]. Conversely, the attribution of the latter is not univocal and different interpretations can be found in the literature. Hoar and Wood [214] and, later, Mansfeld and Kendig [215] ascribed the middle-low frequency time constant to the properties of the barrier layer between the bottom of the pores and the metal oxide. Similarly, Huang et al. [210,211] interpreted the middle-low frequency relaxation process as the contribution of the inner barrier layer of the anodic oxide. On the other hand, Zhu et al. [209] described the low-frequency loop as the superimposition of the contribution of the inner barrier oxide and the charge transfer process: a polarization resistance and a constant phase element (CPE) to account for the electrical double layer and barrier layer where use to fit the relaxation process. Similarly, Usman *et al* [208] associated the low-frequency time constant to the charge transfer processes related to the barrier layer and, for prolonged immersion time, to the corrosion of the substrate. For the sample under investigation, at the beginning of the immersion the $|Z|_{0.01}$ value is relatively high, thus suggesting that the low-frequency response can be attributed to the superimposition of the contribution of the inner barrier oxide and the charge transfer process. A contribution associated with the corrosion process will be introduced for longer immersion time. A similar approach has been employed by other authors [216].

The circuit depicted in Figure 99a was employed to fit the EIS data set at an early stage of immersion (1-120 h): R_s stands for the electrolyte resistance; R_{LDH} and CPE_{LDH} refer to the conductive paths and the dielectric properties of the porous anodization layer+LDH coating, respectively; R_b accounts for the resistance of the barrier oxide, while CPE_b refers to the dielectric response of the electrical double layer and barrier layer [209].

Constant phase element (CPE) was employed instead of pure capacitances, according to the general expression i.e. $Z_{CPE} = 1/(Q(\omega j)^{\alpha}$. CPEs are recognized to be a flexible fitting parameter to account for capacitance distributions originated from surface roughness and heterogeneities, electrode porosity, variation of the coating composition, non-uniform potential, and current distribution [128].

a

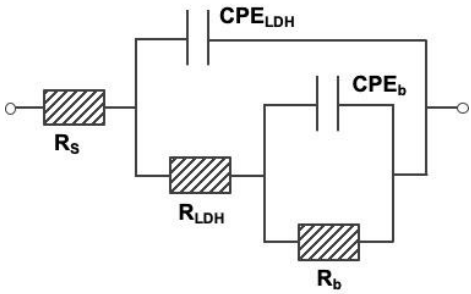

b

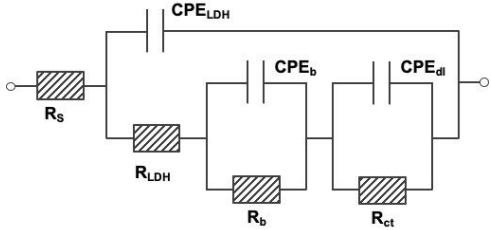

Figure 99. Electrical equivalent circuits employed to fi the EIS experimental data set: (a) at the early stage of immersion (1-120 h) and (b) for prolonged immersion (168-1200 h) in 0.1M NaCl

In the second stage of immersion (168-1200 h), the phase peak in the low-frequency range is no more symmetrical and cannot be properly fitted employing the e.e.c. depicted in Figure 99a. Furthermore, a significant decrease of the impedance modulus in the low-frequency domain is observed (see Figure 98). According to other authors [216] from 168 h of immersion in the saline solution, a contribution of the corrosion process is introduced in the e.e.c. employed to fit the experimental EIS data set (Figure 99b). Notice that an additional time constant to account for the Faradic process is introduced. In particular: R_s stands for the electrolyte resistance; R_{LDH} and CPE_{LDH} refer to the conductive paths and the dielectric properties of the porous anodization layer+LDH coating, respectively; R_b accounts for the resistance of the barrier oxide, while CPE_b refers to its dielectric response; R_{ct} stands for the charge transfer resistance while CPE_{dl} refers to the dielectric response of the double-layer capacitance. The parameter obtained utilizing the fitting of the raw EIS data is reported in Tables 26 and 27.

Table 26. Results of the EIS fittings of CeLDH

	Q_{LDH} Ω^{-1} cm^{-2} s$^{\alpha}$	R_{LDH} cm^2	α_{LDH}	Q_b Ω^{-1} cm^{-2} s$^{\alpha}$	R_b Ω cm^2	α_{dl}	Q_{dl} Ω^{-1} cm^{-2} s$^{\alpha}$	R_{ct} Ω cm^2	α_{dl}
1	3.7×10^{-6}	4.3×10^{3}	0.82	6.1×10^{-6}	2.2×10^{7}	0.78	-	-	-
24	3.5×10^{-6}	1.9×10^{2}	0.86	6.9×10^{-5}	2.0×10^{7}	0.89	-	-	-
72	7.4×10^{-6}	4.4×10^{2}	0.78	6.9×10^{-5}	3.6×10^{6}	0.71	-	-	-
120	2.2×10^{-6}	5.6×10^{2}	0.67	5.8×10^{-6}	9.2×10^{5}	0.78	-	-	-
168	3.9×10^{-6}	3.0×10^{2}	0.77	5.9×10^{-6}	2.0×10^{6}	0.88	6.1×10^{-6}	8.7×10^{8}	0.74
360	2.5×10^{-4}	6.9×10^{2}	0.84	8.2×10^{-6}	6.0×10^{6}	0.66	6.5×10^{-6}	7.4×10^{8}	0.77
720	3.7×10^{-7}	4.9×10^{2}	0.81	3.4×10^{-6}	4.7×10^{5}	0.69	6.8×10^{-6}	5.2×10^{7}	0.79
1080	7.2×10^{-8}	3.4×10^{2}	0.79	8.7×10^{-6}	1.2×10^{5}	0.77	3.6×10^{-6}	3.9×10^{7}	0.69
1200	1.2×10^{-7}	8.3×10^{1}	0.78	4.5×10^{-6}	3.8×10^{5}	0.67	3.9×10^{-6}	7.5×10^{7}	0.71

Table 27. Results of the EIS fittings of CeLDH-H.

	Q_{LDH} Ω^{-1} cm^{-2} s^{α}	R_{LDH} cm^2	α_{LDH}	Q_b Ω^{-1} cm^{-2} s^{α}	R_b Ω cm^2	α_{dl}	Q_{dl} Ω^{-1} cm^{-2} s^{α}	R_{ct} Ω cm^2	α_{dl}
1	1.5×10^{-7}	1.3×10^{3}	0.82	5.7×10^{-6}	1.5×10^{6}	0.78	-	-	-
3	5.6×10^{-8}	8.1×10^{2}	0.82	5.4×10^{-6}	5.4×10^{6}	0.87	-	-	-
5	$4.l\times10^{-6}$	7.8×10^{2}	0.84	2.7×10^{-8}	4.4×10^{5}	0.85	-	-	-
24	2.6×10^{-6}	7.4×10^{2}	0.64	4.2×10^{-6}	5.5×10^{4}	0.89	-	-	-
72	7.4×10^{-6}	4.4×10^{1}	0.84	6.9×10^{-5}	4.6×10^{4}	0.71			
120	2.4×10^{-7}	5.4×10^{1}	0.88	4.1×10^{-6}	1.1×10^{5}	0.78			
168	3.7×10^{-7}	3.0×10^{1}	0.76	1.8×10^{-6}	2.5×10^{5}	0.81	4.8×10^{-6}	8.8×10^{7}	0.88
360	7.2×10^{-7}	4.1×10^{2}	0.78	8.2×10^{-6}	9.7×10^{5}	0.89	6.1×10^{-6}	7.8×10^{7}	0.89
720	3.5×10^{-6}	6.1×10^{1}	0.58	3.4×10^{-6}	7.0×10^{5}	0.87	6.5×10^{-6}	4.7×10^{6}	0.78
1080	3.5×10^{-6}	7.9×10^{1}	0.57	8.7×10^{-6}	6.0×10^{3}	0.66	6.8×10^{-6}	5.8×10^{6}	0.79
1200	3.5×10^{-6}	4.3×10^{1}	0.77	4.5×10^{-6}	4.7×10^{3}	0.76	1.2×10^{-6}	6.3×10^{5}	0.77

As far as the fitting parameters related to the porous oxide / LDH layer are concerned (Q_{LDH}, R_{LDH}, α_{LDH}), notice that the resistances of the porous layer are lower than the associated barrier layer resistance. This is following previous studies which explained this finding with the higher conduction in the sealed pores compared to the barrier layers [216]. The Q_{LDH} values are quite scattered, probably due to the permeable structure of the porous anodic layer as well as the LDH layer. The corresponding values of the exponent of the CPE, α_{LDH}, is in the 0.58-0.84 range during immersion time. This parameter is recognized to be dependent on the fractal nature of the surface (affected by roughness and porosity) [128], on the roughness of the interphase [217] as well as on heterogeneities of the electrode surface [218]. Within this framework, the obtained data suggest a quite significant evolution of the surface roughness and porosity of the porous anodic oxide / LDH layer during immersion time. Partial dissolution of the porous anodic oxide and precipitation of insoluble compounds over the surface of the electrodes are likely to occur and would explain the α_{LDH} values. The surface conditions of the electrodes after the immersion will be investigated at the end of this section to furtherly support this hypothesis. On the other hand, given such values of α_{LDH}, Q_{LDH} cannot be clearly ascribed to a specific physical property. Q_{LDH} is believed to account for the dielectric properties of the porous anodic oxide / LDH layer but a more defined description is not possible.

On the other hand, R_b values, suggesting the barrier properties of dense and porous layers, have shown significant resistance values and demonstrate improved barrier properties for CeLDH compared to the CeLDH-H. It can also be seen that R_b values for CeLDH shown a decrease from 2.2×10^7 and 1.5×10^6 to 3.8×10^5 and 4.7×10^3 for CeLDH and CeLDH-H respectively, with the immersion of 1 hr to 1200 hr in NaCl solution. This attributed to the significant stability of CeLDH after 1200 hrs. *R*ct, which is inversely proportional to corrosion rate, is a parameter representing the resistance of the electron transfer across the metal surface [219].

The higher *R*ct is, the more difficult is the corrosion reaction, hence the lower is the corrosion rate [207]. The obtained findings are in good agreement with the EIS results, which further proves the corrosion resistance performance of CeLDH. XRD the investigated samples after 1200 h of immersion in the electrolyte have been collected to determine the different species developed on the surface. XRD diffraction parameters of CeLDH and CeLDH-H after 1200 hrs of immersions are shown in Figure 100. The X-ray diffraction measurements after contact with 0.1M NaCl solution leads to similar characteristics peaks of LDHs with similar pattern with some additional peaks around 2 theta values of 28.6°, 33.5°, 48°, and 56.2° which depicted the formation of CeO_2 and $Ce(OH)_3$. The low intense cerium oxide/hydroxide peaks confirm the release of Ce from the LDH structure and the consequent precipitation over cathodic sites upon reaction with OH^- species. This mechanism is believed to be responsible for the anticorrosion properties of LDHs due to the inhibition of the cathodic reaction provided by the precipitated compounds (mixed cerium oxide/hydroxides). Matter et al [220] previously investigated the cerium inhibition effect and reported that Ce(III) attributes better inhibitive ability than Ce(IV) and thus Ce(III) addition on the LDHs may be subjected to self-healing properties by the formation of $Ce(OH)_3/CeO_2$ on protective film degradation. The inhibiting ability of cerium salts is already well reported in various works, where the inhibiting mechanism involved the impediment of the cathodic oxygen reduction reaction due to the formation of cerium hydroxides/oxides [221][222][223]. The SEM images of CeLDH after treatment with 0.1M NaCl solution after 360, 720, and 1200 hrs is shown in Figure 101, where results indicated the good intactness and stability of the structure after 360 hrs of immersion and similarly after 720 hrs of immersion, with the initialization of accumulation/defects of corrosive species can be observed that describe the effectiveness of LDH structure to restrain the dissolution of LDH

structure. However, after 1200 h of immersion, the destruction of regular platelet structure can be seen and result in an expansion of platelet structure with accumulating of adsorbed corrosive species on the surface. However, XRD analysis confirms the intactness of LDH geometry after 1200 h immersion on 0.1M NaCl solution. The observation of LDH geometry is well correlated with the EIS findings.

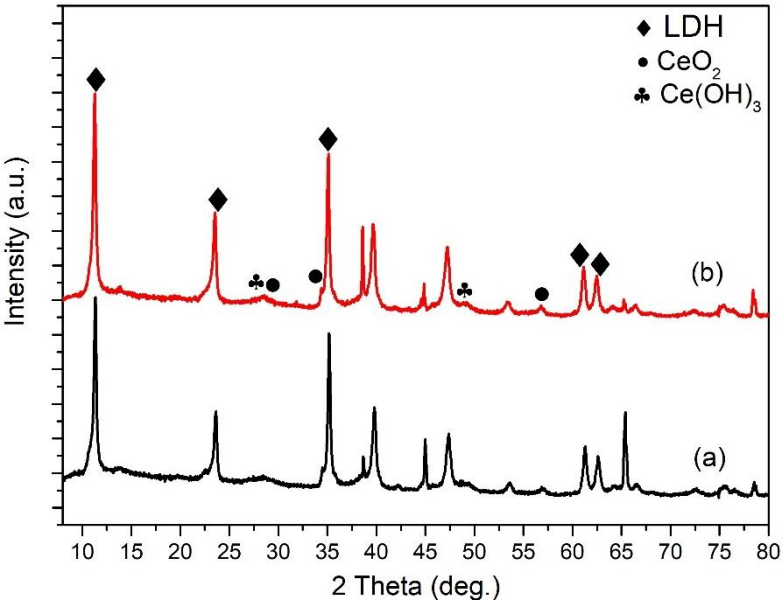

Figure 100. XRD patterns after 1200 hrs immersion in 0.1M NaCl solution, (a) CeLDH-H, (b) Ce-LDH.

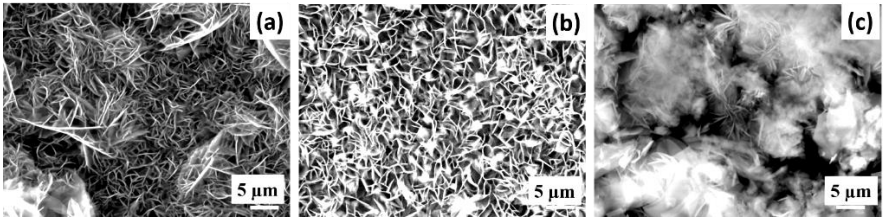

Figure 101. SEM images after (a) 360 hrs of immersion, (b)720 hrs of immersion, (c) 1200 hrs of immersion in 0.1M NaCl solution.

6.1.4. Conclusion

Ce-based MgAl-LDH conversion films were developed by a single-step in-situ growth method on the anodized AA6082 surface. The sealing effect of CeMgAl-LDHs precursors on the anodized porous network and corresponding barrier effect in terms of long-term corrosion resistance behavior and structural evaluation is discussed. The introduction of cerium directly on the anodized porous network (CeLDH) has shown improved corrosion resistance properties, compared to the CeLDH-H which were grown on a “Hot water-sealed” anodized surface. The findings demonstrated that CeLDH provided comparatively better active and passive corrosion protection than other developed specimens. The evaluation of coating parameters defined the corrosion mechanism for LDHs and their behavior on long-term stability against corrosive species. The CeLDH was found intact after 360 hrs of immersion and slightly corroded after 760 hrs of immersion and provided stable longer period protection (1200 hrs) for the underlying AA6082 substrate. Ce oxides/hydroxides were found on the LDH surface after prolonged exposure to the chloride solution. This finding suggested the capability of the film to release cerium cations to the environment and their capability to precipitate in correspondence of the cathodic sites upon reaction with OH^- species. The CeLDH

developed directly on the porous anodic film can be potentially used for further functionalization for the enhanced protection of aluminum alloys.

6.2. Double doped Cerium-based Superhydrophobic Layered double hydroxide Protective films grown on the anodic aluminum surface

6.2.1. Synthesis of CeMgAl-LDH on anodized AA6082

Based on our previous work, CeMgAl-LDH was developed directly on the AA6082 anodized surface [224]. Initially, the surface anodization was performed using 0.1M H_2SO_4 electrolyte at 14V constant voltage for 30 minutes, where a stainless-steel plate was used as cathode and aluminum specimens as the working anode. After anodization, the specimen was dipped in 0.01M $Mg(NO_3)_2.6H_2O$, 0.001 $CeNO_3$, and 0.06 M NH_4NO_3 mixture solution (pH≈10) at 80°C for 18 hr. The obtained CeMgAl-LDH were washed with distilled water and dried at room temperature.

6.2.2. Modification of CeMgAl-LDH

PFDTS solution was prepared by adding 0.1 g PFDTS in 200 mL ethanol by continuous stirring at 40°C for 1 hr. To obtain a superhydrophobic LDH film, the CeMgAl-LDH specimen was dipped in the above solution for 2 hrs at 40°C. The specimen was then dried in the furnace for 30 min at 60°C. The obtained specimen is referred to as S-CeMgAl-LDH for simplicity. Figure 102 describes the general representation of the layered structure and behavior towards the water droplet.

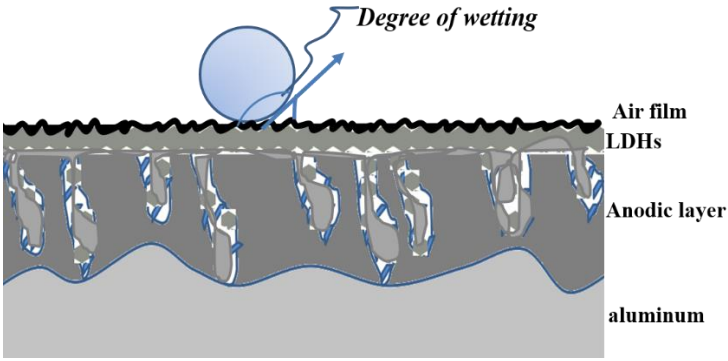

Figure 102. Contact angle diagram and general contact angle measurement representation of S-CeMgAl-LDH.

6.2.3. Results and Discussion

Figure 103 exhibited the XRD spectra of CeMgAl-LDH before and after modification with PFDTS. The XRD patterns of MgAl-LDH and CeMgAl-LDH described the characteristics peaks of LDH at 11.8°, 23°, and 30° which correspond to “003”, “006” and “009” diffraction planes[224]. The basal spacing of the “003” reflection peak corresponds to 0.76 nm, which corresponds to the LDHs network with interlayer carbonate anions [100]. It is found that the incorporation of cerium ions in the LDH network did not make any dominant difference in LDH characteristics peaks, which confirms the possible incorporation of cerium ions inside the LDH network in the amorphous form. Cerium oxides/hydroxides were found to form on the LDH surface after prolonged exposure to the chloride solution. This finding suggested the capability of the film to release cerium cations to the environment (upon disruption of the LDH film) and their capability to re-precipitate in correspondence of the cathodic sites [224]. The higher pH causes the hydrolysis of Ce^{3+}, and this can promote the precipitation of $Ce(OH)_3$ on the anodized surface. The partial oxidation of Ce^{3+} to

Ce^{4+} and can form mixed-species containing CeO_2, $Ce(OH)_4$ depending on the pH of the surrounding solution [205]. Thus, cerium participates in two ways, initially during the sealing process and further diffusion of cerium inside LDH layers in the amorphous form [201]. After modification with PFDTS, the “003” plane peak shifted toward a lower angle, thus suggesting the successful intercalation of PFDTS groups inside the LDH layer indicated the basal spacing of 0.89 nm. The gallery height and corresponding d-spacing are expected for PFDTS anions arranges within LDHs interlayers and suggested that long-chain fluoroalkyl functionalized Mg/Al LDHs were obtained [225]. The general chemical reaction is represented in equation (1-3). The measure cell parameters calculated from XRD patterns are shown in Table 28.

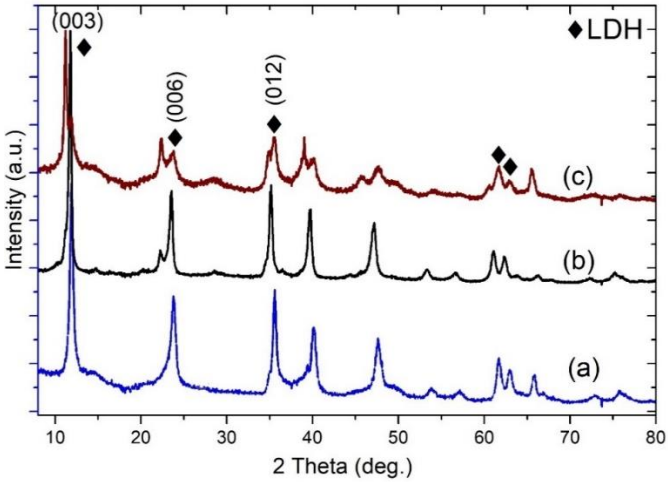

Figure 103. XRD patterns of LDHs films (a) MgAl-LDH, (b) CeMgAl-LDH, (c) S-CeMgAl-LDH.

$$MgAl(OH)_x(CO)_3LDH.H_2O \rightarrow MgAl(OH)_x(CO)_3LDH + 3H_2O$$
(1)

$$CF_3(CF_2)_9CH_2CH_2SiCl_3 \rightarrow CF_3(CF_2)_9CH_2CH_2Si(O^-)_3 + 3H^+$$
(2)

$$MgAl(OH)_x(CO)_3LDH + CF_3(CF_2)_9CH_2CH_2Si(O^-)_3 \rightarrow MgAl(CF_3(CF_2)_9CH_2CH_2Si(O^-)_3) - LDH$$
(3)

Table 28. Cell parameters before and after the modification of LDHs.

	(003)		(006)		(009)		(110)	
specimens	2 theta(°)	d(nm)	2 theta	d(nm)	2 theta (°)	d(nm)	2 theta (°)	d(nm)
MgAl-LDH	11.75	0751	23.58	0.377	35.26	0.252	61.2	0.150
MgAlCeLDH	11.76	0.752	23.56	0.377	35.24	0.254	61.1	0.151
SMgAlCeLDH	11.21	0.788	23.70	0.375	35.22	0.255	61.0	0.152

The top view images collected by SEM are shown in Figure 104, where a well-developed platelet structure of CeMgAl-LDH perpendicular to the substrate can be seen, which covers the entire substrate with the thickness of ~32±3.5 µm. The obtained curvy nest-like structure is in agreement with the previous studies[224]. After immersion with PFDTS, the specimen is transformed into a packed flower-like structure, where the distortion of the curvy platelet structure can be seen. The introduction of PFDTS groups inside LDH interlayers caused stresses in the geometry which results in the disorder in the curvy platelet structure and arranged in a packed flower-like structure. Figure 105 shows the SEM images of cross-sectional S-CeMgAl-LDH. The two-layer structure is formed, while it is reported that anodic film starts dissolving on contact with the LDH precursors and finally result in the formation of LDH film in/on the anodic film and formed a compact

structure. A good surface adhesion and LDH orientation can be seen in Figure 105.

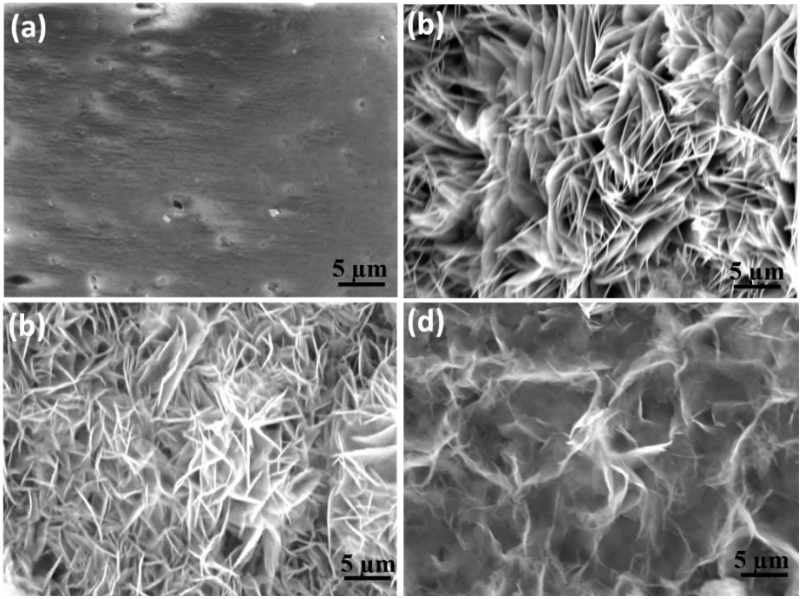

Figure 104. SEM images, (a) anodic AA6082 specimen, (b) MgAl-LDH, (c) CeMgAl-LDH, (d) S-CeMgAl-LDH.

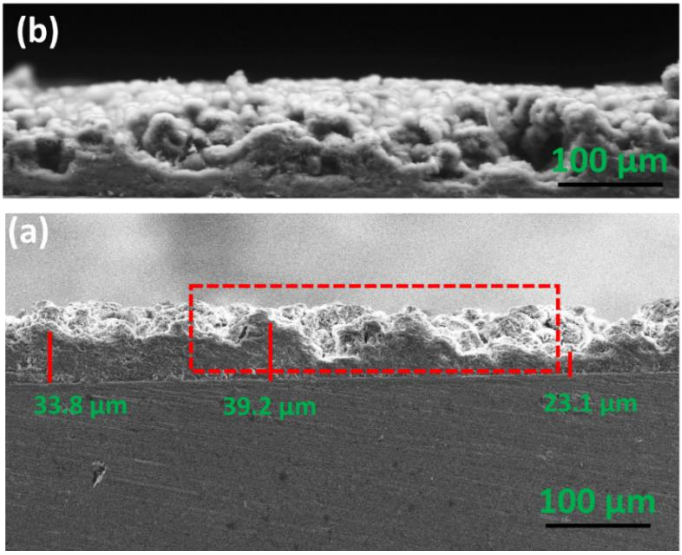

Figure 105. Cross-sectional analysis of S-CeMgAl-LDH.

The LDHs surface modification to superhydrophobic results in effective repellence of water due to lower surface energy. The modified LDHs fall into the Cassie-Baxter regime, where the interaction of water droplet is Liquid/air/solid interaction due to the presence of trapped air layer within the textured surface and this causes the substantial increase of contact angle [226]. Figure 106 shows the water drop contact with the anodized aluminum substrate, CeMgAlLDH, and S-CeMgAlLDH based LDHs. Unmodified LDHs exhibit pure hydrophilic characteristics, as the water contact angle of around 20° indicates, confirmed by the water drop spreading on the surface. On the other hand, PFDTS modified LDHs exhibited almost spherical droplets, corresponding to a water contact angle of around 156° which was attributed to the superhydrophobic groups of the molecules.

To understand the repellent nature of modified LDH against different household liquids, CA measurement was made to evaluate the potential applicability of the coatings. The digital images of coffee, cola, water, and basic solution (1M NaOH) and acidic solution on the PFDTS modified LDHs are shown in Figure 107. Mentioned liquids stood on the LDHs surface and have shown near sphere drop structure exhibiting the good repellency of film against the liquids. Furthermore, the chemical stability of contact with the basic and acidic solution is also investigated. As is shown in Figure 107 (a-f), the water, basic solution, and light acid solution (pH 4), coffee, tea, and cola existed on the S-CeMgAl-LDH surface with a near-spherical shape, while acid droplet spread with a relatively smaller contact angle on the surface. The findings describe the well superhydrophobic nature and its sustainability on interaction with various liquids media. Self-cleaning is another property for coating applicability for potential environmental applications. The self-cleaning properties of the PFDTS modified LDHs were estimated by using the graphite powder as a contamination source, as shown in Figure 108. Initially, the graphite water suspension was used to evaluate the self-cleaning properties and record the digital images. Graphite suspension rolled away from the film surface without any trace and exhibit well repellency against contamination, Figure (108 a-c). Further, graphite powder was deliberately positioned on the modified LDH surface and was washed simply with water drops. The water drops rolled away and take away the graphite powder and without any graphite trace, the initial white film remains. Likewise, the muddy water readily rolled away from the coating without traces (Figure 108(d-f)), indicating that the coating displayed a good self-cleaning property. The self-cleaning characteristics are related to the lower surface energy of LDH after PFDTS modification, where adhesion between the surface and graphite contamination is the very week that did not allow the contaminations to stick on the LDH surface. As a result,

contamination can be easily removed from the surface by water droplets. These observations allow us to conclude that a developed superhydrophobic surface can protect the surface from pollution/contaminations for practical applications. Furthermore, to understand the durability of the developed coatings against sunlight, the water contact angles were measured during 30 days of exposure to UV lamps (λ = 310 nm). The UV blocking properties of LDHs are well-studied phenomena, *Wang. G et al* reported the excellent UV aging resistance of ZnAl-LDH in addition to asphalt to highlight the potential applications of LDHs as an additive for coating systems prone to UV aging. UV shielding properties depend upon the LDHs layer composition and particle size distribution [227]. Herein, the UV test aims to assess the effect of UV light on the superhydrophobic properties of the coatings. The findings demonstrated the stability of the LDH films against UV irradiation, indicating significant resistance to UV irradiation. After 30 days of exposure to UV light, a very slight reduction (~1°) in CA is observed (Figure 109). The LDHs UV blocking resistance is possibly due to the following reasons: (a) shielding effect of the LDH layers, (b) UV absorption by interlayer anions, [228][229]. It is found that LDHs with various intercalated anions can contribute to improving the polymeric/organic materials to resist UV aging without affecting the thermal photostability. Furthermore, the LDH improves the oxygen barrier properties which can inhibit the thermal aging and UV aging processes, since oxygen and free radicals are one of the main paraments affecting the aging processes. Furthermore, LDHs particle size distribution and layered composition also have an influential effect on the UV aging properties as explained by Mie scattering theory and density functional theory calculations [227][230]. S-CeMgAl-LDH has shown excellent UV radiation resistance, compared to the literature studies [231][232].

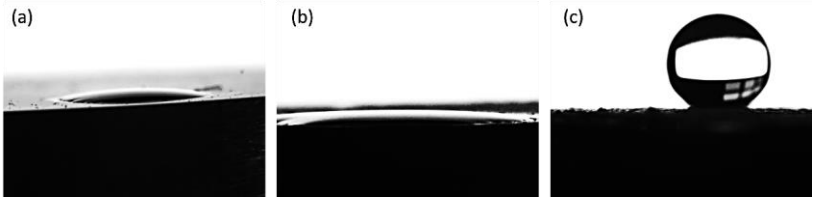

Figure 106. Digital photos and contact angle images of water on different surfaces, (a) anodic film, (b) CeMgAl-LDH, (c) S-CeMgAl-LDH.

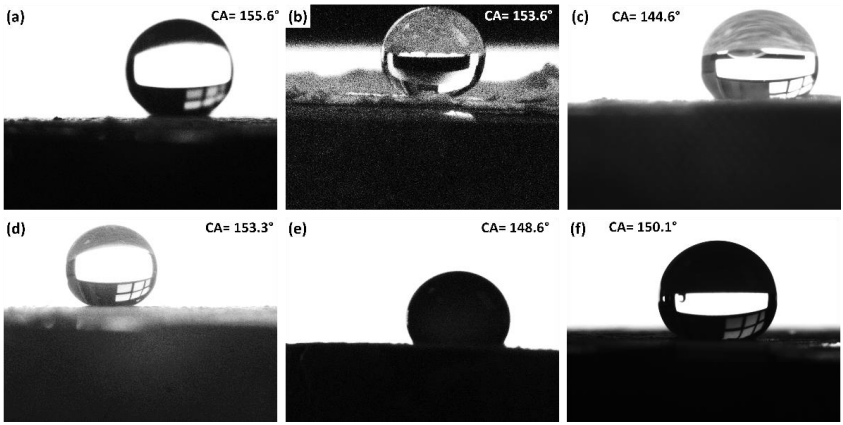

Figure 107. Contact angle images of different solution on contact with S-CeMgAl-LDH, (a) water, (b) 0.1M NaOH, (c) acidic solution (pH ~4), (d) tea, (e) coffee, (f) cola.

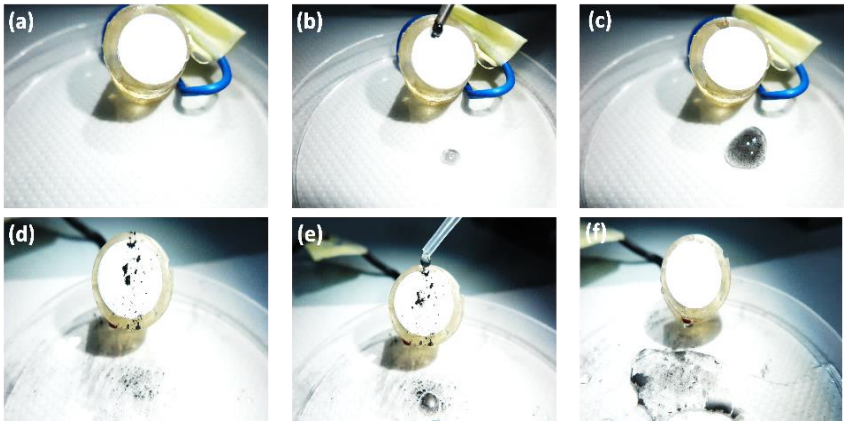

Figure 108. Self-cleaning properties of S-CeMgAl-LDH, (a) original coating, (b) graphite water roll away from the film, (c) clear film after the exposure with the graphite-water system, (d) graphite powder on the film, (e) graphite powder taken away by water droplets.

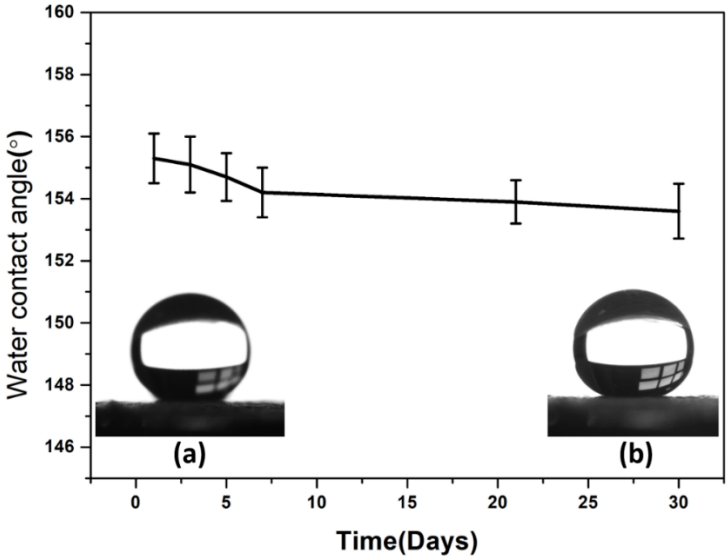

Figure 109. Contact angle measurement on exposure with UV radiations as a function of exposure time; (a) Digital image after 1 day, (b) 30 days.

The corrosion resistance properties of the LDHs before and after PFDTS modification was evaluated by long term EIS measurement in 0.1M NaCl. EIS spectra of all developed samples after 1 h of immersion are represented in Figure 110. For general comparison among different developed LDH films, the impedance modulus at 0.01Hz can be used as a rough estimation of the stability and corrosion resistance of LDHs [206]. The electrolyte has been selected in order to promote degradation of the LDH layer which allows us to compare the systematic inhibitive effect of PFDTS modified and only cerium modified LDH in the time scale investigated. Initially, the introduction of cerium ions in MgAl-LDH is found to effectively enhance the corrosion resistance properties. In our previous work, CeMgAl-LDH corrosion resistance behavior, possible protection mechanism, and long term EIS measurements are reported in detail[224]. The introduction of cerium in LDHs have shown improved corrosion resistance

properties, better active and passive corrosion protection and long-term stability against corrosive species. The significantly enhanced corrosion resistance of cerium based LDHs can be explained by the following; (i) the passive protection of compact LDH layer, (ii) the presence of cerium in the LDH frame, which was found to protect by its inhibition action by dissolving from the LDHs structure, entering the solution and precipitating at the cathodic sites. The modification of CeMgAl-LDH with PFDTS was found to furtherly increase the low-frequency modulus considerably. It is worthy to note that the low-frequency modulus of PFDTS modified LDH is nearly 1.5 orders higher than CeMgAl-LDH and 3 orders higher than virgin MgAl-LDH. The time constant in the high-medium frequency range corresponds to LDH outer porous network contribution, while the time constant in the medium frequency range exhibit the LDH inner barrier layer contribution in corrosion resistance properties, while the time constant in the low-frequency range accounts for the faradic process at the LDH/substrate interface. At the high-frequency range, PFDTS modified CeMgAl-LDH has shown a 40° larger phase angle than CeMgAl-LDH, while 70° higher than virgin MgAl-LDH, which demonstrated the superior characteristic of S-CeMgAl-LDH. S-CeMgAl-LDHs after various time intervals of immersion (from 1h to 1200 h) are shown in Figure 111. It is observed that impedance modulus in the low-frequency range has shown a gradual decline from 1 to 1200 h. The $|Z|_{0.01}$ value of S-CeMgAl-LDH reduced from 10^{8} to about $10^{6.4}$ Ωcm^2 after 1200 hrs, and in the case of cerium based LDH, it reduced from $10^{6.5}$ to about $10^{5.2}$ Ωcm^2, while the decline rate was much higher for MgAl-LDH, where a rapid decline from $10^{5.3}$ to $10^{4.5}$ ($\Omega.cm^2$) was monitored only after 168 hrs of immersion. The findings describe the higher stability of S-CeMgAl-LDH. The $|Z|_{0.01}$ values of modified and unmodified LDHs as a function of immersion time are shown in Figure 112. The $|Z|_{0.01}$ values of PFDTS modified CeMgAl-LDH are much higher than other developed LDH films

throughout the whole immersion period. Moreover, the declining rate of $|Z|_{0.01}$ of S-CeMgAl-LDH is much slower on exposure with corrosive solutions and depicted a much lower $|Z|_{0.01}$ decreasing rate (~0.6 order) after 168 hrs of immersion in 0.1M NaCl solution. The same trend is observed throughout the immersion period till 1200 hrs. After 1200 hrs, PFDTS modified LDH has shown $|Z|_{0.01}$ of $10^{6.5}$ orders, compared to $10^{5.2}$ of CeMgAl-LDHs. That's values are still much higher than the anodic AA6082 film, where anodic film exhibited 4.6 ($\Omega.cm^2$) after 1 hr of immersion. This defined the performance of the dense network of PFDTS CeMgAl-LDH and the influence of cerium addition on the LDH stability. The lower degradation rate of S-CeMgAl-LDH verifying the low anion-exchange process with chlorides, and improved barrier properties which protect the underlying substrate. This long-term stability of the superhydrophobic surface can be ascribed to the presence of PFDTS, which are stretched outside the surface and highly efficient in long-term protection. Overall, different layers of LDH geometry provide a barrier against chloride attack to protect the underlying substrate. The first anodic layer sealed by LDH precursors along with precipitation of cerium hydroxide/oxides on it, the final upper air film between LDH film and corrosive solution, and between them, the presence of dense bilayer LDH network for active protection demonstrated compact system for corrosion protection. PFDTS intercalated LDHs repelled the permeation of water molecules and chlorides, which is a key important parameter of that work. S-CeMgAl-LDH has shown significantly superior corrosion resistance due to the following factors: (a) PFDTS introduction causes the lowering of surface energy and endorses superhydrophobic characteristics which enhanced the active protection for LDHs, (b) the presence of cerium in the LDH frame protect by its inhibition action through reducing the cathodic reaction rate on contact with corrosive media [224][233]. The strong passive and active protection found to develop

compactness and integrity of LDHs which is significant for delaying the corrosion process and is a powerful approach to enhance the anti-corrosion behavior. The SEM images of S-CeMgAl-LDH after different intervals of immersion in the 0.1M NaCl solution are shown in Figure 113. It is cleared that the LDHs structure remains intact after 1200 hrs of immersion, and besides of few LDH curvy plate distortions, no other dominant defects were observed. This is well correlated with the EIS long-term immersion results.

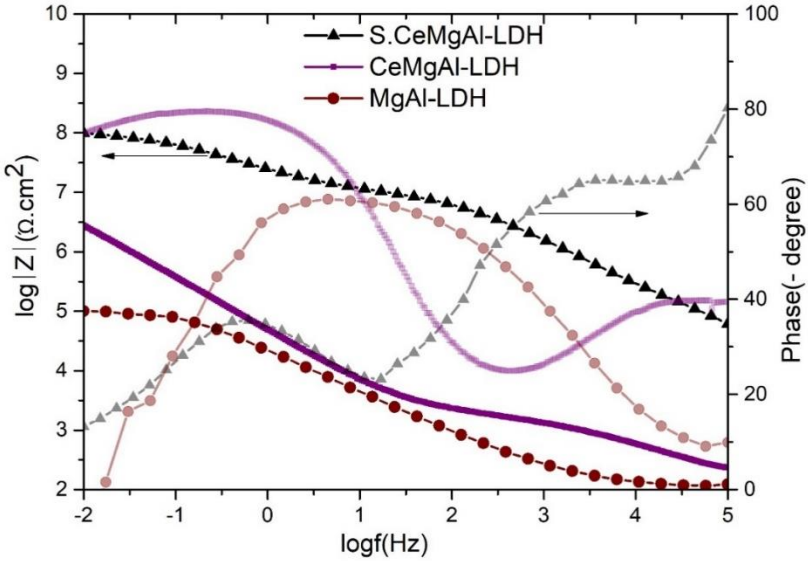

Figure 110. Bode plots of developed LDHs after 1 h immersion in 0.1M NaCl solution.

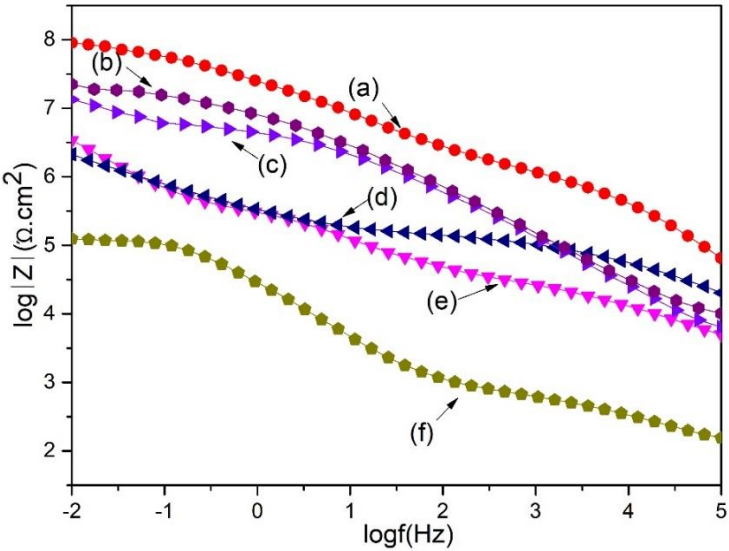

Figure 111. Bode plots of S-CeMgAl-LDH at various immersion times, (a)24 hrs, (b)168 hrs, (c) 504 hrs, (d) 720hrs, (e) 1200 hrs, (f) CeMgAl-LDH after 1200 hrs.

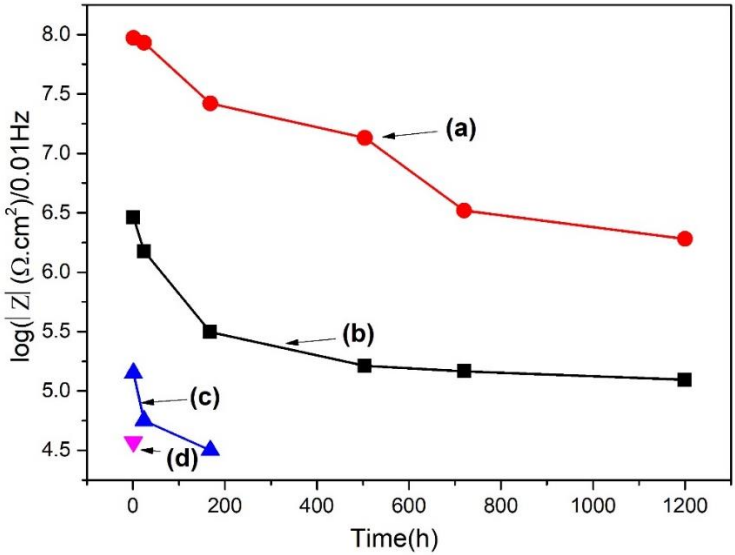

Figure 112. Impedance modulus at 0.01 Hz at various immersion times, (a) S-CeMgAl-LDH (b) CeMgAl-LDH, (c) MgAl-LDH, (d) anodic AA6082.

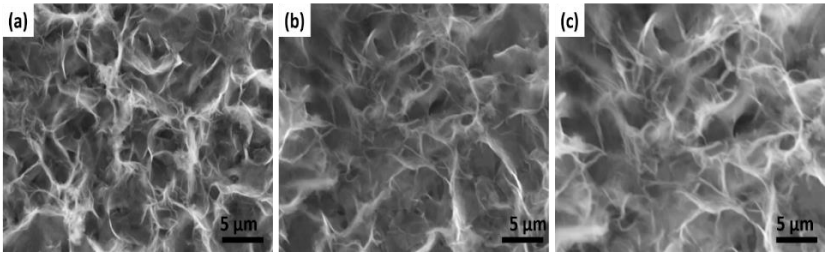

Figure 113. SEM images of S-CeMgAl-LDH after (a) 168 hrs of immersion, (b)720 hrs of immersion, (c) 1200 hrs of immersion in 0.1M NaCl solution.

6.2.4. Conclusion

The PFDTS loaded cerium doped LDHs were fabricated on the porous anodic AA6082 alloy to develop a protective, superhydrophobic, self-clean

multifunctional LDH system. Initially, the cerium modified MgAl-LDH were preferentially grown inside/on porous anodic film to enhance the passive protection of LDH based systems, and further PFDTS groups were intercalated inside LDH galleries through the ion-exchange mechanism to further enhance the corrosion resistance properties. The wettability of the S-CeMgAl-LDH hierarchical structure surface has shown WCA as high as 155.6°, strong UV shielding effect on superhydrophobic properties, and ~$10^{1.5}$ orders decline in $|Z|_{0.01}$ after 1200 hrs immersion in NaCl solution. The developed S-CeMgAl-LDH has exhibited also remarkable stability against common household solutions and has shown interesting long-term anticorrosion behavior.

7. Conclusion of the Thesis

The conclusive remarks have been exposed at the end of each section in the experimental section. However, in this section, an overall summary of the thesis is presented.

Synthesis and characterization of layered double hydroxides

Several LDHs layers were developed directly on the aluminum substrate, where the effect of synthetic conditions i.e. Reaction temperature, Aging time, pH, and initial salts concentrations are thoroughly discussed following the material's physical and electrochemical properties. Herein, Four different types of LDH classes are discussed in detail, including the development of Novel CaAl-LDHs, where different divalent cationic sources (Mg, Zn, Ni, Ca) were used to develop LDH directly on the aluminum (Al) where aluminum provide the source of Al^{3+}. Detailed characterization was done by using SEM-EDS, XRD, FTIR, TEM, and electrochemical properties were evaluated. The major findings of this section were as follows;

- All developed LDHs successfully promote corrosion resistance properties.
- The thickness of the LDHs film lies in the range of 10 to 35 µm and makes an influential impact on the corrosion resistance properties. Films thickness can be controlled with the effect of synthetic conditions.
- LDHs Ion-exchange with the aggressive solution to entrap the chlorides inside the LDHs interlayers and the barrier effect was found the main mechanism for the protection of aluminum alloys.
- Various surface morphologies have shown their distinct ion-exchange properties and barrier effect due to variation in structural compactness, film thickness, and film geometry which make an influence on the corrosion resistance properties.

- The film has shown a good adhesion with the substrate.
- $|Z|_{0.01}$ have shown an increment of 3-5 orders of magnitude in impedance modulus,
- Chloride ions were found in the interlayer's of the LDH samples, demonstrated the LDHs ion-exchange mechanism in contact with the aggressive solution.
- LDHs consist of two dominant layered structures, (a) upper porous layer, (b) bottom compact layer, which participates in defining the corrosion resistance properties.

Although LDHs have shown overall better corrosion resistance properties, a long-time immersion test has shown a rapid decline in impedance modulus of the designed protective system. This is generally due to the upper porous layer which allows direct contact of electrolyte inside the LDHs framework and provides a pathway for the corrosion reaction.

The developed LDHs corrosion resistance properties have shown the following order of impedance modulus; - MgAl-LDH, >ZnAl-LDH, > NiAl-LDH, >CaAl-LDH.

To overcome the long term stability issues, there is a need to modify the LDHs structural geometry to design a protective system with controlled long term corrosion resistance properties

Calcination of MgAl-LDHs

Further, the MgAl-LDHs were calcined from 50 to 250 °C to understand the high-temperature effect on coating structure and electrochemical properties.

- Calcination was found to decompose the interlayered anions inside the LDHs structure and also the decomposition of the hydroxyl group as confirmed by XRD, TGA-DSC analysis.

- The decomposition of anions inside the structure caused the system to be more positive, and also a contraction in basal spacing and compactness was observed.
- That property was found more influential to enhance the corrosion resistance properties of LDHs by taking the advantage of memory effect of LDHs, however, long-term stability in aggressive solutions was still compromising.

Modification of MgAl-LDHs

To overcome the stability issues, the following strategies were followed,

Graphene is introduced inside the framework of LDHs. The interaction of graphene with various surface morphologies of MgAl-LDHs is thoroughly investigated and their effect on anticorrosion resistance properties was concluded;

-

1. Graphene interaction with LDH is confirmed by SEM, FIB, XRD, FT-IR, RAMAN, EIS characterizations.
2. Graphene is found to interact with both LDH layers i.e. upper porous, and the bottom dense layer which is found to help in the sealing of LDH micropores.
3. A more compact LDH/substrate interface after graphene modification is obtained that can protect the metal dissolution against the corrosive species and provide better barrier properties.
4. Impedance modulus against 168 hrs of immersion period in 0.1M NaCl solution is reported, where a decrease of $10^{0.3}$ Ωcm^2 impedance modulus was observed after 168 hrs. This provides the ability of graphene for a considerable long-term protective system.
5. Graphene/LDHs have shown a hydrophobicity nature, which is also a variable to promote corrosion resistance properties.

Further, Two different strategies were employed to enhance the corrosion resistance properties, firstly the anodization of aluminum substrate, and secondly the development of rare eth based LDHs directly on the anodic structure, Cerium based Layered double hydroxide were introduced directly on the anodic aluminum substrate, where LDHs precursors were found to actively interact with the anodic films, sealed the micropores of the anodic film and also act as building blocks to develop LDHs directly on the anodic structure to provide barrier properties to overcome the challenging aspect of long term protection in section 1, and also provide active protection defined by the LDHs, while cerium ions incorporation provide self-healing capability and structure compactness and long term protection.

- The CeMgAl-LDH was found intact after 360 hrs of immersion and slightly corroded after 760 hrs of immersion and provided stable longer period protection (1200 hrs) for the underlying AA6082 substrate.
- Ce oxides/hydroxides were found on the LDH surface after prolonged exposure to the chloride solution. This finding suggested the capability of the film to release cerium cations to the environment and their capability to precipitate in correspondence of the cathodic sites upon reaction with OH^- species.
- The CeMgAl-LDH developed directly on the porous anodic film can be potentially used for further functionalization for the enhanced protection of aluminum alloys.
- Overall, this system proves to be effective in terms of structural durability, compactness, long-term protection, and adhesion with the substrate.

To endorse multifunctional properties, superhydrophobic, self-cleaning properties were achieved, and the effect of UV radiation exposure was discussed to understand the outdoor applications.

1H, 1H, 2H, 2H perfluorododecyl trichlorosilane were incorporated inside the cerium modified LDHs interlayers by taking the advantage of ion-exchange mechanism, where cerium ions and perfluorododecyl trichlorosilane were incorporated inside the LDHs framework, and their combined effect was discussed on structural and electrochemical properties.

- The self-healing capability, interaction with the aggressive solution, EIS long-term analysis, and detailed physical characterization were conducted.

- The wettability of double doped LDHs hierarchical structure surface have shown WCA as high as 155.6°, strong UV shielding effect on superhydrophobic properties, and ~$10^{1.5}$ orders decline in $|Z|_{0.01}$ after 1200 hrs immersion in NaCl solution., far better than cerium based LDHs and also demonstrated the properties for the efficient implementation of LDHs based system
- The developed modified CeMgAl-LDH has exhibited also remarkable stability against common household solutions and has shown interesting long-term anticorrosion behavior.

A general comparison of the corrosion resistance properties of various LDHs in this thesis and LDHs developed by other authors is compared in Table 29. The long-term stability against corrosive media and endorsement of multifunctional characteristics have made the LDHs an attractive class to utilize as an environmentally friendly coating system.

The synthesis procedures adopted in three different ways, considering the synthesis setupe view. In the starting work, development of MgAl-LDHs, and ZnAl-LDHs were perfomed in three bottle neck heating flash with controlled synthesis environment which found to provide higher corrosion resistance and comparatively better controlled synthesis of the LDHs. In the second approach, open synthetic conditions were adopted, by using a general heating flask so that can meet a more easy synthesis way in commercial synthesis point of view. This provided, however, relatively poor corrosion resistance properties but after modification with corrosion inhibitors this way provide significant corrosion resistance properties and more importantly a way better easy synthesis approach. CaAl-LDHs, NiAl-LDHs on the other side were developed at a higher temperature so thus Teflon lined autoclave was used to treat the solution at a temperature higher than 100 °C. The variation in synthesis approaches may have made an impact on the reproducibility of the LDHs thin films on the substrate in that thesis work, but the overall concept of different synthesis ways is helpful to decide which way is more compatible as per the decided criteria. A general comparison of the total resistance of Literature work and current work is made below. However, it must keep in mind that corrosive solution molarity, film thickness, and coating substrate have a significant influence on the final total resistance of the layered double hydroxide-based system and that parameters are influentially different in the Literature work.

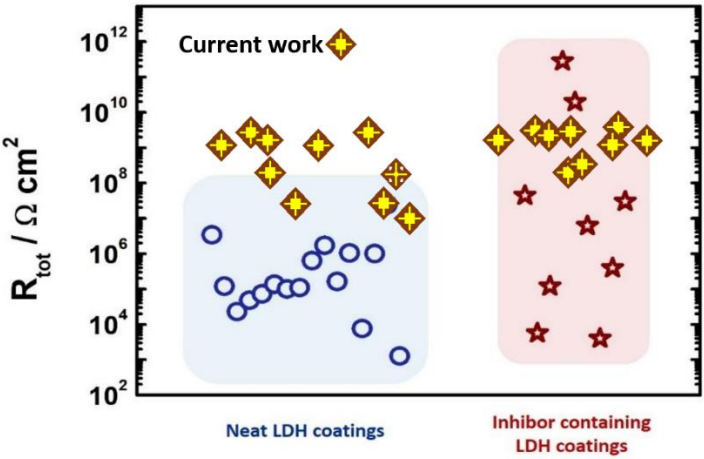

Figure. Comparison of the total resistance obtained from EIS spectra fitting for neat and inhibitor exchanged LDH coatings (Table 14), and current work.

Table 29. Summary of Layered double hydroxide-based systems developed on the aluminum alloys.

LDH	**Substrate**	**Potentiodynamic curves**			**Electrochemical impedance spectroscopy**				**Ref.**
		Electrolyte (NaCl)	i_{corr} sub. (A cm^{-2})	i_{corr} film (A cm^{-2})	Electrolyte (NaCl)	Immersion time (h)	R_{pol} (Ω.cm^2)	R_{coat} (Ω cm^2)	
$ZnAl-NO_3$	2024	--	--	--	0.05	~1000	10^5	--	[93]
$ZnAlV_2O_7$		--	--	--			10^6	2×10^3	
$MgAl-NO_3$	Pure Al	3.5 wt%	1.5×10^{-7}	1.95×10^{-8}	3.5 wt %	336	3.3×10^6	82	[95]
MgAl-8HQ				1.02×10^{-9}			44.3×10^6	128	
$MgAlNO_3$	6061	--			0.05M	10	9.3×10^7	9.0×10^5	[96]
$MgAl-C_6H_5COO$							3.7×10^9	5.2×10^7	
AN.ZnAl	2198	--			0.5M	--	1.0×10^6	6.1×10^2	[97]
$ZnAl-VO_3$							1.0×10^7	8.6×10^2	
$ZnAl-VO_3$							9.7×10^6	4.9×10^3	
PEO-ZnAlVOx	2024	--			0.5 wt %	72		47×10^3	[98]
PEO-$ZnAlNO_3$	2024				0.05M	336	1.8×10^7	2.3×10^4	[99]

PEOZnAlV Ox							--	3.3×10^{4}	
$MgAlNO_3$	6082	0.1 M	7.5×10^{-6}	8.3×10^{-10}	0.1 M	--	--	--	[113]
$MgAlNO_3$	6082	0.1 M	7.5×10^{-6}	1.9×10^{-11}	0.1 M	1	--	4.2×10^{9}	[234]
$MgAlNO_3$				6.3×10^{-10}			3.8×10^{8}	2.3×10^{8}	
$MgAlNO_3$	6082					168	7.8×10^{3}	3.5×10^{5}	[113]
$CaAlNO_3$	6082	0.1M	7.5×10^{-6}	7.0×10^{-10}	0.1 M	--	--	--	[235]
$ZnAlNO_3$	6082	0.1 M	7.5×10^{-6}	3.5×10^{-9}	0.1 M	1	3.6×10^{4}	1.8×10^{4}	[164]
$ZnAlNO_3$	6082	0.1 M	7.5×10^{-6}	5.3×10^{-9}	0.1 M	1	2.3×10^{5}	3.8×10^{5}	[164]
$NiAlNO_3$	6082	0.1M	7.5×10^{-6}	1.4×10^{-9}	0.1 M	1	1.4×10^{6}	2.9×10^{4}	[236]
$CeMgAlNO_3$	6082				0.1 M	1200	7.5×10^{7}	3.8×10^{5}	[237]
$CeMgAlNO_3$	6082				0.1 M	1200	4.7×10^{3}	6.3×10^{5}	[237]
$ZnAlNO_3$	Pure Al	3.5 wt%	4.4×10^{-6}	1.1×10^{-7}	3.5 wt%	1	--	9.9×10^{4}	[238]
ZnAl-La				6×10^{-8}			--	1.2×10^{5}	
$NiAlNO_3$	6082	0.1	7.5×10^{-7}	1.410^{-9}	0.1	1	2.5×10^{9}	1.4×10^{6}	[239]

NiAl-CO_3	Pure Al	3.5 wt%	10^{-6}	10^{-9}	--	--	--	--	[100]
MgAl-oleate	Pure Al	--	--	--	3.5 wt %	168	6.8×10^{6}	8.2×10^{4}	[102]
MgAl Laurate		--	--	--			7.0×10^{11}	9.1×10^{5}	
MgAl stearate		--	--	--			6.0×10^{10}	1.1×10^{6}	
MgAl-SA	5005	3.5 wt%	1.3×10^{-5}	2.0×10^{-8}	--	--	--	--	[94]
ZnAl NO_3	6N01	3.5 wt%	4.7×10^{-6}	5.3×10^{-5}	3.5 wt %	168	--	1.9×10^{10}	[240]
ZnAl/RGO				4.3×10^{-8}			--	2.4×10^{10}	
Zn$AlNO_3$	2024	--	--	--	3.5 wt %	48	7.4×10^{3}	2.3×10^{2}	[105]
ZnAlMO		--	--	--			2.9×10^{4}	9.9×10^{2}	
ZnAlMO/GN		--	--	--			3.9×10^{5}	2.4×10^{3}	
Li$AlNO_3$	A6N01	3.5 wt%	0.32×10^{-6}	0.19×10^{-6}	3.5 wt%	120	3.5×10^{5}	--	[111]
$LiNO_3$/Vanillin			0.32×10^{-6}	0.03×10^{-6}			3.5×10^{7}	3.8×10^{9}	
MgAl-FAS-13	6061	3.5 wt%	1.5×10^{-4}	7.9×10^{-6}	3.5 wt%	408	3.7×10^{3}	--	[131]
MgAl-PVA	5054	--	--	--	3.5 wt%	480	3.3×10^{4}	7.4×10^{4}	[241]

ZnAl V_2O_7	2024	--	--	--	0.5M	1	--	1.0×10^4	[242]

8. Future outlooks

This work summarizes the significant approaches and synthetic conditions used to develop the LDHs on aluminum substrates to develop a smart coating system to protect the metallic surface from corrosion. LDHs based systems have proven an efficient approach to protect aluminum alloys. The hybrid inorganic/organic coating systems, utilization, and investigation of the number of corrosion inhibitors/pigments have created a new generation of multifunctional responsive coatings. Yet the size and geometry of the defects healed following the self-healing characteristics of LDHs, the controlled release of inhibitors in different reactive situations, the response of LDH on the occurrence of multiple damaging, pitting corrosion healing, and facile synthesis of defects free, low time-consuming LDH preparation are still open questions with limited solutions.

9 Appendices

LDHs for the removal of Arsenic from Drinking Water

9.1. Sorption of As(V) from aqueous solution using in-situ growth MgAl-NO_3 layered double hydroxide thin film developed on AA6082

Multifunctional LDHs properties have made them an attractive choice for the development of an environmental pollutants treatments system, that offers unique characteristics along with memory effect where thermal treatment causes the recovery of the original structure. We have studied here the pollutant removal capacity of the LDH, and arsenic is used as a model pollutant. Arsenic contaminations in groundwater are considered a serious hazard for human health as well as for the ecosystem due to their toxicity and carcinogenic nature. According to the World health organization and the United States, Environmental Protection Agency (USEPA) provided guidelines; the maximum arsenic level should be less than 10µg/L in the drinking water [243]. In that scenario, it is very alarming to find a much higher concentration of arsenic in drinking water in different regions throughout the world due to the presence of geological resources of arsenic in that area and also due to anthropogenic pollution from different industrial processes. It is estimated that 150 million people in 70 different countries are at risk of arsenic contaminations [244], while the rapid increase in industry pollutants worldwide is causing more discharge of non-biodegradable heavy metals [245]. Therefore, it is indispensable to develop low-cost efficient water purification technologies to purify drinking water from heavy metals.

Several approaches have been reported to remove arsenic, for instance, solvent extraction electrodialysis, membrane technologies, adsorption, coagulation, and ion exchange with certain limitations. The LDHs have been attained an attractive choice along with versatile properties for the expansion of new applications in various fields. Herein, we have designed LDHs based system for the removal of arsenic from drinking water. The anion exchange mechanism, LDH memory

effect, and corrosion resistance properties all made LDH a better choice for the development of the system for water treatment systems.

9.1.1. Synthesis of Mg-Al layered double hydroxide film.

The in-situ growth layered double hydroxide film is developed on the AA6082 substrate (3.14 cm^2), based on our previous work [113]. The specimens were initially ground with silicon-carbon paper, started from 500 grit paper to 1000, 2400, and 4000-grit respectively. The samples were cleaned with deionized water and further ultrasonically in pure ethanol for 15 minutes. Lastly, the specimens were immersed in a 0.1M aqueous NaOH solution for one minute to etch the oxide layer on the surface of the alloy. From our previous study, we selected two different synthesis conditions to develop distinct MgAl-LDH morphologies i.e. Cauliflower and platelet-shaped structure. The following combinations were used for that purpose, 0.008 $MgNO_3$ & 0.048 NH_4NO_3 and 0.028 $MgNO_3$ & 0.084 NH_4NO_3 at 60 ˚C and 80 ˚C respectively at a pH of 10 for 24 hrs of crystallization time. After that, the developed coated specimens were dried at room temperature.

9.1.2. Characterization

The structural characterization of MgAl-LDH film is done by the SEM (JEOL -IT300 microscope equipped with an EDS detector), while XRD patterns of the calcined and uncalcined LDH coated samples were recorded by X-ray diffraction (XRD) (X'Pert High Score diffractometer - Rigaku, Japan) by using cobalt K-α (λ=1.789 $Å^{-1}$) emission source at 10 mA and 30 kV conditions. The arsenic concentrations in the solution were determined by the atomic absorption spectrophotometer (AAS Vario 6, analytic jena (Germany)). To investigate the adsorption behavior, MgAl-LDH specimens were dipped in 20 mL model solutions of various arsenic concentrations (0.01 to 0.1 M) for 24hrs. To determine

adsorption kinetics, 0.1M arsenic solution (500mL) was used to investigate adsorption behavior as a function time at room temperature. The Lagergren Pseudo-first order and the pseudo-second-order fittings models were employed to understand the mechanism of As(V) sorption on Mg-Al LDHs.

9.1.3. Results and Discussion

Figure 114 shows the XRD patterns of MgAl-LDHs before and after the As(V) adsorption. It can be seen that as-prepared as well-treated specimens have shown the characteristic peaks of layer double hydroxide structure, as described in the literature [246]. The characteristics peaks of (003), (006), (009) crystal planes are attributed to the presence of the MgAl-NO_3 LDH structure. The sharp and symmetric characteristics peaks demonstrated a well crystalline and ordered structure of MgAl-LDH. The LDH structural peaks after As(V) adsorption have shown similar original LDH characteristics peaks, which describe the intactness of layer double hydroxide structure which was further confirmed by the SEM analysis. The intense reflection peaks of (003) at low 2θ value exhibited the interlayer distance (d_{003}) of ≈ 0.90 nm and ≈ 0.89 nm for cauliflower and platelet LDH structure respectively. The comparatively high interlayer thickness of cauliflower LDH structure may be attributed to strong NO_3^{-1} intercalation inside the galleries of brucite-like structure. However, due to the formation of carbonate anions, a small absorption peak of d_{003} for the MgAl-LDH platelet structure can also be observed. The intensity and broadness of the reflection peaks vary after the As(V) intercalations, which indicates the anion exchange interaction between As(V) in the solution and nitrates in the LDH galleries. After the anion exchange, the d_{003} value decreased; possibly due to the new orientation of As(V) inside the layers, the water molecules reorientation during the anion exchange process, and also due to the $HAsO_4^{-2}$ ionic radius, moreover reduced interlayer distance

described the strong electrostatic interaction between the positive layers and the intercalated anions [247]. As revealed from the SEM observations (Figure 115-116), compact and uniform interviewed LDH structures were obtained, which retained almost their original shape after the adsorption, but there can also be seen a few aggregations of particles on the MgAl LDH surface, So we can assume that during the adsorption, two possible interactions took place, (1) physical interaction of LDH surface with the As(V), and (2) anion exchange process between the nitrates and As(V). Figure 117 shown the EDS findings after treatment of MgAl-LDH with a 0.1M arsenic solution, it is clear that after treatment MgAl-LDH structure mainly contains Mg, Al, As, and oxygen, while the small amount of carbon was also evident in EDS study, caused by the contaminations, which results in the formation of carbonate anions.

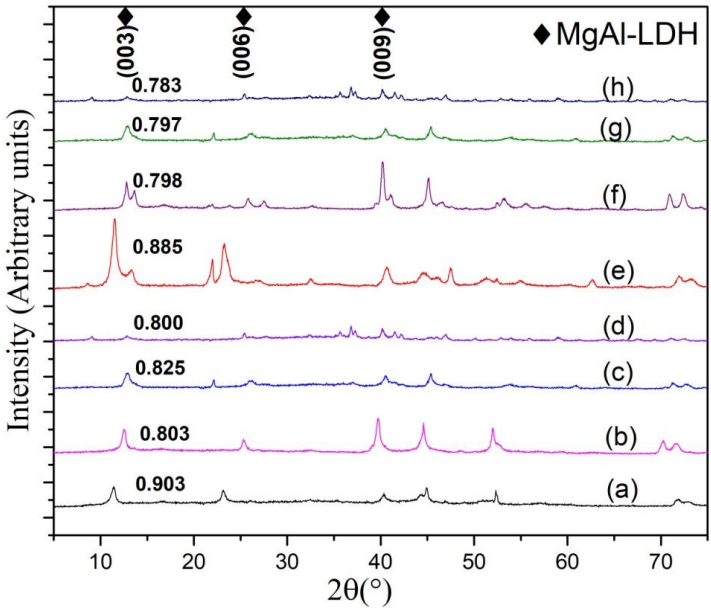

Figure 114. XRD patterns of cauliflower and platelet MgAl-LDH before and after treatment with different sodium arsenate concentrated solutions (a)

Cauliflower MgAl-LDH as prepared (b) 0.06M (c) 0.08M (d) 0.1M, (e) Platelet MgAl-LDH as prepared, (f) 0.06M (g) 0.08M

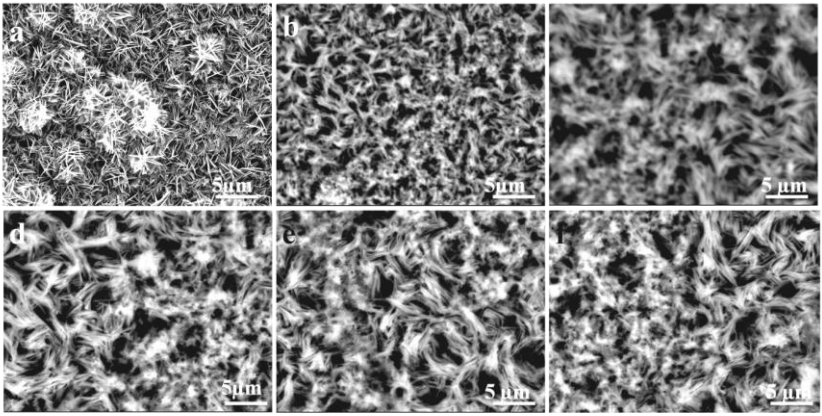

Figure 115. SEM images of platelet MgAl-LDH film with adsorption in different (Na_3AsO_4) concentration solutions for 24 hrs, (a) as prepared LDH, (b) 0.02M (c) 0.04M, (d) 0.06M, (e) 0.08M, (f) 0.1M.

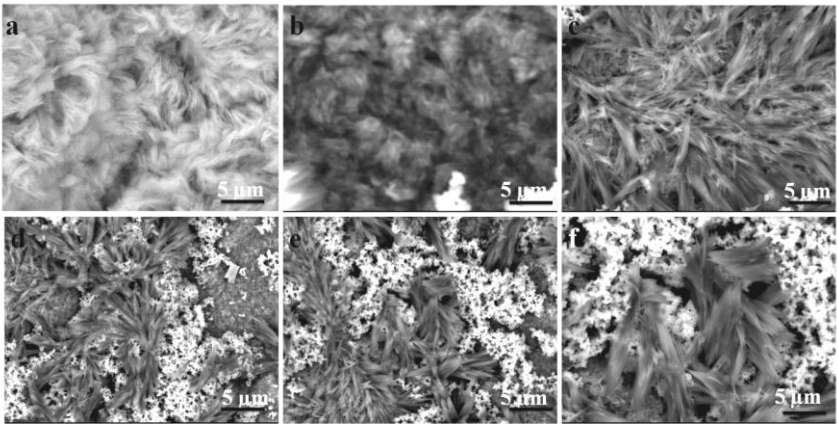

Figure 116. SEM images of cauliflower MgAl-LDH film with adsorption in different (Na_3AsO_4) concentration solutions for 24 hrs, (a) as prepared LDH, (b) 0.02M (c) 0.04M, (d) 0.06M, (e) 0.08M, (f) 0.1M.

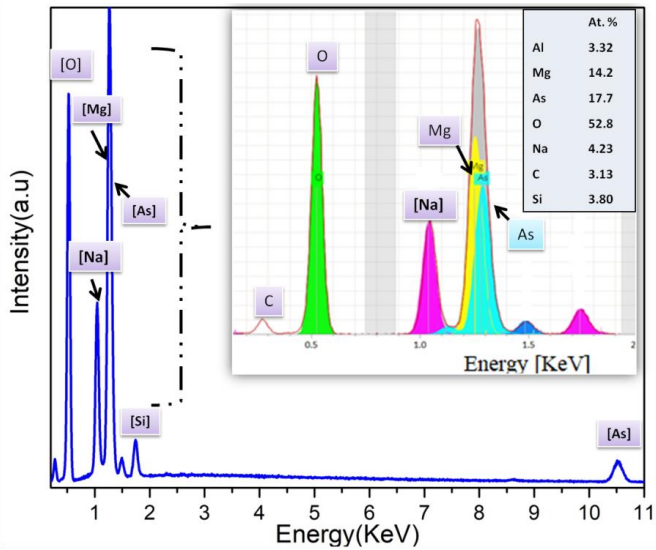

Figure 117. EDS spectrum of MgAl-LDH (cauliflower) after treatment with 0.1M sodium arsenate concentrated solutions.

The arsenic adsorption isotherms (adsorption capacity) were measured by varying the initial arsenic concentrations in the model solution for a contact period of 24 hrs, as shown in Figure 118. The amount of adsorption is found to increase with the increase of arsenic concentration in the solution (from 0.02 to 0.1 M) at a pH of 7. It is also interesting to note that, cauliflower-like LDH structure has shown the highest arsenic adsorption value (239 mg/g) compared to that of platelet structure (206 mg/g), possibly due to its high film thickness and of greater contoured nano-sheets which relatively increase its surface area. But overall, both structures have effectively removed the arsenate from the water. The equilibrium arsenic adsorption amount was calculated by Equation.1 [248].

$$q = \frac{V(C_o - C_t)}{m} \qquad (1)$$

Where "V" is the volume of the solution in L, C_o is the initial arsenic concentration while C_t is the concentration at time t in mg/L. q (mg/g) is the amount of arsenic sorbed (mg/g) at a time "t" on MgAl-LDH, and "m" is the sorbent mass (MgAl-LDH film) "m" in grams calculated by the mass difference of before and after MgAl-LDH formation on AA 6082 substrate (the specimens were dried at 60˚C for 40 min before mass measurement). Figure 118, shows the graphical relationship between q_e and C_e, it is clear that the adsorption capacity of the MgAl-LDH structure increases with the increase of the amount of As(V) in the model solution, because of larger concentration gradient which causes an increase of mass transfer driving force and leads to the availability of more arsenate molecules on the MgAlLDH active sites.

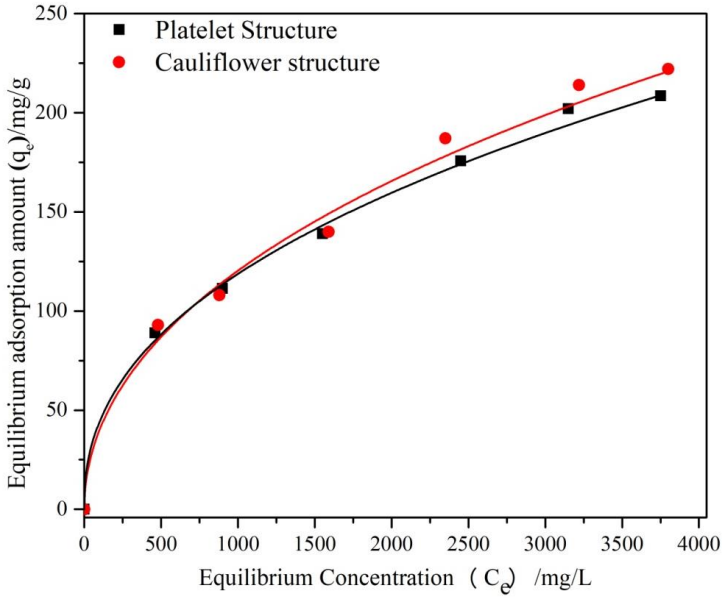

Figure 118. Equilibrium adsorption isotherms of Mg-Al LDHs by varying the initial As(V) concentration in the arsenic solution.

Further, the results of adsorption experiments were fitted by using the Langmuir model and Freundlich model to analyze the adsorption behavior of arsenate on MgAl-LDH. The general assumption of the Langmuir model is the uniform adsorption process with the context that each adsorption surface consisted of identical binding sites with monolayer adsorption behavior. The linear form of the Langmuir model can be written as follow,

$$\frac{C_e}{q_e} = \frac{1}{b \times Q_o} + \frac{C_e}{Q_o} \qquad (2)$$

where C_e/q_e (mg/g)is the equilibrium ratio between the concentration of adsorbate ions and the number of adsorbate ions adsorbed per unit weight of MgAl-LDH, Q_o is associated with the maximum adsorption capacity, while "b" is termed as Langmuir constant. If C_e/q_e is plotted against C_e, then from the slope and intercept of this plot, Q_0 and b can be determined, respectively (Figure 119).

On the other hand, the Freundlich model is another empirical description of non-ideal adsorption on the heterogeneous surface and provided an idea about the multilayer sorption with the description that the binding surface energy reduces with the increase of solute adsorbed on the surface. The Freundlich model is expressed as:

$$\log q_e = \log k + \frac{1}{n} \log C_e \quad (3)$$

By plotting log q_e versus log C_e, the coefficients "k" and "n" can be determined if a straight line is obtained. Freundlich isotherms for As(V) adsorption on MgAl-NO_3 LDHs are shown in Figure 120. The correlation coefficient values and isotherm constants of Langmuir and Freundlich isotherms are listed in Table 30.

From the obtained fitting results, it can be seen that the maximum adsorption capacity of As(v) was found by the Langmuir model with high linearity (Table 31). The maximum adsorption capacities of cauliflower and platelet structure for Langmuir As adsorption isotherms are found to be 239 and 212 mg/g respectively.

The results obtained by the Langmuir model are also in close agreement with the results obtained by Equation (1). So, we can say that the cauliflower-like MgAl-LDH structure has shown slightly better performance than the platelet-like structure. The results obtained here are also relatively higher than the MgAl-LDH synthesized by the co-precipitation method, from literature studies (Table 32). [249][18, 20-23].

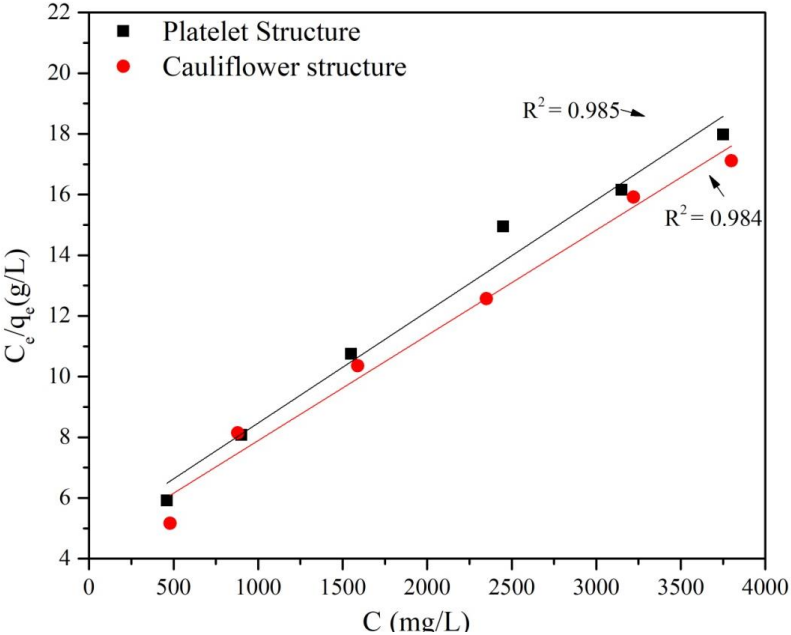

Figure 119. A highly linear Langmuir adsorption isotherm of As(V) by Mg-Al LDHs.

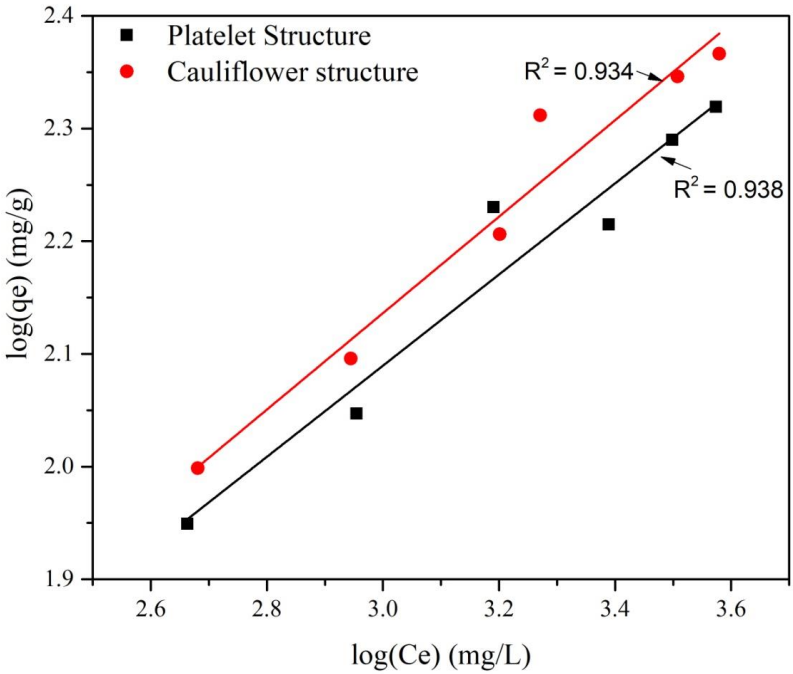

Figure 120. Freundlich isotherm of As(V) by Mg-Al LDHs.

Table 30. Langmuir and Freundlich parameters for As(V) removal by Mg-Al LDHs.

LDH structure	Langmuir Model			
	R^2	Q_o (mg/g)	(L/mg)	Slope
Platelet	0.985	212.8	0.0010	0.0047
Cauliflower	0.984	238.1	0.0008	0.0042
	Freundlich model			
	R^2	K	1/n	Slope
Cauliflower	0.994	6.622165	0.42	0.416
Platelet	0.998	7.063176	0.42	0.421

Table 31. A comparison study with other reports to adsorb As(V) by MgAl-LDHs

Layer double hydroxide (Adsorbents)	Synthesis method	Adsorption capacity (mg/g)	
		As(V)	References
MgAl-NO3LDH (Cauliflower Structure)	Insitu	239	This work
MgAl-NO3-LDH (Platelet Structure)	Insitu	212	This work
$MgAlNO_3$-LDH	co-precipitation	143	Rahman et
$MgAlNO_3$-LDH	co-precipitation	77	Rahman et
$MgAlNO_3$-LDH	co-precipitation	100	Dousova
$MgAlCO_3$-LDH	co-precipitation	45	Wu et
MgAlCl-LDH	co-precipitation	88	Wu et
$MgAlNO_3$-LDH *(calcined)*	co-precipitation	216	Yu et
$MgAlCO_3$-LDH	co-precipitation	121	Huang et

9.1.4. Kinetics of As(V) removal

Figure (121-122) shows the adsorption of arsenate by Mg-Al–NO_3 LDHs as a function of time to understand the kinetics of As(V) removal. With time, As(V) concentration decrease in the solution which caused the declination of the mass transfer due to lowering of static driving forces. Therefore, we can say that the adsorption is rapid initially at the start of the process when there was a high gradient of concentration and then it decreased with time until the system approach equilibrium. For the kinetics modeling and understanding of the mechanism of arsenate adsorption, Lagergren pseudo-first-order and pseudo-second-order were studied. Lagergren equation is used (Equation 4) to understand the adsorption kinetics, in the case of a pseudo-first-order process, the Lagergren equation after integration with the conditions

(q_t=0 at t=0, q_t=q_t at t=t) is expressed in Equation 5. Where q_t is the amount of arsenate adsorbed in mg/g at time t, k_1 is the time constant (min^{-1}), while q_e is the equilibrium adsorption value in mg/g at time t (calculated by the extrapolation of the experimental data). Equation 6, expressed the pseudo-second-order Lagrange equation, where k_2 is the second-order rate constant in g/mg×min. The pseudo-first-order kinetic model provides a general idea about the rate of change of arsenate concentration with time and states that the change in the concentration of the adsorbate and the amount of adsorbent over time is logarithmically proportional [254]. While a pseudo-second-order kinetic model suggests that the number of active sites occupied on the adsorbent is directly proportional to the adsorption capacity. The pseudo-first-order [255] (Eq. 5) and pseudo-second-order (Eq. 6) [256] is described as;

$$\frac{dq_t}{d_t} = k_1(q_e - q_t) \qquad (4)$$

$$\ln(q_e - q_t) = \ln(q_e) - k_1 t \qquad (5)$$

$$\frac{1}{q_t} = \frac{1}{k_2\,(q_e^2)} + \frac{t}{q_e} \qquad (6)$$

The correlation coefficients (R^2-values), rate constants, and other parameters for these two kinetic models were calculated from the respective slope and intercept and tabulated in Table 36. The pseudo-first-order model has shown a lower correlation (low linearity) than the pseudo-second-order model, which indicates the pseudo-second-order model as a better approach for the As(V) removal kinetics. Due to second-order reaction kinetics, we can say that the ion exchange of nitrate with As(V) is the rate-determining step [257]. Therefore we can conclude about the As(V) mechanism, that the reaction rate of arsenate adsorption mainly dependent on the anion exchange process between nitrate ions and As(V) and also that the rate of reaction depends upon the concentrations of NO_3^{-1} ions bound to the MgAl-NO_3-LDH and As(V) ions in the model solution. It can also

be concluded that the anion exchange process effectively takes place between the NO_3 and $HAsO_4^{-2}$, due to the relatively higher charge density of $HAsO_4^{-2}$ ions. The SEM and XRD analysis already confirmed that the basic LDH structure remains almost intact, which is aligned with the above description of the mechanism.

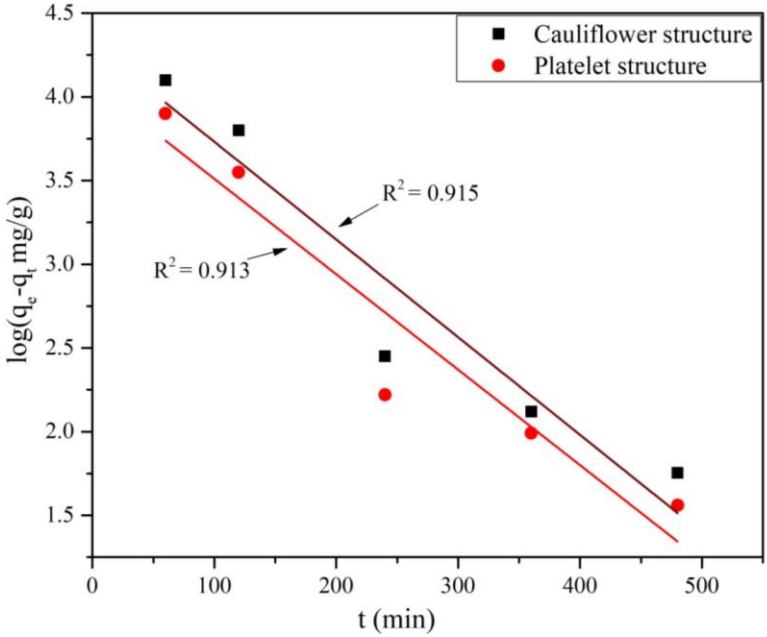

Figure 121. Pseudo-first order model for As(V) removal by Mg-Al LDHs.

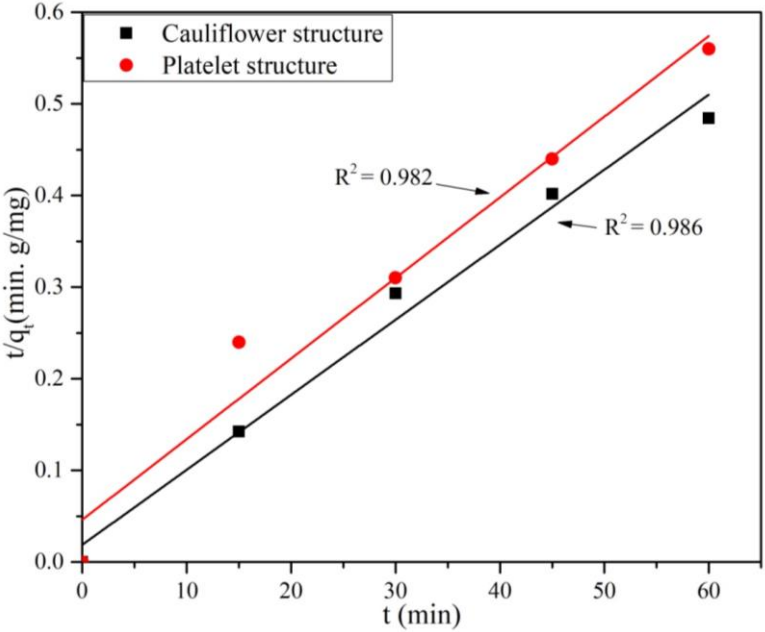

Figure 122. Pseudo-second order model for As(V) removal by Mg-Al LDHs.

Table 32. Kinetic parameters for As(V) removal by Mg-Al LDHs.

Kinetic model	LDH morphology	Q_e (mg/g)	R^2	K_1	slope
Pseudo-first order	Platelet	99.86194	0.913	0.0057	0.0057
	Cauliflower	102.3293	0.915	0.0058	0.0058
	LDH morphology	Q_2(mg/g)	R^2	K_2	slope
Pseudo-second order	Platelet	113.6364	0.986	0.004188	0.0088
	Cauliflower	122.1001	0.982	0.001454	0.0082

Figure 123 shows the as-prepared MgAl-LDH film thickness along with respective EDS analysis in at. % in-plane scanning mode, while the thickness is around 38± 0.98 and 52±1.06 µm for platelet and cauliflower-like structure respectively, measured by the cross-sectional analysis of the film. Figure 123 (insets) shown the MgAl-LDH surface, just for representation, after treatment with 0.1M sodium arsenate solution for 24 hr, the MgAl LDH film have sustained the initial structure and no dissolution was observed on contact with the arsenic solution.

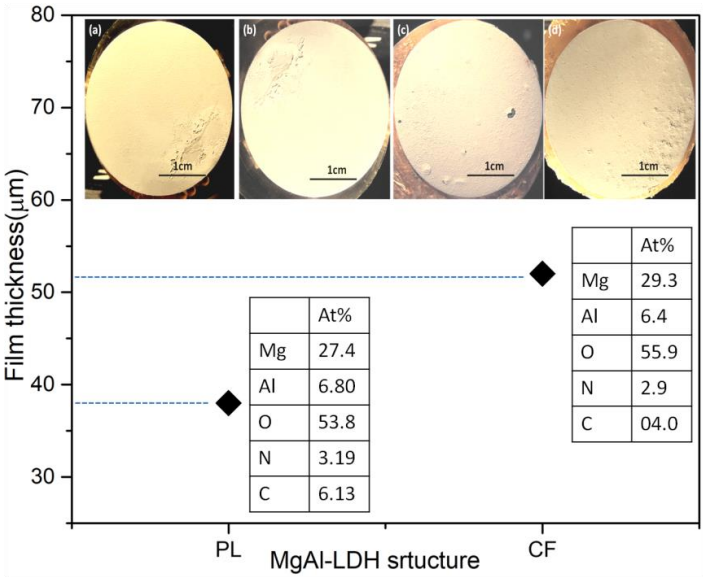

Figure 123. The MgAl-LDH thickness of the as-prepared films; PL-Platelet structure, CF-Cauliflower structure along with EDS atomic percentage, insight is the specimen surfaces after treatment with Sodium arsenate for 24hrs, platelet structure a) 0.08M, b) 0.1M, Cauliflower like structure c) 0.08M, d) 0.1M.

9.1.5. Conclusion

From the obtained findings in this study, it can be concluded that surface morphologies of MgAl-LDH have an influential effect on the arsenic adsorption capacity, and here cauliflower-like structure has shown slightly better adsorption capacity (238mg/g) compared to the platelet structure (212mg/g). The results also showed that the Langmuir model has shown the better fitting of the adsorption capacity while the Lagrange pseudo-second-order equation better translates the kinetics of arsenic adsorption. From the results, it is clear that arsenic adsorption occurs due to (1) surface adsorption, (2) and by the anion exchange of NO_3^{-1} ions with the As(V), but the anion exchange process of NO_3 and As(V) is the main

arsenic adsorption process. The in-situ growth $MgAlNO_3$-LDH adsorption capacity of arsenate was found to be higher as compared to the $MgAlNO_3$ LDH developed by the co-precipitation method (literature study), possibly due to the higher film thickness, high surface area, and layer by layer uniform structural geometry of in-situ growth MgAl-LDH. This work could be useful also as a baseline for the possible utilization of such systems as a coating material for the removal of arsenic.

Bibliography

[1] Esquivel, J., and R. K. Gupta. "Corrosion-Resistant Metastable Al Alloys: An Overview of Corrosion Mechanisms." *Journal of The Electrochemical Society* 167, no. 8 (2020): 081504.

[2] Lashgari, Mohsen, and Ali M. Malek. "Fundamental studies of aluminum corrosion in acidic and basic environments: Theoretical predictions and experimental observations." *Electrochimica Acta* 55, no. 18 (2010): 5253-5257.

[3] Popoola, A. P. I., O. S. Fayomi, and M. O. Popoola. "Comparative studies of microstructural, tribological and corrosion properties of plated Zn and Zn-alloy coatings." *International Journal of electrochemical science* 7 (2012): 4860-4870.

[4] Dennis, Robert V., Vincent Lee, Lasantha Viyannalage, Steven M. Henderson, and Sarbajit Banerjee. "Anti-Corrosive Graphene Coatings: An Active—Passive Alternative to Hexavalent Chromium Coatings." *New York: Department of Chemistry University at Buffalo* (2011).

[5] Trethewey, Kenneth Richard, and John Chamberlain. *Corrosion for students of science and engineering*. 1988.

[6] Umoru, L. E., and O. O. Ige. "Effects of Tin on Aluminum–Zinc–Magnesium Alloy as Sacrificial Anode in Seawater." *Journal of Minerals & Materials Characterization & Engineering* 7, no. 2 (2007): 105-113.

[7] Fontana, Mars Guy. *Corrosion engineering*. Tata McGraw-Hill Education, 2005.

[8] West, John Michael. "Basic corrosion and oxidation." (1986).

[9] Lumley, Roger, ed. *Fundamentals of aluminium metallurgy: production, processing and applications*. Elsevier, 2010.

[10] Umoru, L. E., A. A. Afonja, and B. Ademodi. "Corrosion study of AISI 304, AISI 321 and AISI 430 stainless steels in a tar sand digester." *Journal of Minerals & Materials Characterization & Engineering* 7, no. 4 (2008): 291-299.

[11] Totten, George E., and D. Scott MacKenzie, eds. *Handbook of Aluminum: Volume 2: Alloy Production and Materials Manufacturing*. Vol. 2. CRC press, 2003.

[12] K.D. Efird, E.J. Wright, J.A. Boros, T.G. Hailey, Correlation of steel corrosion in pipe flow with jet impingement and rotating cylinder tests, Corrosion. 49 (1993) 992–1003. https://doi.org/10.5006/1.3316026.

[13] K.A. Yasakau, M.L. Zheludkevich, S. V Lamaka, M.G.S. Ferreira, Role of intermetallic phases in localized corrosion of AA5083, 52 (2007) 7651–7659. https://doi.org/10.1016/j.electacta.2006.12.072.

[14] G.M. Scamans, N. Birbilis, R.G. Buchheit, Corrosion of aluminum and its alloys, in: Shreir's Corros., Elsevier, 2010: pp. 1974–2010. https://doi.org/10.1016/B978-044452787-5.00095-0.

[15] Mutombo, Kalenda, and Madeleine Du Toit. "Corrosion fatigue behaviour of aluminium 5083-H111 welded using gas metal arc welding method." In *Arc Welding*, pp. 642-643. BoD–Books on Demand, 2011. https://doi.org/10.5772/25991.

[16] Searles, J. L., P. I. Gouma, and R. G. Buchheit. "Stress corrosion cracking of sensitized AA5083 (Al-4.5 Mg-1.0 Mn)." *Metallurgical and Materials Transactions A* 32, no. 11 (2001): 2859-2867.https://doi.org/10.1007/s11661-001-1036-3.

[17] Oguocha, I. N. A., O. J. Adigun, and S. Yannacopoulos. "Effect of sensitization heat treatment on properties of Al–Mg alloy AA5083-H116." *Journal of Materials Science* 43, no. 12 (2008): 4208-4214.https://doi.org/10.1007/s10853-008-2606-1.

[18] - Jain, S. M. L. C., M. L. C. Lim, J. L. Hudson, and J. R. Scully. "Spreading of intergranular corrosion on the surface of sensitized Al-4.4 Mg alloys: A general finding." *Corrosion science* 59 (2012): 136-147. https://doi.org/10.1016/j.corsci.2012.02.018.

[19] Baer, Donald Ray, C. F. Windisch Jr, Mark H. Engelhard, Michael J. Danielson, Russell H. Jones, and John S. Vetrano. "Influence of Mg on the corrosion of Al." *Journal of Vacuum Science & Technology A: Vacuum, Surfaces, and Films* 18, no. 1 (2000): 131-136. https://doi.org/10.1116/1.582129.

[20] Goswami, R., G. Spanos, P. S. Pao, and R. L. Holtz. "Precipitation behavior of the ß phase in Al-5083." *Materials Science and Engineering: A* 527, no. 4-5 (2010): 1089-1095.

[21] Vetrano, J. S., C. H. Henager Jr, S. M. Bruemmer, Y. Ge, and C. H. Hamilton. "Use of Sc, Zr and Mn for grain size control in Al-Mg alloys." *Superplasticity and Superplastic Forming 1998* (1998): 89-98.

[22] Aballe, A., M. Bethencourt, F. J. Botana, M. J. Cano, and M. Marcos. "Localized alkaline corrosion of alloy AA5083 in neutral 3.5% NaCl solution." *Corrosion science* 43, no. 9 (2001): 1657-1674.

[23] Jones, R. H., D. R. Baer, M. J. Danielson, and J. S. Vetrano. "Role of Mg in the stress corrosion cracking of an Al-Mg alloy." *Metallurgical and Materials Transactions A* 32, no. 7 (2001): 1699-1711. [24] Ringer, S. P., K. Hono, I. J. Polmear, and T. Sakurai. "Nucleation of precipitates in aged AlCuMg (Ag) alloys with high Cu: Mg ratios." *Acta Materialia* 44, no. 5 (1996): 1883-1898.

[25] Scully, J. R., T. O. Knight, R. G. Buchheit, and D. E. Peebles. "Electrochemical characteristics of the Al2Cu, Al3Ta and Al3Zr intermetallic phases and their relevancy to the localized corrosion of Al alloys." *Corrosion Science* 35, no. 1-4 (1993): 185-195.

[26] Campestrini, P. E. P. M., E. P. M. Van Westing, H. W. Van Rooijen, and J. H. W. De Wit. "Relation between microstructural aspects of AA2024 and its corrosion behaviour investigated using AFM scanning potential technique." *Corrosion Science* 42, no. 11 (2000): 1853-1861.

[27] Guillaumin, Valérie, and Georges Mankowski. "Localized corrosion of 2024 T351 aluminium alloy in chloride media." *Corrosion Science* 41, no. 3 (1998): 421-438.

[28] S.M. Hirth, G.J. Marshall, S.A. Court, D.J. Lloyd, Effects of Si on the aging behaviour and formability of aluminium alloys based on AA6016, Mater. Sci. Eng. A. 319–321 (2001) 452–456. https://doi.org/10.1016/S0921-5093(01)00969-8.

[29] Usta, M., M. E. Glicksman, and R. N. Wright. "The effect of heat treatment on Mg 2 Si coarsening in aluminum 6105 alloy." *Metallurgical and Materials Transactions A* 35, no. 2 (2004): 435-438.

[30] Stelling, O., A. Irretier, O. Kessler, P. Krug, and Bernd Commandeur. "New light-weight aluminium alloys with high Mg2Si-content by spray forming." In *Materials science forum*, vol. 519, pp. 1245-1250. Trans Tech Publications Ltd, 2006. https://doi.org/10.3139/105.100394.

[31] F. Eckermann, T. Suter, P.J. Uggowitzer, A. Afseth, P. Schmutz, The influence of MgSi particle reactivity and dissolution processes on corrosion in Al-Mg-Si alloys, Electrochim. Acta. 54 (2008) 844–855. https://doi.org/10.1016/j.electacta.2008.05.078.

[32] Guillaumin, Valérie, and Georges Mankowski. "Localized corrosion of 6056 T6 aluminium alloy in chloride media." *Corrosion Science* 42, no. 1 (2000): 105-125.

[33] G.O. Ilevbare, O. Schneider, R.G. Kelly, J.R. Scully, In Situ Confocal Laser Scanning Microscopy of AA 2024-T3 Corrosion Metrology, J. Electrochem. Soc. 151 (2004) B453. https://doi.org/10.1149/1.1764780.

[34] A. Boag, A.E. Hughes, A.M. Glenn, T.H. Muster, D. McCulloch, Corrosion of AA2024-T3 Part I: Localised corrosion of isolated IM particles, Corros. Sci. 53 (2011) 17–26. https://doi.org/10.1016/j.corsci.2010.09.009.

[35] G. Sha, A. Cerezo, Characterization of precipitates in an aged 7xxx series Al alloy, Surf. Interface Anal. 36 (2004) 564–568. https://doi.org/10.1002/sia.1702.

[36] Nis, Kemal. "Electrochemical behavior of aluminum-base intermetallics containing iron." *Journal of the Electrochemical Society* 137, no. 1 (1990): 69. https://doi.org/10.1149/1.2086441.

[37] Shingu, Paul H., and Jin-Ichi Takamura. "Grain-Size refining of primary crystals in hypereutectic Al-Si and Al-Ge alloys." *MT* 1, no. 8 (1970): 2339-2340. https://doi.org/10.1007/BF02664262.

[38] Polmear, I. J. "Production of aluminium. Light alloys from traditional alloys to nanocrystals." (2006): 15-16.

[39] Mazurkiewicz, Boguslaw, and Antoni Piotrowski. "The electrochemical behaviour of the Al2Cu intermetallic compound." *Corrosion Science* 23, no. 7 (1983): 697-707.

[40] Cavanaugh, Mary K., Nick Birbilis, Rudi G. Buchheit, and F. Bovard. "Investigating localized corrosion susceptibility arising from Sc containing intermetallic Al3Sc in high strength Al-alloys." *Scripta Materialia* 56, no. 11 (2007): 995-998.

[41] Popoola, A. P. I., O. E. Olorunniwo, and O. O. Ige. "Corrosion resistance through the application of anti-corrosion coatings." *Developments in corrosion protection* 2, no. 12 (2014): 241-270.https://doi.org/10.5772/57420.

[42] Xhanari, Klodian, and Matjaž Finšgar. "Organic corrosion inhibitors for aluminum and its alloys in chloride and alkaline solutions: a review." *Arabian Journal of Chemistry* 12, no. 8 (2019): 4646-4663.

[43] Verma, Chandrabhan, Eno E. Ebenso, and Mumtaz Ahmad Quraishi. "Ionic liquids as green corrosion inhibitors for industrial metals and alloys." *Green Chemistry* (2018). https://doi.org/10.5772/intechopen.70421.

[44] Bibber, John W. "Chromium-free conversion coatings for zinc and its alloys." *Journal of Applied Surface Finishing* 2, no. 4 (2009): 273-275.

[45] Correll, David L. "The role of phosphorus in the eutrophication of receiving waters: A review." *Journal of environmental quality* 27, no. 2 (1998): 261-266. https://doi.org/10.2134/jeq1998.00472425002700020004x.

[46] Oki, Makanjuola. "Studies on chromium-free conversion coatings on aluminum." *Journal of Applied Sciences and Environmental Management* 11, no. 2 (2007).

[47] A.R. Phani, F.J. Gammel, T. Hack, H. Haefke, Enhanced corrosioon resistance by sol-gel-based ZrO2-CeO 2 coatings on magnesium alloys, Mater. Corros. 56 (2005) 77–82. https://doi.org/10.1002/maco.200403823.

[48] O. Lunder, C. Simensen, Y. Yu, K.N.-S. and Coatings, undefined 2004, Formation and characterisation of Ti–Zr based conversion layers on AA6060 aluminium, Elsevier. (n.d.). https://www.sciencedirect.com/science/article/pii/S0257897203012908 (accessed June 3, 2020).

[49] M.F. Montemor, R. Pinto, M.G.S. Ferreira, Chemical composition and corrosion protection of silane films modified with CeO2 nanoparticles, Electrochim. Acta. 54 (2009) 5179–5189. https://doi.org/10.1016/j.electacta.2009.01.053.

[50] Wen, Niann-Tsyr, Chao-Sung Lin, Ching-Yuan Bai, and Ming-Der Ger. "Structures and characteristics of Cr (III)-based conversion coatings on electrogalvanized steels." *Surface and Coatings Technology* 203, no. 3-4 (2008): 317-323. https://doi.org/10.1016/j.surfcoat.2008.09.006.

[51] A. Venugopal, R. Panda, S. Manwatkar, K. Sreekumar, L.R. Krishna, G. Sundararajan, Effect of micro arc oxidation treatment on localized corrosion behaviour of AA7075 aluminum alloy in 3.5 NaCl solution, Trans. Nonferrous Met. Soc. China (English Ed. 22 (2012) 700–710. https://doi.org/10.1016/S1003-6326(11)61234-X.

[52] Amirudin, A., and D. Thieny. "Application of electrochemical impedance spectroscopy to study the degradation of polymer-coated metals." *Progress in organic coatings* 26, no. 1 (1995): 1-28.

[53] Zhang, Xian-man, and Wei-ping Chen. "Review on corrosion-wear resistance performance of materials in molten aluminum and its alloys." *Transactions of Nonferrous Metals Society of China* 25, no. 6 (2015): 1715-1731.

[54] Sriharsha, Pusuluri, Sumith Kumar, Birudala Raga Harshith Reddy, and Rontala Saketh Reddy. "A Review on Corrosion Resistance of Ceramic Coated Materials." *no. April* (2017). https://doi.org/10.5772/57420.

[55] Latnikova, Alexandra. "Polymeric capsules for self-healing anticorrosion coatings." (2012).

[56] Mathiazhagan, A., and Rani Joseph. "Nanotechnology-a New prospective in organic coating-review." *International Journal of Chemical Engineering and Applications* 2, no. 4 (2011): 225. https://doi.org/10.7763/ijcea.2011.v2.108.

[57] S.P. Newman, W. Jones, Synthesis, characterization and applications of layered double hydroxides containing organic guests, New J. Chem. 22 (1998) 105–115. https://doi.org/10.1039/a708319j.

[58] Oh, Jae-Min, Timothy T. Biswick, and Jin-Ho Choy. "Layered nanomaterials for green materials." *Journal of Materials Chemistry* 19, no. 17 (2009): 2553-2563. https://doi.org/10.1039/b819094a.

[59] Evans, David G., and Robert CT Slade. "Structural aspects of layered double hydroxides." In *Layered double hydroxides*, pp. 1-87. Springer, Berlin, Heidelberg, 2006. https://doi.org/10.1007/430_005.

[60] Yu, Jingfang, Jingjing Liu, Abraham Clearfield, Johnathan E. Sims, Michael T. Speiegle, Steven L. Suib, and Luyi Sun. "Synthesis of layered double hydroxide single-layer nanosheets in formamide." *Inorganic Chemistry* 55, no. 22 (2016): 12036-12041. https://doi.org/10.1021/acs.inorgchem.6b02203.

[61] Liu, Zhen-Lei, De-Ying Tian, Shu-Ping Li, Xiao-Dong Li, and Tian-Hong Lu. "MTX/LDHs hybrids synthesized from reverse microemulsions: particle control and bioassay study." *International journal of pharmaceutics* 473, no. 1-2 (2014): 414-425. https://doi.org/10.1016/j.ijpharm.2014.07.044.

[62] Chitrakar, Ramesh, Yoji Makita, Akinari Sonoda, and Takahiro Hirotsu. "Synthesis of a novel layered double hydroxides [MgAl4 (OH) 12](Cl) 2· 2.4 H2O and its anion-exchange properties." *Journal of Hazardous Materials* 185, no. 2-3 (2011): 1435-1439. https://doi.org/10.1016/j.jhazmat.2010.10.066.

[63] Cai, Xiaoqing, Xiaoping Shen, Lianbo Ma, Zhenyuan Ji, Chen Xu, and Aihua Yuan. "Solvothermal synthesis of NiCo-layered double hydroxide nanosheets decorated on RGO sheets for high performance supercapacitor." *Chemical Engineering Journal* 268 (2015): 251-259. https://doi.org/10.1016/j.cej.2015.01.072.

[64] Iqbal, Muhammad Ahsan, Humaira Asghar, Muhammad Adeel Iqbal, and Michele Fedel. "Sorption of As (V) from aqueous solution using in situ growth MgAl–NO 3 layered double hydroxide thin film developed on AA6082." *SN Applied Sciences* 1, no. 7 (2019): 666. https://doi.org/10.1007/s42452-019-0669-z.

[65] Laipan, Minwang, Haoyang Fu, Runliang Zhu, Luyi Sun, Rachel M. Steel, Sujuan Ye, Jianxi Zhu, and Hongping He. "Calcined Mg/Al-LDH for acidic wastewater treatment: Simultaneous neutralization and contaminant removal." *Applied Clay Science* 153 (2018): 46-53. https://doi.org/10.1016/j.clay.2017.12.002.

[66] Zhao, Cang, Kamel Fezzaa, Ross W. Cunningham, Haidan Wen, Francesco De Carlo, Lianyi Chen, Anthony D. Rollett, and Tao Sun. "Real-time monitoring of laser powder bed fusion process using high-speed X-ray imaging and diffraction." *Scientific reports* 7, no. 1 (2017): 1-11. https://doi.org/10.1038/s41598-017-07775-8.

[67] Xu, Yin, Wenjie Huang, Xiaoying Chen, Fei Ge, Runliang Zhu, and Luyi Sun. "Self-assembled ZnAl-LDH/PMo12 nano-hybrids as effective catalysts on the degradation of methyl orange under room temperature and ambient pressure." *Applied Catalysis A: General* 550 (2018): 206-213. https://doi.org/10.1016/j.apcata.2017.11.012.

[68] Yang, Jae-Hun, Yang-Su Han, Man Park, Taeun Park, Seong-Ju Hwang, and Jin-Ho Choy. "New inorganic-based drug delivery system of indole-3-acetic acid-layered metal hydroxide nanohybrids with controlled release rate." *Chemistry of Materials* 19, no. 10 (2007): 2679-2685. https://doi.org/10.1021/cm070259h.

[69] X. Guo, F. Zhang, Q. Peng, S. Xu, X. Lei, D.G. Evans, X. Duan, Layered double hydroxide/eggshell membrane: An inorganic biocomposite membrane as

an efficient adsorbent for Cr(VI) removal, Chem. Eng. J. 166 (2011) 81–87. https://doi.org/10.1016/j.cej.2010.10.010.

[70] Li, Feng, and Xue Duan. "Applications of layered double hydroxides." In *Layered double hydroxides*, pp. 193-223. Springer, Berlin, Heidelberg, 2006. https://doi.org/10.1007/430_007.

[71] Guo, Lian, Wei Wu, Yongfeng Zhou, Fen Zhang, Rongchang Zeng, and Jianmin Zeng. "Layered double hydroxide coatings on magnesium alloys: A review." *Journal of materials science & technology* 34, no. 9 (2018): 1455-1466. https://doi.org/10.1016/j.jmst.2018.03.003.

[72] K. Okamoto, N. Iyi, T. Sasaki, Factors affecting the crystal size of the MgAl-LDH (layered double hydroxide) prepared by using ammonia-releasing reagents, Appl. Clay Sci. 37 (2007) 23–31. https://doi.org/10.1016/j.clay.2006.10.008.

[73] Iqbal, Muhammad Ahsan, and Michele Fedel. "Effect of synthesis conditions on the controlled growth of MgAl–LDH corrosion resistance film: structure and corrosion resistance properties." *Coatings* 9, no. 1 (2019): 30. https://doi.org/10.3390/coatings9010030.

[74] Bukhtiyarova, M. V. "A review on effect of synthesis conditions on the formation of layered double hydroxides." *Journal of Solid State Chemistry* 269 (2019): 494-506. https://doi.org/10.1016/j.jssc.2018.10.018.

[75] Miyata, Shigeo. "Anion-exchange properties of hydrotalcite-like compounds." *Clays and Clay minerals* 31, no. 4 (1983): 305-311.

[76] Bravo-Suárez, Juan J., Edgar A. Páez-Mozo, and S. Ted Oyama. "Review of the synthesis of layered double hydroxides: a thermodynamic approach." *Quimica Nova* 27, no. 4 (2004): 601-614. https://doi.org/10.1590/S0100-40422004000400015.

[77] Yan, Kai, Guosheng Wu, and Wei Jin. "Recent Advances in the Synthesis of Layered, Double-Hydroxide-Based Materials and Their Applications in Hydrogen and Oxygen Evolution." *Energy Technology* 4, no. 3 (2016): 354-368. https://doi.org/10.1002/ente.201500343.

[78] Chubar, Natalia, Robert Gilmour, Vasyl Gerda, Matej Mičušík, Maria Omastova, Katja Heister, Pascal Man, Jacques Fraissard, and Vladimir Zaitsev. "Layered double hydroxides as the next generation inorganic anion exchangers: Synthetic methods versus applicability." *Advances in colloid and interface science* 245 (2017): 62-80. https://doi.org/10.1016/j.cis.2017.04.013.

[79] Wang, Qiang, and Dermot O'Hare. "Recent advances in the synthesis and application of layered double hydroxide (LDH) nanosheets." *Chemical reviews* 112, no. 7 (2012): 4124-4155. https://doi.org/10.1021/cr200434v.

[80] Nalawade, P., B. Aware, V. J. Kadam, and R. S. Hirlekar. "Layered double hydroxides: A review." (2009).

[81] Theiss, Frederick L., Godwin A. Ayoko, and Ray L. Frost. "Synthesis of layered double hydroxides containing Mg2+, Zn2+, Ca2+ and Al3+ layer cations by co-precipitation methods—A review." *Applied Surface Science* 383 (2016): 200-213. https://doi.org/10.1016/j.apsusc.2016.04.150.

[82] Salak, Andrei N., João Tedim, Alena I. Kuznetsova, José L. Ribeiro, Luís G. Vieira, Mikhail L. Zheludkevich, and Mário GS Ferreira. "Comparative X-ray diffraction and infrared spectroscopy study of Zn–Al layered double hydroxides: Vanadate vs nitrate." *Chemical Physics* 397 (2012): 102-108. https://doi.org/10.1016/j.chemphys.2012.01.026.

[83] R.G. Buchheit, H. Guan, S. Mahajanam, F. Wong, Active corrosion protection and corrosion sensing in chromate-free organic coatings, Prog. Org. Coatings. 47 (2003) 174–182. https://doi.org/10.1016/j.porgcoat.2003.08.003.

[84] S.P.V. Mahajanam, R.G. Buchheit, Characterization of inhibitor release from Zn-Al-[V10 O28]6- hydrotalcite pigments and corrosion protection from hydrotalcite-pigmented epoxy coatings, Corrosion. 64 (2008) 230–240. https://doi.org/10.5006/1.3278468.

[85] G. Williams, H.N. McMurray, Anion-exchange inhibition of filiform corrosion on organic coated AA2024-T3 aluminum alloy by hydrotalcite-like pigments, Electrochem. Solid-State Lett. 6 (2003) 9–11. https://doi.org/10.1149/1.1539771.

[86] G. Williams, H.N. McMurray, Inhibition of filiform corrosion on polymer coated AA2024-T3 by hydrotalcite-like pigments incorporating organic anions, Electrochem. Solid-State Lett. 7 (2004) 13–15. https://doi.org/10.1149/1.1691529.

[87] M.L. Zheludkevich, S.K. Poznyak, L.M. Rodrigues, D. Raps, T. Hack, L.F. Dick, T. Nunes, M.G.S. Ferreira, Active protection coatings with layered double hydroxide nanocontainers of corrosion inhibitor, Corros. Sci. 52 (2010) 602–611. https://doi.org/10.1016/j.corsci.2009.10.020.

[88] M.A. Iqbal, L. Sun, M. Fedel, Synthesis of novel cone - shaped CaAl - LDH directly on aluminum alloy by a facile urea hydrolysis method, SN Appl. Sci. (2019). https://doi.org/10.1007/s42452-019-1474-4.

[89] S.K. Poznyak, J. Tedim, L.M. Rodrigues, A.N. Salak, M.L. Zheludkevich, L.F.P. Dick, M.G.S. Ferreira, Novel inorganic host layered double hydroxides intercalated with guest organic inhibitors for anticorrosion applications, ACS Appl. Mater. Interfaces. 1 (2009) 2353–2362. https://doi.org/10.1021/am900495r.

[90] T. Stimpfling, F. Leroux, H. Hintze-Bruening, Organo-modified layered double hydroxide in coating formulation to protect AA2024 from corrosion,

Colloids Surfaces A Physicochem. Eng. Asp. 458 (2014) 147–154. https://doi.org/10.1016/j.colsurfa.2014.01.042.

[91] T. Stimpfling, F. Leroux, H. Hintze-Bruening, Unraveling EDTA corrosion inhibition when interleaved into Layered Double Hydroxide epoxy filler system coated onto aluminum AA 2024, Appl. Clay Sci. 83–84 (2013) 32–41. https://doi.org/10.1016/j.clay.2013.08.005.

[92] Liu, Jianhua, You Zhang, Mei Yu, Songmei Li, Bing Xue, and Xiaolin Yin. "Influence of embedded ZnAlCe-NO3− layered double hydroxides on the anticorrosion properties of sol–gel coatings for aluminum alloy." *Progress in Organic Coatings* 81 (2015): 93-100. https://doi.org/10.1016/j.porgcoat.2014.12.015.

[93] J. Tedim, M.L. Zheludkevich, A.N. Salak, A. Lisenkov, M.G.S. Ferreira, Nanostructured LDH-container layer with active protection functionality, J. Mater. Chem. 21 (2011) 15464–15470. https://doi.org/10.1039/c1jm12463c.

[94] F. Zhang, L. Zhao, H. Chen, S. Xu, D.G. Evans, X. Duan, Corrosion resistance of superhydrophobic layered double hydroxide films on aluminum, Angew. Chemie - Int. Ed. 47 (2008) 2466–2469. https://doi.org/10.1002/anie.200704694.

[95] L. Wang, K. Zhang, H. He, W. Sun, Q. Zong, G. Liu, Enhanced corrosion resistance of MgAl hydrotalcite conversion coating on aluminum by chemical conversion treatment, Surf. Coatings Technol. 235 (2013) 484–488. https://doi.org/10.1016/j.surfcoat.2013.08.007.

[96] M. Kaseem, Y.G. Ko, Benzoate intercalated Mg-Al-layered double hydroxides (LDHs) as efficient chloride traps for plasma electrolysis coatings, J. Alloys Compd. (2019) 772–778. https://doi.org/10.1016/j.jallcom.2019.02.124.

[97] Y. Li, S. Li, Y. Zhang, M. Yu, J. Liu, Enhanced protective Zn-Al layered double hydroxide film fabricated on anodized 2198 aluminum alloy, J. Alloys Compd. 630 (2015) 29–36. https://doi.org/10.1016/j.jallcom.2014.12.176.

[98] M. Serdechnova, M. Mohedano, B. Kuznetsov, C.L. Mendis, M. Starykevich, S. Karpushenkov, J. Tedim, M.G.S. Ferreira, C. Blawert, M.L. Zheludkevich, PEO coatings with active protection based on in-situ formed LDH-nanocontainers, J. Electrochem. Soc. 164 (2017) C36–C45. https://doi.org/10.1149/2.0301702jes.

[99] B. Kuznetsov, M. Serdechnova, J. Tedim, M. Starykevich, S. Kallip, M.P. Oliveira, T. Hack, S. Nixon, M.G.S. Ferreira, M.L. Zheludkevich, Sealing of tartaric sulfuric (TSA) anodized AA2024 with nanostructured LDH layers, RSC Adv. 6 (2016) 13942–13952. https://doi.org/10.1039/c5ra27286f.

[100] Y. Liu, T. Yu, R. Cai, Y. Li, W. Yang, J. Caro, One-pot synthesis of NiAl-CO3 LDH anti-corrosion coatings from CO2-saturated precursors, RSC Adv. 5 (2015) 29552–29557. https://doi.org/10.1039/c5ra01969a.

[101] F. Zhang, C.L. Zhang, L. Song, R.C. Zeng, Z.G. Liu, H.Z. Cui, Corrosion of in-situ grown MgAl-LDH coating on aluminum alloy, Trans. Nonferrous Met. Soc. China (English Ed. 25 (2015) 3498–3504. https://doi.org/10.1016/S1003-6326(15)63987-5.

[102] Y. Wang, D. Zhang, Z. Lu, Hydrophobic Mg-Al layered double hydroxide film on aluminum: Fabrication and microbiologically influenced corrosion resistance properties, Colloids Surfaces A Physicochem. Eng. Asp. 474 (2015) 44–51. https://doi.org/10.1016/j.colsurfa.2015.03.005.

[103] X. Guo, S. Xu, L. Zhao, W. Lu, F. Zhang, D.G. Evans, X. Duan, One-step hydrothermal crystallization of a layered double hydroxide/alumina bilayer film on aluminum and its corrosion resistance properties, Langmuir. 25 (2009) 9894–9897. https://doi.org/10.1021/la901012w.

[104] F. Zhang, C.L. Zhang, L. Song, R.C. Zeng, L.Y. Cui, H.Z. Cui, Corrosion resistance of superhydrophobic mg-al layered double hydroxide coatings on aluminum alloys, Acta Metall. Sin. (English Lett. 28 (2015) 1373–1381. https://doi.org/10.1007/s40195-015-0335-4.

[105] Y. Zhang, P. Yu, J. Wang, Y. Li, F. Chen, K. Wei, Y. Zuo, LDHs/graphene film on aluminum alloys for active protection, Appl. Surf. Sci. 433 (2018) 927–933. https://doi.org/10.1016/j.apsusc.2017.10.126.

[106] D. Álvarez, A. Collazo, M. Hernández, X.R. Nóvoa, C. Pérez, Characterization of hybrid sol-gel coatings doped with hydrotalcite-like compounds to improve corrosion resistance of AA2024-T3 alloys, Prog. Org. Coatings. 68 (2010) 91–99. https://doi.org/10.1016/j.porgcoat.2009.09.023.

[107] W. Li, X. Zhang, J. Yang, F. Miao, In situ growth of superhydrophobic and icephobic films with micro/nanoscale hierarchical structures on the aluminum substrate, J. Colloid Interface Sci. 410 (2013) 165–171. https://doi.org/10.1016/j.jcis.2013.07.063.

[108] M. Mohedano, M. Serdechnova, M. Starykevich, S. Karpushenkov, A.C. Bouali, Active protective PEO coatings on AA2024 : Role of voltage on in-situ LDH growth, Mater. Des. 120 (2017) 36–46. https://doi.org/10.1016/j.matdes.2017.01.097.

[109] Y. Li, S. Li, Y. Zhang, M. Yu, J. Liu, Fabrication of superhydrophobic layered double hydroxides films with different metal cations on anodized aluminum 2198 alloy, Mater. Lett. 142 (2015) 137–140. https://doi.org/10.1016/j.matlet.2014.11.148.

[110] R. Subasri, K.R.C. Soma Raju, D.S. Reddy, A. Jyothirmayi, V.S. Ijeri, O. Prakash, S.P. Gaydos, Environmentally friendly Zn–Al layered double hydroxide (LDH)-based sol–gel corrosion protection coatings on AA 2024-T3, J. Coatings Technol. Res. (2019). https://doi.org/10.1007/s11998-019-00229-y.

[111] K. Lin, X. Luo, X. Pan, C. Zhang, Y. Liu, Enhanced corrosion resistance of LiAl-layered double hydroxide (LDH) coating modified with a Schiff base salt on aluminum alloy by one step in-situ synthesis at low temperature, Appl. Surf. Sci. 463 (2019) 1085–1096. https://doi.org/10.1016/j.apsusc.2018.09.034.

[112] Z. Liang, Y. Ma, K. Li, Y. Liao, B. Yang, L. Liu, P. Zhu, Surface & Coatings Technology Formation of layered double hydroxides fi lm on AA2099-T83 Al-Cu-Li alloy and its e ff ect on corrosion resistance, 378 (2019). https://doi.org/10.1016/j.surfcoat.2019.124967.

[113] M.A. Iqbal, M. Fedel, The effect of the surface morphologies on the corrosion resistance of in situ growth MgAl-LDH based conversion film on AA6082, Surf. Coatings Technol. 352 (2018). https://doi.org/10.1016/j.surfcoat.2018.08.006.

[114] A. V Radha, P.V. Kamath, C. Shivakumara, Mechanism of the anion exchange reactions of the layered double hydroxides (LDHs) of Ca and Mg with Al, 7 (2005) 1180–1187. https://doi.org/10.1016/j.solidstatesciences.2005.05.004.

[115] kumar Allada, Rama, Alexandra Navrotsky, Hillary Thompson Berbeco, and William H. Casey. "Thermochemistry and aqueous solubilities of hydrotalcite-like solids." *Science* 296, no. 5568 (2002): 721-723.

[116] J. Tedim, A. Kuznetsova, A.N. Salak, F. Montemor, D. Snihirova, M. Pilz, M.L. Zheludkevich, M.G.S. Ferreira, Zn-Al layered double hydroxides as chloride nanotraps in active protective coatings, Corros. Sci. 55 (2012) 1–4. https://doi.org/10.1016/j.corsci.2011.10.003.

[117] J. Tedim, M.L. Zheludkevich, A.C. Bastos, A.N. Salak, A.D. Lisenkov, M.G.S. Ferreira, Influence of preparation conditions of Layered Double Hydroxide conversion films on corrosion protection, Electrochim. Acta. 117 (2014) 164–171. https://doi.org/10.1016/j.electacta.2013.11.111.

[118] H.D. Johansen, C.M.A. Brett, A.J. Motheo, Corrosion protection of aluminium alloy by cerium conversion and conducting polymer duplex coatings, Corros. Sci. 63 (2012) 342–350. https://doi.org/10.1016/j.corsci.2012.06.020.

[119] S.B. Lyon, R. Bingham, D.J. Mills, Progress in Organic Coatings Advances in corrosion protection by organic coatings : What we know and what we would like to know, Prog. Org. Coatings. 102 (2017) 2–7. https://doi.org/10.1016/j.porgcoat.2016.04.030.

[120] Szauer, T. "Impedance measurements for the evaluation of protective nonmetallic coatings." *Progress in Organic Coatings* 10, no. 2 (1982): 171-183.

[121] Mansfeld, F., M. W. Kendig, and S. Tsai. "Evaluation of corrosion behavior of coated metals with AC impedance measurements." *Corrosion* 38, no. 9 (1982): 478-485. https://doi.org/10.5006/1.3577363.

[122] Macdonald, Digby D. "Reflections on the history of electrochemical impedance spectroscopy." *Electrochimica Acta* 51, no. 8-9 (2006): 1376-1388. https://doi.org/10.1016/j.electacta.2005.02.107.

[123] Bacon, R. Charles, Joseph J. Smith, and Frank M. Rugg. "Electrolytic resistance in evaluating protective merit of coatings on metals." *Industrial & Engineering Chemistry* 40, no. 1 (1948): 161-167. https://doi.org/10.1021/ie50457a041.

[124] Murray, John N. "Electrochemical test methods for evaluating organic coatings on metals: an update. Part I. Introduction and generalities regarding electrochemical testing of organic coatings." *Progress in Organic Coatings* 30, no. 4 (1997): 225-233.

[125] Macdonald, J. Ross, A. Hooper, and A. P. Lehnen. "Analysis of hydrogen-doped lithium nitride admittance data." *Solid State Ionics* 6, no. 1 (1982): 65-77.

[126] Boukamp, Bernard A. "A nonlinear least squares fit procedure for analysis of immittance data of electrochemical systems." *Solid state ionics* 20, no. 1 (1986): 31-44.

[127] ZHENG, Qi-fei, Shuang-qing SUN, and Jun-guo WEN. "Atmospheric Corrosion and Its Influencing Factors of Aluminum and Aluminum Alloys [J]." *Corrosion & Protection* 6 (2009).

[128] Jorcin, Jean-Baptiste, Mark E. Orazem, Nadine Pébère, and Bernard Tribollet. "CPE analysis by local electrochemical impedance spectroscopy." *Electrochimica Acta* 51, no. 8-9 (2006): 1473-1479. https://doi.org/10.1016/j.electacta.2005.02.128.

[129] Wang, Lianying, Cang Li, Miao Liu, David G. Evans, and Xue Duan. "Large continuous, transparent and oriented self-supporting films of layered double hydroxides with tunable chemical composition." *Chemical communications* 2 (2007): 123-125.

[130] Zhou, Bingtao, Xiaofeng Wei, Youbin Wang, Qiuyu Huang, Biao Hong, and Yuezhou Wei. "Effect of lanthanum addition on microstructures and corrosion behavior of ZnAl-LDHs film of 6061 aluminum alloys." *Surface and Coatings Technology* 379 (2019): 125056. https://doi.org/10.1016/j.surfcoat.2019.125056.

[131] Wang, Fengyi, and Zhiguang Guo. "Insitu growth of durable superhydrophobic Mg–Al layered double hydroxides nanoplatelets on aluminum alloys for corrosion resistance." *Journal of Alloys and Compounds* 767 (2018): 382-391. https://doi.org/10.1016/j.jallcom.2018.07.086.

[132] Walter, G. W. "The application of impedance spectroscopy to study the uptake of sodium chloride solution in painted metals." *Corrosion science* 32, no. 10 (1991): 1041-1058.

[133] Frechette, E., C. Compere, and E. Ghali. "Evaluation of the corrosion resistance of painted steels by impedance measurements." *Corrosion science* 33, no. 7 (1992): 1067-1081.

[134] Bierwagen, Gordon, Kerry Allahar, Brian Hinderliter, Alda MP Simões, Dennis Tallman, and Stuart Croll. "Ionic liquid enhanced electrochemical characterization of organic coatings." *Progress in Organic Coatings* 63, no. 3 (2008): 250-259.https://doi.org/10.1016/j.porgcoat.2008.07.019.

[135] Amand, Sylvain, Marco Musiani, Mark E. Orazem, Nadine Pébère, Bernard Tribollet, and Vincent Vivier. "Constant-phase-element behavior caused by inhomogeneous water uptake in anti-corrosion coatings." *Electrochimica Acta* 87 (2013): 693-700.v https://doi.org/10.1016/j.electacta.2012.09.061.

[136] Mikhailau, Aliaksandr, Hanna Maltanava, Sergey K. Poznyak, Andrei N. Salak, Mikhail L. Zheludkevich, Kiryl A. Yasakau, and Mário GS Ferreira. "One-step synthesis and growth mechanism of nitrate intercalated ZnAl LDH conversion coatings on zinc." *Chemical Communications* 55, no. 48 (2019): 6878-6881.. https://doi.org/10.1039/c9cc02571e.

[137] J.T. Kloprogge, R.L. Frost, Fourier transform infrared and Raman spectroscopic study of the local structure of Mg-, Ni-, and Co-hydrotalcites, J. Solid State Chem. 146 (1999) 506–515. https://doi.org/10.1006/jssc.1999.8413.

[138] S. Aisawa, H. Hirahara, H. Uchiyama, S. Takahashi, E. Narita, Synthesis and thermal decomposition of Mn-Al layered double hydroxides, J. Solid State Chem. 167 (2002) 152–159. https://doi.org/10.1006/jssc.2002.9637.

[139] K. Abdellaoui, I. Pavlovic, M. Bouhent, A. Benhamou, C. Barriga, A comparative study of the amaranth azo dye adsorption/desorption from aqueous solutions by layered double hydroxides, Appl. Clay Sci. 143 (2017) 142–150. https://doi.org/10.1016/j.clay.2017.03.019.

[140] Rives, Vicente. *Layered double hydroxides: present and future*. Nova Publishers, 2001.

[141] F. Cavani, F. Trifirò, A. Vaccari, Hydrotalcite-type anionic clays: Preparation, properties and applications., Catal. Today. 11 (1991) 173–301. https://doi.org/10.1016/0920-5861(91)80068-K.

[142] Zheming, Ni, Xia Shengjie, Fang Caiping, Wang Ligeng, and Hu Jun. "Synthesis, characterization and thermal property of Cu/Co/Mg/Al hydrotalcite like compounds." *Rare Metal Materials and Engineering S* 2 (2008).

[143] Iqbal, Muhammad Ahsan, Luyi Sun, Allyson T. Barrett, and Michele Fedel. "Layered Double Hydroxide Protective Films Developed on Aluminum and Aluminum Alloys: Synthetic Methods and Anti-Corrosion Mechanisms." *Coatings* 10, no. 4 (2020): 428.

[144] Inman, Keith, and Norah Rudin. *Principles and practice of criminalistics: the profession of forensic science*. CRC Press, 2000.

[145] Zhang, Caixia, Xiaohu Luo, Xinyu Pan, Liying Liao, Xiaosong Wu, and Yali Liu. "Self-healing Li-Al layered double hydroxide conversion coating modified with aspartic acid for 6N01 Al alloy." *Applied Surface Science* 394 (2017): 275-281.

[146] Wang, Fengyi, and Zhiguang Guo. "Insitu growth of durable superhydrophobic Mg–Al layered double hydroxides nanoplatelets on aluminum alloys for corrosion resistance." *Journal of Alloys and Compounds* 767 (2018): 382-391. https://doi.org/10.1016/j.jallcom.2018.07.086.

[147] Lin, Kaidong, Xiaohu Luo, Xinyu Pan, Caixia Zhang, and Yali Liu. "Enhanced corrosion resistance of LiAl-layered double hydroxide (LDH) coating modified with a Schiff base salt on aluminum alloy by one step in-situ synthesis at low temperature." *Applied Surface Science* 463 (2019): 1085-1096.

[148] Tedim, Joao, M. L. Zheludkevich, A. C. Bastos, A. N. Salak, A. D. Lisenkov, and M. G. S. Ferreira. "Influence of preparation conditions of layered double hydroxide conversion films on corrosion protection." *Electrochimica Acta* 117 (2014): 164-171.

[149] Liu, Zhaoping, Renzhi Ma, Minoru Osada, Nobuo Iyi, Yasuo Ebina, Kazunori Takada, and Takayoshi Sasaki. "Synthesis, anion exchange, and delamination of Co− Al layered double hydroxide: assembly of the exfoliated nanosheet/polyanion composite films and magneto-optical studies." *Journal of the American Chemical Society* 128, no. 14 (2006): 4872-4880.https://doi.org/10.1021/ja0584471.

[150] Kameda, Tomohito, Yuki Fubasami, and Toshiaki Yoshioka. "Kinetics and equilibrium studies on the treatment of nitric acid with Mg–Al oxide obtained by thermal decomposition of NO3--intercalated Mg–Al layered double hydroxide." *Journal of colloid and interface science* 362, no. 2 (2011): 497-502.

[151] Marappa, Shivanna, S. Radha, and P. Vishnu Kamath. "Nitrate-Intercalated Layered Double Hydroxides–Structure Model, Order, and Disorder." *European Journal of Inorganic Chemistry* 2013, no. 12 (2013): 2122-2128.https://doi.org/10.1002/ejic.201201405.

[152] K. Abderrazek, N. Frini Srasra, E. Srasra, Synthesis and Characterization of [Zn-Al] Layered Double Hydroxides: Effect of the Operating Parameters, J. Chinese Chem. Soc. 64 (2017) 346–353. https://doi.org/10.1002/jccs.201600258.

[153] Seftel, E. M., E. Popovici, M. Mertens, K. De Witte, G. Van Tendeloo, P. Cool, and E. F. Vansant. "Zn–Al layered double hydroxides: synthesis, characterization and photocatalytic application." *Microporous and Mesoporous Materials* 113, no. 1-3 (2008): 296-304.

[154] Ke, Xinyuan, Susan A. Bernal, and John L. Provis. "Uptake of chloride and carbonate by Mg-Al and Ca-Al layered double hydroxides in simulated pore

solutions of alkali-activated slag cement." *Cement and Concrete Research* 100 (2017): 1-13. https://doi.org/10.1016/j.cemconres.2017.05.015.

[155] Zhang, Caixia, Xiaohu Luo, Xinyu Pan, Liying Liao, Xiaosong Wu, and Yali Liu. "Self-healing Li-Al layered double hydroxide conversion coating modified with aspartic acid for 6N01 Al alloy." *Applied Surface Science* 394 (2017): 275-281.https://doi.org/10.1016/j.apsusc.2016.10.034.

[156] Wang, Fengyi, and Zhiguang Guo. "Insitu growth of durable superhydrophobic Mg–Al layered double hydroxides nanoplatelets on aluminum alloys for corrosion resistance." *Journal of Alloys and Compounds* 767 (2018): 382-391.

[157] Chen, Jun, Yingwei Song, Dayong Shan, and En-Hou Han. "In situ growth of Mg–Al hydrotalcite conversion film on AZ31 magnesium alloy." *Corrosion Science* 53, no. 10 (2011): 3281-3288.

[158] M. Serdechnova, … M.M.-J. of T., undefined 2017, PEO Coatings with Active Protection Based on In-Situ Formed LDH-Nanocontainers, Electrochem. Soc. 164 (2017) C36–C45. https://doi.org/10.1149/2.0301702jes.

[159] Szabados, Márton, Rebeka Mészáros, Szabolcs Erdei, Zoltán Kónya, Ákos Kukovecz, Pál Sipos, and István Pálinkó. "Ultrasonically-enhanced mechanochemical synthesis of CaAl-layered double hydroxides intercalated by a variety of inorganic anions." *Ultrasonics Sonochemistry* 31 (2016): 409-416.

[160] S. Marappa, S. Radha, P.V. Kamath, Nitrate-Intercalated Layered Double Hydroxides - Structure Model, Order, and Disorder, Eur. J. Inorg. Chem. 2013 (2013) 2122–2128. https://doi.org/10.1002/ejic.201201405.

[161] H.S. Panda, R. Srivastava, D. Bahadur, Synthesis and in situ mechanism of nuclei growth of layered double hydroxides, Bull. Mater. Sci. 34 (2011) 1599–1604. https://doi.org/10.1007/s12034-011-0364-1.

[162] M.A. Iqbal, M. Fedel, Ordering and disordering of in situ grown MgAl-layered double hydroxide and its effect on the structural and corrosion resistance properties, 26 (2019) 1570–1577.

[163] Kloprogge, J. Theo, and Ray L. Frost. "Fourier transform infrared and Raman spectroscopic study of the local structure of Mg-, Ni-, and Co-hydrotalcites." *Journal of Solid State Chemistry* 146, no. 2 (1999): 506-515.

[164] M.A. Iqbal, M. Fedel, Effect of operating parameters on the structural growth of ZnAl layered double hydroxide on AA6082 and corresponding corrosion resistance properties, J. Coatings Technol. Res. 16 (2019) 1423–1433. https://doi.org/10.1007/s11998-019-00227-0.

[165] M.A. Iqbal, L. Sun, A.T. Barrett, M. Fedel, Layered Double Hydroxide Protective Films Developed on Aluminum and Aluminum Alloys: Synthetic Methods and Anti-Corrosion Mechanisms, Coatings. 10 (2020) 428. https://doi.org/10.3390/coatings10040428.

[166] Ye, Xin, Zimin Jiang, Linxin Li, and Zhi-Hui Xie. "In-situ growth of nial-layered double hydroxide on AZ31 Mg alloy towards enhanced corrosion protection." *Nanomaterials* 8, no. 6 (2018): 411.

[167] L. Wang, B. Li, X. Zhao, C. Chen, J. Cao, Effect of Rare Earth Ions on the Properties of Composites Composed of Ethylene Vinyl Acetate Copolymer and Layered Double Hydroxides, 7 (2012). https://doi.org/10.1371/journal.pone.0037781.

[168] Hibino, Toshiyuki, and Hitoshi Ohya. "Synthesis of crystalline layered double hydroxides: Precipitation by using urea hydrolysis and subsequent hydrothermal reactions in aqueous solutions." *Applied Clay Science* 45, no. 3 (2009): 123-132. https://doi.org/10.1016/j.clay.2009.04.013.

[169] Szabados, Márton, Rebeka Mészáros, Szabolcs Erdei, Zoltán Kónya, Ákos Kukovecz, Pál Sipos, and István Pálinkó. "Ultrasonically-enhanced

mechanochemical synthesis of CaAl-layered double hydroxides intercalated by a variety of inorganic anions." *Ultrasonics Sonochemistry* 31 (2016): 409-416. https://doi.org/10.1016/j.ultsonch.2016.01.026.

[170] Rousselot, Isabelle, Christine Taviot-Guého, Fabrice Leroux, Philippe Léone, Pierre Palvadeau, and Jean-Pierre Besse. "Insights on the structural chemistry of hydrocalumite and hydrotalcite-like materials: investigation of the series Ca2M3+ (OH) 6Cl· 2H2O (M3+: Al3+, Ga3+, Fe3+, and Sc3+) by X-ray powder diffraction." *Journal of Solid State Chemistry* 167, no. 1 (2002): 137-144.

[171] Constantino, Vera RL, and Thomas J. Pinnavaia. "Basic properties of Mg2+ 1-xAl3+ x layered double hydroxides intercalated by carbonate, hydroxide, chloride, and sulfate anions." *Inorganic Chemistry* 34, no. 4 (1995): 883-892. https://doi.org/10.1021/ic00108a020.

[172] Bontchev, Ranko P., Shirley Liu, James L. Krumhansl, James Voigt, and Tina M. Nenoff. "Synthesis, characterization, and ion exchange properties of hydrotalcite Mg6Al2 (OH) 16 (A) x (A ‘) 2-x 4H2O (A, A ‘= Cl-, Br-, I-, and NO3-, 2≥ x≥ 0) derivatives." *Chemistry of materials* 15, no. 19 (2003): 3669-3675. https://doi.org/10.1021/cm034231r.

[173] Wu, Qinglan, Anja Olafsen, Ørnulv B. Vistad, Jaan Roots, and Poul Norby. "Delamination and restacking of a layered double hydroxide with nitrate as counter anion." *Journal of Materials Chemistry* 15, no. 44 (2005): 4695-4700.https://doi.org/10.1039/b511184f.

[174] Zheming, Ni, Xia Shengjie, Fang Caiping, Wang Ligeng, and Hu Jun. "Synthesis, characterization and thermal property of Cu/Co/Mg/Al hydrotalcite like compounds." *Rare Metal Materials and Engineering S* 2 (2008).

[175] Chitrakar, Ramesh, Satoko Tezuka, Akinari Sonoda, Kohji Sakane, and Takahiro Hirotsu. "A new method for synthesis of Mg− Al, Mg− Fe, and Zn− Al layered double hydroxides and their uptake properties of bromide ion." *Industrial*

& engineering chemistry research 47, no. 14 (2008): 4905-4908. https://doi.org/10.1021/ie0716417.

[176] Wang, Qiang, Hui Huang Tay, Desmond Jia Wei Ng, Luwei Chen, Yan Liu, Jie Chang, Ziyi Zhong, Jizhong Luo, and Armando Borgna. "The Effect of Trivalent Cations on the Performance of Mg-M-CO3 Layered Double Hydroxides for High-Temperature CO2 Capture." *ChemSusChem* 3, no. 8 (2010): 965-973. https://doi.org/10.1002/cssc.201000099.

[177] Hussein, Mohd Zobir Bin, Taufiq-Yap Yun-Hin, Mohd Maulana bin Tawang, and Rodhyrolin Shahadan. "Thermal degradation of (zinc–aluminium-layered double hydroxide-dioctyl sulphosuccinate) nanocomposite." *Materials chemistry and physics* 74, no. 3 (2002): 265-271. https://doi.org/10.1016/S0254-0584(01)00481-3.

[178] Warren, BE T., and P. Bodenstein. "The shape of two-dimensional carbon black reflections." *Acta Crystallographica* 20, no. 5 (1966): 602-605. https://doi.org/10.1107/s0365110x66001464.

[179] Aisawa, Sumio, Hidetoshi Hirahara, Hiroaki Uchiyama, Satoshi Takahashi, and Eiichi Narita. "Synthesis and thermal decomposition of Mn–Al layered double hydroxides." *Journal of Solid State Chemistry* 167, no. 1 (2002): 152-159.

[180] Venugopal, B. R., C. Shivakumara, and Michael Rajamathi. "A composite of layered double hydroxides obtained through random costacking of layers from Mg–Al and Co–Al LDHs by delamination–restacking: Thermal decomposition and reconstruction behavior." *Solid state sciences* 9, no. 3-4 (2007): 287-294. https://doi.org/10.1016/j.solidstatesciences.2007.01.006.

[181] Zhang, Fen, Chang-lei Zhang, S. O. N. G. Liang, Rong-chang Zeng, Zhen-guo Liu, and Hong-zhi Cui. "Corrosion of in-situ grown MgAl-LDH coating

on aluminum alloy." *Transactions of Nonferrous Metals Society of China* 25, no. 10 (2015): 3498-3504.

[182] Elhalil, Alaâeddine, Meryem Farnane, Aicha Machrouhi, Fatima Zahra Mahjoubi, Rachid Elmoubarki, Hanane Tounsadi, Mohamed Abdennouri, and Noureddine Barka. "Effects of molar ratio and calcination temperature on the adsorption performance of Zn/Al layered double hydroxide nanoparticles in the removal of pharmaceutical pollutants." *Journal of Science: Advanced Materials and Devices* 3, no. 2 (2018): 188-195. https://doi.org/10.1016/j.jsamd.2018.03.005.

[183] Yan, Zhaoxiong, Bicheng Zhu, Jiaguo Yu, and Zhihua Xu. "Effect of calcination on adsorption performance of Mg–Al layered double hydroxide prepared by a water-in-oil microemulsion method." *RSC advances* 6, no. 55 (2016): 50128-50137. https://doi.org/10.1039/c6ra05253c.

[184] Liang, Aoyan, Xiaosong Jiang, Xin Hong, Yixin Jiang, Zhenyi Shao, and Degui Zhu. "Recent developments concerning the dispersion methods and mechanisms of graphene." *Coatings* 8, no. 1 (2018): 33. https://doi.org/10.3390/coatings8010033.

[185] Du, Hongjian, and Sze Dai Pang. "Dispersion and stability of graphene nanoplatelet in water and its influence on cement composites." *Construction and Building Materials* 167 (2018): 403-413. https://doi.org/10.1016/j.conbuildmat.2018.02.046.

[186] Kameda, Tomohito, Yuki Fubasami, and Toshiaki Yoshioka. "Kinetics and equilibrium studies on the treatment of nitric acid with Mg–Al oxide obtained by thermal decomposition of NO3--intercalated Mg–Al layered double hydroxide." *Journal of colloid and interface science* 362, no. 2 (2011): 497-502. https://doi.org/10.1016/j.jcis.2011.06.065.

[187] Serdechnova, Maria, Andrei N. Salak, Filipe S. Barbosa, Daniel EL Vieira, João Tedim, Mikhail L. Zheludkevich, and Mário GS Ferreira. "Interlayer intercalation and arrangement of 2-mercaptobenzothiazolate and 1, 2, 3-benzotriazolate anions in layered double hydroxides: In situ X-ray diffraction study." *Journal of SolidState Chemistry* 233 (2016): 158-165. https://doi.org/10.1016/j.jssc.2015.10.023.

[188] Mitran, Gheorghiţa, Thomas Cacciaguerra, Stéphane Loridant, Didier Tichit, and Ioan-Cezar Marcu. "Oxidative dehydrogenation of propane over cobalt-containing mixed oxides obtained from LDH precursors." *Applied Catalysis A: General* 417 (2012): 153-162. https://doi.org/10.1016/j.apcata.2011.12.038.

[189] Bontchev, Ranko P., Shirley Liu, James L. Krumhansl, James Voigt, and Tina M. Nenoff. "Synthesis, characterization, and ion exchange properties of hydrotalcite Mg6Al2 (OH) 16 (A) x (A ‘) 2-x⊙ 4H2O (A, A ‘= Cl-, Br-, I-, and NO3-, 2≥ x≥ 0) derivatives." *Chemistry of materials* 15, no. 19 (2003): 3669-3675. https://doi.org/10.1021/cm034231r.

[190] Iqbal, Muhammad Ahsan, Maria Secchi, Muhammad Adeel Iqbal, Maurizio Montagna, Caterina Zanella, and Michele Fedel. "MgAl-LDH/graphene protective film: Insight into LDH-graphene interaction." *Surface and Coatings Technology* 401 (2020): 126253.

[191] Zheming, Ni, Xia Shengjie, Fang Caiping, Wang Ligeng, and Hu Jun. "Synthesis, characterization and thermal property of Cu/Co/Mg/Al hydrotalcite like compounds." *Rare Metal Materials and Engineering S* 2 (2008).

[192] J.T. Kloprogge, L. Hickey, R.L. Frost, FT-Raman and FT-IR spectroscopic study of synthetic Mg/Zn/Al-hydrotalcites, J. Raman Spectrosc. 35 (2004) 967–974. https://doi.org/10.1002/jrs.1244.

[193] Malard, L. M., Marcos Assunção Pimenta, Gene Dresselhaus, and M. S. Dresselhaus. "Raman spectroscopy in graphene." *Physics reports* 473, no. 5-6 (2009): 51-87. https://doi.org/10.1016/j.physrep.2009.02.003.

[194] Ferrari, Andrea C. "Raman spectroscopy of graphene and graphite: Disorder, electron–phonon coupling, doping and nonadiabatic effects." *Solid state communications* 143, no. 1-2 (2007): 47-57. https://doi.org/10.1016/j.ssc.2007.03.052.

[195] M. Castriota, E. Cazzanelli, D. Pacilè, L. Papagno, Ç.O. Girit, J.C. Meyer, A. Zettl, M. Giarola, G. Mariotto, Spatial dependence of Raman frequencies in ordered and disordered monolayer graphene, Diam. Relat. Mater. 19 (2010) 608–613. https://doi.org/10.1016/j.diamond.2009.12.013.

[196] Cao, Cheng-Fei, Guo-Dong Zhang, Li Zhao, Li-Xiu Gong, Jie-Feng Gao, Jian-Xiong Jiang, Long-Cheng Tang, and Yiu-Wing Mai. "Design of mechanically stable, electrically conductive and highly hydrophobic three-dimensional graphene nanoribbon composites by modulating the interconnected network on polymer foam skeleton." *Composites Science and Technology* 171 (2019): 162-170. https://doi.org/10.1016/j.compscitech.2018.12.014.

[197] Wu, Qian, Li-Xiu Gong, Yang Li, Cheng-Fei Cao, Long-Cheng Tang, Lianbin Wu, Li Zhao et al. "Efficient flame detection and early warning sensors on combustible materials using hierarchical graphene oxide/silicone coatings." *ACS nano* 12, no. 1 (2018): 416-424. https://doi.org/10.1021/acsnano.7b06590.

[198] Wang, Jian-Nan, Yong-Lai Zhang, Yan Liu, Wanhua Zheng, Luke P. Lee, and Hong-Bo Sun. "Recent developments in superhydrophobic graphene and graphene-related materials: from preparation to potential applications." *Nanoscale* 7, no. 16 (2015): 7101-7114. https://doi.org/10.1039/c5nr00719d.

[199] Qiang, Fei, Li-Li Hu, Li-Xiu Gong, Li Zhao, Shi-Neng Li, and Long-Cheng Tang. "Facile synthesis of super-hydrophobic, electrically conductive and mechanically flexible functionalized graphene nanoribbon/polyurethane sponge for efficient oil/water separation at static and dynamic states." *Chemical Engineering Journal* 334 (2018): 2154-2166. https://doi.org/10.1016/j.cej.2017.11.054.

[200] Böhm, Siva. "Graphene against corrosion." *Nature nanotechnology* 9, no. 10 (2014): 741-742. https://doi.org/10.1038/nnano.2014.220.

[201] G. Zhang, L. Wu, A. Tang, Y. Ma, G.L. Song, D. Zheng, B. Jiang, A. Atrens, F. Pan, Active corrosion protection by a smart coating based on a MgAl-layered double hydroxide on a cerium-modified plasma electrolytic oxidation coating on Mg alloy AZ31, Corros. Sci. 139 (2018) 370–382. https://doi.org/10.1016/j.corsci.2018.05.010.

[202] M. Kaseem, Y.G. Ko, A novel composite system composed of zirconia and LDHs film grown on plasma electrolysis coating: Toward a stable smart coating, Ultrason. Sonochem. 49 (2018) 316–324. https://doi.org/10.1016/j.ultsonch.2018.08.023.

[203] N.C. Rosero-Navarro, S.A. Pellice, A. Durán, M. Aparicio, Effects of Ce-containing sol-gel coatings reinforced with SiO2 nanoparticles on the protection of AA2024, Corros. Sci. 50 (2008) 1283–1291. https://doi.org/10.1016/j.corsci.2008.01.031.

[204] C. Ke, Y. Wu, Y. Qiu, J. Duan, N. Birbilis, X.B. Chen, Influence of surface chemistry on the formation of crystalline hydroxide coatings on Mg alloys in liquid water and steam systems, Corros. Sci. 113 (2016) 145–159. https://doi.org/10.1016/j.corsci.2016.10.017.

[205] J.J. De Damborenea, B. Davo, Use of rare earth salts as electrochemical corrosion inhibitors for an Al – Li – Cu (8090) alloy in 3 . 56 % NaCl, 49 (2004) 4957–4965. https://doi.org/10.1016/j.electacta.2004.06.008.

[206] F. Zhang, Z. Liu, R. Zeng, S. Li, H. Cui, L. Song, E. Han, Surface & Coatings Technology Corrosion resistance of Mg – Al-LDH coating on magnesium alloy AZ31, Surf. Coat. Technol. (2014). https://doi.org/10.1016/j.surfcoat.2014.07.017.

[207] B. Dou, Y. Wang, T. Zhang, B. Liu, Y. Shao, G. Meng, F. Wang, Growth Behaviors of Layered Double Hydroxide on Microarc Oxidation Film and Anti-Corrosion Performances of the Composite Film, 163 (2016) 917–927. https://doi.org/10.1149/2.1141614jes.

[208] B.J. Usman, F. Scenini, M. Curioni, Corrosion Testing of Anodized Aerospace Alloys: Comparison Between Immersion and Salt Spray Testing using Electrochemical Impedance Spectroscopy, J. Electrochem. Soc. 167 (2020) 041505. https://doi.org/10.1149/1945-7111/ab74e3.

[209] B. Zhu, M. Fedel, N.-E. Andersson, P. Leisner, F. Deflorian, C. Zanella, Effect of Si Content and Morphology on Corrosion Resistance of Anodized Cast Al-Si Alloys, J. Electrochem. Soc. 164 (2017) C435–C441. https://doi.org/10.1149/2.1631707jes.

[210] Y. Huang, H. Shih, J. Daugherty, F. Mansfeld, Evaluation of the properties of anodized aluminum 6061 subjected to thermal cycling treatment using electrochemical impedance spectroscopy (EIS), Corros. Sci. 51 (2009) 2493–2501. https://doi.org/10.1016/j.corsci.2009.06.031.

[211] Y. Huang, H. Shih, H. Huang, J. Daugherty, S. Wu, S. Ramanathan, C. Chang, F. Mansfeld, Evaluation of the corrosion resistance of anodized aluminum 6061 using electrochemical impedance spectroscopy (EIS), Corros. Sci. 50 (2008) 3569–3575. https://doi.org/10.1016/j.corsci.2008.09.008.

[212] D. Veys-Renaux, R. Drevet, C. Petitjean, L. Aranda, N. David, P. Berthod, Electrochemical behavior of CoSb3 in sulfuric and oxalic acids over the potential range 0 to 40 V, J. Solid State Electrochem. 22 (2018) 2821–2828. https://doi.org/10.1007/s10008-018-3990-3.

[213] F. Zhang, C. Örnek, J.O. Nilsson, J. Pan, Anodisation of aluminium alloy AA7075 – Influence of intermetallic particles on anodic oxide growth, Corros. Sci. 164 (2020). https://doi.org/10.1016/j.corsci.2019.108319.

[214] T.P. Hoar, G.C. Wood, On the Assessment of Sealing of Anodic Oxide Films on Aluminium, Trans. IMF. 37 (1960) 7–10. https://doi.org/10.1080/00202967.1960.11869796.

[215] F. Mansfeld, Analysis and interpretation of EIS data for metals and alloys, Solartron Tech. Rep. 26 (1999) 77. https://doi.org/10.1645/0022-3395(2002)088[0972:AMPOMP]2.0.CO;2.

[216] V. Moutarlier, M.P. Gigandet, B. Normand, J. Pagetti, EIS characterisation of anodic films formed on 2024 aluminium alloy, in sulphuric acid containing molybdate or permanganate species, Corros. Sci. 47 (2005) 937–951. https://doi.org/10.1016/j.corsci.2004.06.019.

[217] J.H. Scofield, Comment on Fractal model for the ac response of a rough interface, Phys. Rev. Lett. 56 (1986) 268. https://doi.org/10.1103/PhysRevLett.56.268.

[218] L. Bouchama, N. Azzouz, N. Boukmouche, J.P. Chopart, A.L. Daltin, Y. Bouznit, Enhancing aluminum corrosion resistance by two-step anodizing process, Surf. Coatings Technol. 235 (2013) 676–684. https://doi.org/10.1016/j.surfcoat.2013.08.046.

[219] D. Zhu, W.J. Van Ooij, Corrosion protection of AA 2024-T3 by bis- [3-(triethoxysilyl) propyl] tetrasulfide in sodium chloride solution . Part 2 :

mechanism for corrosion protection, 45 (2003) 2177–2197. https://doi.org/10.1016/S0010-938X(03)00061-1.

[220] E.A. Matter, S. Kozhukharov, M. Machkova, V. Kozhukharov, Comparison between the inhibition efficiencies of Ce(III) and Ce(IV) ammonium nitrates against corrosion of AA2024 aluminum alloy in solutions of low chloride concentration, Corros. Sci. 62 (2012) 22–33. https://doi.org/10.1016/j.corsci.2012.03.039.

[221] D. Raps, T. Hack, J. Wehr, M.L. Zheludkevich, A.C. Bastos, M.G.S. Ferreira, O. Nuyken, Electrochemical study of inhibitor-containing organic – inorganic hybrid coatings on AA2024, Corros. Sci. 51 (2009) 1012–1021. https://doi.org/10.1016/j.corsci.2009.02.018.

[222] H. Shi, E.H. Han, F. Liu, S. Kallip, Protection of 2024-T3 aluminium alloy by corrosion resistant phytic acid conversion coating, Appl. Surf. Sci. 280 (2013) 325–331. https://doi.org/10.1016/j.apsusc.2013.04.156.

[223] M.A. Arenas, J.J. De Damborenea, Growth mechanisms of cerium layers on gal v anised steel, 48 (2003) 3693–3698. https://doi.org/10.1016/S0013-4686(03)00507-3.

[224] Iqbal, Muhammad Ahsan, and Michele Fedel. "Protective Cerium-Based Layered Double Hydroxides Thin Films Developed on Anodized AA6082." *Advances in Materials Science and Engineering* 2020 (2020). https://doi.org/10.1155/2020/5785393.

[225] Z. Wang, X. Shen, T. Qian, K. Xu, Q. Sun, C. Jin, Fabrication of superhydrophobic Mg/Al layered double hydroxide (LDH) coatings on medium density fiberboards (MDFs) with flame retardancy, Materials (Basel). 11 (2018) 13–15. https://doi.org/10.3390/ma11071113.

[226] J.T. Simpson, S.R. Hunter, T. Aytug, Superhydrophobic materials and coatings: A review, Reports Prog. Phys. 78 (2015). https://doi.org/10.1088/0034-4885/78/8/086501.

[227] G. Wang, D. Rao, K. Li, Y. Lin, UV blocking by Mg-Zn-Al layered double hydroxides for the protection of asphalt road surfaces, Ind. Eng. Chem. Res. 53 (2014) 4165–4172. https://doi.org/10.1021/ie403901n.

[228] G. Wang, S. Xu, C. Xia, D. Yan, Y. Lin, M. Wei, Fabrication of host-guest UV-blocking materials by intercalation of fluorescent anions into layered double hydroxides, RSC Adv. 5 (2015) 23708–23714. https://doi.org/10.1039/c5ra00589b.

[229] Y. Cao, D. Zheng, X. Li, J. Lin, C. Wang, S. Dong, C. Lin, Enhanced Corrosion Resistance of Superhydrophobic Layered Double Hydroxide Films with Long-Term Stability on Al Substrate, ACS Appl. Mater. Interfaces. 10 (2018) 15150–15162. https://doi.org/10.1021/acsami.8b02280.

[230] Y. Huang, Z. Feng, H. Zhang, J. Yu, Effect of Layered Double Hydroxides (LDHs) on Aging Properties of Bitumen, 40 (2020) 734–739.

[231] L. Li, T. Huang, J. Lei, J. He, L. Qu, P. Huang, W. Zhou, N. Li, F. Pan, Robust Biomimetic-Structural Superhydrophobic Surface on Aluminum Alloy, (2015). https://doi.org/10.1021/am505582j.

[232] N. Wang, D. Xiong, Y. Deng, Y. Shi, K. Wang, Mechanically Robust Superhydrophobic Steel Surface with Anti- Icing, UV-Durability, and Corrosion Resistance Properties, (2015). https://doi.org/10.1021/acsami.5b00558.

[233] T. Yan, S. Xu, Q. Peng, L. Zhao, X. Zhao, X. Lei, F. Zhang, Self-Healing of Layered Double Hydroxide Film by Dissolution / Recrystallization for Corrosion Protection of Aluminum, 160 (2013) 480–486. https://doi.org/10.1149/2.053310jes.

[234] M.A. Iqbal, M. Fedel, Effect of synthesis conditions on the controlled growth of MgAl-LDH corrosion resistance film: Structure and corrosion resistance properties, Coatings. 9 (2019). https://doi.org/10.3390/coatings9010030.

[235] M.A. Iqbal, L. Sun, A.M. LaChance, H. Ding, M. Fedel, In situ growth of a CaAl-NO 3 − -layered double hydroxide film directly on an aluminum alloy for corrosion resistance , Dalt. Trans. (2020). https://doi.org/10.1039/c9dt01773a.

[236] M.A. Iqbal, L. Sun, H. Asghar, M. Fedel, Chlorides Entrapment Capability of Various In-Situ Grown NiAl-LDHs: Structural and Corrosion Resistance Properties, Coatings. 10 (2020) 384. https://doi.org/10.3390/coatings10040384.

[237] Iqbal, Muhammad Ahsan, and Michele Fedel. "Protective Cerium-Based Layered Double Hydroxides Thin Films Developed on Anodized AA6082." *Advances in Materials Science and Engineering* 2020 (2020).

[238] Y. Cao, D. Zheng, X. Li, J. Lin, C. Wang, S. Dong, C. Lin, Enhanced Corrosion Resistance of Superhydrophobic Layered Double Hydroxide Films with Long-Term Stability on Al Substrate, ACS Appl. Mater. Interfaces. 10 (2018) 15150–15162. https://doi.org/10.1021/acsami.8b02280.

[239] Iqbal, Muhammad Ahsan, Luyi Sun, Humaira Asghar, and Michele Fedel. "Chlorides Entrapment Capability of Various In-Situ Grown NiAl-LDHs: Structural and Corrosion Resistance Properties." *Coatings* 10, no. 4 (2020): 384.

[240] Luo, Xiaohu, Song Yuan, Xinyu Pan, Caixia Zhang, Shuo Du, and Yali Liu. "Synthesis and enhanced corrosion protection performance of reduced graphene oxide nanosheet/ZnAl layered double hydroxide composite films by hydrothermal continuous flow method." *ACS Applied Materials & Interfaces* 9, no. 21 (2017): 18263-18275. https://doi.org/10.1021/acsami.7b02580.

[241] Imanieh, Iman, and Abdollah Afshar. "Corrosion protection of aluminum by smart coatings containing layered double hydroxide (LDH) nanocontainers." *Journal of Materials Research and Technology* 8, no. 3 (2019): 3004-3023. https://doi.org/10.1016/j.jmrt.2018.05.030.

[242] K.A. Yasakau, A. Kuznetsova, S. Kallip, M. Starykevich, J. Tedim, M.G.S. Ferreira, M.L. Zheludkevich, A novel bilayer system comprising LDH conversion layer and sol-gel coating for active corrosion protection of AA2024, Corros. Sci. 143 (2018) 299–313. https://doi.org/10.1016/j.corsci.2018.08.039.

[243] World Health Organization. "Guidelines for third edition recommendations drinking-water quality." *Geneva: World Health Organization* (2004).

[244] Sambu, Sammy, and Richard Wilson. "Arsenic in food and water–a brief history." *Toxicology and industrial health* 24, no. 4 (2008): 217-226.

[245] He, Fan, Ziyang Lu, Minshan Song, Xinlin Liu, Hua Tang, Pengwei Huo, Weiqiang Fan, Hongjun Dong, Xiangyang Wu, and Guoliang Xing. "Construction of ion imprinted layer modified ZnFe2O4 for selective Cr (VI) reduction with simultaneous organic pollutants degradation based on different reaction channels." *Applied Surface Science* 483 (2019): 453-462.

[246] Zhang, Fen, Chang-lei Zhang, S. O. N. G. Liang, Rong-chang Zeng, Zhen-guo Liu, and Hong-zhi Cui. "Corrosion of in-situ grown MgAl-LDH coating on aluminum alloy." *Transactions of Nonferrous Metals Society of China* 25, no. 10 (2015): 3498-3504.

[247] Ardau, Carla, Franco Frau, and Pierfranco Lattanzi. "New data on arsenic sorption properties of Zn–Al sulphate layered double hydroxides: Influence of competition with other anions." *Applied clay science* 80 (2013): 1-9.

[248] Lu, Ziyang, Zehui Yu, Jinbo Dong, Minshan Song, Yang Liu, Xinlin Liu, Zhongfei Ma, Hang Su, Yongsheng Yan, and Pengwei Huo. "Facile microwave

synthesis of a Z-scheme imprinted ZnFe2O4/Ag/PEDOT with the specific recognition ability towards improving photocatalytic activity and selectivity for tetracycline." *Chemical Engineering Journal* 337 (2018): 228-241.. https://doi.org/10.1016/j.cej.2017.12.115.

[249] Rahman, Mir Tamzid, Tomohito Kameda, Shogo Kumagai, and Toshiaki Yoshioka. "Adsorption isotherms and kinetics of arsenic removal from aqueous solution by Mg–Al layered double hydroxide intercalated with nitrate ions." *Reaction Kinetics, Mechanisms and Catalysis* 120, no. 2 (2017): 703-714. https://doi.org/10.1007/s11144-016-1116-4.

[250] Dousova, B., V. Machovic, D. Kolousek, F. Kovanda, and V. Dornicak. "Sorption of As (V) species from aqueous systems." *Water, air and soil pollution* 149, no. 1-4 (2003): 251. https://doi.org/10.1023/A:1025632005981.

[251] Wu, Xilin, Xiaoli Tan, Shitong Yang, Tao Wen, Hongli Guo, Xiangke Wang, and Anwu Xu. "Coexistence of adsorption and coagulation processes of both arsenate and NOM from contaminated groundwater by nanocrystallined Mg/Al layered double hydroxides." *Water research* 47, no. 12 (2013): 4159-4168. https://doi.org/10.1016/j.watres.2012.11.056.

[252] Yu, Xin-Yao, Tao Luo, Yong Jia, Ren-Xia Xu, Chao Gao, Yong-Xing Zhang, Jin-Huai Liu, and Xing-Jiu Huang. "Three-dimensional hierarchical flower-like Mg–Al-layered double hydroxides: highly efficient adsorbents for As (V) and Cr (VI) removal." *Nanoscale* 4, no. 11 (2012): 3466-3474. https://doi.org/10.1039/c2nr30457k.

[253] P.P. Huang, C.Y. Cao, F. Wei, Y. Bin Sun, W.G. Song, MgAl layered double hydroxides with chloride and carbonate ions as interlayer anions for removal of arsenic and fluoride ions in water, RSC Adv. 5 (2015) 10412–10417. https://doi.org/10.1039/c4ra15160g.

[254] Kitis, Mehmet, Emine Karakaya, Nevzat O. Yigit, Gokhan Civelekoglu, and Ata Akcil. "Heterogeneous catalytic degradation of cyanide using copper-impregnated pumice and hydrogen peroxide." *Water Research* 39, no. 8 (2005): 1652-1662.

[255] Xiong, Yang Yang, Jian Qiang Li, Xue Feng Feng, Li Na Meng, Le Zhang, Pan Pan Meng, Ming Biao Luo, and Feng Luo. "Using MOF-74 for Hg2+ removal from ultra-low concentration aqueous solution." *Journal of Solid State Chemistry* 246 (2017): 16-22.

[256] Li, Linnan, Wen Ma, Sensen Shen, Hexiang Huang, Yu Bai, and Huwei Liu. "A combined experimental and theoretical study on the extraction of uranium by amino-derived metal–organic frameworks through post-synthetic strategy." *ACS Applied Materials & Interfaces* 8, no. 45 (2016): 31032-31041. https://doi.org/10.1021/acsami.6b11332.

[257] Bagherifam, Saeed, Sridhar Komarneni, Amir Lakzian, Amir Fotovat, Reza Khorasani, Wenyan Huang, Jianfeng Ma, and Yujue Wang. "Evaluation of Zn–Al–SO4 layered double hydroxide for the removal of arsenite and arsenate from a simulated soil solution: isotherms and kinetics." *Applied clay science* 95 (2014): 119-125.